Direct Frequency Comb Spectroscopy: Commissioning a New Apparatus and Investigating the Rovibrational Spectroscopy of CH_2X_2 Molecules

Frances Charlotte Roberts

Submitted in accordance with the requirements for the degree of Doctor of Philosophy

The University of Leeds

School of Chemistry

July 2022

Intellectual Property and Publications Statements

The candidate confirms that the work submitted is her own, except where work which has formed part of jointly authored publications has been included. The contribution of the candidate and the other authors to this work has been explicitly indicated below. The candidate confirms that appropriate credit has been given within the thesis where reference has been made to the work of others.

Work in Chapters 2 and 3 has appeared in the following publication: Roberts, F.C., Lewandowski, H.L., Hobson, B.F. and Lehman, J.H. *A Rapid, Spatially Dispersive Frequency Comb Spectrograph Aimed at Gas Phase Chemical Reaction Kinetics.* Mol. Phys., 2020. **118**: 16. The candidate was responsible for building to optical system used for measurements, co-created the analysis code in *MATLAB*, and contributing to the writing of the paper. Julia H. Lehman: built the optical system, collected the experimental data, co-created the analysis code in *MATLAB*, contributed the most to the writing of the paper. H.J. Lewandowski (University of Colorado Boulder): built the optical system, collected the experimental data, wrote the paper. Billy F. Hobson (University of Leeds): created the code for the HAPI simulation. The figures shown in Chapters 2 and 3 are reproduced from the manuscript with permission:

This is an 'Accepted/Original Manuscript' of an article published by Taylor & Francis Group in Molecular Physics on 26 Feb 2020, available online: https://wwww.tandfonline.com/10.1080/00268976.2020.1733116.

Work in Chapter 4 has appeared in the following publication: Roberts, F.C. and J.H. Lehman, *Infrared frequency comb spectroscopy of CH_2I_2: Influence of hot bands and pressure broadening on the ν_1 and ν_6 fundamental transitions.* The Journal of Chemical Physics, 2022. **156**(11): p. 114301. The candidate was responsible for collecting all experimental data (room temperature spectrum and pressure broadening data), analysis of all experimental data to create the spectrum shown in Chapter 4, analysis of computational data, analysis of pressure broadening spectra, completion of the *PGOPHER* simulations, and significantly wrote the manuscript. Julia H. Lehman: Collected computational data, assisted with analysis, wrote the manuscript. The figures and tables shown in Chapter 4 are reproduced from the manuscript with permission:

Reprinted from Roberts, F.C. and J.H. Lehman, *Infrared frequency comb spectroscopy* *of CH_2I_2: Influence of hot bands and pressure broadening on the ν_1 and ν_6 fundamental transitions.* The Journal of Chemical Physics, 2022. **156**(11): p. 114301. with the permission of AIP Publishing.

Work in Chapter 5 is part of an ongoing collaboration between the candidate, J. H. Lehman, I. Sadiek (Leibniz Institute for Plasma Science and Technology), A. F. Foltynowicz (UMEÅ University), and A. Hjalten (UMEÅ University), and titled: Optical frequency comb based measurements and revisited assignment of high resolution spectra of CH_2Br_2 in the 2960 to 3120 cm^{-1} region. The candidate was responsible for collecting all experimental data for the VIPA spectrum (presented in the thesis), analysis of the VIPA experimental spectra, collecting all the pressure broadening data, analysing the pressure broadening data, and contributed to the writing of the manuscript. Julia H. Lehman: collected computational data, assisted with analysis, contributed to the writing of the manuscript. Ibrahim Sadiek: completed the *PGOPHER* analysis of the spectrum. As part of the collaboration, the manuscript also shows the experimental spectrum collected using an FTS set-up, however, these results are not published in this thesis as they belong to Adrian Hjalten and Aleksandra Foltynowicz.

This copy has been supplied on the understanding that it is copyright material and that no quotation from the thesis may be published without proper acknowledgement.

The right of Frances Charlotte Roberts to be identified as Author of this work has been asserted by Frances Charlotte Roberts in accordance with the Copyright, Designs and Patents Act 1988.

© 2022 The University of Leeds and Frances Charlotte Roberts.

Acknowledgements

Firstly, I’d like to acknowledge and thank my two supervisors: Dr Julia Lehman and Professor Dwayne Heard. To Julia, for five years you’ve been my supervisor, from scared little MChem student to fully sarcastic 4th year PhD student. I will miss your eclectic and varied music tastes in lab, but I’m so grateful for all the guidance and advice for the last five years. Hopefully you’ll fondly remember me as your first ever (proper) PhD student. Thank you to Dwayne for offering advice and expertise when needed, your wealth of knowledge did come in use occasionally! I’d also like to acknowledge Professor Heather Lewandowski at the University of Colorado Boulder. Heather became a pseudo-supervisor during my time at Leeds, and her astonishing physics knowledge helped to bolster my physics-lacking chemistry education. I still refuse to use LaTeX and measure things in inches though!

Secondly, I’d like to thank past group members Billy Hobson and Aaron Downing for their contributions. Billy, Laidlaw Scholar from 2019-2021, created the HAPI simulation python code which was used to quantify the initial methane measurements. Aaron, MChem from 2020-2021, recorded initial spectra of CH_2Br_2 and helped to develop the experimental parameters, which I then took over when his project ended. I’d also like to thank current group members Dan Lucas and Dr Théo Guillaume for keeping me entertained the past year, and not laughing too much when I start dancing in lab!

Next, I need to express my thanks to the late Dr Colin Western, University of Bristol, for his help with the *PGOPHER* program. The simulations presented in this thesis would have never been achieved without his input and advice. I’m extremely sad he never had the chance to see the final published results for the CH_2I_2 and CH_2Br_2 spectra. In addition, I need to thank Dr Ibrahim Sadiek, INP, for his help on the *PGOPHER* band-head fitting procedure and his contributions to the final *PGOPHER* simulations for CH_2Br_2. Furthermore, to the CH_2Br_2 ongoing collaboration with Adrian Hjalten and Professor Aleksandra Foltynowicz, UMEÅ University in regards to the CH_2Br_2 spectral results

Finally, I’d like to thank all my family and friends for their ongoing support. To my mum, my sister, Trevor, George, and even the dogs, Bailey and Ronnie, I am eternally grateful to you all for your support and encouragement, even if you do not full understand my research. In particular, thank you for not getting too annoyed with me when I’ve been really stressed.

Abstract

Direct Frequency Comb Spectroscopy is a powerful technique that allows for high spectral resolution and sensitive detection of molecules over a broad spectral bandwidth. While there are many different types of frequency comb lasers and different detection methods, this thesis utilizes a mid-infrared frequency comb laser and a two-dimensional spatially dispersive detection method. The first part of thesis describes the work undertaken to build, commission, and characterise the frequency comb spectrometer. Much of the development work was focused on constructing and optimizing the 2D spatially dispersive detection method, which is composed of a virtually imaged phased array dispersion optic, a diffraction grating, and an infrared thermal imaging camera. In addition, an analysis method in *MATLAB* was developed in order to convert the acquired images to absorption spectra.

The latter half of this thesis utilises this new spectrometer to acquire room temperature, mid-IR (2960 to 3125 cm^{-1}) rovibrational spectra of CH_2I_2 and CH_2Br_2, with an sample pressure of 0.7 to 1 mbar. In general, CH_2X_2 (where X = F, Cl, Br, or I) molecules are atmospherically relevant due to their large global warming potentials (CH_2F_2) or contributions to stratospheric ozone depletion and affecting the tropospheric HO_x and NO_x cycles (CH_2Cl_2, CH_2Br_2, and CH_2I_2). Within the high resolution spectra of CH_2I_2 and CH_2Br_2 the observed vibrational transitions includes the fundamental 6_0^1 and 1_0^1 transitions, alongside hypothesised hot-band transitions $6_0^1 4_n^n$ and $1_0^1 4_n^n$, where $n \leq 5$. For each of the excited vibrational states, spectroscopic rotational constants are determined using a fitting procedure within *PGOPHER*. In addition, the effects of pressure broadening by N_2 and Ar on the observed rovibrational spectra of CH_2I_2 and CH_2Br_2 was studied and discussed. Finally, comparisons are made between mid-infrared rovibrational spectra for all four dihalomethane molecules and the measured pressure broadening coefficients are discussed in comparison to broadening coefficients for CH_2X_2 and CH_3X molecules.

Table of Contents

Intellectual Property and Publications Statements iii
Acknowledgements v
Abstract vii
Table of Contents ix
List of Figures xiii
List of Tables xv
List of Abbreviations xvii
1. Introduction 1
  1.1. Dihalomethane Molecules 1
    1.1.1. Atmospheric Relevance 1
    1.1.2. Previous Studies 4
  1.2. Absorption Spectroscopy 7
    1.2.1. Einstein *A* and *B* Coefficients 8
    1.2.2. Transition Dipole Moment 10
    1.2.3. Beer-Lambert Law 13
    1.2.4. Line Broadening 15
      1.2.4.1. Natural Lifetime Broadening 15
      1.2.4.2. Doppler Broadening 16
      1.2.4.3. Pressure Broadening 16
      1.2.4.4. Instrument Line-shape Function 17
    1.2.5. Absorption Spectroscopy Techniques 18
  1.3. Vibrational and Rotational Spectroscopy 19
    1.3.1. Rotational Spectroscopy 19
    1.3.2. Vibrational Spectroscopy 23
    1.3.3. Rovibrational Spectroscopy 30
    1.3.4. Asymmetric Top Molecules 32
    1.3.5. Resonances and Couplings 33
  1.4. Frequency Comb Spectroscopy 34

1.4.1. Types of Frequency Comb Lasers 36

1.4.2. Detection Methods of Frequency Comb Lasers 37

1.4.3. Comparison of IR Light Sources 39

1.4.4. Applications of Frequency Comb Lasers 40

1.4.4.1. Reaction Kinetics 40

1.4.4.2. Trace-gas monitoring 42

1.4.4.3. High Resolution Spectroscopy 44

2. Experimental: Theory and Techniques 45

2.1. How Frequency Comb Lasers Work 45

2.1.1. Mode-Locking Mechanism 45

2.1.2. Lasing Medium 49

2.1.3. Lasing Cavity 50

2.2. Experimental Apparatus 54

2.2.1. The Optical Layout 54

2.2.2. Frequency Comb Laser 56

2.2.3. Sample Apparatus 59

2.2.3.1. Herriott Cell Fundamentals 59

2.2.3.2. Deployment 62

2.2.4. Gas Delivery 66

2.2.4.1. Gas Sample Line 67

2.2.4.2. Mass Flow Controllers 69

2.2.4.3. Flow Cell 69

2.2.4.4. Free-Jet Expansion Chamber 70

2.2.5. Fibre Coupling 71

2.2.5.1. Theory 71

2.2.5.2. Deployment 72

2.2.6. Detection Method 73

2.2.6.1. VIPA Optic 73

2.2.6.1. Diffraction Grating ... 75
2.2.6.2. Detection Camera ... 76
2.2.6.3. VIPA-Grating-Camera Detection Alignment ... 77
3. Commissioning and Characterising of a Frequency Comb Spectrometer ... 83
3.1. Acquisition ... 83
3.1.1. Changing Imaging Frequencies ... 83
3.1.2. IRBIS Software Control ... 86
3.2. Processing ... 87
3.2.1. Dark Counts on Camera ... 87
3.2.2. MATLAB ... 89
3.2.3. Origin ... 94
3.3. Analysis ... 97
3.3.1. PGOPHER ... 97
3.3.2. Semi-Empirical Method ... 102
3.4. Instrument Line-shape Function ... 103
3.5. Noise ... 106
3.5.1. Uninterruptable Power Source ... 108
3.6. Initialisation of the Free-Jet Expansion Experiment ... 111
3.6.1. Initial Results ... 113
3.7. Conclusion ... 117
4. Rovibrational Absorption Spectroscopy of CH_2I_2 from 2960 to 3125 cm^{-1} ... 119
4.1. Background of CH_2I_2 ... 119
4.2. Experiments ... 123
4.2.1. 300 K Rovibrational Spectrum ... 123
4.2.2. Pressure Broadening ... 125
4.2.3. Computational Calculations ... 126
4.3. Results and Discussions ... 127
4.3.1. 300 K Rovibrational Spectrum ... 127

4.3.1.1. Fitting results of the ν_6 band 131

4.3.1.1. Fitting results of the ν_1 band 138

4.3.1.2. Additional Peaks 142

4.3.2. Pressure Broadening Coefficients 143

4.3.3. Computational Calculations 147

4.4. Conclusion 154

5. Rovibrational Absorption Spectroscopy of CH_2Br_2 from 2925 to 3125 cm^{-1} 155

5.1. Background of CH_2Br_2 155

5.2. Experiments 159

5.2.1. 300 K Rovibrational Spectrum 159

5.2.2. Pressure Broadening 160

5.2.3. Computational Calculations 160

5.3. Results and Discussions 161

5.3.1. 300 K Rovibrational Spectrum 161

5.3.1.1. Fitting results of the ν_6 band 165

5.3.1.2. Fitting results of the ν_1 band 169

5.3.2. Pressure Broadening Coefficients 172

5.3.3. Computational Calculations 175

5.4. Conclusion 188

6. Comparison of CH_2X_2 Molecules 189

6.1. Room Temperature Mid-IR Spectra 189

6.2. Pressure Broadening Coefficients 196

7. Final Remarks 199

7.1. Future Work 199

7.1.1. Enhanced Optical Cavity 199

7.1.2. Cold Spectra Prediction 200

7.2. Conclusion 205

8. References 207

List of Figures

Figure 1-1 Two State System. 9
Figure 1-2 Pressure Broadening Oscillating Dipole Moment. 17
Figure 1-3 Harmonic and Anharmonic Potential Energy Surfaces. 25
Figure 1-4 Rovibrational Energy Levels. 31
Figure 1-5 Projection of J as quantum number K. 32
Figure 2-1 Fourier Transforming Femtosecond Pulses. 48
Figure 2-2 Erbium Laser Emission. 50
Figure 2-3 Carrier Envelope Offset. 53
Figure 2-4 Optical Layout. 55
Figure 2-5 Frequency Generation Modular Compartments. 57
Figure 2-6 Spectral Profile of the Frequency Comb. 58
Figure 2-7 Schematic Herriott Cell Laser Spot Patterns. 61
Figure 2-8 Pictures of Herriott Beam Patterns. 62
Figure 2-9 Interaction Regions of Molecules and Optical Cavities. 64
Figure 2-10 Pictures of Sample Apparatus. 65
Figure 2-11 Free-Jet Expansion. 67
Figure 2-12 Gas Sample Line. 68
Figure 2-13 Series 9 Solenoid Pulsed Valve. 70
Figure 2-14 Virtually Imaged Phased Array Optic Schematic. 75
Figure 2-15 Diffraction Grating Schematic. 76
Figure 2-16 VGC Detection Layout Schematic. 78
Figure 2-17 Camera Alignment Images. 82
Figure 3-1 Acquired Images. 85
Figure 3-2 Local Minima Between Fringes. 91
Figure 3-3 Local Minima Between Comb Modes. 91
Figure 3-4 MATLAB Spectrum. 92
Figure 3-5 Multiple Repetition rates. 95
Figure 3-6 Example Spectrum. 96
Figure 3-7 PGOPHER Starter File. 98
Figure 3-8 Constants and Overlay Window. 100
Figure 3-9 Band-head Fitting Line List Creation. 102
Figure 3-10 CH_4 Instrument Line-shape Function. 105

Figure 3-11 50 μs vs 5 μs Camera Integration Times. 108
Figure 3-12 Electrical Baseline Noise. 110
Figure 3-13 Standard Deviation vs Total Integration Time. 112
Figure 3-14 CH_4 300 K and ~40 K Comparison Spectra. 114
Figure 3-15 20 Hz vs 100 Hz Acquisition Method.. 115
Figure 3-16 $CHBr_3$ 300 K and ~40 K Comparison Spectra. 117
Figure 4-1 Full Experimental CH_2I_2 Spectrum. 128
Figure 4-2 Comparison of Experimental and Reference Spectra of CH_2I_2. 130
Figure 4-3 Comparison of CH_2I_2 ν_6 Simulation to Experimental Spectrum. 133
Figure 4-4 CH_2I_2 ν_6 Simulation Breakdown. 134
Figure 4-5 Comparison of CH_2I_2 ν_1 Simulation and Experimental Spectra. 141
Figure 4-6 CH_2I_2 ν_1 Simulation Breakdown. 142
Figure 4-7 CH_2I_2 Pressure Broadening Linear Fit. 145
Figure 4-8 CH_2I_2 Computational Simulated Spectra. 148
Figure 4-9 CH_2I_2 ν_6 wB97X/Def2QZVPP Simulation Comparison Results. 150
Figure 4-10 CH_2I_2 ν_1 wB97X/Def2QZVPP Simulation Comparison Results. 151
Figure 5-1 Full Experimental CH_2Br_2 Spectrum. 162
Figure 5-2 Comparison of Experimental and Reference Spectra of CH_2Br_2. 164
Figure 5-3 Comparison of CH_2Br_2 ν_6 Simulation to Experimental Spectrum. 167
Figure 5-4 CH_2Br_2 ν_6 Simulation breakdown. 168
Figure 5-5 CH_2Br_2 Pressure Data. 174
Figure 5-6 CH_2Br_2 Computational Simulated Spectra.. 177
Figure 5-7 CH_2Br_2 ν_6 wB97X/Def2QZVPP Simulation Comparison Results. 179
Figure 5-8 CH_2Br_2 ν_1 wB97X/Def2QZVPP Simulation Comparison Results. 181
Figure 6-1 Comparison of Room Temperature CH_2I_2 and CH_2Br_2 Spectra. 190
Figure 6-2 Reference Spectra Compare. 193
Figure 6-3 Vibrational Frequencies of CH_2X_2 Molecules and Types of Coupling Between the Vibrational States. 195
Figure 7-1 Comparison of CH_2I_2 Spectra at 300 K and 30 K. 203
Figure 7-2 Comparison of CH_2Br_2 Spectra at 300 K and 30 K. 204

List of Tables

Table 1-1 C_{2v} Character Table. 29

Table 1-2 C_{2v} Product Table. 29

Table 4-1 Literature CH_2I_2 Fundamental Vibrational Band Origins. 122

Table 4-2 Experimentally determined rotational constants for CH_2I_2 for the vibrational modes ν_1 (v = 1), ν_6 (v = 1), ν_1 (v = 1) + ν_4 (v ≤ 4), and ν_6 (v = 1) + ν_4 (v ≤ 5). 139

Table 4-3 CH_2I_2 Pressure Broadening Coefficients. 145

Table 4-4 CH_2I_2 ν_6 Semi-empirical Computational Values. 152

Table 4-5 CH_2I_2 ν_1 Semi-empirical Computational Values. 153

Table 5-1 Literature CH_2Br_2 Fundamental Vibrational Band Origins. 158

Table 5-2 Experimentally determined rotational constants for CH_2Br_2 for the vibrational ν_6 (v = 1) state for each isotopologue. 170

Table 5-3 Experimentally determined rotational constants for CH_2Br_2 for the vibrational states ν_4 (v ≤ 3) and ν_4 (v ≤ 3) + ν_6 (v = 1) for each isotopologue. 171

Table 5-4 CH_2Br_2 Pressure Broadening Coefficients. 174

Table 5-5 $CH_2{}^{79}Br^{79}Br$ ν_6 Semi-empirical Computational Values. 182

Table 5-6 $CH_2{}^{79}Br^{81}Br$ ν_6 Semi-empirical Computational Values. 183

Table 5-7 $CH_2{}^{81}Br^{81}Br$ ν_6 Semi-empirical Computational Values. 184

Table 5-8 $CH_2{}^{79}Br^{79}Br$ ν_1 Semi-empirical Computational Values. 185

Table 5-9 $CH_2{}^{79}Br^{81}Br$ ν_1 Semi-empirical Computational Values. 186

Table 5-10 $CH_2{}^{81}Br^{81}Br$ ν_1 Semi-empirical Computational Values. 187

Table 6-1 Fundamental Vibrational Frequencies of CH_2X_2 Molecules. 192

Table 6-2 Pressure Broadening Coefficients of Various Halogenated Molecules. 198

List of Abbreviations

AR	Anti-Reflective
CCD	Charged Coupled Device
CE-DFCS	Cavity Enhanced Direct Frequency Comb Spectroscopy
CEO	Carrier-Envelope Offset
CFC	Chlorofluorocarbon
CRDS	Cavity Ring-down Spectroscopy
CW	Continuous Wave
DCS	Dual Comb Spectroscopy
DDS	Digital Delay Synthesier
DFCS	Direct Frequency Comb Spectroscopy
DFG	Difference Frequency Generation
DFT	Density Functional Theory
FAGE	Fluorescence Assay by Gas Expansion
FL	Focal Length
FPA	Focal Plane Array
FSR	Free Spectral Range
FT	Fourier Transform
FTIR	Fourier Transform Infrared
FWHM	Full-width-at-half-maximum
GC-MS	Gas Chromatography Mass Spectrometry
GWP	Global Warming Potential
HCFC	Hydrochlorofluorocarbon
HFC	Hydrofluorocarbon
HR	Highly-Reflective
HWM	Half-width-at-half-maximum
ILS	Instrument Line Shape
IR	Infrared
LASER	Light Amplification by Stimulated Emission of Radiation

LIF	Laser-Induced Fluorescence
MFC	Mass Flow Controller
MM	Multi-Mode
NA	Numerical Aperture
NEA	Noise Equivalent Absorption
NOLM	Non-linear Optical Loop Mirror
OPD	Optical Path Difference
OPO	Optical Parametric Oscillator
PDH	Pound-Drever-Hall
PID	Proportional-Integral-Derivative
PPLN	Periodically Poled Lithium Niobate
PR	Partially-Reflective
PTFE	Polytetrafluoroethylene
QCL	Quantum Cascade Laser
SCCM	Standard Cubic Centimetres per Minute
SM	Single-Mode
SNR	Signal-to-Noise Ratio
TDLAS	Tuneable Diode Laser Absorption Spectroscopy
TDM	Transition Dipole Moment
TEM	Transverse Electromagnetic Mode
TOD	Third-Order Dispersion
TOF-MS	Time-of-Flight Mass Spectrometry
UPS	Uninterruptable Power Supply
UV	Ultra-Violet
VGC	VIPA-Grating-Camera
VIPA	Virtually Imaged Phased Array
VOC	Volatile Organic Compound

1. Introduction

This first chapter introduces initial concepts which are important throughout this thesis. Firstly, the dihalogenated methane molecules which are the main study of this thesis are discussed. Secondly, the concepts of absorption spectroscopy, rotational spectroscopy, and vibrational spectroscopy are discussed. In addition, the added topics of rovibrational spectroscopy and asymmetric top molecules are introduced. Finally, a general discussion of frequency comb spectroscopy is presented: different types of frequency comb lasers and different detection methods for frequency comb lasers. In addition, there is a comparison of infrared frequency combs lasers to other infrared light sources. Within the frequency comb spectroscopy section three applications of frequency comb lasers are highlighted.

1.1. Dihalomethane Molecules

1.1.1. Atmospheric Relevance

Of the many molecules within Earth's atmosphere, halogenated molecules (F-, Cl-, Br-, or I-containing) are particularly interesting. [1-3] The work of Molina and Rowland, in particular, brought the role of chlorofluorocarbon (CFC) molecules to the attention of the world with their theory that the photodissociation of chlorine-containing molecules gives rise to a significant concentration of chlorine radicals, which causes the catalytic conversion of stratospheric ozone into oxygen. [4] Consequently, this discovery led to the Montreal Protocol of 1987, [5] which banned the usage of CFCs and HCFCs (hydrochlorofluorocarbons), the latter of which are significant greenhouse gases.

There are numerous sources around the globe for the different halide-containing molecules and global mixing ratios range from ppbv to pptv depending on the specific molecule. (Throughout this thesis, ppt is standard for parts per trillion, not thousands). For example, ClO has a mixing ratio is 30 to 125 pptv in polar locations, [6] whereas BrO has a mixing ratio of 13 pptv in similar polar locations, [7] and IO has a mixing ratio of 50 pptv in the marine boundary layer. [8] In terms of global locations for halogen containing molecules, there are a wide range of sources including biogenic and anthropogenic. For biogenic sources, seawater is a primary source for Cl- and Br-containing molecules, [9-11] whereas I-containing molecules are largely sourced from marine algae. [12, 13] In opposition to coastal locations, for natural sources of F-containing molecules, they are primarily found in rocks such as minerals and volcanoes, however this is only a minute contribution to the global concentration. [14] Anthropogenic sources, on the other hand, contribute a larger percentage to the mixing ratio of F-containing molecules from sources such as fertilizer factories and glass manufacturing. Cl- and Br-containing molecules are also released from anthropogenic sources such as coal combustion processes, waste incineration, water treatment processes, and biomass burning, however these are only small contributions compared to the natural sources described above. [9, 15] For I-containing molecules, no major anthropogenic sources have been identified. [10]

Although there are many types of halogenated molecules in the atmosphere, this thesis will focus on the dihalomethane molecules, CH_2X_2, where X = F, Cl, Br, or I. Within the troposphere, CH_2Cl_2, CH_2Br_2, and CH_2I_2 can all be photolysed to create various radicals (X, CH_2X, CHX_2 etc.), which react then with other atmospherically relevant molecules. For example, the generated X radicals cause stratospheric ozone depletion through a known cycle: [10, 16]

$$CH_2X_2 + h\nu \rightarrow CH_2X + X$$ **_Reaction 1-1_**

$$X + O_3 \rightarrow XO + O_2$$ **_Reaction 1-2_**

$$XO + O \rightarrow X + O_2$$ **_Reaction 1-3_**

In addition, the tropospheric HO_x and NO_x cycles (where $x \leq 2$) can be affected by the halogen molecules: [17, 18]

$$CH_2X_2 + OH \rightarrow CHX_2 + H_2O$$ **_Reaction 1-4_**

$$XO + HO_2 \rightarrow HOX + O_2$$ **_Reaction 1-5_**

$$HOX + h\nu \rightarrow X + OH$$ **_Reaction 1-6_**

$$XO + NO_2 \rightarrow XONO_2$$ **_Reaction 1-7_**

In contrast, CH_2F_2 is generally an unreactive molecule but it does have a large global warming potential (GWP) of 677 making it a greenhouse gas. [19] Due to their involvement in the various atmospheric processes and contributions to global warming, it is useful to know the mixing ratios of the CH_2X_2 molecules. For the CH_2X_2 molecules, the observed mixing ratio depends on the location, for example such molecules are more present at coastal locations. CH_2F_2 had a global average mixing ratio of 11.9 ppt in 2016. [20] Specifically studies at an inland location in Switzerland gave an average mixing ratio of 5.5 ppt whereas coastal measurements near Svalbard gave an average mixing ratio of 9 ppt. [19] CH_2Cl_2 has average mixing ratios ranging from 8.9(2) ppt at Cape Grim (Tasmania), [21] 47(7) ppt at Mace Head Atmospheric Research Station (Ireland) in 2012, [22] to 45.4 ppt at Alert (Canadian Artic). [23] A number of studies have observed the mixing ratio of CH_2Br_2 in the atmosphere to be around 1 pptv: 0.88 pptv over the western Pacific Ocean, [24] 0.85 to 1.75 pptv over the East China Sea, [25] and 1.08(17) pptv at Cape Point, South Africa. [26] CH_2I_2 has average mixing ratios ranging from 0.1 pptv around the west coast of Ireland, [27] to 0.001 pptv at Cape Verde in the North Atlantic Ocean. [28] Outside of these costal locations, the presence of CH_2Cl_2, CH_2Br_2, and CH_2I_2 is virtually non-existent. Further descriptions of the mixing ratios for CH_2Br_2 and CH_2I_2 can be found later in sections 5.1 and 4.1, respectively.

While all of the values quoted above were acquired through GC-MS (gas chromatography mass spectrometry) of air samples, spectroscopic measurements can also be used. Various spectroscopic measurements for atmospheric molecules include: open path dual comb spectroscopy (discussed further in section 1.4.4.2), laser heterodyne spectroscopy, photoacoustic spectroscopy, and cavity ring-down spectroscopy (CRDS). [29] Spectroscopic techniques do have some advantages over GC-MS measurements. For example, the GC-MS technique requires a high temperature at the inlet (300 °C), which can cause degradation of some molecules. This degradation means that some molecules are not accurately analysed. [30] Furthermore, the mass spectrometer part of the technique requires ionisation of the molecules within the sample. This ionisation process can cause selectivity for some molecules over others depending on the ionization source, and fragmentation of the molecules can also occur. This fragmentation becomes an issue if there are multiple similar molecules being analysed, such as the alkanes ethane and pentane. The chromatogram can easily become congested with fragmentations of CH_3^+, $CH_3CH_2^+$ etc. and it becomes harder to quantitatively analyse the amount of a molecule present in the sample.

Spectroscopic techniques, which are appropriate for atmospheric analysis, do not have these issues as they are non-invasive techniques. In particular infrared (IR) light sources can be a good technique for atmospheric observations as the light is low in pulse energy, such that the light is less harmful. IR sources are discussed further in section 1.4.3. In addition, similar molecules can be better distinguished due to their unique vibrational spectra. This distinguishing of molecules can be achieved particularly well in the "fingerprint" region of IR spectroscopy from 600 to 1400 cm^{-1}. However, any vibrational spectra acquired between 600 and 3500 cm^{-1} can be useful in differentiating similar molecules. Although most experimental vibrational spectra can be beneficial to the understanding of the molecule, spectra acquired at high resolution, such that rovibrational absorption peaks can be observed, are particularly useful. Observing rovibrational absorption peaks within a vibrational spectrum means that spectroscopic constants for specific vibrational states can be obtained. Not only does this mean that computationally derived spectra can be compared to experimental spectra for verification, but further predications can also be made for similar molecules. For example, the experimental results for a high resolution spectrum of CH_2I_2, can be used to predict a comparable spectrum for the CH_2Br_2 molecule in terms of overall spectral pattern.

However, while spectroscopic methods are interesting for atmospheric detection, this does require a prior knowledge of the spectra of the molecule. In order to propose using a spectroscopic method for studying CH_2X_2 molecules (or indeed any molecule), the spectroscopic knowledge gaps, in particular for gas-phase vibrational spectroscopy, within available literature need to be identified.

1.1.2. Previous Studies

For the four different CH_2X_2 molecules, there is a wide range of available spectroscopic literature. However, such literature is not evenly distributed between the four molecules. The amount of available literature decreases with increasing halogen weight, such that CH_2F_2 has been studied the most and CH_2I_2 has been studied the least. This section briefly identifies the different areas of gas-phase spectroscopic research (electronic, vibrational, and rotational) for each molecule, and an emphasis is placed on vibrational spectroscopic studies. In some cases, liquid, solid and computational based vibrational studies are also acknowledged.

As stated above, there have been a plethora of gas-phase spectroscopy based studies for CH_2F_2. The high level of studies is indicative of the fact that CH_2F_2 is a hydrofluorocarbon (HFC) molecule, designated as HFC-32, with a GWP 677 times that of CO_2. [19] Firstly, for electronic spectroscopy, there have been many studies detailing the vacuum-ultraviolet

(UV) absorption spectra [31, 32] and photoelectron spectra. [31, 33] Furthermore, there have been studies into the valence and Rydberg states of CH_2F_2 [34] and computational studies have been used to predict anharmonic vibronic spectra. [35] Secondly, for vibrational spectroscopy, there is a range of studies from simply reporting IR absorption intensities and transition energies to understanding the couplings of different vibrational states. [36-49] Within these studies, there are also high resolution vibrational spectrum studies which report rovibrational analysis, resonances and couplings between different vibrational modes. Such studies cover couplings and resonances between 3_0^1 and 9_0^1, [43] 5_0^1 and 7_0^1, [42] 2_0^1 and 8_0^1, [44] 6_0^1 and 2_0^2, [46] and 3_0^1, 5_0^1, 7_0^1, 9_0^1, and 4_0^2 transitions. [39] In addition, a number of computational based papers have been published which use high level theory to predict and explain vibrational energies and couplings within experimental spectra. [50, 51] Finally, for rotational spectroscopy, there are once again many studies detailing the observed microwave spectrum of CH_2F_2 and reporting spectroscopic rotational constants across different vibrational states. [52-55] Further studies have also probed hyperfine structure in CH_2F_2 and looked at how different complexes affect the observed rotational spectra. [56, 57]

Moving onto CH_2Cl_2, there have been many electronic spectroscopy studies covering the vacuum-UV absorption spectrum reporting absorption cross section as a function of wavenumber and temperature. [58-62] In addition, there have also been reported high resolution photoelectron spectra and studies into the fragmentation of CH_2Cl_2 after photon impact. [31, 33, 58, 63] For rotational spectroscopy, there has been a total of three studies detailing the spectroscopic rotational constants for the ground vibrational state alongside the isotopic differences for the three isotopologues of CH_2Cl_2. [64-66] However, there have been more studies concerning the vibrational spectra of CH_2Cl_2. The available vibrational spectroscopic information for CH_2Cl_2 ranges from simple absorption spectra to *ab initio* calculations of the vibrational frequencies. [51, 67-72] In addition, there have been high resolution vibrational spectra of the molecule, which gave insight into the different couplings between the 1_0^1, 6_0^1, $2_0^1 8_0^1$, 2_0^2 and 8_0^2 vibrational transitions [73] and coupling between 7_0^1 and 8_0^1, and 2_0^1 and 8_0^1 transitions. [74] Beyond pure gas-phase vibrational studies, there has also been studies into the liquid-phase and solid-state IR spectra of CH_2Cl_2. [75-78]

For CH_2Br_2, there have been many studies into the electronic spectrum, in particular understanding its photolysis rates as a function of UV light. [79-85] For rotational spectroscopy studies, there are six studies probing the ground vibrational state. [86-91]

Furthermore, one of these studies also determines rotational constants for the ν_4 (v = 1) vibrational state but only for the 79/81 isotopologue. [90] For vibrational studies of CH_2Br_2 there have only been five studies focusing on the gas-phase IR spectrum. [92-96] Three of these papers covers a broad range of the IR spectrum, from 400 to 4000 cm^{-1}. However, the other two papers detail the high resolution spectra of three different vibrational transitions: 8_0^1, 1_0^1, and 6_0^1. In addition to these three gas phase studies, there are further liquid IR, [97] solid state IR, [76, 98] and computational studies, [99, 100] for CH_2Br_2.

Finally, for the CH_2I_2 molecule, there are overall less available gas-phase spectroscopic studies. Justifiably, there is a plethora of studies surrounding the electronic spectroscopy and photolysis pathways of CH_2I_2 (for example, references [80, 82, 101-104] and references therein). For rotational spectroscopy, there have only been two significant studies by the same research group. [105, 106] Which gives spectroscopic rotational constants for the ground (v = 0) and ν_4 ($v \leq 4$) vibrational states. Moving onto vibrational spectroscopy, there has been one recent (2006) published study on the gas-phase IR spectrum of CH_2I_2, [95, 107] and a second study reporting transition energies for only five out of the nine fundamental vibrational transitions. [108] Both studies use the simple technique of Fourier Transform Infrared (FTIR) with a lamp light source to acquire the spectra. Due to the nature of this technique, the spectra are acquired at low resolution and give no further spectral information outside of vibrational transition frequencies. In addition, there are other studies covering solid state, [75, 109, 110] liquid, [108, 111, 112] and computational results [113] for vibrational spectroscopy. None of these studies report any high resolution information on the different vibrational states of CH_2I_2 or witness any rovibrational structure.

When considering the available vibrational spectra of the CH_2X_2 molecules, there is one noticeable absence for high resolution spectra: CH_2I_2. Therefore, this thesis proposes to use the emerging technique of direct frequency comb spectroscopy to understand the room temperature mid-IR rovibrational spectrum of CH_2I_2 from 2960 to 3125 cm^{-1}. In addition, efforts will be undertaken to obtain a similar rovibrational spectrum for CH_2I_2 at low temperatures (< 40 K). As both acquired spectra will be of high resolution, specific spectroscopic constants of the different observed vibrational states can be calculated as a function of temperature. From the two sets of temperature dependent spectroscopic constants, constants for further temperatures can be interpolated/extrapolated to. This is useful as if vibrational spectra were obtained from different sections of the atmosphere, there would be a temperature difference that needs to be accounted for. Furthermore, we can also investigate how increasing the surrounding pressure of the molecule changes the spectrum. These types of pressure broadening experiments are useful for atmospheric observation, as there is a broadening of the transitions and a frequency shift when moving to atmospheric pressure (1013 mbar). In addition, understanding how the spectra change as a function of pressure means that further interpolation/extrapolation can be undertaken so predicted spectra can be obtained for any pressure and temperature combination. However, the results and analysis for CH_2I_2 rovibrational spectrum prompted further research into a comparable spectrum for CH_2Br_2. Therefore, this thesis also presents a mid-IR rovibrational spectrum of CH_2Br_2 from 2920 to 3125 cm^{-1} and the effects of pressure broadening on its spectrum.

1.2. Absorption Spectroscopy

In order to study the rovibrational spectroscopy of the CH_2X_2 molecules, the absorption spectroscopy technique of direct frequency comb spectroscopy (DFCS) will be implemented. While the theory (section 2.1) and background (section 1.4) of frequency combs are discussed elsewhere, this section will focus on the fundamental technique of absorption spectroscopy. Furthermore, the specifics surrounding rotations, vibrations, and their respective spectroscopic theories are discussed in the next section (**Error! Reference source not found.**).

Spectroscopy is the study of how light interacts with matter. Light, or electromagnetic radiation, can be thought of as an oscillating electric and magnetic field propagating through space as a wave. [114] For the purposes of this discussion, the magnetic field will be ignored. As the light is a wave, constructive and destructive interference processes are possible, where constructive interference occurs when two waves are in phase and destructive interference occurs when two waves are out of phase. However, light also has a particle aspect, and as such can be referred to as photons. These two attributes gives rise to the well documented wave-particle duality of light. [115] Considering the energy (*E*) of the light, each photon must have a discrete energy, as suggested in Planck's law, however the wave aspect of the light means there is an associated wavelength (λ, m) of energy:

$$E = h\nu = \frac{hc}{\lambda} \qquad \textbf{\textit{Equation 1-1}}$$

Where h is Planck's constant (J s), c is the speed of light (m s^{-1}), and ν is the frequency (s^{-1}). Spectroscopy can also be thought of as the exchange of energy between the light and the matter. Therefore if a photon of light has energy, we need to consider how this energy is transferred to the molecule. [114]

1.2.1. Einstein *A* and *B* Coefficients

Consider a molecule with two different states, E_0 and E_1, separated in energy by $h\nu_{10}$, where the population between the two states (N_0 and N_1), can be determined using the Boltzmann population equation: [115]

$$\frac{N_1}{N_0} = \exp(-\frac{h\nu_{10}}{kT}) \qquad \textbf{\textit{Equation 1-2}}$$

where *k* is the Boltzmann constant, and *T* is the temperature of the system (and *h* is Planck's constant). Within the molecule, an incoming photon has 3 options: absorption, spontaneous emission, or stimulated emission (Figure 1-1).

If the molecule in state E_0 absorbs a photon with energy $h\nu_{10}$, the density of radiation, $\rho_\nu(\nu_{10})$, can be used to determine a rate of population change in the excited state:

$$\frac{dN_1}{dt} = B_{1\leftarrow 0}\rho_v(\nu_{10})N_0 \qquad \textbf{\textit{Equation 1-3}}$$

here, $B_{1\leftarrow 0}$ is the Einstein *B* coefficient. [114] Similarly, if the molecule is already in the excited state E_1, then the incoming photon can cause stimulated emission, with a rate of:

$$\frac{dN_1}{dt} = -B_{1\rightarrow 0}\rho_v(\nu_{10})N_1 \qquad \textbf{\textit{Equation 1-4}}$$

where $B_{1\rightarrow 0}$ is also the Einstein *B* coefficient. This then generates two photons of equal energy, with the second photon travelling in the same direction as the incoming photon. On the other hand, spontaneous emission can also occur while the molecule is in the E_1 state:

$$\frac{dN_1}{dt} = -A_{1\rightarrow 0}N_1 \qquad \textbf{\textit{Equation 1-5}}$$

with the $A_{1\rightarrow 0}$ rate constant denoted as the Einstein *A* coefficient. [114] This spontaneous process does not require an incident photon. In addition, the Einstein *A* coefficient is inversely related to the lifetime of the excited state. At equilibrium, the rate of absorption and emission must be equal:

$$B_{1\leftarrow 0}\rho_v(\nu_{10})N_0 = A_{1\rightarrow 0}N_1 + B_{1\rightarrow 0}\rho_v(\nu_{10})N_1 \qquad \textbf{\textit{Equation 1-6}}$$

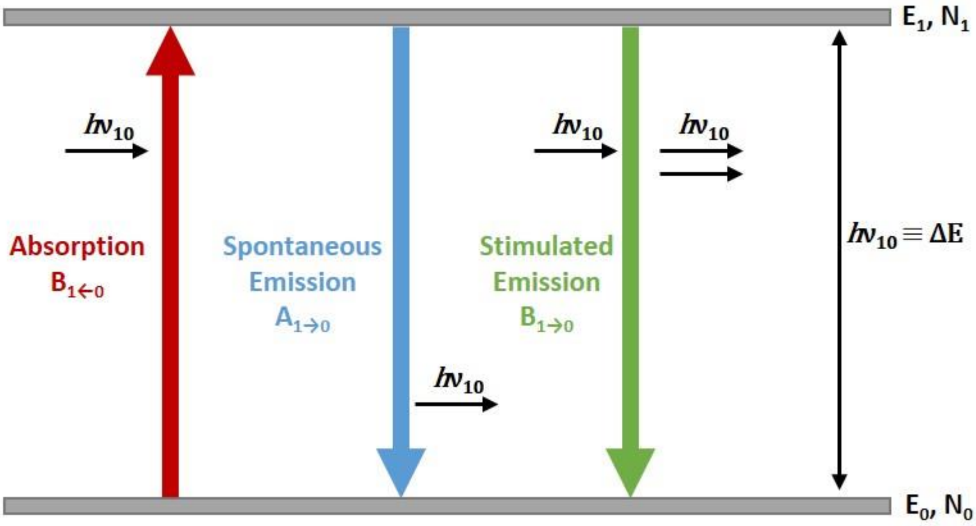

Figure 1-1 Two State System. Schematic showing a two state system within a molecule showing the lower state, E_0, with population N_0, and the upper state, E_1, with population N_1. The two states are separated in energy by ν_{10}. An incoming photon with energy, ν_{10}, can either be absorbed by the system (red) or induced stimulated emission (green). These are denoted by the Einstein *B* coefficients of $B_{1\leftarrow0}$ for absorption and $B_{1\rightarrow0}$ for stimulated emission. In addition, the system can undergo spontaneous emission (blue), which is denoted using the Einstein *A* coefficient: $A_{1\rightarrow0}$.

hence:

$$\frac{N_1}{N_0} = \frac{B_{1\leftarrow0}\rho_\nu}{A_{1\rightarrow0} + B_{1\rightarrow0}\rho_\nu} = \exp(-\frac{h\nu_{10}}{kT}) \qquad \textbf{\textit{Equation 1-7}}$$

solving for $\rho_\nu(\nu_{10})$, yields Equation 1-8. However, as $\rho_\nu(\nu_{10})$ is also related to the Planck function, Equation 1-9 can also be obtained:

$$\rho_\nu(\nu_{10}) = \frac{A_{1\rightarrow0}}{B_{1\leftarrow0}\exp\left(\frac{h\nu_{10}}{kT}\right) - B_{1\rightarrow0}} \qquad \textbf{\textit{Equation 1-8}}$$

$$\rho_\nu(\nu_{10}) = \frac{8\pi h\nu_{10}^3}{c^3}\frac{1}{\exp\left(\frac{h\nu_{10}}{kT}\right) - 1} \qquad \textbf{\textit{Equation 1-9}}$$

However, for both of these equations to be true, the two Einstein *B* coefficients must be equal to each other ($B_{1\leftarrow0} = B_{1\rightarrow0}$), and the Einstein *A* coefficient must relate to the *B* coefficient through: [114]

$$A_{1\rightarrow0} = \frac{8\pi h\nu_{10}^3}{c^3}B_{1\leftarrow0} \qquad \textbf{\textit{Equation 1-10}}$$

While it is interesting that spontaneous and stimulated emission can be linked together, the ν_{10}^3 factor plays an important role in the competition between the two processes. [114]

1.2.2. Transition Dipole Moment

Each energy level of the molecule can be obtained by the solution of the time-independent Schrödinger equation:

$$\hat{H}\psi = E\psi$$ ***Equation 1-11***

where $\hat{H}$ is the Hamiltonian operator, ψ is the wavefunction, and *E* is the energy. In addition, for the case in Equation 1-11, the electromagnetic radiation is treated classically. Using the two level system again (Figure 1-1), the incoming photons can be used to excite from the lower state, E_0, to the upper state, E_1. As the molecule consists of nuclei and electrons at positions $\boldsymbol{r}_i$ and possess charges of q_i, the system as a whole has a net dipole moment **μ**, which can be written using Cartesian coordinates: [114]

$$\mu_x = \sum x_i q_i$$ ***Equation 1-12***

$$\mu_y = \sum y_i q_i$$ ***Equation 1-13***

$$\mu_z = \sum z_i q_i$$ ***Equation 1-14***

where, *x*, *y*, and *z* are the coordinates of the atoms relative to the centre of mass of the molecule. The interaction of the photons with the molecule system is taken into account by the addition of the time-dependent perturbation:

$$\hat{H}' = -\boldsymbol{\mu} \cdot E_0 \cos(\boldsymbol{k} \cdot \boldsymbol{r} - \omega t)$$ ***Equation 1-15***

Where ***k*** is the wave vector with magnitude |k|= 2π/λ and has a direction along the *z*-axis. The probability of the transition occurring is then obtained by solving the time-dependent Schrödinger equation:

$$i\hbar\frac{\partial\Psi}{\partial t} = [\hat{H} + \hat{H}'(t)]\Psi$$ ***Equation 1-16***

in the absence of $\hat{H}'$, the two time-dependent solutions of Equation 1-16 are: [114]

$$\Psi_0 = \psi_0 \exp\left(-\frac{iE_0 t}{\hbar}\right) = \psi_0 \exp(-i\omega_0 t)$$ ***Equation 1-17***

$$\Psi_1 = \psi_1 \exp\left(-\frac{iE_1 t}{\hbar}\right) = \psi_1 \exp(-i\omega_1 t)$$ ***Equation 1-18***

with $\omega_i = E_i/\hbar$. The wavefunctions for the perturbed system is given by the linear combination of the complete set of functions of Ψ_0 and Ψ_1:

$$\Psi(t) = a_0 \psi_0 \exp(-i\omega_0 t) + a_1 \psi_1 \exp(-i\omega_1 t)$$ ***Equation 1-19***

where a_0 and a_1 are time-dependent coefficients. Substituting Equation 1-19 into Equation 1-16 leads to: [114]

$$\begin{gathered} \mathrm{i}\hbar(\dot{a}_0 \psi_0 \exp(-i\omega_0 t) + \dot{a}_1 \psi_1 \exp(-i\omega_1 t) = \\ \hat{H}' a_0 \psi_0 \exp(-i\omega_0 t) + \hat{H}' a_1 \psi_1 \exp(-i\omega_1 t) \end{gathered}$$ ***Equation 1-20***

where the dot notation is used to indicate derivatives with respect to time. [114] Equation 1-20 can then be multiplied by the wavefunction, followed by an integration over all space, which yields two coupled differential equations: [114]

$$\mathrm{i}\hbar\dot{a}_0 = a_0 \langle \psi_0 | \hat{H}' | \psi_0 \rangle + a_1 \langle \psi_1 | \hat{H}' | \psi_1 \rangle \mathrm{e}^{-\mathrm{i}\omega_{10}\mathrm{t}}$$ ***Equation 1-21***

$$\mathrm{i}\hbar\dot{a}_1 = a_0 \langle \psi_0 | \hat{H}' | \psi_0 \rangle \mathrm{e}^{-\mathrm{i}\omega_{10}\mathrm{t}} + a_1 \langle \psi_1 | \hat{H}' | \psi_1 \rangle$$ ***Equation 1-22***

here the Dirac bracket notation has been used to represent the integration of the wavefunctions. However, both of these integrations can be approximated to zero, which reduces Equation 1-21 and Equation 1-22 to:

$$\mathrm{i}\hbar\dot{a}_0 = -a_1 M_{01} E \mathrm{e}^{-\mathrm{i}\omega_{10}\mathrm{t}} \cos(\omega t)$$ ***Equation 1-23***

$$\mathrm{i}\hbar\dot{a}_1 = -a_0 M_{01} E \mathrm{e}^{-\mathrm{i}\omega_{10}\mathrm{t}} \cos(\omega t)$$ ***Equation 1-24***

where M_{01} (= M_{10}) is the transition dipole moment, and is often written as $\boldsymbol{\mu}_{10}$. [114] This transition dipole moment is the most important factor in determining the selection rules and line intensities of transitions within a molecule. Using the Rabi frequency: [116]

$$\omega_R = \frac{M_{10}E}{\hbar} \qquad \textbf{\textit{Equation 1-25}}$$

and the identity:

$$\cos(\omega t) = \frac{e^{i\omega t} + e^{-i\omega t}}{2} \qquad \textbf{\textit{Equation 1-26}}$$

Equation 1-23 and Equation 1-24 can be rewritten as:

$$\dot{a}_0 = \frac{ia_1\omega_R E(e^{-i(\omega_{10}-\omega)t} + e^{-i(\omega_{10}+\omega)t})}{2} \qquad \textbf{\textit{Equation 1-27}}$$

$$\dot{a}_1 = \frac{ia_0\omega_R E(e^{i(\omega_{10}-\omega)t} + e^{i(\omega_{10}+\omega)t})}{2} \qquad \textbf{\textit{Equation 1-28}}$$

from this, the probability for finding the molecule in excited state, E_1, after time, t, is:

$$\begin{aligned} \mathrm{P}_{1\leftarrow 0} = |a_1|^2 &= \frac{\omega_R^2}{\Delta^2} sin^2\left(\frac{\Delta t}{2}\right) \\ &= \frac{\mu_{10}^2 E^2}{\hbar^2} \frac{sin^2[\frac{(\omega - \omega_{10})t}{2}]}{(\omega - \omega_{10})^2} \end{aligned} \qquad \textbf{\textit{Equation 1-29}}$$

however, this equation assumes a monochromatic photon source and short interaction times. These two properties are not consistent due to the Heisenberg uncertainty principle. [114] Therefore, if a monochromatic photon is applied to the system for a time, Δt, then the molecule absorbs a photon of width $\Delta\nu = 1/(2\pi\Delta t)$ in the frequency domain. This uncertainty principle means that before the probability can be calculated, the effects of a finite frequency spread of the photons must be included. Assuming the photons are broad band in frequency, they have a radiation density of $\rho = \varepsilon_0 E^2/2$. Then, the total transition probability is found by integrating over all frequencies, such that: [117]

$$\mathrm{P}_{1\leftarrow 0} = \frac{\mu_{10}^2}{\varepsilon_0\hbar^2}\rho_\nu(\omega_{10})\pi t \qquad \textbf{\textit{Equation 1-30}}$$

in which ρ(ω) is assumed to be slowly varying near ω_{10} so that it can be removed from the integration. Then, the absorption rate per molecule is:

$$\frac{dP_{1\leftarrow 0}}{dt} = \frac{\mu_{10}^2}{\varepsilon_0 \hbar^2}\rho_\nu(\omega_{10})\pi t$$ ***Equation 1-31***

in order to derive the absorption coefficient as a function of transition dipole moment, the absorption rate can be divided by the population, *N*, to give the transition probability per molecule:

$$\frac{dP_{1\leftarrow 0}}{dt} = B_{1\leftarrow 0}\rho_\nu(\nu_{10})$$ ***Equation 1-32***

assuming that the photons are travelling in the *z* direction. Since only the *z*-axis sees the incoming photons, this is the axis undergoing a transition, and as ρ(ν) = 2πρ(ω), the Einstein *A* and *B* coefficients can be rewritten as: [116]

$$B_{1\leftarrow 0} = \frac{1}{6\varepsilon_0 \hbar^2}\mu_{10}^2 = \frac{2\pi^2}{3\varepsilon_0 h^2}\mu_{10}^2$$ ***Equation 1-33***

$$A_{1\rightarrow 0} = \frac{16\pi^3\nu^3}{3\varepsilon_0 h c^3}\mu_{10}^2$$ ***Equation 1-34***

in terms of the transition dipole moments. However, as collisions occur between the photons and the molecules, and that there is a spontaneous lifetime of the E_1 state, these must be added to the Einstein *A* and *B* coefficients as a line-shape function: $g(\nu - \nu_{10})$, yielding: [114]

$$(B_{1\leftarrow 0})_\nu = \frac{2\pi^2}{3\varepsilon_0 h^2}\mu_{10}^2 g(\nu - \nu_{10})$$ ***Equation 1-35***

$$(A_{1\rightarrow 0})_\nu = \frac{16\pi^3\nu^3}{3\varepsilon_0 h c^3}\mu_{10}^2 g(\nu - \nu_{10})$$ ***Equation 1-36***

1.2.3. Beer-Lambert Law

For the majority of spectroscopic measurements, the results are recorded as intensity signal as a function of wavenumber. However, the intensity observed can vary depending on the amount of sample and the distance the photons travel through the sample. Therefore, there needs to be a way to relate the amount of sample to the observed intensity signal. If we consider a sample, with N_0 molecules per cubic metre in the ground state and N_1 molecules in an excited state, a flux of photons (*F*) can be passed through the sample:

$$F = I_0/h\nu$$ **Equation 1-37**

where I_0 is the intensity of the light. [114] As the light travels through the sample, the molecules can either absorb the photons, the photons can induce stimulated emission, or the photons can be scattered by the molecules. After the photons have passed through a distance *L* of the sample, the resulting intensity of the light (*I*) can be measured. If only absorption and stimulated emission have occurred, then the following can be written:

$$\frac{dN_1}{dt} = -B_{1\to 0}\rho_v N_1 + B_{1\leftarrow 0}\rho_v N_0$$ **Equation 1-38**

$$\frac{dN_1}{dt} = \frac{2\pi^2\mu_{10}^2}{3\varepsilon_0 h^2}(N_0 - N_1)g(\nu - \nu_{10})\rho$$ **Equation 1-39**

$$\frac{dN_1}{dt} = \frac{2\pi^2\mu_{10}^2\nu}{3\varepsilon_0 h^2 c}(N_0 - N_1)g(\nu - \nu_{10})F$$ **Equation 1-40**

$$\frac{dN_1}{dt} = \sigma F(N_0 - N_1)$$ **Equation 1-41**

where $\rho = I/c = h\nu F/c$ (radiation density), and ε_0 is the permittivity of a vacuum. [114] Equation 1-41 introduces σ which is referred to as the absorption cross section and is a mathematical interpretation of the effective area that a molecule presents to a stream of photons in a flux: [114]

$$\sigma = \frac{2\pi^2\mu_{10}^2}{3\varepsilon_0 h^2 c}\nu g(\nu - \nu_{10})$$ **Equation 1-42**

If the flux of photons passes through a small portion of sample (*dx*) of the total length, that has a cross-sectional area of 1 m^2, then the change in flux of passing through the sample is:

$$dF = -\sigma F(N_0 - N_1)\,dx$$ **Equation 1-43**

Integrating Equation 1-43 across the total length (*L*) of the sample, this becomes:

$$\ln\left(\frac{F}{F_0}\right) = \ln\left(\frac{I}{I_0}\right) = -\sigma(N_0 - N_1)L$$ ***Equation 1-44***

This can be rewritten into the more recognisable Beer-Lambert law:

$$\mathrm{A}_\nu = \ln\frac{I_\nu}{I_{0,\mathrm{v}}} = N\sigma_\nu L_{path}$$ ***Equation 1-45***

where A_ν is the absorbance of the sample at frequency, ν, $I_{0,v}$ is the intensity of the light with no sample, I_v is the intensity of the light after passing through the sample, *N* is the concentration of the sample (molecule cm^{-3}), σ_ν is the absorption cross section (cm^2 molecule^{-1}) of the corresponding molecule, and L_{path} is the path length of the light through the sample (cm).

1.2.4. Line Broadening

While the incoming photons for absorption spectroscopy have discrete energies, as described by the Heisenberg uncertainty principle, observations within recorded spectra are not always a discrete peak of intensity at a specific frequency. Each observed absorption transition can be broadened due to different line-shape function effects. All line-shape functions are either homogeneous or inhomogeneous. [114] Homogeneous line-shapes occur when all molecules in the system are affected by the same line-shape function, and inhomogeneous line-shapes occur when molecules are in slightly different environments. For spectroscopy, there are six different types of line-shape functions which broaden the observed transitions within a spectrum: Natural lifetime, Doppler, pressure, the instrument line-shape function, transit-time, and power broadening. [114] The last of these two effects are not discussed here as they are not applicable to the topics covered in this thesis.

1.2.4.1. Natural Lifetime Broadening

The natural lifetime broadening of an absorption is the absolute limit on how narrow a spectral line can be. As the excited state has a certain lifetime (τ_{sp}), as determined by the Einstein *A* coefficient:

$$A_{1\to 0} = \frac{1}{\tau_{sp}}$$ ***Equation 1-46***

the time-energy uncertainty relationship states that the product of the energy and the lifetime must be greater than $h/2\pi$. [114] Therefore, the full-width-at-half-maximum (FWHM) of the spectra line (Δν) can be related to the lifetime of the excited state and the Einstein *A* coefficient:

$$\Delta\nu \approx \frac{A_{1\to0}}{2\pi} \approx \frac{1}{2\pi\tau_{sp}}$$ ***Equation 1-47***

1.2.4.2. Doppler Broadening

Doppler broadening is a type of inhomogeneous line-shape function, which as the name suggests, is broadening of the observed spectral lines due to the Doppler effect. The Doppler effect is when there is a change in frequency of a wave in relation to an observer who is moving relative to the wave source. [118] As the molecules have a distribution of velocities, as governed by the Maxwell-Boltzmann distribution:

$$p_v dv = (\frac{m}{2\pi kT})^{1/2} \exp\left(\frac{-mv^2}{2kT}\right) dv$$ ***Equation 1-48***

Where *m* is the mass of the molecule and *v* is the velocity of the molecules (not to be confused with ν which is used to denote vibrational modes, see section 1.3.2). This means that for absorption spectroscopy, as different molecules move with different velocities along the fixed laboratory frame, there is a broadening of the observed spectral lines. This FWHM broadening can be calculated for each molecule:

$$\Delta\nu = 2\nu_0 \sqrt{\frac{2kTln(2)}{mc^2}}$$ ***Equation 1-49***

where, ν_0 is the frequency of the observed spectral line. In addition, as the FWHM of the Doppler broadening increases with increasing temperature, some research groups use cooling techniques on molecules in order to obtain Doppler-free spectra. [119]

1.2.4.3. Pressure Broadening

Also known as collisional broadening, the pressure broadening effect occurs when the sample molecule interacts with other molecules in the system. These other molecules can either be the same as the sample molecule (self-broadening), or different than the sample molecule. If the collision between the two molecules is strong enough, then the oscillating dipole moments of the molecules are affected. [114] Assuming the average time between

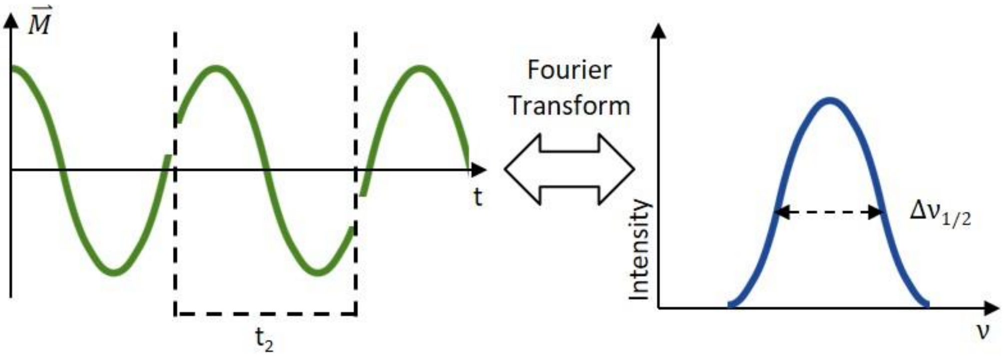

Figure 1-2 Pressure Broadening Oscillating Dipole Moment. Schematic showing an oscillating dipole moment (green) of a molecule (time domain) is interrupted by collisions giving cosine wave lengths of t_2. The Fourier transform of this short cosine wave gives a peak in the frequency domain with a FWHM of $\Delta\nu_{1/2} = 1/\pi t_2$. Adapted from ref. [114]

collisions is t_2, then the oscillating cosine wave (of the dipole moment) is broken down into multiple pieces of average length t_2 (Figure 1-2). If the cosine wave was infinitely long, then the corresponding Fourier transform would be an infinitely narrow peak in the frequency domain. However, as the cosine wave is now broken down into parts of length t_2, taking the Fourier transform of each part of the cosine wave, means the resulting peak in the frequency domain now has a defined width. This defined width can be described by a Lorentzian function with a FWHM of:

$$\Delta\nu_{1/2} = \frac{1}{\pi t_2}$$ ***Equation 1-50***

This is a type of homogeneous line-shape function. In addition, as the average time between collisions is proportional to pressure, p, Equation 1-50 can be rewritten as:

$$\Delta\nu_{1/2} = bp$$ ***Equation 1-51***

where b is the pressure broadening parameter and values for b are approximately 1 cm^{-1} atm^{-1}. [114] In addition, as Equation 1-51 suggests, increasing the pressure of the system for the observed molecule increases the observed broadening of the spectral peaks.

1.2.4.4. Instrument Line-shape Function

As the name suggests, the instrument line-shape (ILS) function is the broadening of the observed transitions due to the limitation of the instrumentation such as the detection method. Depending on the ILS of the system, the broadening by the ILS could be the limiting factor in the minimum observed spectral line width. While this is an important aspect of the acquired spectra, the observed broadening is unique to each system. For example, a pioneering technique using a frequency comb laser and matching the maximum delay range of the spectrometer to the comb line spacing yields an ILS-free spectrum. [120] Thus the detection method is not a limiting factor in recording absorption peaks. This pioneering technique is a complicated and large area of research currently being led by Jun Ye and Aleksandra Foltynowicz. [120-122] However, other techniques can have a large ILS, such as 0.58 cm^{-1} for a standard Fourier Transform spectrometer. [123] This large ILS significantly limits the ability to collect high resolution spectra. The specific instrument line-shape function for the work in this thesis will be discussed in section 3.4.

1.2.5. Absorption Spectroscopy Techniques

As a generalised approach, for absorption spectroscopy, different light sources are used to observe different properties of molecules and atoms. Generally, microwave radiation is used for rotational spectroscopy, IR is used for vibrational spectroscopy, visible and UV light is used for studying electronic transitions, and X-rays are used to understand the structure of molecules. [115] Furthermore, for each of these light sources different detection techniques have been developed. For example, LIF (laser induced fluorescence) is a sensitive technique which excites a specific electronic transitions within molecules such as OH, and then collects the fluorescence as the molecule relaxes back to its ground electronic state. LIF is a common technique used to qualitatively determine the concentration of a product in reaction kinetic experiments. [124] A standard benchtop UV-Vis spectrometer is another instrument used to determine the absorptivity of a molecule across a broad range of wavelengths, typically using a lamp or other UV-Vis light source and either measuring absorption or fluorescence emission. While both of these techniques use visible and UV light, they offer different results.

Furthermore, absorption spectroscopy within literature falls into two general categories: direct and indirect. While these two categories may contain similar light sources, the difference between the two methodologies depends on what is occurring during the course of the experiment. For direct methods, the molecules are being measured directly, whereas for indirect spectroscopy an action is measured, therefore indirect spectroscopy is often referred to as action spectroscopy. A good example of the difference between these two methods is looking at the IR spectrum of the *syn*-CH_3CHOO Criegee intermediate. The works of Liu *et al.* [125] and Lin *et al.* [126] are both concerned with recording vibrational spectra of the *syn*-CH_3CHOO Criegee intermediate. While both studies use the same method to generate the intermediate, photolysing CH_3CHI_2 in the presence of O_2, the experimental method used to obtain the vibrational spectra are different. Firstly, Lin *et al.* [126] utilise a simple step-scan FTIR method to record a vibrational spectrum of *syn*-CH_3CHOO from 830 to 1550 cm^{-1}. Due to the nature of the technique, an absolute value for absorption can be determined. Secondly, Liu *et al.* [125] use a more complicated IR action spectroscopy technique to record a vibrational spectrum of *syn*-CH_3CHOO from 5500 to 6200 cm^{-1}. Within this method, it is important to understand the overall reactions taking place during the course of the experiment: intermediate generated by photolysing CH_3CHI_2 in the presence of O_2, and the syn-CH_3CHOO dissociating into OH + CH_2CHO. Focusing on the syn-CH_3CHOO and the OH species, the *syn*-intermediate can be excited using IR radiation in the CH stretch overtone region or a UV laser can be employed to electronically excite OH which then fluoresces (LIF detection method). If the *syn*-CH_3CHOO intermediate is excited by IR light, then there is less of the un-excited intermediate to dissociate into OH, thus giving less OH detection signal by the LIF method. As the IR laser is scanned across the wavenumber region (5500 to 6200 cm^{-1}), the LIF signal can be observed as a function of the IR wavenumber. This gives an IR action spectrum of the *syn*-CH_3CHOO intermediate. However, in order to derive absolute absorptivity in this method an assumption would have be made that the branching ratio of dissociation is known or that 100% dissociation of CH_3CHOO into OH occurs. Without this knowledge, only a relative intensity IR spectrum can be obtained.

1.3. Vibrational and Rotational Spectroscopy

This section will cover the theory surrounding rotations and vibrations of molecules and how they correspond to spectroscopic observations. In addition, the concept of rovibrational spectroscopy will be discussed, as will the specifics surrounding asymmetric top molecules. Finally, there will be section covering the different resonances and couplings within the rovibrational spectra.

1.3.1. Rotational Spectroscopy

Rotational spectroscopy is used to understand how molecules rotate, where the incoming radiation is used to excite the molecule, causing transitions between rotational states. [115] The rotational transitions are typically low in energy (1 to 100 cm^{-1}), and require microwave radiation in order to undergo the transitions. While rotational spectroscopy can be used like a “molecular fingerprint”, molecular collisions can significantly broaden observed rotational transitions. For example, a rotational study of OCS showed that increasing the pressure of the sample from 0.5 to 3.5 Torr caused a factor of 6 increase of the observed line width, from 2.5 MHz to 15 MHz. [127] This means that rotational spectroscopy is only useful for low pressure measurements of small molecules in the gas phase.

This section will cover the derivation of rotation based on linear molecules and further sections will talk about rotations in the context of rovibrational spectroscopy (1.3.3) and asymmetric top molecules (1.3.4). However, the rotational constants and selection rules are differ for each type of molecule, therefore this section is only valid for linear molecules. In order to understand the rotational energy levels and hence rotational transitions of a molecule, they must be derived. The most rigorous method would be to solve the appropriate rotational energy Schrödinger equation for each molecule, however this is very complicated and extremely time consuming. Instead, a classical mechanics equation for a rotating molecule can be used and specific angular momentum elements of quantum mechanics can be brought in. For the classical representation, we have to consider the moment of inertia (I) of a rigid body about an axis: [114]

$$I = \sum_i m_i r_i^2 \qquad \textbf{Equation 1-52}$$

where m_i is the mass of the element *i* and r_i is the perpendicular distance of element *i* from the axis of rotation. While Equation 1-52 is the rigorous approach for any molecule, a simplification can be made:

$$I = \mu r^2 \qquad \textbf{Equation 1-53}$$

where μ is the reduced mass of the system, and *r* is the bond length (for a diatomic molecule). This simplification assumes that axis of rotation is a fixed point of infinitesimal mass and the moving body has mass, μ. As there are 3 axes of rotation possible (*a, b,* and *c*), each axes can be associated with a moment of inertia: I_a, I_b, and I_c. These three axes can be either be similar or different from each other for each classification of a rotational molecule. For example, for a linear molecule $I_b = I_c$ and $I_a = 0$, whereas for an asymmetric top molecule $I_c \geq I_b \geq I_a$. [115] The moment of inertia can be considered as the rotational equivalent of mass. Therefore, the classical momentum equation used for linear motion can be converted to angular momentum:

$$p = mv \ \rightarrow J = I\omega \qquad \textbf{Equation 1-54}$$

Where *p* is momentum, *v* is velocity, ω is angular frequency, and *J* is angular momentum. Then, using the momentum conversion, the kinetic energy of the rotations can be rewritten: [114]

$$E = \frac{1}{2}mv^2 \rightarrow E = \frac{1}{2}I\omega^2 \ \rightarrow E = \frac{1}{2}I_a\omega_a^2 + \frac{1}{2}I_b\omega_b^2 + \frac{1}{2}I_c\omega_c^2$$

Equation 1-55

where the final part of the equation is used for a multi-axis system. This kinetic energy can then substituted into the specific Schrödinger equation for a spherical harmonic wave function (ψ): [114]

$$\frac{\hat{J}^2\psi}{2I} = E\psi \ \rightarrow \frac{\hat{J}^2\psi}{2I} = \frac{J(J+1)h^2\psi}{8\pi^2 2I} = BJ(J+1)\psi$$

Equation 1-56

Therefore:

$$F(J) = BJ(J+1)$$

Equation 1-57

$$B = \frac{h^2}{8\pi^2 I}\ (joules)\ or\ \frac{h}{8\pi^2 cI} \times 10^{-2}(cm^{-1})$$

Equation 1-58

Where *B* is often referred to as the rotational constant and is unique for each molecule. In addition, J represents the total angular momentum of a molecule and is referred to as the quantum number for rotations. These two equations hold true for linear molecules. However, as asymmetrical top molecules are investigated in this thesis, the alteration to these equations will be discussion in section 0.

However, J can only be positive integer values, meaning the energy levels are considered to be quantised. Alongside quantum number J, M_J can also be defined which is the projection of J onto a space fixed axis, and has values from −J to +J. Therefore M_J has 2J+1 possible values. For example, for a J value of 2, M_J = −2, −1, 0, 1, 2. However, as the orientation of the molecule is random around an arbitrary space-fixed axis, the energy of the M_J levels are degenerate. Hence, for a value of J, there are 2J+1 degenerate levels. For example, for a J value of 2, there are five degenerate levels. Furthermore, as J can be zero, there is no zero-point energy for rotational levels as F(0) = 0. This means, that a molecule can exist in a state where it has zero rotational energy.

In order for a rotational transition to occur, selection rules must be followed. The gross selection rule for rotational transitions is that the molecule must have a permanent dipole moment (μ_{fi}): [114]

$$\boldsymbol{\mu_{fi}} = \int Y^{*}_{Jf,Mj,f}\, \boldsymbol{\hat{\mu}_i} Y_{Ji,Mj,i} d\tau \qquad \textbf{\textit{Equation 1-59}}$$

If Equation 1-59 is solved for a linear molecule, then the specific selection becomes ΔJ = ±1, and ΔM_J = 0, ±1. This specific selection rule can also be justified when thinking about conservation of momentum. As a photon has one unit of angular momentum, J must change by one unit in order to conserve momentum when the molecule absorbs a photon.

In addition to the specific selection rules, a state must have population in order to undergo a transition. Using the Boltzmann equation, the population distribution of the rotational levels can be determined (using an altered version of Equation 1-2):

$$N_J = N g_J \exp(-\frac{h\nu_{10}}{kT}) \qquad \textbf{\textit{Equation 1-60}}$$

where g_J is the degeneracy of level J. This also gives rise to a general expression for a maximum value of J: [114]

$$J_{max} = (\frac{kT}{2hB})^{1/2} - \frac{1}{2} \qquad \textbf{\textit{Equation 1-61}}$$

For the transitions between rigid rotor rotational levels, the energy is determined to be:

$$F(J + 1 \leftarrow J) = 2B(J + 1) \qquad \textbf{\textit{Equation 1-62}}$$

As each J rotational level is located at $2B$, $6B$, $12B$... and so forth, the difference between consecutive J rotational levels is $2B$, $4B$, $6B$… and so forth. Therefore, as a rotational spectrum measures rotational transitions, the spacing between peaks in a pure rotational spectrum will be $2B$.

However, the above energy equations for rotational transitions relies on the molecules remaining as a “rigid rotor”. In real life, this is not the case, as molecules act as “non-rigid rotors”. This non-rigid molecule can be considered as two weights separated by a spring, so as the molecule rotates the bond will stretch and contract giving rise to centrifugal distortion. This distortion causes changes in bond lengths, meaning the moments of inertia increases, and thus the rotational constants decrease. In order to include the distortion in the rotational levels, a correction factor is added to Equation 1-57: [114]

$$F(J) = BJ(J+1) - D_J J^2 (J+1)^2$$ **Equation 1-63**

$$D = \frac{4B^3}{\nu_e^2}$$ **Equation 1-64**

where *D* is known as the distortion constant, and ν_e is the equilibrium vibrational frequency. This correction factor also means that with increasing J, the rotational levels get closer together. Therefore, the observed difference between peaks in a rotational spectrum is no longer set to 2*B*, and now rely on the distortion constant:

$$F(J+1 \leftarrow J) = 2B(J+1) - 4D(J+1)^3$$ **Equation 1-65**

1.3.2. Vibrational Spectroscopy

Vibrational spectroscopy is used to understand how molecules vibrate, where the incoming light is used to excite the molecule between vibrational states. The vibrational transitions are higher in energy than rotational transitions (100 to 5000 cm^{-1}), and require IR radiation in order to undergo the transitions. Just as for rotational spectroscopy, we can consider the molecule as two weights separated by a spring. The potential energy (*V*) of this spring, can be written as a function of the spring's stiffness, using the force constant k_f, and the distance of the bond length (*r*) from the equilibrium position (r_e):

$$V = \frac{1}{2} k_f x^2$$ **Equation 1-66**

$$x = r - r_e$$ **Equation 1-67**

Furthermore, the potential energy can be plotted as a function of the bond length giving a harmonic oscillator potential energy surface (Figure 1-3, part A). This function can be written as a simple parabola: [114]

$$V(x) = V(0) + (\frac{dV}{dx})_0 x + \frac{1}{2}(\frac{d^2V}{dx^2})_0 x^2$$ **Equation 1-68**

The lowest energy of the potential energy surface can be written as:

$$V(x) \approx \frac{1}{2}(\frac{d^2V}{dx^2})_0 x^2 \qquad \textbf{\textit{Equation 1-69}}$$

Combining Equation 1-66 and Equation 1-69 yields:

$$k_f = (\frac{d^2V}{dx^2})_0 \qquad \textbf{\textit{Equation 1-70}}$$

Therefore, the curvature of the potential is directly related to the spring force constant. Essentially, for a weaker bond the curve of the potential is very shallow, whereas for a strong bond the curve of the potential is very steep. In order to calculate the energy levels of the vibrational states, the concept of "particle in a box" is used, however the "box" is now a parabolic function: [114]

$$\hat{H} = -\frac{h^2}{2mc}\frac{d^2}{dx^2} + V(x) \qquad \textbf{\textit{Equation 1-71}}$$

$$-\frac{h^2}{2mc}\frac{d^2\psi}{dx^2} + V\psi = \hat{E}\psi \qquad \textbf{\textit{Equation 1-72}}$$

The corresponding eigenvalues for the wavefunction then yields the quantized energy levels:

$$E_{\mathrm{v}} = \left(\mathrm{v} + \frac{1}{2}\right)h\nu \qquad \textbf{\textit{Equation 1-73}}$$

Where E_{v} is the energy, v is the vibrational quantum number, which can be any positive integer value, and ν is the vibrational frequency. This vibrational frequency can also be calculated using the force constant:

$$\nu = \frac{1}{2\pi}(\frac{k_f}{\mu})^{1/2} \qquad \textbf{\textit{Equation 1-74}}$$

Unlike for rotations, for vibrations in the v = 0 state, the energy is non-zero. This means that as the temperature of the molecule approaches absolute zero, there must always be some form of vibrational motion.

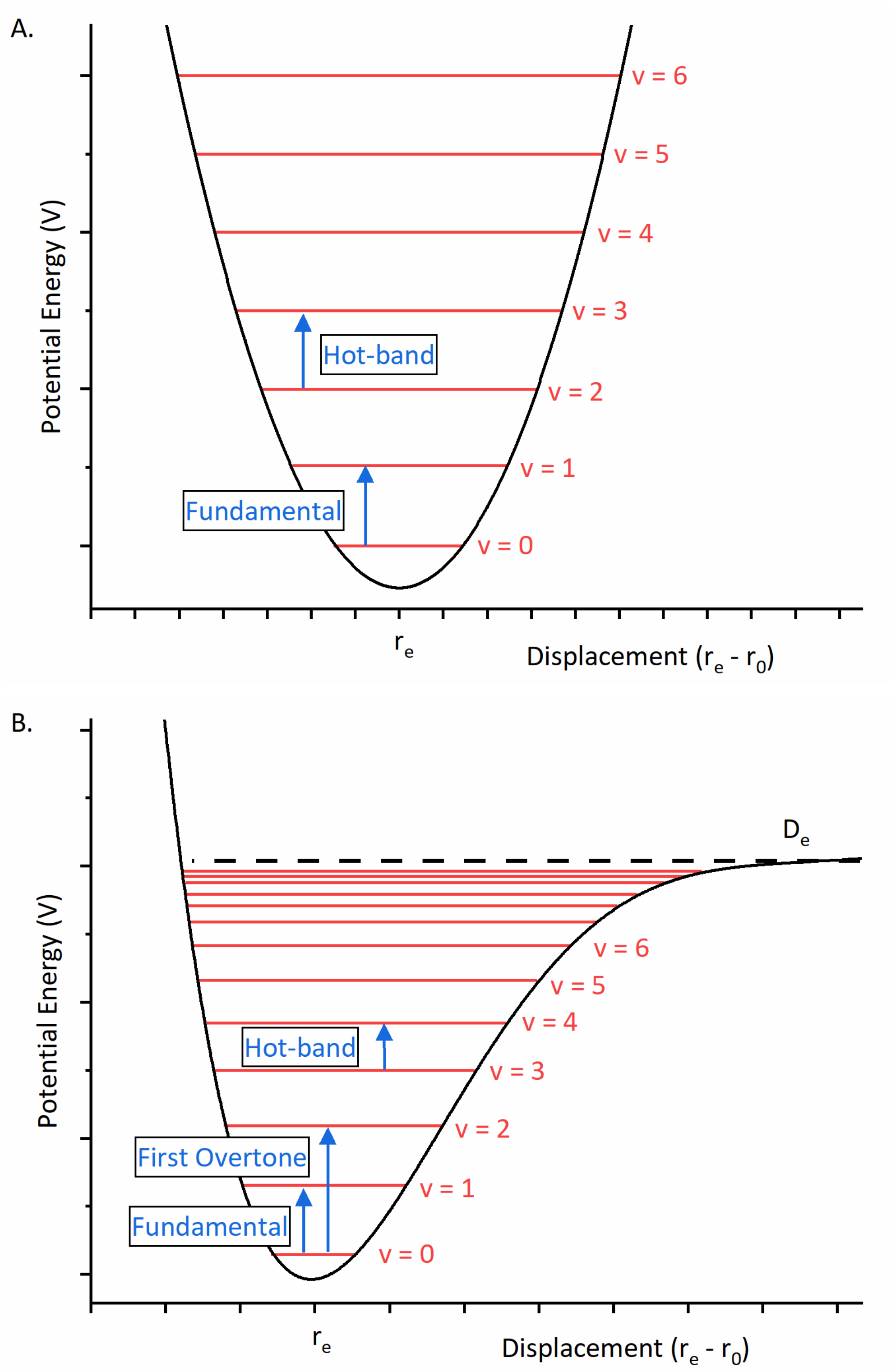

Figure 1-3 Harmonic and Anharmonic Potential Energy Surfaces. A. Schematic of harmonic oscillator potential energy surface as a function of displacement from the equilibrium position r_e. The vibrational states (red) are evenly spaced by $h\nu$. Selection rules mean only a fundamental or hot-band transition is possible, where Δv = +1. B. Schematic of anharmonic oscillator potential energy surface as a function of displacement from the equilibrium position r_e. The vibrational states (red) are no longer evenly spaced, and as the vibrational states increase in energy, the states get closer together. This decreasing energy gap means more types of transitions are possible such as overtones and combination bands where Δv = +1, +2, +3 etc. The dissociation energy is D_e.

However, the harmonic oscillator and the equations presented above are only useful for a molecules behaving in a perfect manner. Instead, for most molecules an anharmonic oscillator is used to describe the vibrational potential energy surface. Anharmonicity arises from two possible sources: mechanical or electrical. In the case of mechanical anharmonicity, the relationship between force and displacement is not linear, but depends upon the amplitude of the displacement. For electrical anharmonicity arises from the polarizability of the molecule. [128] This different energy surface can be described using a Morse potential (Figure 1-3, part B): [114]

$$V(r) = hc\widetilde{D}_e(1 - \exp(-a(r - r_e)))^2 \qquad \textbf{\textit{Equation 1-75}}$$

$$a = (\frac{\mu\tilde{v}^2}{2h\widetilde{D}_e})^{1/2} \qquad \textbf{\textit{Equation 1-76}}$$

Where $\tilde{D}_e$ is the dissociation energy, and $\tilde{v}$ is the vibrational wavenumber in cm^{-1}. Wherever, the tilde, ~, appears above a constant, this denotes that the constant is in units of cm^{-1}. This then allows for Schrödinger equation to be solved giving the following vibrational energy levels: [114]

$$G(\tilde{v}) = \left(\mathrm{v} + \frac{1}{2}\right)\tilde{v} - (\mathrm{v} + \frac{1}{2})^2 x_e\tilde{v} \qquad \textbf{\textit{Equation 1-77}}$$

$$x_e = \frac{\tilde{v}}{4\widetilde{D}_e} \qquad \textbf{\textit{Equation 1-78}}$$

Where x_e is the anharmonicity constant.

Just as for rotational transitions, for vibrational transitions to occur the selection rules must be followed. For vibrational spectroscopy, the gross selection rule states that there must be a change in transition dipole moment as a function of nuclear displacement along the vibrational motion. For harmonic oscillators, there is only one specific selection rule, where $\Delta v = \pm 1$, meaning the vibrational quantum can change by +1 for an absorption or −1 for an emission. For a fundamental transition where $\Delta v = 1 \leftarrow 0$, the vibrational transition energy can be written as $\Delta G = \nu$. As such, the vibrational transitions are not dependent on the vibrational quantum number. However, for anharmonic oscillators, the vibrational transition energy is slightly different. For a fundamental $\Delta v = 1 \leftarrow 0$ transition, the vibrational transition frequency is:

$$\Delta G = \nu - 2(\mathrm{v} + 1)x_e\nu \qquad \textbf{\textit{Equation 1-79}}$$

Furthermore, anharmonicity allows for other transitions such as overtones. Overtone transitions are defined as having transitions of $\Delta\mathrm{v} = \pm2, \pm3$, etc, so for the first overtone band of $\Delta\mathrm{v} = 2 \leftarrow 0$, the vibrational transition frequency is:

$$\Delta G = 2\nu - 2(2\mathrm{v} + 3)x_e\nu \qquad \textbf{\textit{Equation 1-80}}$$

In addition to fundamental and overtone transitions, hot band transitions are sometimes possible in molecules. Hot band transitions occur when population resides in a vibrational state other than the ground state ($\mathrm{v} = 0$). This means that transitions can occur from an excited state to another excited state, such as $\Delta\mathrm{v} = 2 \leftarrow 1$.

Alongside the selection rules, the population of the vibrational states also need to be considered. Once again, the Boltzmann distribution is used (Equation 1-60), but the degeneracy is now just 1. At room temperature (approximately 300 K), the available thermal energy is circa. 200 cm^{-1}, which represents the average thermal energy in the distribution. As vibrational transitions are normally much higher in energy than 200 cm^{-1}, typically only the ground vibrational state has population. This also means, that hot band transitions (as described above), are an uncommon but not unfeasible in vibrational spectra.

While the above applies to diatomic molecules where there is only one bond, polyatomic molecules have more atoms and hence more bonds. Furthermore, there are many other different types of vibrations to consider within polyatomic molecules. In order to differentiate the different types of vibrations, the concept of normal modes is introduced. Normal modes are defined as independent, synchronous motion of atoms or groups of atoms, where excitation of one normal mode does not cause another normal mode to be excited. Furthermore, excitation of a normal mode does not involve translation or rotation of the molecule as a whole, and importantly the centre of mass does not move.

In order to calculate the number of normal modes for a certain molecule, we have to consider the coordinates of each atom in the molecule and the other possible motions of the molecule. Using Cartesian coordinates, there are three coordinates for each atom (x, y, and z), and there 3 × N total coordinates per molecule, where N is the number of atoms in the molecule. For the translational motion of the molecule, there can be three displacements to describe the overall translation. For rotations of the molecules, there is a different amount of rotational degrees of freedom depending on the geometry of the molecule: for linear molecules there are two degrees of freedom, and for non-linear molecules there are three. Overall, this means for a molecule of N atoms, there are 3N − 5 vibrational normal modes for a linear molecule, and 3N − 6 vibrational normal modes for a non-linear molecule. [114]

Using the irreducible representation (Γ) for each point group, the normal modes of vibrations for a molecule can be assigned a symmetry label. For example, the CH_2X_2 molecules belong to the C_{2v} point group and have 9 normal modes. Each of these normal modes can be assigned a symmetry label: A_1, A_2, B_1, or B_2. In order to ascertain which vibrational mode belongs to which symmetry label, the contributions of translational and rotational motion must be determined first. The full irreducible representation of a C_{2v} molecule can be written as:

$$\Gamma(3\mathrm{N}) = 5\Gamma^{A1}\otimes 2\Gamma^{A2}\otimes 4\Gamma^{B1}\otimes 4\Gamma^{B2}$$ ***Equation 1-81***

where ⊗ denotes the product of two matrices. For the case of C_{2v}, the translations of the molecules can be given a symmetry label using the character table (Table 1-1). Where translation along the *x*-axis behaves as a B_1, translation along the *y*-axis behaves as B_2, and translation along the *z*-axis behaves as A_1. For the rotational motion, the symmetry is more difficult to assign, where the rotations about the *x*-, *y*-, and *z*-axes are designated as R_x, R_y and R_z. Applying the different symmetry operations, C_2 (z), σ_v(xz), and σ_v(yz) on the molecule shows that the R_z rotation behaves as A_2, the R_y rotation behaves as B_1 and the R_x rotation behaves as B_2.

These six symmetries from the translational and rotational motions can be removed from Equation 1-81 to yield:

$$\Gamma(\mathrm{vib}) = 4\Gamma^{A1}\otimes 1\Gamma^{A2}\otimes 2\Gamma^{B1}\otimes 2\Gamma^{B2}$$ ***Equation 1-82***

These remaining symmetry modes can then be assigned a vibrational mode depending on the motion of the normal mode. The normal modes are labelled in numerical order, and where applicable in descending fundamental transition frequency. For example, for CH_2F_2: ν_1 (a_1) = 2947.9 cm^{-1}, ν_2 (a_1) = 1509.6 cm^{-1}, ν_3 (a_1) = 1111.61 cm^{-1}, ν_4 (a_1) = 528.34 cm^{-1}, ν_5 (a_2) = 1256.8 cm^{-1}, etc.

Table 1-1 C_{2v} Character Table.

C_{2v}	E	C_2 (z)	σ_v(xz)	σ_v(yz)	Linear rotations
A_1	1	1	1	1	z
A_2	1	1	-1	-1	R_z
B_1	1	-1	1	-1	x, R_y
B_2	1	-1	-1	1	y, R_x

Table 1-2 C_{2v} Product Table.

C_{2v}	A_1	A_2	B_1	B_1
A_1	A_1	A_2	B_1	B_2
A_2		A_1	B_2	B_1
B_1			A_1	A_2
B_2				A_1

Within polyatomic molecules, the possibility for combination bands exist. This occurs when the quantum number of two or more different normal vibrational modes change, such that $\Delta v \neq 0$. These combination bands can also be assigned a symmetry label, which is dependent on the symmetry of the normal modes. This new symmetry label can be determined using a product table (Table 1-2). For example, combining two normal modes which have symmetry of A_1 and B_1, results in the combination band having the symmetry of B_1.

Lastly, a side note for the notations used within this thesis. For each different vibrational state can be written as, ν_x, where x is the vibrational normal mode number. In addition, the quantum number, v, is then also defined, for example, ν_1 (v = 1). This type of notation is used as the formal notation. However, for a vibrational transition, a shorthand notation can be used: X_{n1}^{n2}, where X is the vibrational normal mode number, n_1 is the initial vibrational state, and n_2 is the vibrational state upon excitation. [129] For example, 1_0^2 is the first overtone band for the ν_1 vibrational mode where the formal notation is: ν_1 (v = 2 ← 0). Combination bands can also be written in the same way. For example, $1_0^1 2_0^1$ is the combination band of $\nu_1 + \nu_2$ where the formal notation would be: ν_1 (v = 1 ← 0) + ν_2 (v = 1 ← 0).

1.3.3. Rovibrational Spectroscopy

Despite the two above sections being written separately, vibrational spectroscopy is not separable from rotational spectroscopy. Each vibrational state contains many rotational energy levels (Figure 1-4). This means, as the vibrational quantum number changes, the rotational quantum number can also change. For linear molecules, each rotational level within a vibrational level the energy can be calculated using (which ignores contributions from centrifugal distortion and assumes a harmonic oscillator): [130]

$$S(\mathrm{v},J) = G(\mathrm{v}) + F(J) = \left(\mathrm{v} + \frac{1}{2}\right)\nu + BJ(J+1)$$ ***Equation 1-83***

For rovibrational spectroscopy, the same selection rules still apply Δv = +1 (for a fundamental transition), and ΔJ = ±1, however there is also the added selection rule of ΔJ = 0. This is possible, as although the molecule must change its angular momentum by one unit, this is no longer restricted to changing the rotational angular momentum. Other possibilities include changing the electron spin, electronic angular momentum, or orbital angular momentum. Therefore, as long as the angular momentum is conserved, ΔJ = 0 is possible.

As there are now three different ΔJ values, these are referred to as different "branches": P-branch has ΔJ = −1, Q-branch has ΔJ = 0, and the R-branch has ΔJ = +1. For these three branches, the rovibrational transition for the fundamental vibrational transitions can be calculated for each branch (for a harmonic oscillator and assuming no centrifugal distortion): [130]

$$\Delta S_P(\mathrm{v},J) = \nu - 2BJ$$ ***Equation 1-84***

$$\Delta S_Q(\mathrm{v},J) = \nu$$ ***Equation 1-85***

$$\Delta S_R(\mathrm{v},J) = \nu + 2B(J+1)$$ ***Equation 1-86***

however, as the molecule undergoes vibrational transitions, the change in bond length will change the rotational constant (*B*) for each vibrational state. Instead, a new vibrationally averaged rotational constant, B_v, is used:

$$B_v = B_e + \alpha_e(v + \frac{1}{2})$$ ***Equation 1-87***

where B_e is the rotational constant at the equilibrium structure, and α_e is a constant which reflects the shape of the potential energy curve. Therefore Equation 1-84 to Equation 1-86 needs to be altered: [130]

$$\Delta S_P(v,J) = \nu - (B_1 + B_0)J + (B_1 + B_0)J^2$$ ***Equation 1-88***

$$\Delta S_Q(v,J) = \nu + (B_1 + B_0)J(J + 1)$$ ***Equation 1-89***

$$\Delta S_R(v,J) = \nu + (B_1 + B_0)(J + 1) + (B_1 + B_0)(J + 1)^2$$ ***Equation 1-90***

where B_1 is the v = 1 rotational constant, and B_0 is the v = 0 rotational constant.

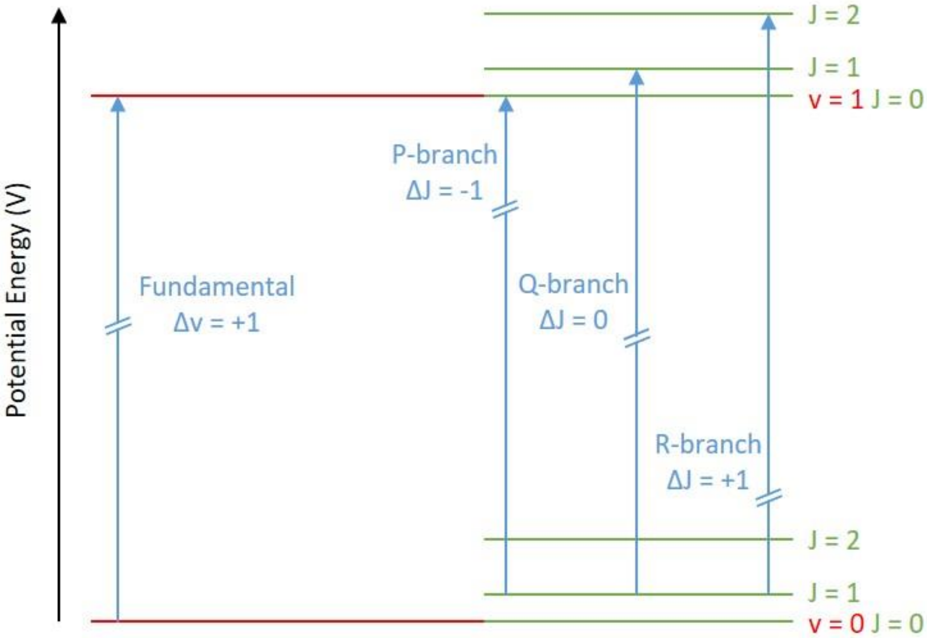

Figure 1-4 Rovibrational Energy Levels. Schematic showing the first two vibrational states (red) and a fundamental transition from v = 1 ← 0. Within both vibrational states, there are rotational states (green). Therefore within fundamental transition with Δv = +1, quantum number J can also change. There are three labels of rovibrational transitions: P-branch with ΔJ = −1, Q-branch with ΔJ = 0, R-branch with ΔJ = +1.

1.3.4. Asymmetric Top Molecules

The previous sections focused on using linear molecules as the example for the equations and diagrams as they are the simplest type of molecules to explain. However, more complex molecule structures exist, such that all molecules can be classified into one of four categories based on the moments of inertia: linear, symmetric tops, spherical tops, or asymmetric tops. However, this thesis focuses on CH_2X_2 molecules which are designated as asymmetric top molecules. Such designation means the three moments of inertia are all different, and hence there are 3 rotational constants: *A*, *B*, and *C*. Within the asymmetric top classification, the molecules are split into two groups: prolate or oblate. For prolate molecules, $I_A < I_b \approx I_c$, which means (using Equation 1-58), the relationship of the rotational constants is A > B ≈ C. For oblate molecules, the opposite applies: $I_A \approx I_b < I_c$ meaning that A ≈ B > C. [131] To determine if a molecule is a prolate or oblate, the kappa value, κ, can be calculated, where if κ = −1 the molecule is prolate, and if κ = +1 the molecule is oblate: [131]

$$\kappa = \frac{2B - A - C}{A - C} \qquad \textbf{\textit{Equation 1-91}}$$

For kappa values that are close to −1 molecules are designated as near-prolate. On the other hand, kappa values close to +1 are described as near-oblate. A molecule with a kappa value close to zero signifies a large degree of asymmetry. [114]

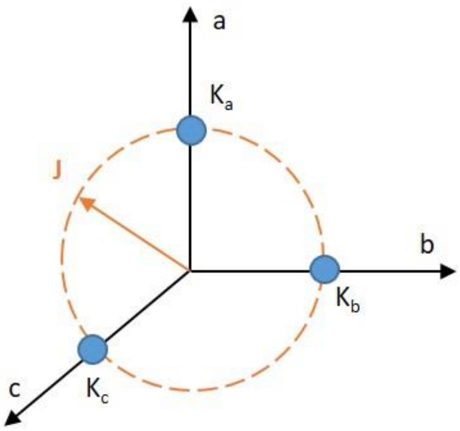

Figure 1-5 Projection of J as quantum number K. Schematic showing a three axis system with the axes labelled as as *a*, *b*, and *c*. The project of quantum number, J, is shown in orange, and the projection of J on each of the axes (blue dots), is either K_a, K_b, or K_c, depending on the axis. Adapted from ref. [131].

Asymmetric top molecules differ from linear molecules in that a second quantum number is needed to define the rotational levels. Quantum number K is introduced, where K defines the vector component of the rotational angular momentum along the principle symmetric axis (Figure 1-5). In other words, K is the projection of J onto the body-fixed axis, and ranges in integer values from -J to +J. As the K quantum number is linked to the angular momentum and hence the moment of inertia, for asymmetric tops there are 3 different K numbers: K_a, K_b, and K_c. In addition, K now replaces J as the rigorous quantum number. [131]

For asymmetric top molecules, as each axis of the molecule is different, they are separately labelled as either *a*, *b*, or *c* (Figure 1-5). Therefore, vibrational transitions are classed as either *a*-type, *b*-type, or *c*-type transitions. Each of these types of transitions are defined by which axis the dipole moment lies in. While the gross selections for rotational and vibrational still apply, the specific selection rules for asymmetric molecules are different to those described in previous sections due to the introduction of the K quantum number and the 3 different types of vibrational transitions. For *a*-type transitions: $\Delta K_a = 0$, $\Delta K_c = \pm 1$, and $\Delta J = 0, \pm 1$ (except where $K_a' = 0 \leftarrow K_a'' = 0$, as only $\Delta J = \pm 1$ is possible). For *b*-type transitions: $\Delta K_a = \pm 1$, $\Delta K_c = \pm 1$, and $\Delta J = 0, \pm 1$. For *c*-type transitions: $\Delta K_a = \pm 1$, $\Delta K_c = 0$, and $\Delta J = 0, \pm 1$ (except where $K_c' = 0 \leftarrow K_c'' = 0$, as only $\Delta J = \pm 1$ is possible). [131]

1.3.5. Resonances and Couplings

To fully understand the absorption peaks within a vibrational spectrum, different types of resonances and couplings must be considered. For rovibrational spectroscopy measurements, there are three main types of resonances and couplings: Fermi resonances, Darling-Dennison resonances, and Coriolis coupling. [130]

Firstly, a Fermi resonance causes a shift in energy and a redistribution of intensity of two vibrational transitions that are both close in energy and have the same symmetry label. Fundamentally, the wavefunctions of the two vibrational states mix according to their harmonic oscillator approximations. [114] This mixing results in a shift in energy and a change in intensity of the observed absorption peaks. Furthermore, for a shift to be labelled as a Fermi resonance, one of the vibrational transitions must be a fundamental transition, where the quantum number, v, changes by + 1 only. [132] For example, the 1_0^1 vibrational transition of CH_2Cl_2 has the symmetry label a_1 and an energy of 2997.66 cm^{-1}, in addition the 2_0^2 vibrational state also has the symmetry label a_1 and an energy of 2853.66 cm^{-1}. [73] As these two vibrational states have the same symmetry and are of similar energy, a Fermi resonance is possible.

A similar principle is true for Darling-Dennison resonances. In this case, two vibrational transitions have the same symmetry and are of similar energy, but occur between overtone and combination vibrational transitions. [133] For example, the 1_0^2 and 6_0^2 vibrational states of CH_2Cl_2 have the same symmetry (a_1) and similar energies of 5910.84 cm^{-1} and 6071.96 cm^{-1}, respectively, and have a documented resonance. [73]

Finally, Coriolis couplings are different to the two resonances discussed above and only occur between vibrational states of similar energy, but different symmetry labels. Coriolis couplings arise from the Coriolis effect which is an inertial force that acts on objects in motion with a frame of reference. [114] Therefore, as bonds within molecules vibrate from their equilibrium position, the Coriolis effect means the atoms move in a direction perpendicular to the original oscillations which changes the vibrational angular momentum for each vibrational mode. This change in vibrational angular momentum means that the energy level for each vibrational state is altered, and a Coriolis coupling constant can be determined for each altered vibrational state.

As the frame of reference for molecules has 3 axes, there are three types of Coriolis coupling: *a*-axis, *b*-axis, or *c*-axis. Between similar energy vibrational transitions an *a*-axis coupling occurs between two vibrational states with symmetries of a_1 and b_1. Conversely, *b*-axis coupling occurs between two vibrational states with symmetries of b_1 and b_2, and *c*-axis coupling between two vibrational states with symmetries of a_1 and b_2. [131] For example, CH_2F_2 demonstrates an *a*-axis Coriolis interaction between the 2_0^2 and 6_0^1 bands. [46] Coupling to a vibrational state with the symmetry of a_2 is not possible in IR spectroscopy, as the a_2 modes are not IR active.

1.4. Frequency Comb Spectroscopy

In order to study the rovibrational spectra of CH_2X_2 molecules in this thesis, the technique of direct frequency comb spectroscopy (DFCS) will be used. While the underlying theory of how a frequency comb laser works and the specifics of the set up used in this thesis will be discussed in Chapter 2, this section covers why frequency comb lasers are advantageous to use, the different types of frequency comb lasers, and the different detection methods. Furthermore, a select choice of frequency comb applications are discussed.

Frequency comb lasers operate on a femtosecond timescale and are defined as having a series of discrete and equally spaced frequencies over a broad spectral range. In 2005 John

Hall and Theodor Hänsch won half of the Nobel Prize in Physics for their work in developing the optical frequency comb. [134] Typical nanosecond lasers can be of high spectral resolution but have a narrow frequency bandwidth. [135] On the other hand, typical femtosecond lasers have a wide frequency bandwidth but do not always exhibit a high spectral resolution. [135] Frequency comb lasers simultaneously combine a broad spectral bandwidth, typically spanning over 300 cm^{-1}, with a high resolution of discrete frequencies, typically less than 0.01 cm^{-1} between adjacent frequencies (specific examples are given in the next section). This combination means that multiple molecules can be detected by one comb system at the same time, so long as there is a measureable absorption within the spectral window. For example, typical near-IR combs operate from 1300 to 1600 nm (7500 to 6250 cm^{-1}) which can be used to monitor combination or overtone vibrational bands. [136] Some mid-IR combs operate from 3000 to 3500 nm (3300 to 3000 cm^{-1}) which is useful for detecting fundamental vibrational frequencies caused by X-H stretches, which are common in many small molecules. [137] Furthermore, absorption cross sections are larger for fundamental vibrational transitions, meaning the detection of such vibrational transitions is easier. As a frequency comb laser operates with a high resolution, with a frequency comb spectrometer typically having a data spacing of less than 0.01 cm^{-1}, rovibrational structure within the vibrational spectra can be resolved. Furthermore, molecules which exhibit similar bonds and hence very similar vibrational spectra can be distinguished within one experiment. For example, the four CH_2X_2 molecules exhibit the same vibrational modes with similar fundamental transitions frequencies. Using a high resolution instrument ensures that the different fundamental vibrational transitions for each molecule can be differentiated.

However, there are disadvantages which come with operating a frequency comb laser. Firstly, frequency combs require a considerable amount of electronics for operation and the laser itself takes up a large proportion of the optics table. However, recent developments are working towards smaller frequency comb lasers, such as micro-combs. [138] Although frequency comb systems have recently become commercialised, the lasers are still expensive and hence not easily used or chosen for certain applications. Secondly, for many applications of a comb, specialist optics and detection methods are needed, and as expected these come with a considerable expense. Finally, the frequency comb modes can become saturated when a large concentration of molecules are present. For instance, when detecting frequencies from 3000 to 3300 cm^{-1}, the water vapour molecules present in the atmosphere have a large absorption cross section in this region. Therefore if there is

100% absorption by water vapour in the spectral range used, then there is no measurable difference between the background spectrum and the signal spectrum of the molecule of interest. This is especially detrimental to absorption spectra experiments if the water vapour vibrational frequencies directly overlap with the vibrational frequencies of the sample molecules. To overcome this issue, a closed boxed which encompasses the entire optical set up can be purged with N_2 gas, which does not exhibit an active IR spectrum. This purging system dilutes and replaces the water vapour within the surrounding area of the experiment, which lessens the saturation issues.

1.4.1. Types of Frequency Comb Lasers

Currently, there are four main ways to generate frequency comb lasers: mode-locked lasers, micro-resonator combs (also referred to as a Kerr frequency comb), electro-optic comb, or quantum cascade laser comb (QCL). [139, 140] The most popular type of frequency comb lasers are generated using mode-locked femtosecond lasers, which is the type of laser used in this thesis, and as such is the main point of discussion in Chapter 2, and specifically section 2.1. There are two main types of mode-locked lasers to produce frequency comb lasers: Ti:Sapphire [141] or fibre based, [142] each with their own unique set of properties.

A Ti:Sapphire laser consists of a solid-state lasing medium of sapphire (Al_2O_3) doped with Ti^{3+} ions, which is pumped with another solid-state laser operating near 514 to 532 nm. Typical outputs of a Ti:Sapphire laser span across nearly the whole visible spectrum and into near-IR (400 to 1200 nm), with the highest efficiency centred at 800 nm. [143] Furthermore, the data-point spacing of a Ti:Sapphire can reach 0.03 to 0.003 cm^{-1} (which is related to the repetition rate of the laser, as will be discussed in section 2.1.3). [144] Although Ti:Sapphire lasers have good tunability and high power outputs (0.5 to 2.5 Watts), the open-path nature of the system leads to stability problems. Furthermore, the size and cost of the systems needed to sustain the solid-state lasers means that the Ti:Sapphire based frequency comb lasers have limited applicability outside of research laboratories.

More recently, optical fibres have been used to generate frequency comb lasers due to their inexpensive and compact nature. In addition, as the fibres are an enclosed system, not only are they more stable than the Ti:Sapphire alternative, but the comb light can be directed through fibre-coupling mechanisms rather than relying on large optical set-ups. Two commonly used options for fibre laser are either erbium-doped or ytterbium-doped, with the former giving a wavelength range of 1400 to 1600 nm, and the latter a 1000 to 1100 nm range. [145, 146] In addition, the fibre based systems offer higher data point spacing than Ti:Sapphire combs, and typically offer discrete frequencies separated by 0.0016 to 0.008 cm^{-1}.

However, the examples given above all operate within the visible to near-IR regions which are only applicable to studying electronic spectroscopy and observing vibrational overtones and combination transitions. To extend combs into the mid-IR wavelength region where fundamental vibrational frequencies occur, non-linear optical techniques are needed. Two methods are available for this; difference frequency generation (DFG) and using an optical parametric oscillators (OPOs). [140, 147] Unfortunately, these processes require extra space and additional costs to basic comb systems. DFG works by mixing two separate comb structures in a phase-matching non-linear crystal to generate one output with a centre frequency which is the difference of the two original frequency structures (to satisfy energy conservation). For example, mixing the two outputs of the Er-fibre (1400 to 1600 nm) and the Yb-fibre (1000 to 1100 nm) gives a comb structure centred at 3200 nm. [137]

Conversely, OPOs can be exploited to give higher power combs with longer wavelengths compared to DFG and are typically tuneable over a broad bandwidth. The OPO method works by introducing a high-energy photon to generate two lower-energy photons, such that the incoming photon is equal to the sum of the two outgoing photons. [148] Although this can be initially inefficient, the OPO process can be improved by creating a resonant cavity to build up the photons to emit up to 1 W of power. [149]

1.4.2. Detection Methods of Frequency Comb Lasers

For detection methods of a frequency comb laser, there are multiple options. These methods range from a simple Fourier-transform (FT) interferometer to the more complicated method of spatially dispersing the comb light into a two-dimensional (2D) array. Other methods include, dual comb spectroscopy (DCS), [150-152] Vernier spectroscopy, [153-156] photoacoustic spectroscopy, [157, 158] transient absorption spectroscopy, [159, 160] and electrical-optical sampling. [161, 162] This section will describe three of the detection methods: FT, VGC, and DCS.

Firstly, the cross-dispersive method is a unique approach to detecting the frequency comb laser and is not a commonly used method due to the complexity of the set-up. [137, 163-165] This requires two optics to spatially disperse the comb modes into a 2D array, and can be achieved through the combination of any two dispersive optics such as two diffraction grating optics or two virtually imaged phased array (VIPA) etalons. The self-termed VIPA-grating-camera (VGC) method utilizes one of each of these optics alongside a position sensitive imaging camera. Although dependent on the specific optics and experimental set-up, the VGC method is capable of achieving "comb mode resolution", which means each individual frequency of the comb laser can be detected. [137] It is this technique which is used in this thesis, and therefore the specifics surrounding the detection method are further described in section 2.2.6.

Secondly, the most general method for detecting a comb is using a FT interferometer. This method is used in the same way as commercially available FT spectrometers, and in general, works by scanning a delay stage to self-interfere the comb light in order to generate an interferogram. [135, 166] However, this technique does have some disadvantages which negate some of the positive aspects of using a frequency comb laser. Most FT comb spectrometers can detect molecules on a 100 to 10 ppb limit and can achieve spectral resolution from 0.01 to 0.002 cm^{-1}. [166] The spectral resolution in cm^{-1} is equal to the inverse of the maximum of the optical-path difference (OPD) of an interferogram, [135] and the speed with which the interferogram is detected. To improve the spectral resolution, a longer OPD is needed, but the alignment and moving parts of the spectrometer needs to be precisely controlled which becomes more challenging at longer OPDs. In addition, an instrument line-shape function arises from the Fourier transform algorithm used to convert the interferogram data, which can broaden the resulting spectral lines. Fast-scanning FT comb measurements are capable of achieving a noise equivalent absorption (NEA) sensitivity of 3.4×10^{-11} cm^{-1} $Hz^{-1/2}$ per spectral element for 6 s of acquisition time alongside a signal-to-noise ratio (SNR) above 1000 and a resolution of 380 MHz. [167] An alternative to the FT method is the usage of DCS.

DCS operates in a similar way to the FT method, in that it is a time-domain measurement based on interferometry. However, instead of a moving delay stage, two combs with slightly different repetition rates overlap spatially and temporally to interfere and give an interferogram which can be recorded with a photodetector. [151, 152] Typically, the repetition rates of the two frequency comb lasers differ by a few hundred Hz. The main difference between DCS and FT spectroscopy is the elimination of moving parts, which reduces background noise issues and gives an improved line-shape function determination. [122] Furthermore, the reduction in background noise increases the SNR. For example, one study demonstrates an SNR of 10^6 alongside a time resolution of 55 fs. [168]

1.4.3. Comparison of IR Light Sources

As this thesis focuses on a mid-IR frequency comb light source, it is prudent to compare this light source to others which also generate mid-IR light. While only frequency comb lasers can combine high resolution with a broad spectral bandwidth, many different lasers are capable of producing light within the near to mid-infrared region from 0.78 to 50 µm or 200 to 12800 cm^{-1}. Such mid-IR lasers include Lead Salt lasers, Doped Insulator Bulk lasers, and gas and chemical based lasers. [169] Furthermore, generic lamp sources, typically used in commercial FTIR set-ups, can generate IR light across a broad bandwidth, but are not lasers and so cannot efficiently couple into enhancement cavities. They also have limited spectral resolution, but this is based on the quality of the spectrometer and not the light source itself. Quantum Cascade Lasers (QCLs), Optical Parametric Oscillators (OPOs), and fibre based laser systems can also be used to generate mid-IR light. While these types of lasers were covered in section 1.4.1 in the context of being frequency comb lasers, a few extra key points will be covered here.

Lead salt diode lasers are an older generation of laser that have been slowly phased out due to the introduction of QCLs. [169] They classed as semiconductor lasers and are comprised of a lattice structure of $Pb_{1-x}Eu_xSe_yTe_{1-y}$ which generates tuneable light from 3 to 20 µm depending on the composition. [170] Unfortunately, their limited output power (~ 1 mW) and need for cryogenic cooling (< 100 K) meant they were not common or easy to use lasers. However, in their heyday, lead salt lasers provided a mid-IR light source for high resolution applications, as the linewidth was on the order of 10 MHz. [171] Out of the large range of doped insulator bulk lasers, only a few emit in the mid-IR region: Cr^{2+}:ZnSe (3.5 µm) and Fe^{2+}:ZnSe (3.7 to 5.1 µm). [172] However, the output power of both lasers are low (< 1 W), and they often cannot be used with atmospheric air in the laser resonator. As such, both types of doped insulator lasers need to be used in dry atmospheres which greatly reduces their usability within simple laboratory settings.

Helium-neon lasers (commonly referred to as HeNe lasers) are some of the cheapest gas-based lasers available. As the name suggests, the gas mixture within the laser is a mixture of helium and neon, in a ratio of 10:1 and at a total pressure of 1 torr. [169] While the HeNe lasers are capable of generating different mid-IR wavelengths such as 1.15 µm, 1.52 µm, and 3.39 µm, the most well-known HeNe laser operates at 632.8 nm. [135] While the generation of mid-IR wavelengths are easy, the lasers offer a narrow spectral bandwidth and tuning across a large range of wavelengths is not easy or achievable. Furthermore, the output power is low (< 50 mW), and the lasers have a short life-time of less than 10,000 hours of usage. Alongside HeNe lasers, CO_2 based lasers are also capable of operating at mid-IR wavelengths between 9.6 and 10.6 μm. [135]

While all of the above mentioned lasers offer mid-IR wavelengths at a high resolution and tuneable across a range of wavelengths, to use them in spectroscopy to record a rovibrational spectrum covering different rovibrational transitions would take a large amount of experimental time. Frequency comb lasers negate this long experimental time by offering the high resolution simultaneously with the broad bandwidth of wavelengths.

1.4.4. Applications of Frequency Comb Lasers

This section will focus on a few applications of frequency comb spectroscopy, with a particular focus on reaction kinetics, trace-gas monitoring, and high resolution spectroscopic measurements. These applications have been chosen for discussion as they are relevant to the work presented in this thesis and are of particular interest to the wider research goals of the Lehman Research group. However, a number of reviews and book chapters have covered a wide range of applications of different types of frequency comb lasers and the different detection methods of the lasers. See references [140, 173-178] and references therein for the further examples of different applications.

1.4.4.1. Reaction Kinetics

Frequency comb lasers have recently been implemented for recording accurate reaction rate coefficients for a number of different reactions, all with a different detection method and different types of frequency comb lasers. [179-185] In all such cases, the frequency comb lasers are used as the detection light source, as opposed to the reaction initiation light source. This distinction is due to the frequency range of the combs: high energy UV light (< 300 nm) is typically needed to initiate a reaction, as opposed to the mid-IR and near-IR (> 1000 nm) energies of a frequency comb laser. In addition, frequency comb lasers do not have the sufficient power within a comb pulse necessary to photolyse molecules.

The major advantage of using a frequency comb laser means that within the broad spectra bandwidth both reactants and products can be simultaneously monitored as a function of time. Not only does this give multiple rate coefficients from one experiment, but there can also be a greater understanding to branching ratios within more complex reactions. In theory, a frequency comb can be applied to monitor any reaction providing there is an IR-active vibration which can be observed within the wavelength range produced by the frequency comb. However, detection methods for frequency combs lasers are temporally limited, so only certain reactions can be monitored. [137] Furthermore, if products are generated at low concentrations, then the ability of the experimental apparatus to detect the product will be significantly reduced. Depending on the specific parameters of the experimental apparatus and target molecules, minimum observable concentrations of 10^{11} molecule cm^{-3} are possible. [137] For typical reaction kinetic experiments, concentrations range from 10^{15} to 10^{17} molecule cm^{-3} for the excess reactant (in pseudo first-order conditions) and 10^{13} to 10^{15} molecule cm^{-3} for the non-excess reactants. Then, depending on the branching ratios of the specific reaction, product molecules are typically seen at concentrations of 10^{10} to 10^{12} molecule cm^{-3}. [182]

This section will focus on two different reaction kinetic studies. Both of these studies utilise a frequency comb laser as the detection light source, however the type of frequency comb laser and the detection method are different.

Firstly, Bjork *et al.* used a mid-IR DFG based frequency comb laser to study the OD + CO reaction, in particular they wanted to understand more about the pathways of the reaction and the intermediate isomer molecule, DOCO. [182, 183] While they initially wanted to study OH + CO, the limitations of the comb wavelength meant the deuterated version was used. However, using the kinetic isotope effect, approximate rate coefficients for the OH + CO reaction can be determined. In addition to using the deuterated version of OH, the reaction was monitored using the two natural carbon isotopes, ^{12}C and ^{13}C. The observation of the two carbon isotopes meant that the formation of the DOCO intermediate could be confirmed.

For this study, the 2D spatial dispersion method, specifically a VGC, detection system was used. Images containing spectral information from 2650 to 2710 cm^{-1} were recorded on a 20 to 100 µs timescale. Within the spectral acquisition window, the Ye research group saw evidence of OD, D_2O, and for the first time in literature coming from the OD + CO, the *trans*-DOCO and *cis*-DOCO intermediates. Initially, the observed rate coefficient of reaction 1-9, showed a strong pressure and a non-Arrhenius temperature dependence. These factors were theorised to be caused by the formation of the DOCO* intermediate, and the tunnelling from this intermediate to the products D + CO_2. This led to the proposed pathway of:

$$OD + CO \rightleftharpoons DOCO^{*} \rightarrow D + CO_2$$ **Reaction 1-8**

$$DOCO^{*}(+M) \overset{[M]}{\leftrightarrow} DOCO$$ **Reaction 1-9**

$$trans\text{-}DOCO \overset{[M]}{\leftrightarrow} cis\text{-}DOCO$$ **Reaction 1-10**

$$cis\text{-}DOCO \rightarrow D + CO_2$$ **Reaction 1-11**

Alongside the proposed pathway, several rate coefficients were measured, including the rate coefficient for the formation of each DOCO isomer, k_{cis} and k_{trans}. These coefficients then allowed for the equilibrium constant for the isomerisation process, K_{iso}, to be calculated.

In the second example, Luo *et al.* employed a QCL-DCS system to record the self-reactions of two Criegee intermediates: CH_2OO and CH_3CHOO. [181, 186] This was achieved by observing the fundamental vibrational ν_6 transitions of both molecules, which is caused by the stretching of the O-O bond between 880 and 932 cm^{-1}. For this study, the usage of a frequency comb laser and the DCS detection method facilitated the high spectral resolution of 0.0015 cm^{-1} and a fast temporal resolution of 0.4 µs, which was needed in order to distinguish between the two molecules. Within the acquired spectrum, over 2000 rotationally resolved transitions were observed and spectral transitions solely dependent on the *syn*-CH_3CHOO isomer were identified for the first time. Furthermore, the $6_0^1 7_1^1$ hot-band was also witnessed for the CH_2OO intermediate. These results could have only been achieved with a high spectral resolution and sensitive detection method. In addition, the high temporal resolution meant that the rate coefficients for both self-reactions (k_{self}) could be determined, such that the k_{self} of CH_3CHOO was determined to be almost twice that of CH_2OO.

1.4.4.2. Trace-gas monitoring

Another application of frequency comb lasers is for trace-gas monitoring. This application exploits the high resolution property of a frequency comb laser alongside the high sensitivity and the possibility for real-time analysis. In addition, the broad spectral bandwidth of frequency comb lasers, means that multiple molecules can be detected within one measurement. Such applications cover a wide range of uses from breath analysis [174, 187] to monitoring pollutants and greenhouses during open-path measurements. [136, 188-195] Examples of these applications will be discussed in the following section.

Firstly, for breath analysis, there have been multiple studies detailing the capabilities of a frequency comb laser for detecting a variety of molecules down to ppt levels. [196] A recent study, [187] used a mid-IR frequency comb laser (3.4 to 3.6 µm) coupled to an enhanced cavity (cavity enhanced direct frequency comb spectroscopy, CE-DFCS) to simultaneously detect and monitor as a function of time multiple molecules: CH_3OH, CH_4, H_2O, HDO, H_2CO, C_2H_6, OCS, C_2H_4, CS_2, and NH_3. For this study, a home-built FTIR was utilized as the fundamental detection method of the frequency comb laser. This detection method demonstrated an ultra-high detection sensitivity which was comparable to other well-used laser-based techniques such as cavity ring-down spectroscopy (CRDS) and tuneable diode laser absorption spectroscopy (TDLAS). For example, using the CE-DFCS method a minimum observable concentration of 126 ppt is achieved for H_2CO (formaldehyde), [187] on the other hand using a GCMS technique the minimum observable concentration is closer to 5 ppb . [197] Although, it is not uncommon to observe detection limits close to 0.1 ppt for other molecules depending on the specific GCMS equipment. [198]

Secondly, there have been many studies where frequency comb lasers have been used for open path measurements of atmospheric molecules. [136, 188-195] The most common technique is to use DCS, as this provides multi-species detection, fast real-time detection (millisecond timescales) and low sensitivity to turbulent air paths. In one such study, Ycas *et al.*, utilised DCS to record concentrations of volatile organic compounds (VOCs) over a kilometre scale path length. [192] Within 1 minute of data acquisition and averaging, a ppm·m level of sensitivity for various molecules on was achieved. For example, a sensitivity of 5.7 ppm·m was achieved for $(CH_3)_2CO$ (acetone) and 2.4 ppm·m was achieved for C_3H_8O (isopropanol), where the unit ppm·m denotes the path integrated concentration. Furthermore, this method also achieved a SNR of 120. [193] Further work on open-path DCS showed it was possible to determine mixing ratios for horizontal and vertical profiles alongside spatial mapping of gas molecules in real time. [189] The ability of the DCS equipment to rapidly scan across long path lengths and provide continuous and regional coverage means the apparatus can be applied to many fields such as monitoring gas leaks [195] and quantifying emissions from cars. [194]

Despite the benefit of monitoring multiple molecules at once, the DCS apparatus is limited in sensitivity for some molecules. For example, the concentration of OH radicals in the atmosphere cannot be measured using frequency combs. While DCS can typically measure concentrations close to 2000 ppt in 100 seconds, [195] this is not sensitive enough for OH radicals, which are typically seen at a concentration of 0.04 pptv using the FAGE technique (Fluorescence Assay by Gas Expansion). [124]

1.4.4.3. High Resolution Spectroscopy

Owing to the high resolution of frequency combs spectrometers, they are useful in measuring high resolution spectroscopy of molecules and atoms. [119, 199-204] Most notably, a rotationally resolved vibrational spectrum of the buckminsterfullerene molecule, C_{60}, (buckminsterfullerene) was measured for the first time. [203] At room temperature, many rotational and vibrational levels of C_{60} molecules are populated, which makes the vibrational spectrum of buckminsterfullerene to be highly congested. Using an ultra-cold buffer gas cooling method, the population distribution of the molecules collapses to a few rotational levels within the ground state, therefore recorded rovibrational spectrum has fewer transitions. The use of a high resolution frequency comb laser coupled to an FT detection method results in a rotationally resolved vibrational spectrum of the buckminsterfullerene molecules. [204]

Alongside difficult to observe molecules, frequency comb lasers have significantly added to the field of sub-Doppler spectroscopic experiments. Although there are many literature studies dedicated to sub-Doppler experiments, references [119, 200] have been chosen as select examples. In particular, the work of Foltynowicz *et al*. developed a sub-Doppler double resonance spectroscopy technique to probe the vibrational spectrum of CH_4 around 3.3 µm. [119] This double resonance technique used a continuous wave laser as the “pump” mechanism, and a frequency comb laser as the “probe”, and yielded a centre frequency accuracy of 1.7 MHz. Such accuracy was only limited by the frequency stability of the pump laser. The main outcomes of this pump/probe sub-Doppler experiment, allowed for the accurate assignment of many rovibrational transitions which are not normally distinguished in Doppler-broadened experiments. Furthermore, predictions of spectral absorptions given by the TheoReTs database [205] were verified with the new sub-Doppler assignment of CH_4. Further Doppler-free measurements by Gambetta *et al.* employed a QCL frequency comb which yielded a frequency resolution of 160(10) KHz. Alongside this very high frequency resolution, a high SNR of 7000 was achieved within a 10 second integration time. [200]

2. Experimental: Theory and Techniques

This chapter will cover the theory and techniques for the various equipment and optical components used in this project. Firstly, the concept of how frequency comb lasers work will be discussed. Secondly, the underpinning theory and deployment of important optical components will be outlined. Thirdly, how the two gas delivery systems operate will be described. Finally, the detection method and the alignment procedure of the detection method will be described and discussed. Following on from this chapter, the characterisation and commissioning of the new frequency comb experimental apparatus will be discussed (Chapter 3).

2.1. How Frequency Comb Lasers Work

Frequency comb lasers are a type of ultrafast mode-locked laser, which operate on a 10^{-15} seconds per pulse time-scale (femtosecond, fs) and exhibit a broad spectral bandwidth. To generate the laser output, three components are needed: a lasing medium with an associated pump, a build-up cavity, and a cavity output-coupling mechanism.

For an ultrafast frequency comb laser, the output-coupling mechanism is achieved through a mode-locking technique which is necessary in order to reach the ultrafast femtosecond time scale per pulse. The lasing medium defines the spectral region of the broad frequency bandwidth, and the laser cavity gives the comb-tooth structure. Each of these three aspects will be explored in the following sections, where the section on the laser cavity also discusses pulsed repetition rate of the frequency comb laser and carrier-envelope offset stabilisation, which are key in transforming an ultrafast laser into a frequency comb laser.

2.1.1. Mode-Locking Mechanism

To generate an ultrashort pulse, a standard Q-switch laser cannot be used as these only produce pulses on nanosecond to picosecond timescales. For example, a Q-switched microchip laser can reach a maximum pulse width close to 100 ps. [206] A continuous wave (cw) laser cannot be used either, as it does not produce pulses by definition. Instead, the technique of mode-locking is used to generate narrow pulses in time, which form part of a pulse train. [207] A lasing medium (see section 2.1.2) is enclosed in an optical cavity, which is flanked on either end by two high finesse mirrors, separated by a specific length. Within this cavity, only certain longitudinal modes are supported. These modes depend on the distance between the mirrors, L, and the frequency of the light, ν in Hz, such that:

$$\nu = n\frac{c}{2L} \qquad \textbf{\textit{Equation 2-1}}$$

Here, the allowed longitudinal modes are defined as an integer multiple, *n*, of the inverse cavity roundtrip time, τ. The difference between adjacent modes, Δν, is then related to the time taken for one round trip of the cavity:

$$\Delta\nu = \frac{c}{2L} = \frac{1}{\tau} = f_r \qquad \textbf{\textit{Equation 2-2}}$$

The cavity roundtrip time is also related to the repetition rate of the laser, f_r. Normally, supported modes within the cavity oscillate independently of each other and produce a random output pattern in time. However, when cavity modes are in phase, the cavity is able to output a short time pulse due to the complete constructive interference of the supported modes. A mode-locked laser exploits this in-phase relationship, where, as the modes propagate through the cavity, the phase relationship between the modes is fixed and is at the maximum constructive pattern. This fixed-phase relationship allows only the in-phase interference pattern to be released from the cavity and results in short bursts of intense laser light, where the width of the pulse is on the femtosecond timescale. The more modes that are in phase, as part of the mode-locking mechanism, the narrower in time the pulse from the cavity will be. Because the laser pulse is narrow in time, the observed spectral bandwidth is broad (see Figure 2-1 part A). This can be seen from the Fourier Transform relationship between the time and frequency domains. However, there is a limit on the observed spectral bandwidth, as governed by the Heisenberg uncertainty principle, which is a natural property of the Fourier Transform. This property is termed the time-bandwidth product, where the duration of the pulse and the spectral width of the pulse are multiplied together to give a value limit. For example, a gaussian shaped pulse has a time-bandwidth product of 0.44, this means a 100 fs pulse must have a minimum bandwidth of 4.4 THz. [208] Many mode-locked lasers operate as nearly bandwidth-limited pulses, meaning the pulse duration is as short as possible depending on the spectral width and spectral shape.

In addition, within the cavity, the modes are all in phase at a time corresponding to the time taken for a round-trip of the cavity. This means there is a pulse train of the in-phase modes which are emitted with a separation of time, *T* and related to cavity length, *L*. Provided the repetition rate of the laser is the same from pulse to pulse, the multiple pulses within the pulse train constructively interfere to give a broad structure containing discrete frequencies which are separated by the repetition rate of the frequency comb. The more pulses within the pulse train the more defined the frequency structure will be, while still retaining the FWHM associated with the Fourier Transform of the corresponding femtosecond pulse width. For example, Figure 2-1 shows the difference in frequency structure depending on the number of pulses within the train. For a single 100 fs pulse the corresponding frequency profile is a single, broad peak with a FWHM of 150 cm^{-1} (part A). Having two of these 100 fs pulses in the train means the pulses begin to constructively and destructively interfere (part B), this causes the original broad peak to be resolved into multiple peaks. By adding more and more 100 fs pulses to the pulse train, the frequency structure becomes extremely well resolved, all the while retaining the original FWHM of 150 cm^{-1} (part C).

There are two mechanisms used to mode-lock a laser: active or passive mode locking. Active mode-locking works by allowing the laser light out of the cavity at times corresponding to the round-trip cavity time using a modulator of the phase or cavity losses, such as an acousto-optic or electro-optic modulator. Passive mode-locking utilises a non-linear optic or crystal at one end of the lasing cavity which displays decreased light absorption as a function of increasing light intensity. [207] Therefore, when the mode-locked phase (which has the highest intensity of light) reaches the optic or crystal, the decreased absorption results in the laser light being released from the cavity. Saturable absorbers are the most commonly used material for passive locking, however, limitations arise from their slow recovery time and wavelength dependency. More recently, a non-linear optical loop mirror (NOLM) laser resonator [209] has been developed and patented by *Menlo Systems GmBH*. Commercially referred to as a “figure 9” geometry resonator, this laser resonator has a shorter fibre optic path alongside adjustable cavity lengths for repetition rate tuning. In addition, the “figure 9” resonator presents reproducible and long-term stable operation. This is of particular interest, and this is the mode-locking of the frequency comb laser used in this project.

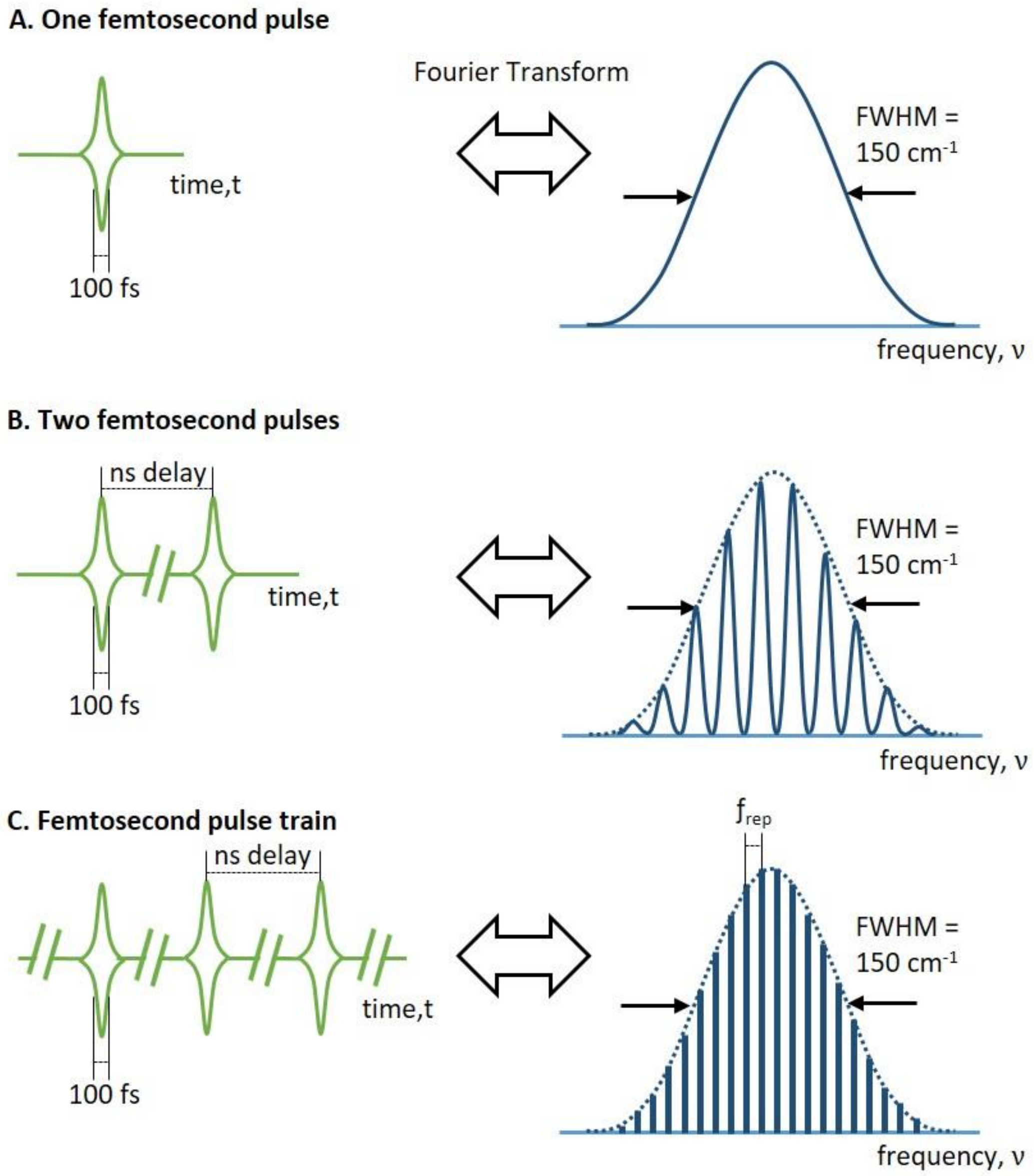

Figure 2-1 Fourier Transforming Femtosecond Pulses. All panels are pure schematics, and not to scale A. One 100 femtosecond pulse can undergo Fourier Transform to give a single broad frequency peak with a FWHM of 150 cm^{-1}. B. Two 100 femtosecond pulses also undergo Fourier Transform to give a broad structure which spans the same frequency range as just one pulse. However the two pulses constructively and destructively interfere to give multiple frequency peaks. C. The resulting Fourier Transform from a pulse train is a broad frequency structure consisting of many peaks (10^4 to 10^5) where the frequency FWHM matches that of the one 100 femtosecond pulse.

2.1.2. Lasing Medium

As with any laser system, a lasing medium is needed to generate light. For ultrafast lasers, such as a frequency comb laser, it is beneficial to choose a lasing medium that is able to emit light over a broad spectral bandwidth. This section will describe how the lasing medium emits light using Erbium-doped fibres as an example, as it is a common lasing fibre material and relevant to this thesis. The lasing medium defines the wavelength of the laser output light, so different materials are often chosen for different applications.

In order to understand how a laser fundamentally works, the Einstein *A* and *B* coefficients have to be considered. Recalling from section 1.2.1, the Einstein *A* coefficient describes spontaneous emission, and the Einstein *B* coefficient describes the absorption and stimulated emission processes. Using a two electronic state system (as shown in Figure 1-1), the rate of absorption equals the rate of stimulated emission, meaning there is never a build-up of photons within the lasing cavity. Instead for lasers, a population inversion system is needed, which can only be achieved by using a minimum of three or four electronic states. Population inversion is necessary to generate Light Amplification for Stimulation Emission of Radiation (a LASER). Only certain materials can be used as lasing media since a minimum of three or four electronic state systems are needed.

Generally, as shown in Figure 2-2 (with erbium-doped fibres as an example), a three-state laser system works as follows: [207] A light source (pump) excites an electronic transition within the molecules of the lasing medium from an initial state (state 1) to a higher energy electronic state (state 2). Another electronic transition follows, allowing the molecule to relax to an intermediate energy electronic state (state 3), causing a population inversion with a lower energy electronic state (state 1). The lasing transition in this example is the transition from state 3 to state 1. The molecules in state 3 undergoes spontaneous emission, allowing a transition back to state 1, releasing a photon of energy. The spontaneously emitted photons can cause stimulated emission for other population in state 3 to generate two photons at the final photon energy of the laser. Furthermore, there is a directionality component of the photons to consider. Spontaneous emission causes the photons to be released in random directions, whereas for stimulated emission the photons are emitted in the same direction as the incoming photon. This ensures the light travels together through the cavity, and builds up in intensity between the cavity mirrors before the light leaves the cavity (once the exit conditions are met).

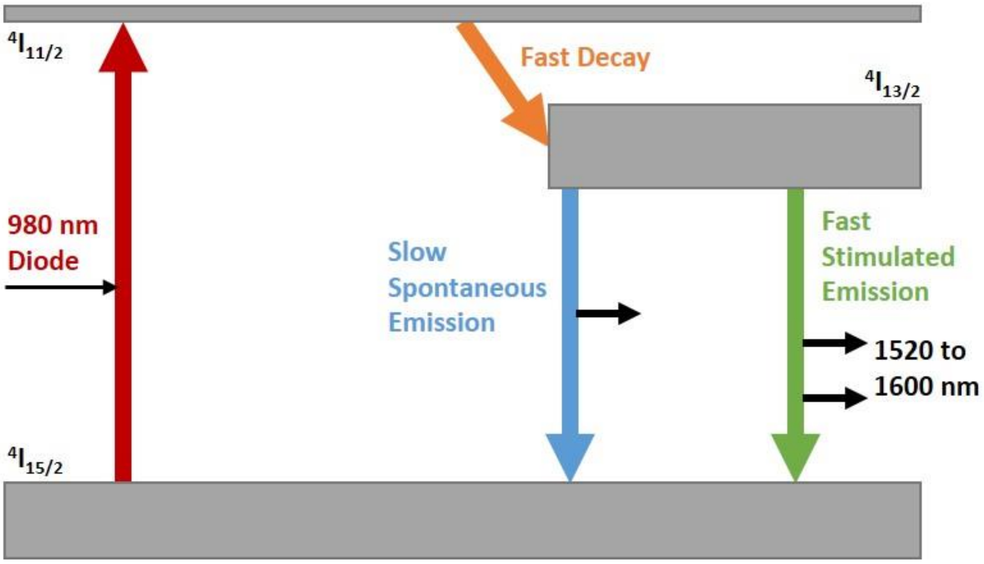

Figure 2-2 Erbium Laser Emission. Schematic showing the erbium ions within the lasing medium are excited from the ground state, $^4I_{15/2}$, to an excited electronic state, $^4I_{11/2}$, using 980 nm generated from a diode. The ions then undergo fast decay to an intermediate state, $^4I_{13/2}$, causing a population inversion. From this electronic state the ions slowly undergo spontaneous emission back to the ground state. The emitted photons can drive directional stimulated emission from the intermediate electronic state to the ground state. As the close packed ions exhibit a band structure, the emitted photons cover a broad wavelength range. Adapted from reference [145].

As shown in Figure 2-2, for erbium-doped fibres, a 980 nm laser diode is needed to excite the Er^{3+} ions within the doped fibre from its initial ground state ($^4I_{15/2}$) to an excited state ($^4I_{11/2}$). The ions then undergo fast decay to a lower energy intermediate state ($^4I_{13/2}$), with slower spontaneous emission to the ground state which causes the needed population inversion. As mentioned above, these spontaneously emitted photons can drive stimulated emission which helps to build up the power in the light output. The close packed ion structure of the fibre material gives rise to an energy band structure within the ground state ($^4I_{15/2}$) and the intermediate state ($^4I_{13/2}$). This means photons of over a small range of energies are emitted and causes a continuous wavelength range to be observed. For erbium-doped fibres, this range is from 1520 to 1600 nm.

2.1.3. Lasing Cavity

Within the optical cavity, the lasing cavity has a defined length, L, which is the distance between the two highly reflective mirrors. This length is directly related to the repetition rate of the laser, f_r, which can be seen using equation 2-2 from section 2.1.1. For example, a cavity length of 100 cm gives a repetition rate of 150 MHz and a cavity round-trip time of 7 ns.

As previously mentioned, the pulse train of femtosecond pulses are separated by the round-trip time of the cavity, which is determined by the length of the lasing cavity. Therefore, so long as the repetition rate of the laser, and therefore the length of the cavity, is the exact same from pulse to pulse (as achieved with mode-locking the laser), the multiple pulses within the pulse train constructively interfere to give the discrete frequency pattern needed for the frequency comb laser. However, vibrations and small fluctuations in temperature causes the cavity mirrors to contract and expand, thus changing the length of the cavity on micrometre or sub-micrometre scales. Consequently, this change in cavity length changes the repetition rate of the laser, and the frequency bandwidth structure is no longer comprised of many discrete frequencies, but rather begins to resemble the less defined and broader frequency peaks associated with two femtosecond pulses (as seen in Figure 2-1, part B). To achieve a well-defined comb structure, the repetition rate of the laser is “locked” to ensure the complete constructive interference of all the supported modes. It is this repetition rate stabilisation, alongside the carrier-envelope offset stabilisation discussed later in this section, which sets apart a frequency comb laser from other mode-locked ultrafast lasers.

Locking the repetition rate requires two pieces of equipment: a reference for the repetition rate and a way to actively move one of the cavity mirrors. Typically, a stable frequency standard such as a caesium or rubidium atomic clock, is used to generate the reference repetition rate, such that each roundtrip of the cavity is the exact same length, and hence the same repetition rate. To change the cavity length in order to match the repetition rate, a fast response piezoelectric device is used to alter the mirror position at one end of the cavity. By responding to an electrical signal, the piezoelectrical crystal will either contract or lengthen itself to match the cavity repetition rate conditions. This is achieved using a PID loop (proportional-integral-derivative), which calculates an error value as the difference between the set-point and the process variable, and applies a correction. In this case, the set-point is determined by the rubidium atomic clock, and the correction is applied to the piezoelectrical crystal.

However, frequency comb lasers exhibit a carrier-envelope offset (CEO) phase, whereby the carrier wave and the maximum intensity of the time pulse differ on a pulse to pulse basis ($\Delta\phi_{ceo}$). [147, 176] This difference is due to the difference between the phase and group velocity of the pulses. As shown in Figure 2-3, the time pulse is shown in green and the carrier wave in black dashed lines, the difference between the peak of the time pulse and the peak of the carrier wave is the offset, $\Delta\phi_{ceo}$. This offset then carries through to the frequency comb structure in the frequency domain, where the observed frequency, ν_n, is calculated by the repetition rate frequency, f_r, multiplied by an integer mode number, *n*, and the CEO frequency, f_0:

$$\nu_n = f_0 + nf_r \qquad \textbf{Equation 2-3}$$

In addition, the CEO frequency, f_0, and the pulse to pulse shift, $\Delta\varphi_{ceo}$, are related by:

$$f_0 = \frac{1}{2\pi} f_r \Delta\phi_{ceo} \qquad \textbf{Equation 2-4}$$

As this carrier-envelope offset property changes for each time pulse, the absolute frequency of each comb line changes as the pulse-to-pulse shift changes. It is therefore necessary to either characterise or remove the CEO frequency, which can be done through two methods. The first method is to use difference frequency generation (DFG), which takes the frequency difference between two comb structures that were generated from the same source. This means, that the frequency offset is removed through basic mathematics:

$$\nu_n = (f_0 + n_1 f_r) - (f_0 + n_2 f_r) = (n_1 f_r - n_2 f_r) \qquad \textbf{Equation 2-5}$$

The second method involves is known as *f*-to-2*f* self-referencing. If a low frequency, nf_r, peak is doubled to its second harmonic value, $2(nf_r)$, it will have approximately the same frequency as the corresponding $2nf_r$ on the high frequency side of the spectrum. By measuring the heterodyne beat ($2\nu_n - \nu_n$) between these two frequencies, this generates a difference which is just the CEO frequency (f_0): [176]

$$2\nu_n - \nu_n = 2(nf_r + f_0) - (2nf_r + f_0) = f_0 \qquad \textbf{Equation 2-6}$$

Thus, the system can directly measure the frequency offset value, hence the term self-referencing.

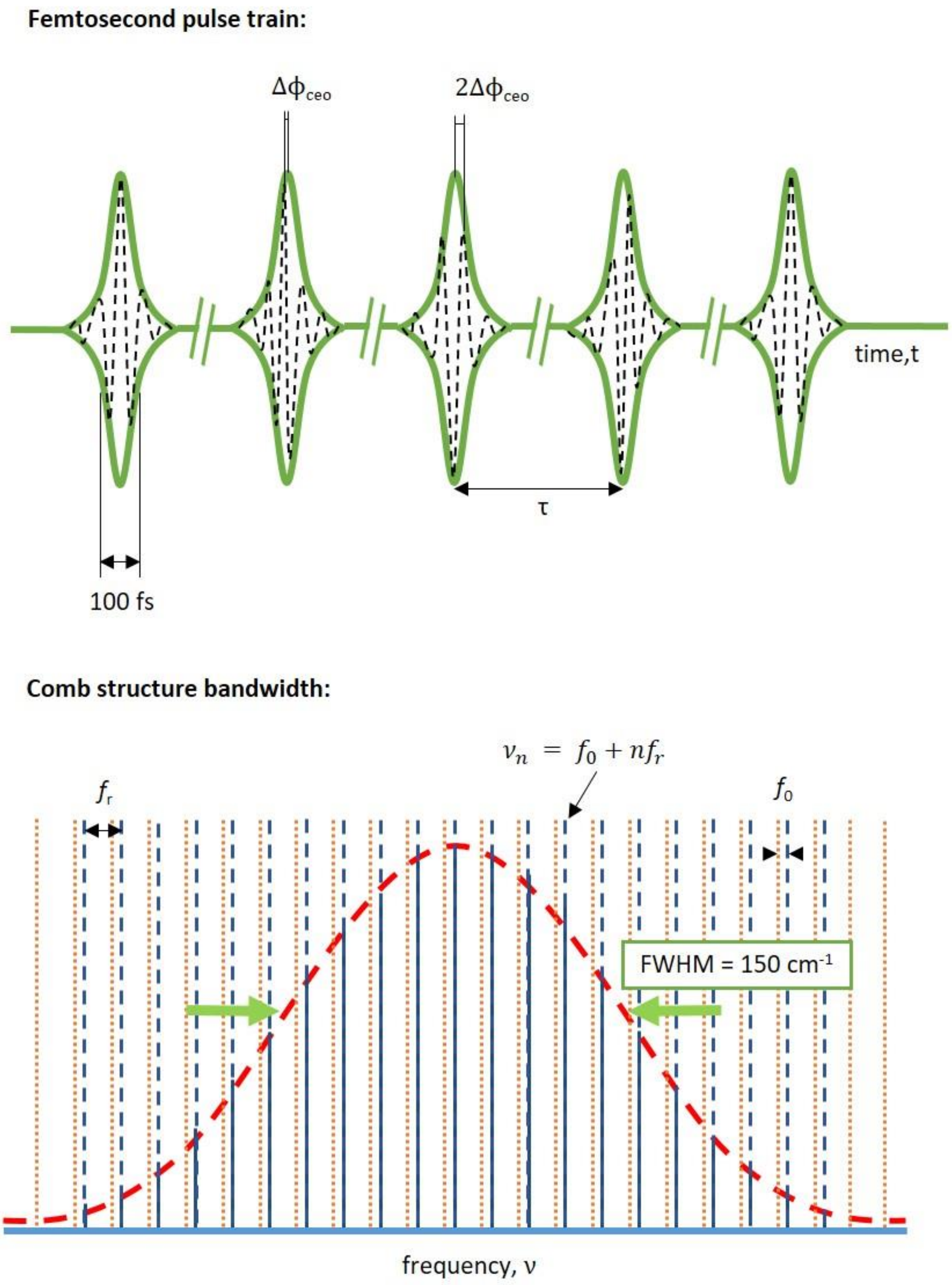

Figure 2-3 Carrier Envelope Offset. Schematic showing how a frequency comb laser outputs a stabilized pulse train of femtosecond time pulses, where each pulse is separated by the round-trip time of the cavity, τ. Within the pulse envelope there is a difference between the pulse intensity and the carrier wave, defined as the carrier envelope offset (CEO), or $\Delta\varphi_{ceo}$. Within the frequency domain, the broad spectral bandwidth related to the time domain through the Fourier transform relationship, also exhibits CEO, f_0. This offset changes the observed comb teeth frequency ν_n, through simple addition: $\nu_n = f_0 + nf_r$, where n is the mode number of the comb tooth and f_r is the repetition rate frequency between adjacent comb teeth. Adapted from reference [147].

2.2. Experimental Apparatus

2.2.1. The Optical Layout

Figure 2-4 shows a pure schematic of the entire optical layout, incorporating both experiment apparatuses and the VGC detection set-up. The entire box outline within the figure does not represent the full optical table which is 2.5 m x 1.5 m in size, as the free-jet expansion experiment is housed on a different optical table. However, the optical table is the same orientation as the figure box, and the general layout is correct. Within the following sections, and where appropriate, the optic or lens has been labelled to match the label in Figure 2-4. Presently, the mid-IR comb from 2900 to 3600 nm, or 2750 to 3400 cm^{-1} is to the right of the optics table, from which the output is directed towards the flow cell and the free-jet expansion chamber: a magnetic mirror mount (R1) is used to direct the beam towards either one of these. After the frequency comb has passed through the appropriate gaseous sample in either apparatus, the output is fibre coupled to the VGC detector, which consists of, in order of notable optics, a five times beam magnification (L3 and L4), a +100 mm FL (focal length) cylindrical lens (L5), an 8.1 x 25.4 x 76.2 mm CaF_2 VIPA optic (Light Machinery), a 50 x 50 mm diffraction grating with 450 groves per mm, a + 440 mm FL lens (L6), and finally a + 50 mm FL achromatic doublet lens (L7). Finally the 2D array of the frequency comb is imaged onto the InSb detection camera.

All simple lenses and mirrors in this set-up are 1” in diameter and are constructed from either AR (anti-reflective) coated CaF_2 (Thorlabs) or coated with *Silflex* (Materion Balzers Optics), which are specifically designed for the mid-IR region. Other optics such as the VIPA, the diffraction grating, and the imaging lenses were sourced from other companies and described in their respective sections below.

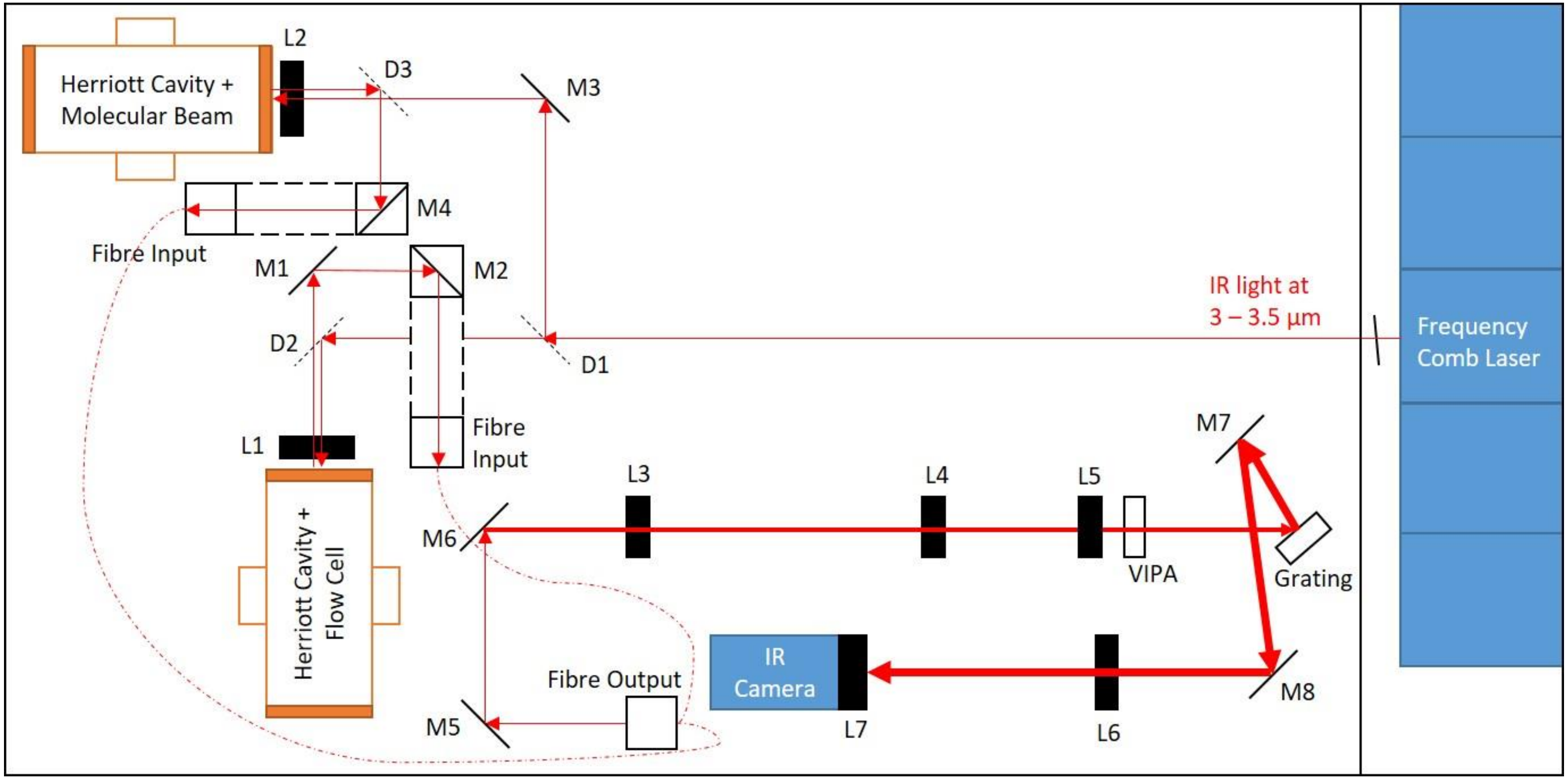

Figure 2-4 Optical Layout. Schematic of the full optical layout for frequency comb laser, the two optical gas cavities and the detection setup. While the general layout is correct, the diagram is not to scale. The red lines show the direction of the mid-IR comb at 2750 to 3400 cm^{-1}, the solid black lines are mirrors (labelled M), black dotted lines are either ‘D’ optics (labelled D) or removable mirrors (R), and black boxes are focusing lenses (labelled L). The frequency comb is passed through either the Herriott cavity in the flow cell, or the Herriott cavity and the free-jet expansion apparatus. Through the use of fibre coupling, the comb is then directed through the detection set up which is further detailed in section 2.2.6.

2.2.2. Frequency Comb Laser

The commercial frequency comb laser this thesis uses is produced by Menlo Systems GmbH (Munich, Germany). This system uses a single fibre laser and multiple non-linear optical techniques to produce a frequency comb laser output centred at 3125 cm^{-1} (3200 nm) and a spectral range of approximately 2750 to 3400 cm^{-1} (2800 to 3600 nm). Figure 2-5 shows the five compartments which generate the frequency comb output: Firstly, inside the M-comb compartment (box 5), a 980 nm diode is used to pump the erbium-doped fibre to generate a seed light at 9615 cm^{-1} (1560 nm), with a laser repetition rate of approximately 250 MHz, or 0.008 cm^{-1}. This repetition rate is set by the length of the cavity (as previously discussed in section 2.1.3). To ensure that a known and controllable repetition rate is used, the cavity length is repetition rate locked. The reference frequency is generated by frequency mixing 245 MHz, created from a 10 MHz rubidium frequency standard clock (SRS FS725), with 5 MHz produced from a 20 MHz source. The 20 MHz source is from a Marconi Signal Generator, also referenced to the rubidium clock. The generated 250 MHz is then the reference point for a piezoelectric crystal on which one cavity mirror is mounted. This crystal changes in length in response to an electrical signal. A PID (Proportional-Integral-Differential) locking scheme is employed to ensure a tight lock to this repetition rate. In addition, the 250 MHz repetition can be changed by altering the 20 MHz signal given by the digital delay synthesiser (DDS). During an experiment, this is typically done in 400 Hz step sizes, corresponding to changes of 100 Hz to the repetition rate. The benefit of this change in repetition rate means different wavenumbers can be implemented over the course of an experiment. This is further discussed in section 3.1.

After generation of the seed light at 6410 cm^{-1} (1560 nm), this light is then amplified in two separate parts (inside box 4, the Er-Amp). One part is used directly as 6410 cm^{-1} and the other part is used to pump the ytterbium-doped fibre (box 1) to generate the 9615 cm^{-1} (1040 nm) light through a non-linear process. The 9615 cm^{-1} is also amplified and then subjected to a compressor inside the TOD section (Third Order Dispersion, box 2), which broadens the frequency range as the non-linear process narrows the temporal profile of the laser. Finally, the two amplified sources are mixed (box 3) in a temperature controlled PPLN (Periodically Poled Lithium Niobate) crystal where the energies undergo difference frequency generation (DFG) which subtracts the two energies to give the broad comb structure centred at 3125 cm^{-1} (3200 nm) with a FWHM bandwidth of 250 cm^{-1}.

The PPLN crystal used is a quasi-phase-matched material where the refractive index of the crystal allows for phase matching of two or more energies as the light travels through the medium. [210] When the correct temperature is set for the PPLN (135 °C for this system), the generated photons are always in constructive interference with each other, thus yielding highly efficient conversion. Other crystals used for DFG processes within ultrafast lasers are required to be very short in length, sacrificing conversion efficiency, in order for the pulse to not experience temporal broadening. PPLN crystals do not experience this broadening due to the phase-matching properties as the light propagates through the crystal.

However, the DFG process in the PPLN crystal is not the only non-linear process which occurs. Other wavenumbers of light can be generated, provided the energy is conserved. For example, the two fibre outputs at 6410 cm^{-1} (1560 nm) and 9615 cm^{-1} (1040 nm) can

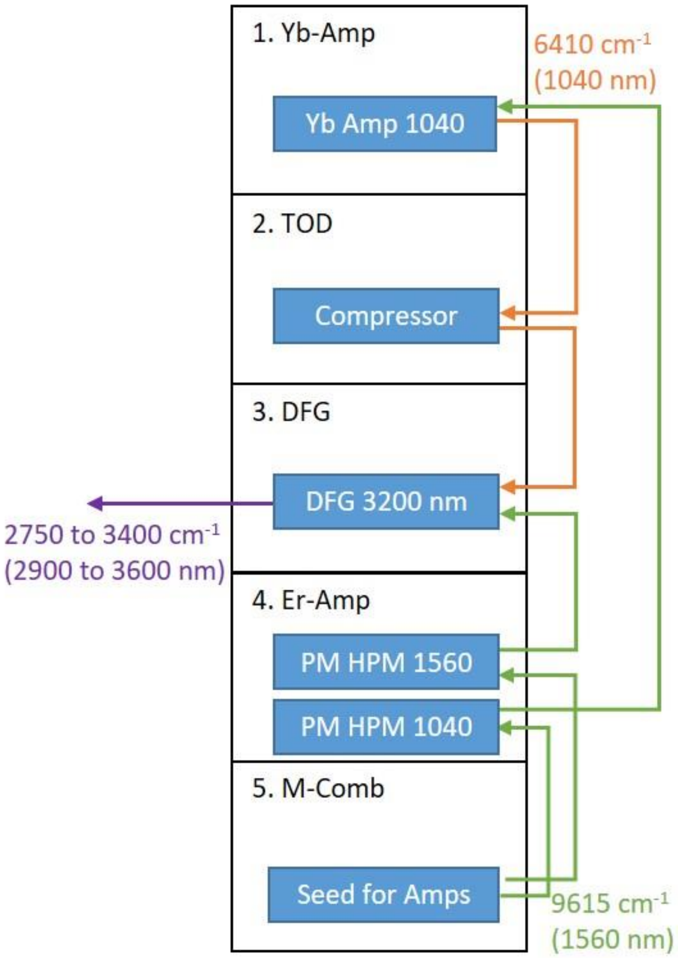

Figure 2-5 Frequency Generation Modular Compartments. Schematic diagram of the 5 components which generate the frequency comb laser centered at 3200 cm^{-1}. M comb = Primary Oscillator; TOD = Third Order Dispersion; PM = Polarization Maintaining; HPM = High Power Measurement; DFG = Difference Frequency Generation; PPLN = Periodically Poled Lithium Niobate. Adapted from reference [211]

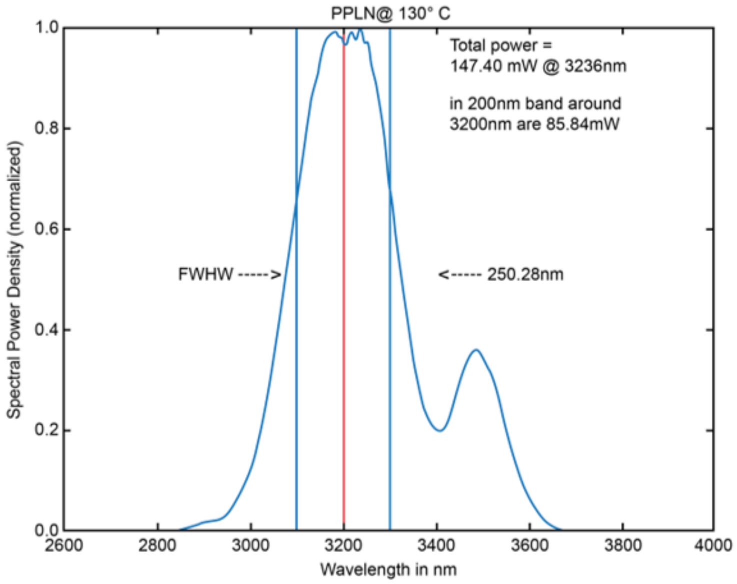

Figure 2-6 Spectral Profile of the Frequency Comb. This graph shows the spectral profile of the frequency comb from 2800 to 3600 nm, or 2750 to 3400 cm^{-1}. The profile has a FWHM of 250 nm or 245 cm^{-1}, with the maximum power output of 147.40 mW at 3236 nm or 3090 cm^{-1}. Taken from reference [211].

undergo sum frequency generation (SFG) to generate orange light at 16025 cm^{-1} (625 nm), or second-harmonic generation (SHG) to generate green light at 19230 cm^{-1} (520 nm) and near-infrared light at 12820 cm^{-1} (780 nm). As this project is only interested in the mid-IR output centred at 3205 cm^{-1} (3120 nm), a removable filter is used immediately after the output of the laser.

For the PPLN crystal set to 135°C, the wavenumber output is centred at 3205 cm^{-1} with a FWHM of 250 cm^{-1}, spans from 2750 to 3400 cm^{-1}, and has a total output power of 147 mW (as shown in Figure 2-6). This range is ideal for probing C-H stretches which appears strongly from 2850 to 3300 cm^{-1}, alongside some O-H and N-H vibrational stretching frequencies depending on the structure of the molecule. For example, N-H antisymmetric stretches, which in amides appear from 3330 to 3400 cm^{-1} cannot be measured by our frequency comb, but some N-H symmetric vibrational stretches in aliphatic amines, which appear from 3250 to 3300 cm^{-1} could be visible. There is limited tunability of the centre of the frequency comb output. However, it can be slightly tuned, by approximately 50 to 100 cm^{-1} by changing the PPLN crystal temperature or the time delay between the temporal overlap of the 6410 cm^{-1} and the 9615 cm^{-1} energies.

2.2.3. Sample Apparatus

There are two different experimental apparatuses used, but both are currently using the same optical arrangement surrounding the gaseous samples. In addition, both experiments use a vacuum-sealed chamber to house the gaseous sample, and have a Herriott cell beam pattern which allows for an extended path length of the comb light which interacts with the sample.

2.2.3.1. Herriott Cell Fundamentals

For absorption spectroscopy, we use the Beer-Lambert Law to measure the absorption of light by the molecule: [114]

$$\mathrm{A}_{\nu} = \ln\frac{I}{I_0} = N\sigma_{\nu}L_{path} \qquad \textbf{\textit{Equation 2-7}}$$

(This has been previously defined in section 1.2.3). To increase the observed absorbance of the specific sample, there are only two factors which can be changed: N and L_{path}. The absorption cross section, σ_{ν}, is a property that is specific to the molecule that is being observed and the value can only be increased by changing the temperature of the molecule, which in most cases is not feasible. The concentration of the sample can be increased to a certain extent, however, increasing the concentration introduces complications such as saturation, scattering issues, potential dimerisation of the molecules, or broadened spectra from pressure effects. Therefore, most sensitive absorption techniques increase the path length of the light through the sample, as increasing the path length leads to a direct increase in the measured absorbance. There is also the added benefit that the longer the path length, lower concentrations can potentially be detected of the sample molecules and or the possibility of detecting molecules with smaller σ_{ν}.

Herriott cells work by reflecting the light between two curved mirrors (H1 and H2) multiple times, [212, 213] where the number of passes between the mirrors depends on the focal length, distance between the mirrors, and the entrance angle of the input light (Figure 2-7). For two mirrors of focal length, f, and spaced at distance, d, the angle, θ in radians, between adjacent rays can be calculated: [213]

$$\cos(\theta) = 1 - (\frac{d}{2f}) \qquad \textbf{\textit{Equation 2-8}}$$

This calculated angle can then be used to find the Cartesian coordinates of each ray, x_n and

y_n. In addition, the number of round-trips through the cavity can be determined through the θ angle: [213]

$$2n\theta = 2\pi \qquad \textbf{\textit{Equation 2-9}}$$

where *n* is the integer number of return trips, or two passes, through the optical cavity. For example, when *d* = *f*, *n* is 3, so six total passes through the gas sample. When an optical cavity fulfils the conditions in Equation 2-9, the pattern of the rays looks like that as shown in part A, Figure 2-7. Consecutive rays proceed around the mirrors in an almost 90° pattern before exiting the cavity. While this method gives many passes, there is a maximum number of passes and thus a limit on the path length. More complicated ray paths are obtained when: [213]

$$2\mathrm{v}\theta = 2\mu\pi \qquad \textbf{\textit{Equation 2-10}}$$

where μ is an integer number, not equal to *n*. This condition then gives rise to patterns as shown in part B, Figure 2-7, where the consecutive rays are separated by more than 90°.

Although hard to show in a figure, the ray pattern shown in part B has many more passes than the ray pattern shown in part A. Essentially, the first *x* amount of rays are evenly spaced around H1 and H2, where *x* is an integer number, for example the first 10 rays. Then, instead of meeting the exit conditions, the 11th ray hits directly next to where the 1st ray hit H2, this pattern continues around both mirrors for another 9 rays, subsequently the 21st ray hits H2 directly next to where the 11th ray hit and so forth until the exit conditions are matched for the focal length, *f*, and the distance between the two optics, *d*. This more complicated path gives rise to a much longer path length. [214] Furthermore, the beam undergoes less distortion in this more complicated alignment, and despite being a much longer beam path length, the photon flux of the beam exiting the optical cavity is higher than the equivalent number of passes in a standard Herriott alignment. Both types of Herriott patterns have been utilised in this project, with the more complicated ray pattern, as shown in Figure 2-7 part B, being the current alignment of the room temperature flow cell, and the simpler ray pattern being used for the free-jet expansion apparatus. Figure 2-8 shows photographic images of the two different Herriott cell patterns. Picture A shows the typical pattern and picture B shows the more complicated pattern. For both images, the red dots are caused by the visible light output from the frequency comb. While this is a good approximation for the mid-IR comb light, it is not an exact overlap of the two wavelengths.

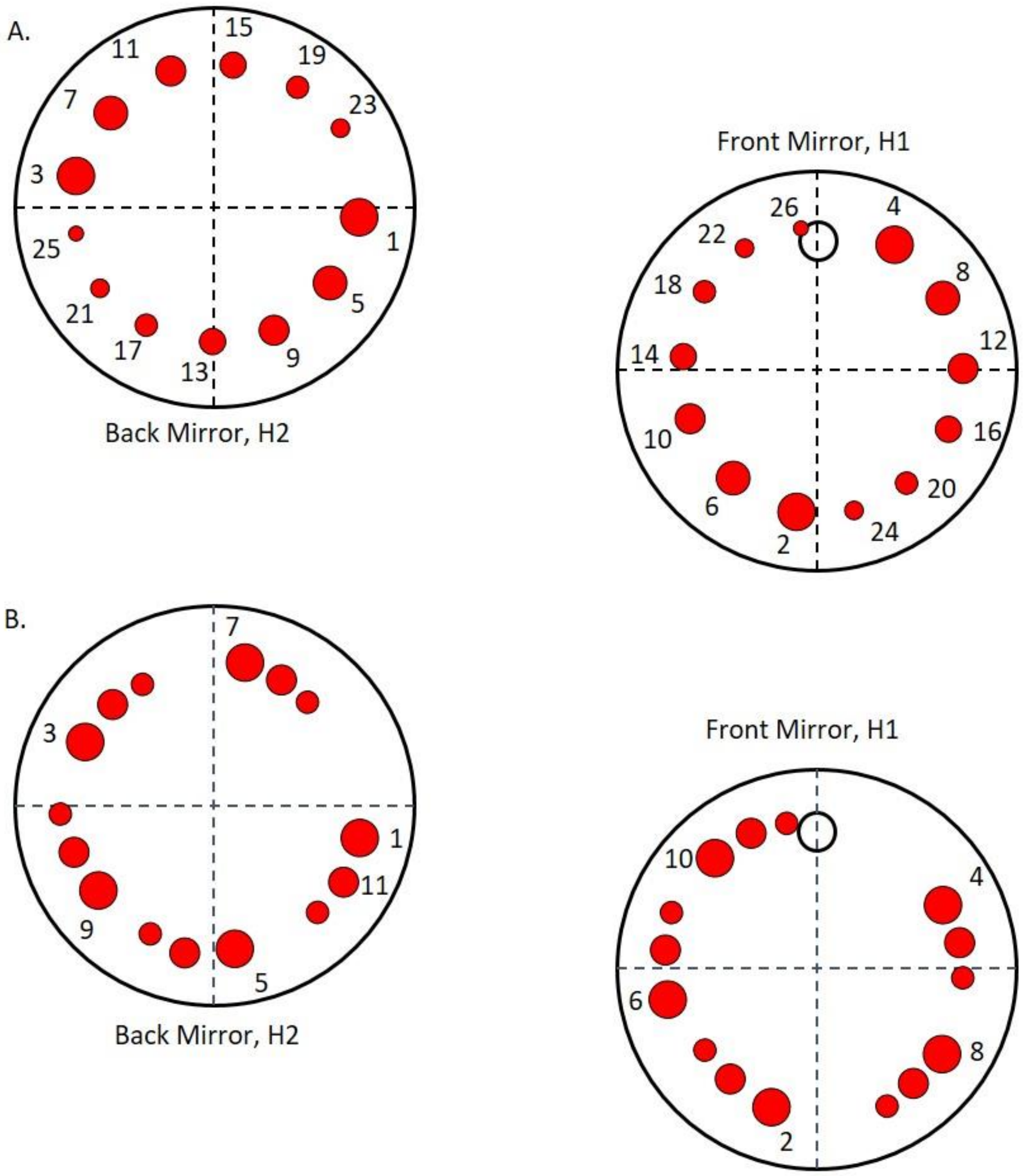

Figure 2-7 Schematic Herriott Cell Laser Spot Patterns. A. Typical Herriott cell pattern featuring 26 passes (each red dot represents where the laser hits the mirror) between two concave mirrors (H1 and H2). The numbers next to each red dot is the pass number, and follows a clockwise pattern where each *n* + 1 pass is almost a 90° turn from the *n*th pass. B. A more complicated Herriott cell pattern showing the first 7 passes through the cavity. The first four passes follow a similar pattern to the simpler pattern shown in part A, but the 5th pass is then further away from the 1st pass and so forth.

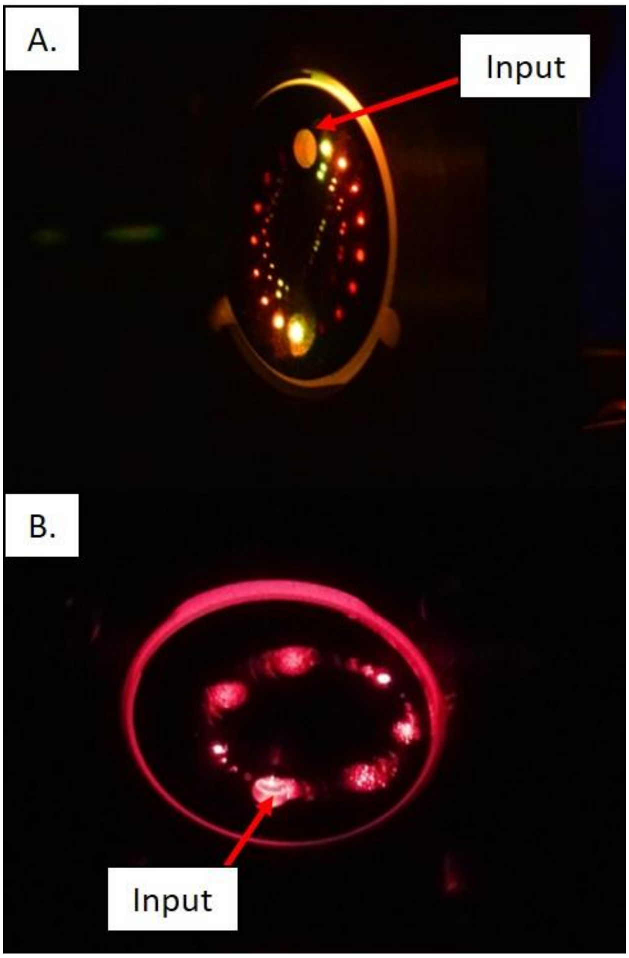

Figure 2-8 Pictures of Herriott Beam Patterns. A. Picture of a typical Herriott cell pattern taken from an old configuration where H1 was on the outside of the cell. B. Picture of complicated Herriott cell pattern taken from inside the free-jet expansion chamber. Pictures were acquired using the visible light output from the frequency comb, and is not a direct overlap of the mid-IR light.

2.2.3.2. Deployment

The Herriott cell in the room temperature flow set-up consists of two +100 mm FL, gold coated, concave mirrors (ThorLabs), which reflect light in the IR region. The comb light is introduced to the cell through a small 3 mm hole towards the top of the mirror, rather than in the centre of the mirror, as this allows for a greater number of passes. Over the course of the project, the Herriott cell has been re-aligned many times, meaning the distance between the two mirrors and the number of passes changes with each realignment. This realignment process therefore means we operate with a different path length across different experiments. However, for each of the experiments in this project, the Herriott cell length is kept consistent for each spectra acquisition. For each change in the path length of the Herriott cavity, the new path length is determined by recording a spectrum with a known concentration of CH_4 and comparing to a reference spectrum from *HITRAN*. [215, 216] Typical path lengths given by the Herriott cell range from 400 cm during the early development stages of the project to the current 1200 cm path length. The specific path length and number of passes is stated in the experimental methods for each experiment.

The interaction region between the gas sample and the Herriott cavity is shown in Figure 2-9, part A. As the gas is flowed through the cell, it can be assumed that the entire volume of the sample cell contains the gas sample (as shown in blue), therefore the only limiting factor for the interaction region is the full path length of the frequency comb laser (as shown in red). Subsequently, this means the calculated path length, as determined from a CH_4 spectrum, can be thought of as the entire path length of the frequency comb through the cavity.

In comparison, the free-jet expansion experiment is housed inside a custom built 6 way cross chamber, with DN160 CF or LF attachments, and is directly attached to an *Edwards* Turbo vacuum pump on the sixth flange. A Herriott cell cavity was also used in the initial stages of development, with the two +100 FL, gold coated, concave mirrors (ThorLabs) caged mounted inside the chamber. However, the alignment for this optical set-up was difficult, and due to large uncertainty in the concentration of the sample in the free-jet expansion (see section 2.2.4.4), and the physical size of the free-jet expansion, the actual path length is hard to quantify. In addition, the free-jet expansion method gives a lower concentration of molecules in the chamber than the flow method, and has a smaller interaction region with the frequency comb laser (Figure 2-9, part B). Therefore, to increase the path length and thus increase the observed absorption we will move to an enhancement cavity. This enhancement cavity will use two high finesse mirrors with focal lengths of +1000 mm (Layertec). Currently, the enhancement cavity is under construction and further discussion of this work can be found in section 7.1.1. The current interaction region between the free-jet expansion and the optical cavity is shown in Figure 2-9, part B, however this is a pure schematic as the size of the free-jet expansion is unknown.

Photographs of both sample cells, along with the approximate interaction regions, are shown in Figure 2-10. For the flow cell, the Herriott cavity mirrors are directly attached to the flanges at either end of the cell with external adjustable mounts. Whereas for the free-jet expansion apparatus, the cavity mirrors are internally mounted on adjustable mounts. This means that to adjust either cavity mirror, the chamber must be opened.

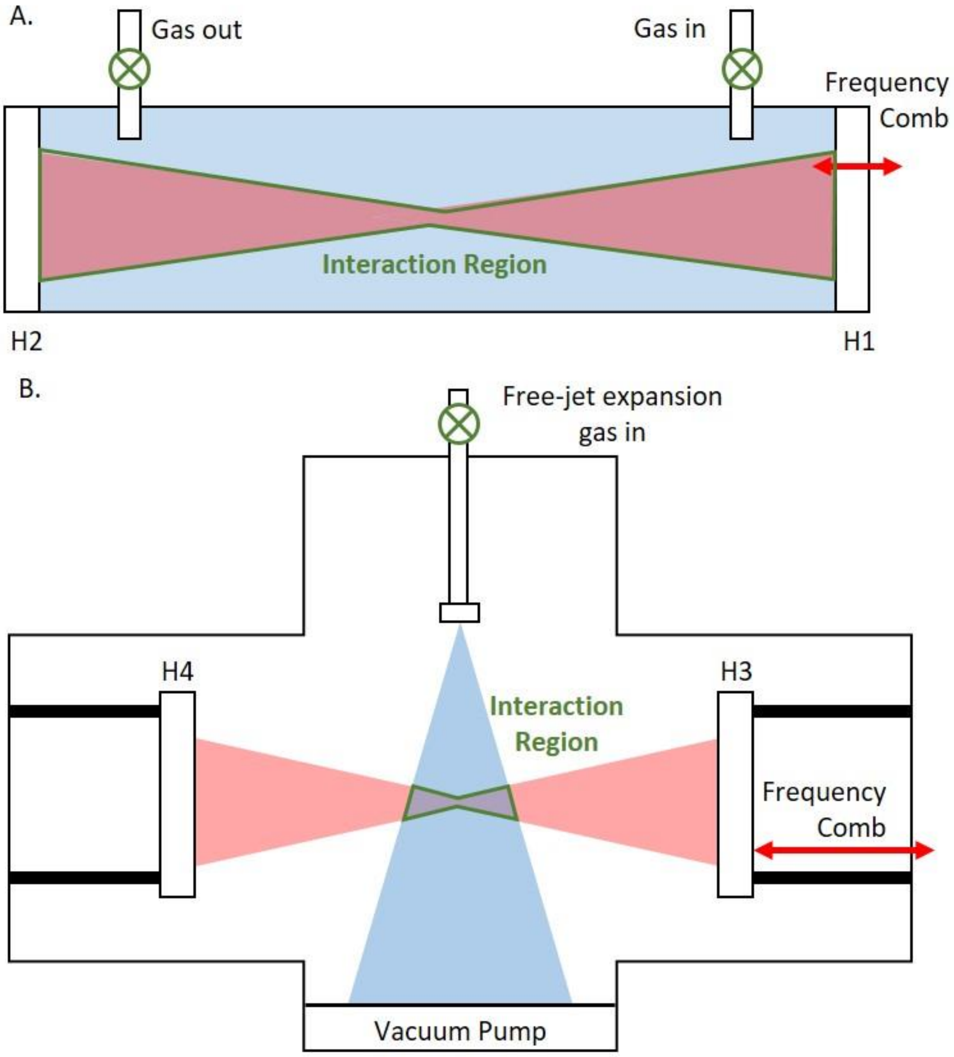

Figure 2-9 Interaction Regions of Molecules and Optical Cavities. A. Schematic of the flow cell showing the approximate path of the Herriot cell (red) between the two mirrors (H1 and H2), and the volume of gas (blue) in the cell, and the interaction region of the two (green box). B. Schematic of the free-jet expansion chamber showing the approximate path of the Herriott cell (red) between the two mirrors (H3 and H4), and the free-jet expansion (blue) in the chamber, and the interaction region of the two (green box).

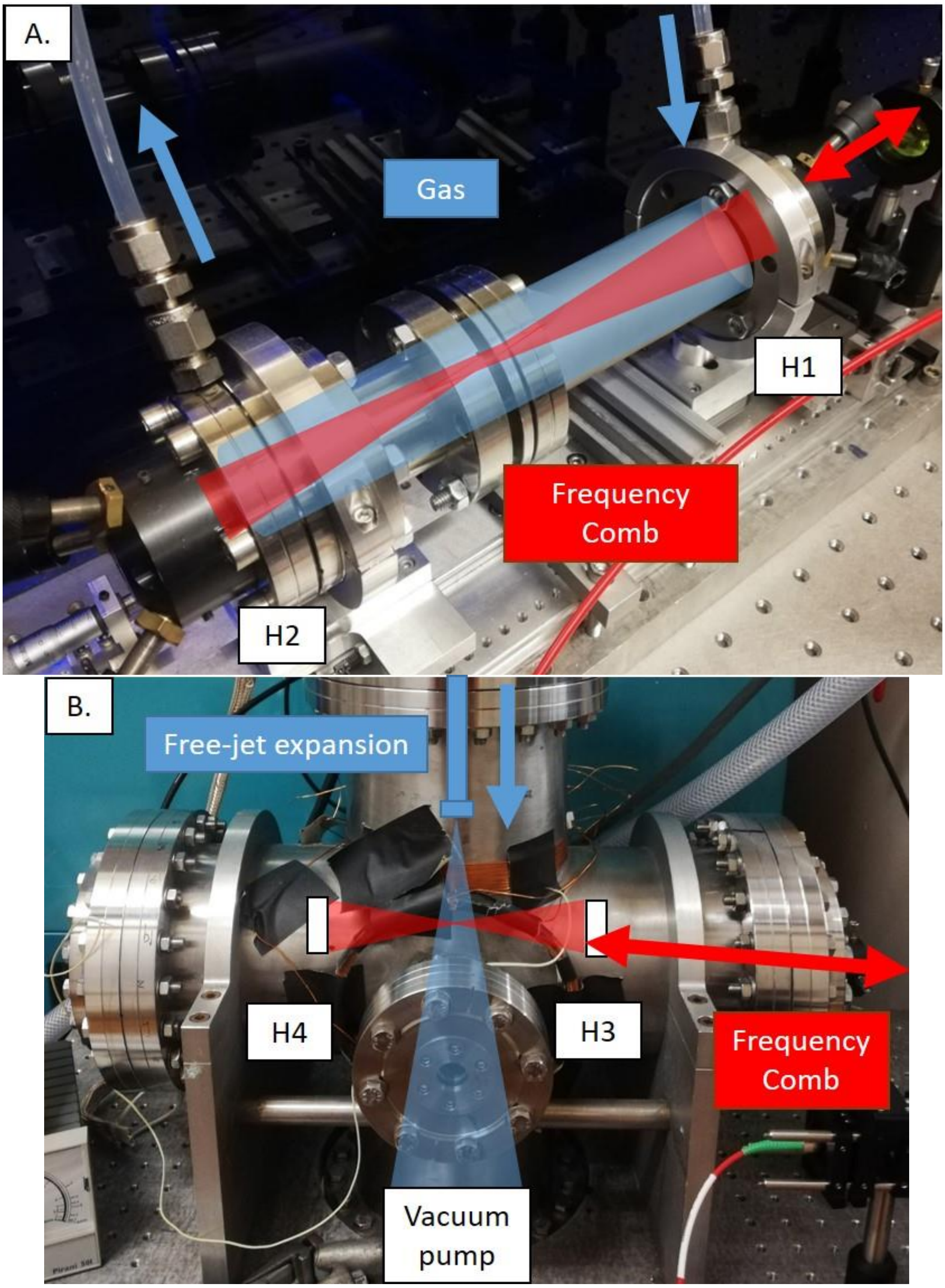

Figure 2-10 Pictures of Sample Apparatus. A. Picture of the flow cell showing the gas flow direction and the approximate frequency comb light path through the cell. B. Picture of the free-jet expansion chamber showing the free-jet expansion trajectory and the approximate frequency comb light path through the cell.

2.2.4. Gas Delivery

Alongside having two different optical cavities for the room temperature and cold temperature absorption spectra experiments, there is also a different gas delivery system. For the room temperature cavity, only a simple static cell or flow cell is required to achieve detectable concentrations, where typical concentrations start at 8×10^{11} molecule cm^{-3}. [137] A static cell just simply requires filling the cell to a certain pressure for taking measurements. However, static cells are not often used as it can be difficult to fill the cell with the required pressure and ensure that pressure is maintained throughout the experiment. In addition, it can be difficult to recreate the conditions for further experiments, and difficult to control the concentration of target molecule in a bath gas mixture. Therefore, it is better for repeatable experiments to control the flow of gases through the cell. This flow is achieved using mass flow controllers (MFC). An MFC works by applying a set voltage to the controller, this regulates the flow of the gas in relation to the pressure on the output side. Although referred to as a "mass" FC, the sensor inside the MFC is actually responding to the change in temperature of the gas flow. Similar to how the lasing cavity uses a PID feedback loop (section 2.1.3), MFC's work on a comparable feedback mechanism. Firstly, the initial flow rate is converted to an electrical signal based on the proportional change in temperature. This electrical signal is then sent to the comparison control circuits, where the flow rate setting signal and the actual flow signal are compared, and a difference signal is sent to the valve driving circuit. Lastly, the flow rate control valve moves in an appropriate manner to remove the difference between the set flow rate and the actual flow rate. [217]

In addition to controlling the pressure within the flow cell, the temperature of the flow cell can be increased by using resistive heating tape to record measurements above room temperature. However, this flow cell cannot be efficiently cooled down, therefore a different type of apparatus is required for the cold temperature experiments. However, the cold temperature apparatus requires a different approach for gas delivery, as it is the gas delivery method which causes the cooling of the molecules. For this project, a free-jet expansion is used to rapidly cool the molecules down to rotational temperatures ranging from 5 to 30 K. Free-jet expansions are generated by expanding a gas through an orifice into a vacuum at pressure P_B. [218] Before the gas exits through the orifice, we have a starting temperature, T_0, and a starting pressure, P_0. The difference in pressure before and after the orifice ($P_0 - P_B$) accelerates the gas, which then decreases the enthalpy of the gas and thus cools the molecules in the gas. [219] This cooling process can be further explained by

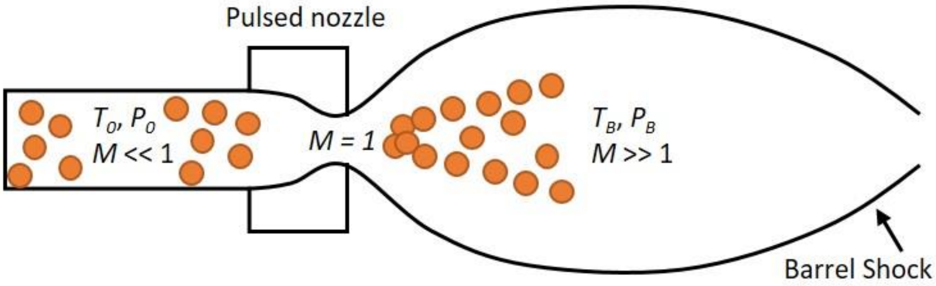

Figure 2-11 Free-Jet Expansion. Schematic of how a gas expands as a supersonic expansion. The gas before the nozzle is at temperature, T_0, pressure, P_0, and with M (Mach number) << 1. At the nozzle orifice M = 1. In the supersonic expansion, the gas is at temperature, T_B, pressure, P_B, and with M >> 1.
Adapted from references [218, 220]

understanding the conversation of momentum, the internal energy of the gas molecules is converted to kinetic energy, and therefore as the internal energy decreases the rotational temperature of the molecule must also decrease. If the ratio between the pressures, P_0/P_b is larger than 2, the gas undergoes supersonic expansion (Figure 2-11). In this supersonic expansion, the expansion of the gas can be characterised by pressure, P, temperature, T, the density of the molecules in the gas, n, and the velocity of the gas, v. Furthermore, across the gas expansion, the Mach number, M which is a dimensionless quantity representing the ratio of gas velocity to the speed of sound, can be characterised as M << 1 where the pressure = P_0, M = 1 at the nozzle orifice, and M >> 1 in the vacuum chamber (Figure 2-11). [218] Due to vacuum pumping constraints, the free-jet expansion is not used as a continuous flow source, but instead the gas is pulsed through the nozzle. This pulsed nozzle is explained further in section 2.2.4.4.

2.2.4.1. Gas Sample Line

To introduce gas to either the flow cell or the free-jet expansion set-up, a leak proof gas sample line capable of being placed under vacuum is used. In order to introduce liquid samples and control the flow of the gas mixtures, a new sample line was constructed. Certain requirements were needed for the new gas sample line: be able to isolate sections of the gas sample line so liquid samples can be changed or certain sections can be placed under vacuum, be able to dilute target molecules with a bath gas, and have the ability to quickly switch the flow of gas from the flow cell to the free-jet expansion.

For all components of the gas sample line, the metal framework is constructed from 6 mm (outer diameter) stainless steel tubing and 6 mm (outer diameter) flexible PTFE (polytetrafluoroethylene) tubing, with joints and other connections being made using *Swagelok* compression fittings. A simple diagram showing the full gas sample line is shown in Figure 2-12. Either Ar or N_2 can be introduced to the sample line as either the carrier gas for a liquid sample, or directed straight to either apparatus for background measurements. These two gases were chosen as the bath gas as they are inert and do not any exhibit IR frequencies. A third gas source, a 4.5% mix of CH_4 in N_2 is also attached to the sample line, as this mixture is used for the frequency calibration in experiments (see section 3.2.3).

As this project handles liquid samples, namely $CHBr_3$, CH_2I_2, and CH_2Br_2, there has to be a system to get the liquid samples into the gas phase. This is achieved using two different liquid sample containers (LSC): one for the flow cell (attached to MFC-1) and one for the free-jet expansion (attached directly to the chamber). Both work by passing either bath gas over the liquid sample and a portion of the sample is entrained into the buffer gas, as determined by the liquid's saturated vapour pressure. However, this process is done in two slightly different ways. For the liquid sample towards the flow cell, the liquid is placed in a small vacuum sealed container and the buffer gas "bubbled" through the sample. On the other hand, for the free-jet expansion liquid sample, a piece of glass wool is saturated with the liquid and then placed into a small stainless steel container and the buffer gas is passed through the glass wool. This glass wool method helps to get more of the liquid sample into

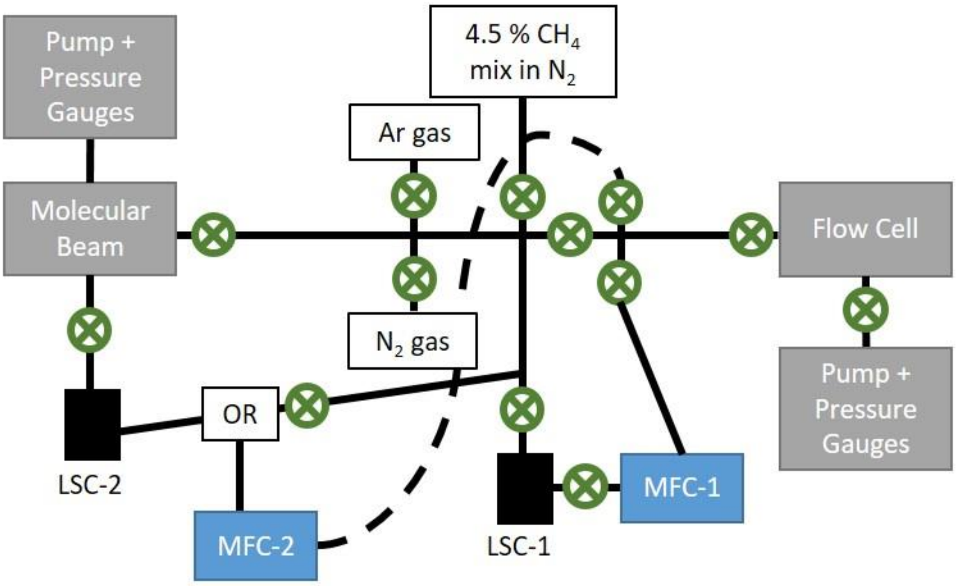

Figure 2-12 Gas Sample Line. Schematic of the gas sample line. 3 attached gas lines: N_2, Ar, and a 4.5% mix of CH_4 in N_2. Quarter turn valves are shown in green. Attached to the line are two LSCs (liquid sample containers) and two MFCs (mass flow controllers). Configuration of the sample line can be altered to have either the MFC-2 or LSC-2 in use.

the gas phase, while also being physically closer to the free-jet expansion. In addition, the use of an MFC is not needed as we do not need to have fine control of the concentration of the molecules in the free-jet expansion, we just want to get as much of the sample in the jet as possible.

2.2.4.2. Mass Flow Controllers

Currently, this project has three MFCs to use, each with a different maximum flow rate: 1000, 500 and 30 standard cubic centimetres per minute (sccm) (*Tylan FC-280*). These MFCs will be used in pairs so that one controller will be used to flow a precursor molecule and the other used to flow a buffer gas (N_2 or Ar) to reduce the percentage concentration of the precursor in the overall sample mixture. To calibrate the set voltages and relate them to the flow units' sccm, the MFCs are connected to a known gas, typically N_2. The gas is then flowed through a solution of soap and water to create bubbles, these bubbles then travel through a burette and the time taken for the bubble to travel a set volume at a specific voltage is recorded. From this data, the flow rates are then converted to sccm and plotted for each MFC. As gases have different thermal properties, to switch between calibration and operation gases, conversion factors are used, e.g. for N_2 it is 1, for O_2 it is 0.98, and for CH_4 it is 0.76. [217] In addition, volumetric flow rates can be affected by changes in ambient temperature and pressure, so further corrections are needed to convert flow rates at different operating temperatures and pressures.

2.2.4.3. Flow Cell

The flow cell is a stainless steel DN40CF tube with an approximate volume of 800 cm^3, and directly attached to an Edwards vacuum pump. When under vacuum, the cell is held at <0.001 mbar and can withstand pressures up to atmospheric pressure, if not higher pressures (however this is untested).

After the gas cell, there are two pressure readers: an MKS Baratron (0 to 100 mbar) and a capacitance manometer (100 to 1000 mbar). The MKS Baratron reads a direct pressure within the gas cell in mbar, and the manometer shows a pressure relative to atmospheric pressure in mbar. For later experiments, specifically those involving the pressure broadening measurements for CH_2Br_2, an Omega Engineering Inc*.* pressure transducer (0 to 350 mbar) replaced the manometer. For flowing the gas through the cell, the pressure is controlled via the opening of a needle valve to the roughing pump. This control of the needle is particularly useful for increasing the pressure in the gas cell without changing the MFC flow settings.

2.2.4.4. Free-Jet Expansion Chamber

The free-jet expansion chamber is much larger than the flow cell. As stated above, it is a custom 6 way cross chamber, and is directly attached to an Edwards Turbomolecular vacuum pump. Within the chamber, there is a hot-filament ionization gauge which reads an average pressure inside the chamber. Under vacuum, the pressure is close to 1×10^{-8} mbar, and during experimental operating conditions (i.e. the free-jet expansion is pulsing) the pressure reads approximately 2×10^{-4} mbar. However, this pressure reading is an average of the pressure within the entire chamber, and so cannot be recorded as the absolute concentration of the sample. As the pressure of the gas before the chamber is over 1000 mbar (operating pressures are typically close to 2000 mbar), this gives a good pressure difference for the supersonic expansion to work well and give free-jet expansion temperatures of approximately 20 to 40 K for the gas samples tested.

While it is possible to run the free-jet expansion as a continuous flow, this project uses a pulsed valve to selectively introduce the gas sample to the chamber due to pumping speed constraints. The valve is a Series 9 Solenoid Pulsed valve available from Parker Hannifin [221] and a schematic of the valve is shown in Figure 2-13. In simple terms, the

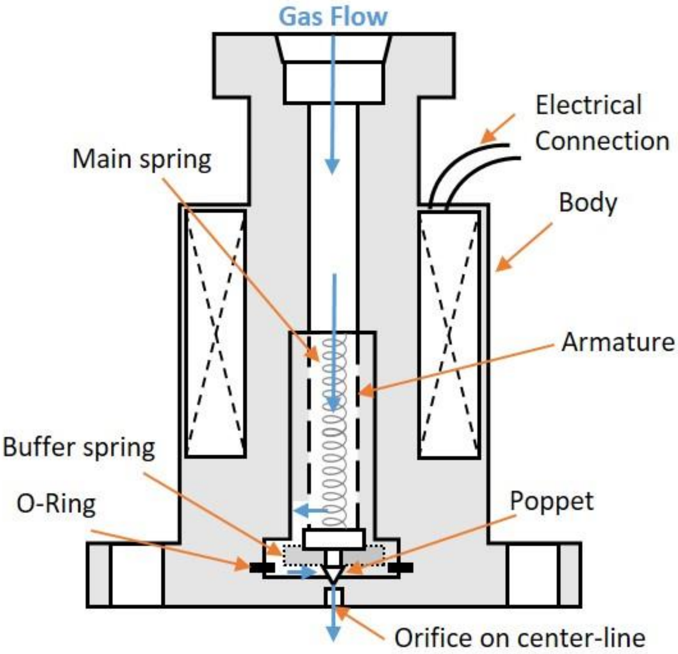

Figure 2-13 Series 9 Solenoid Pulsed Valve. Diagram of the Series 9 solenoid pulsed valve used for the free-jet expansion. The difference between the high pressure before the pulsed valve and the low pressure after the pulsed valve is maintained by the O-ring within the valve and the poppet on the center-line. All important parts have been labeled in orange, and the flow of the gas sample is shown with blue arrows. Adapted from reference [221].

valve works by moving an armature back and forth in response to an applied voltage across a solenoid. This voltage has a certain start time relative to the camera detection start time and has a pulse width of 350 to 450 µs. As the armature moves back and forth (facilitated by the two springs), the poppet, which sits in the orifice, also moves back and forth causing a hole for which the gas flow expands through and into the main chamber.

2.2.5. Fibre Coupling

2.2.5.1. Theory

To help direct the comb light between the sample cells and the VGC detector, the laser is fibre coupled into a single-mode (SM) mid-IR fibre. Not only does this help to reduce the number of optics on the optical bench, but the fibre output is a TEM_{00} (transverse electromagnetic mode) transverse Gaussian beam which does not exhibit significant divergence. In addition, the use of the fibre means it is easy to switch between the two gas cell apparatus, flow cell or molecular beam chamber, while not affecting the VGC detector set-up. In addition, any change in the alignment of either apparatus means there is no need to realign the VGC detection alignment which is a long and repetitive process (section 2.2.6.3).

Optical fibres are comprised of a cylindrical core, with a refractive index n_1, and an encasing cladding of refractive index, n_2. For the light to be confined to the core of the fibre, n_1 must be greater than n_2. For the light to be efficiently coupled into the fibre, the numerical aperture (NA) between the laser (related to the beam size) and the fibre must be matched. For the fibre, the NA is related to the refractive indices of the core and cladding, and is essentially a dimensionless characterisation of the range of angles within which the light will be transmitted into the fibre:

$$\Delta = \frac{n_1^2 - n_2^2}{2n_1^2} \qquad \textbf{\textit{Equation 2-11}}$$

$$NA = n_1\sqrt{2\Delta} \qquad \textbf{\textit{Equation 2-12}}$$

where Δ is related to the relative differences between the refractive indices, and for coupling to be effective, $\Delta << 1$. To match the NA between the laser and the fibre, an aspherical lens is implemented which focuses the light to the correct beam size. [222]

The size of the fibre core gives a limit on the number of modes supported in the fibre, and thus limits the number of modes which the fibre outputs on the other side. For a core size of less than 10 µm, the fibre is said to be single-mode (SM), however if the core is greater than 10 µm the fibre is multi-mode (MM). [223, 224] SM fibres, as the name suggests, only support the lowest-order mode which is TEM_{00} Gaussian shaped beam, whereas the MM fibres can support multiple modes, depending on the size of the fibre core. However, the more modes coupled into the fibre leads to more intermodal dispersion due to the differential time delay between modes of light inside the narrow fibre. This dispersion can be limited through the use of the graded-index fibre. There are two types of index fibres: if both refractive indices are consistent across the fibre, then the fibre is said to be a step-index fibre, but if n_1 varies with the radius of the fibre core, it is a graded-index fibre. [223] Furthermore, inside the SM fibre, the only dispersion possible is intramodal dispersion which is caused by variation of group velocity with respect to wavelength in the singular mode. Fortunately, the dispersion problems are limited by the use of the aspherical lens.

2.2.5.2. Deployment

For the fibre coupling of the frequency comb laser associated with this project, ZrF_4 fibres are used: 2 m from the enhanced cavity to the VGC detection and 1 m from the Herriott cell to the VGC detection (both from ThorLabs). The fibres in use are only 9 µm in diameter, therefore they are single-mode fibres and only output TEM_{00} Gaussian beams. Furthermore, the fibre material efficiently supports wavelengths in the range 2300 to 4100 nm with a transmission of > 98% from 2500 to 3500 nm. The aspherical lens chosen to the focus the comb into the fibre is specifically coated for the mid-IR wavelengths and has a short focal length of 4 mm. For these ZrF_4 fibres the numerical aperture (NA) is 0.19, this means the beam size needs to be a corresponding 1.02 mm, as determined by the following equation:

$$NA = \frac{n_1 D}{2f}$$

Equation 2-13

where, D is the diameter of the laser beam, f is the focal length of the aspherical lens (+4 mm FL, ThorLabs), and n_1 is assumed to be 1.49 at 3200 nm. As the FWHM beam size of the laser before the fibre coupling is approximately 1 mm, no further magnification was needed.

However, the use of the fibre coupling leads to a 60% power loss of the comb light, which is due to a combination of the loss of unsupported modes inside the fibre and imperfections within the fibre. Unfortunately, this 60% loss of power is much higher than expected, as theoretically the power loss within the fibre should only be 7.5 % for a 2 m cable. Other factors influencing the observed power loss is misalignment into the fibre, unclean fibre ends, and numerical aperture mismatch, although these factors can be easily controlled within the laboratory. As the power loss within the fibre is higher than expected, this loss has to be taken into consideration as the loss of brightness affects the imaging detection as the VGC detection requires a minimum power input.

2.2.6. Detection Method

This section will cover the specific optics used in the direct frequency comb detection method, and briefly describe the detector array used to acquire the 2D array of comb frequencies. Then, there will be a detailed description and discussion on how to align the detector optical layout.

2.2.6.1. VIPA Optic

Although there are a few different techniques of detecting frequency comb lasers as discussed in the introduction (section 1.4.2), this project focuses on spatially dispersing the comb frequencies into a 2D array and then imaging the result onto an IR camera. To create the 2D array, two specialised optics are used to spatially separate the light. In our apparatus, the light is first dispersed in the vertical direction and then in the horizontal direction. To spatially disperse the comb frequencies in the vertical direction an optic called a VIPA is used. In the simplest terms, the VIPA (Virtually Imaged Phased Array) produces a series of parallel output beams which constructively interfere at a set angle which is dependent on the wavelength of the incoming light. [225] In our apparatus, the output appears as a single vertical stripe. The acronym VIPA is derived from two properties of the etalon. “Phased array” is derived from the output parallel beams increasing in phase and displacement, and “virtually imaged” arises from the idea that each parallel beam is formed from a virtual image (see Figure 2-14). [225]

While not strictly an etalon optic (also known as a Fabry-Pérot interferometer), VIPAs can be thought of as titled etalons, made of solid material and with three different high reflective or anti-reflective coatings. As shown in Figure 2-14, the front has two distinctive coatings and the rear has one coating. The bottom front of the VIPA has an anti-reflective (AR) coating which is where the comb light couples into the optic, and the top front has a highly reflective (HR) coating (>99.0%) that directs the light back and forth through the optic. Finally, the rear of the optic has a partially reflective coating (PR) which transmits a small portion of the light from inside the optic cavity, while the remainder is directed back to the highly reflective front of the optic. The initial reflected light then further reflects off the highly reflective coating at a set angle (θ) back towards the partially reflective coating where another small portion of light is transmitted. This reflection and transmission process continues as the light propagates upwards on the inside of the VIPA cavity, and the single input beam is converted to a series of multiple parallel output beams of gradually decreasing intensity. [226] These multiple transmission beams then constructively interfere at an angle dependent on the wavelength. For the high resolution required in this project, more reflections through the VIPA are needed, which can be thought of as a many slit experiment. Therefore, the VIPA is held at small angles between 1° and 4° (with respect to the normal incidence). [227]

As an etalon, the width of the VIPA can be related to the Free Spectral Range (FSR) of the optic. The conversion between the width, L_{vipa}, and the FSR relies on the refractive index of the solid material, n_g, and the angle the VIPA is set at: [228]

$$FSR = \frac{c}{2n_g L_{VIPA} \cos\theta}$$ ***Equation 2-14***

As θ is typically very small for the VIPA (1° to 4°), the cos(θ) term can be approximated to one. With over 70,000 unique frequencies in the spectral bandwidth of the frequency comb laser, each frequency constructively interferes at a unique angle upon exiting the VIPA cavity. Furthermore, there is as an additional element of filtering the frequency comb, such that a certain number of comb “teeth” are contained within one VIPA FSR. For example, for a VIPA with an FSR of 10 GHz and a comb laser with a repetition rate of 200 MHz, there are 50 comb frequencies within one FSR of the VIPA optic. This results in a repeating pattern of 10 GHz over the entirety of the frequency comb bandwidth, where each of the 50 unique frequencies of the comb within 1 VIPA FSR are vertically spatially separated.

Within this thesis, the specific VIPA (Light Machinery) used in the detection for the vertical dispersion is an 8.1 x 25.4 x 76.2 mm CaF_2 solid etalon with three coatings: the HR coating (>99.2%), PR coating (between 94.9% and 96.1%, wavelength dependent), and the AR coating. As the VIPA is 8.1 mm wide and held at an angle close to 2°, this corresponds to a FSR of 12.9 GHz, and means 51 comb modes (sometimes referred to as teeth) are contained within one FSR. However, this repeating pattern of the frequencies are horizontally overlapped, meaning a second diffraction optic is necessary to further separate each VIPA FSR. This concept is better shown in section 2.2.6.3 and Figure 2-17.

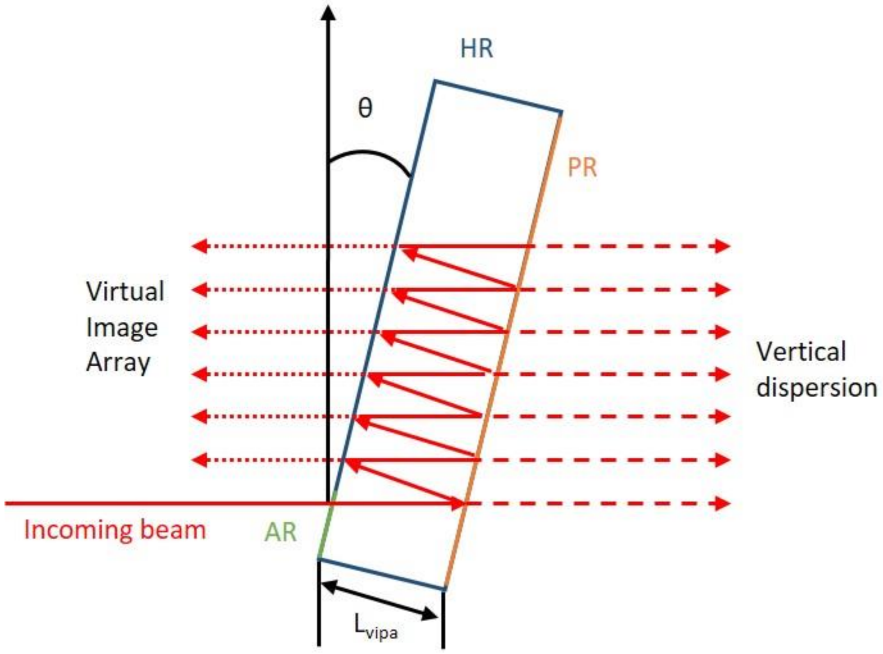

Figure 2-14 Virtually Imaged Phased Array Optic Schematic. Schematic of the VIPA (Virtually Imaged Phased Array). The VIPA has three coatings: HR, AR, and PR. The incoming beam enters the front of the VIPA through the AR section, the light then reflects off the back of the VIPA and is directed towards the HR coating at an angle, θ, which is set by tilting the VIPA. When the beam hits the VIPA on the back side, a portion of the light is transmitted through the optic. As the light propagates up the VIPA optic, the light is transmitted from the cavity as a series of parallel beams of decreasing intensity. Adapted from reference [227].

2.2.6.1. Diffraction Grating

The transmitted light directly from the VIPA would be imaged on the detection camera as a thin, vertical stripe of light. Therefore, a second optic is used to create the 2D array needed for extracting frequency information from the comb. For the horizontal separation of the comb frequencies, a blazed diffraction grating is used. Each blazed diffraction grating has three main characteristics: blaze wavelength, blaze angle, and groove spacing (α). As the laser beam diffracts off the blazed grating surface, the frequencies are horizontally separated at an m^{th} order reflection angle, θ_m, and is dependent on the wavelength: [222]

$$\alpha \ \sin(\theta_m) = m\lambda$$ ***Equation 2-15***

For the 2D array, the first order diffraction (m = 1) is used. Consider the comb light hitting one groove on the diffraction grating, this would separate out the frequencies into a continuous spectrum from shortest to longest wavelength. If two grooves are illuminated,

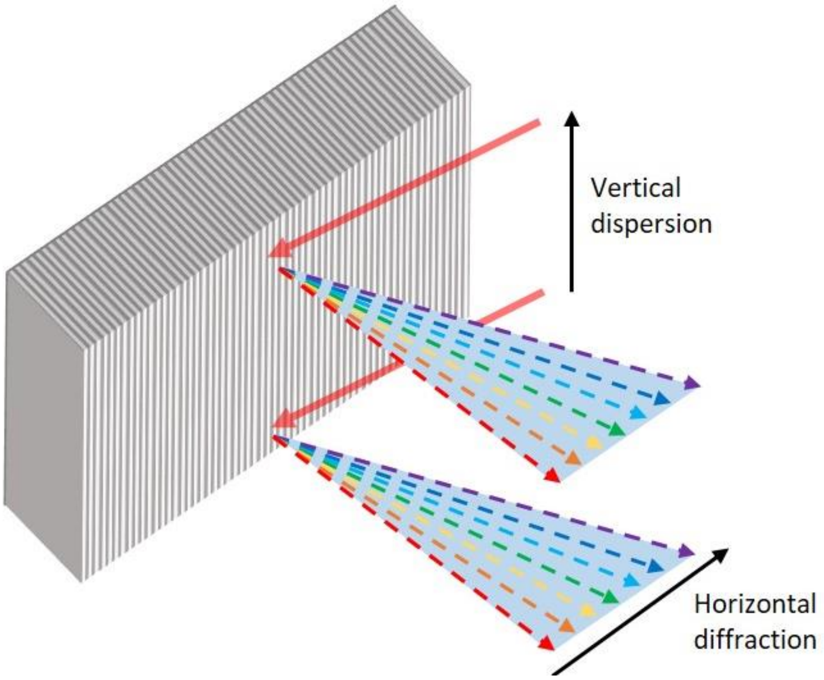

Figure 2-15 Diffraction Grating Schematic. The incoming vertical dispersion is horizontally diffracted by the diffraction grating as a function of incoming wavelength. Each groove on the grating disperses the light as a function of wavelength, and each individual dispersion constructively and destructively interferes to give a resolved light pattern.

the frequencies are separated on each groove. These frequencies are then able to constructively interfere to give a weak interference pattern. Therefore, the more grooves illuminated on the blazed diffraction grating, the more resolved the interference pattern. Expanding the laser beam before the diffraction grating and having a large (grazing) angle of incidence on the grating contributes to illuminating more grooves (further discussed in section 2.2.6.3).

Within this thesis, a 50 x 50 mm Al coated diffraction grating (Laser Components) is utilised for the horizontal diffraction. This grating is blazed with 450 grooves per mm, which is designed to give the maximum grating efficiency in the specific first order diffraction. [229]

2.2.6.2. Detection Camera

To detect the frequency comb array, a Stirling cooled InSb detector array is used, which is commercially available under the product name *ImageIR® 8320 MWIR* and manufactured by InfraTec GmbH, Germany. The detector is a Focal Plane Array camera (FPA), which is a 2D array of infrared detector pixels which capture the entire view of the camera. For each pixel, an electrical signal is generated which is directly proportional to the intensity of IR light impinging on that pixel within a certain period of time (integration time). Integration times of 1 to 20,000 µs is possible, but for flow cell measurements 50 µs is implemented and for the free-jet expansion measurements 150 to 200 µs is used.

The detector array (referred to as the camera) is capable of detecting wavelengths in the range 2000 to 5700 nm. Full images have a pixel array of 640 x 512 with a pitch size of 15 µm, meaning the true size of the pixel array is 9.6 x 7.68 mm. All of the camera functions are remotely controlled through the IRBIS® 3 program which is available on a laptop positioned close to the camera. In addition, the camera has the option of being externally triggered by a timing box, which means the time at which the data is acquired can be controlled in relation to other aspects of the experiment such as the free-jet expansion trigger time. Section 3.1.2 covers the concept of externally triggering the camera further. However, for the majority of experiments, the camera is internally triggered using a 125 Hz frame rate.

2.2.6.3. VIPA-Grating-Camera Detection Alignment

For optimal imaging conditions, the VGC set-up has to be aligned precisely and accurately. However, this alignment is difficult due to the numerous degrees of freedom from the optical alignment and the precise alignment nature of the diffraction grating and VIPA. Multiple challenges arise within the VGC set-up: the need to increase the size of the laser beam, the need to ensure light is precisely coupled into the front of the VIPA, and finally to ensure the largest proportion of the grating is illuminated. The entire optical set-up for the detection method is shown in Figure 2-16, and the alignment process is described below.

After the comb light has propagated through the appropriate sample via a Herriott multipass cavity, the comb is directed through the fibre coupling. A small focusing lens (aspherical +4 mm FL) is used directly after the fibre coupling output; this returns the beam to its original size and collimates the beam. For the main alignment, firstly the beam is expanded using two CaF_2 plano-convex lenses (L3 and L4). This beam expansion is done for two reasons help keep the beam collimated, and to illuminate a large area of the diffraction grating. After testing out various combinations of convex and concave lenses at differing focal lengths, the optimal pairing of lenses for beam expansion was determined to be a +100 mm FL plano-convex lens (L3) followed by a +500 mm FL plano-convex lens (L4). This optical set-up is commonly referred to as a Keplerian telescope, where the plano sides of the lenses are facing each other, the distance between the centre of the lenses is the sum of the focal

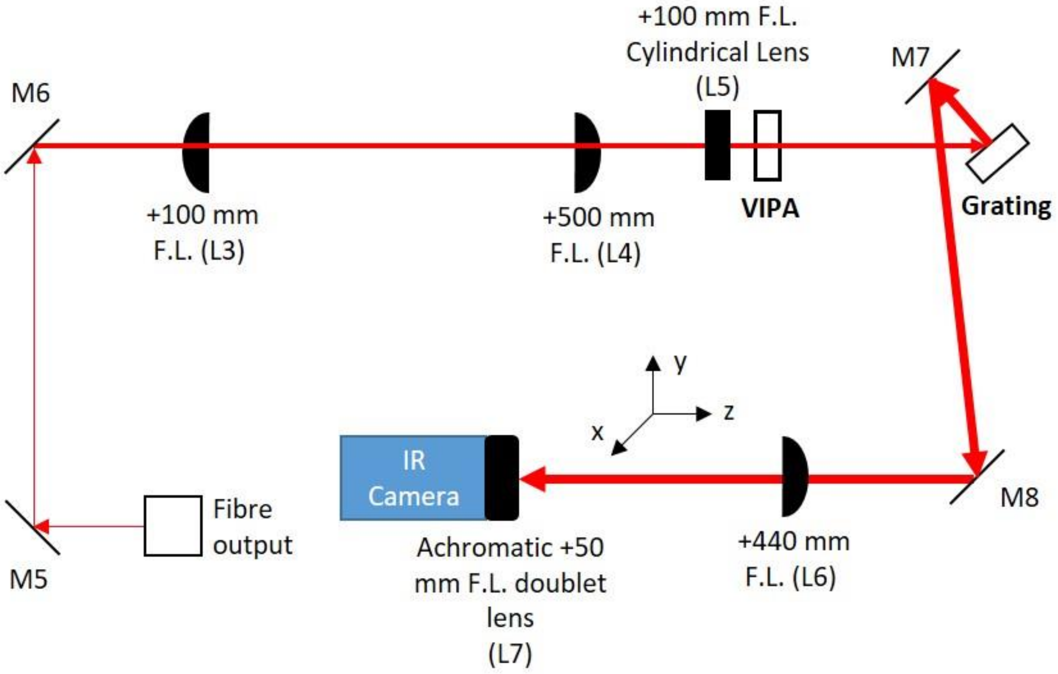

Figure 2-16 VGC Detection Layout Schematic. From the fibre coupling output, the beam is directed through beam expansion optics. This five times magnification utilises a +100 mm FL plano-convex lens (L3) and a +500 mm FL plano-convex lens (L4) which are placed 600 mm apart. The beam is then flattened to a thin line through the use of a +100 mm cylindrical lens (L5), which is positioned 100 mm away from the front side of the VIPA. Vertical dispersion and horizontal diffraction are caused by the VIPA optic and diffraction grating. Finally, the beam is directed via two mirrors (M7 and M8) through two imaging optics: +440 mm focusing lens (L6) and a +50 mm FL achromatic doublet lens (L7). These optics allow for the 2D array to be imaged on the IR camera and fill the full imaging pixel array.

lengths (in this case 600 mm), resulting in a five times (5x) beam magnification.

Next, the beam is directed through a +100 mm FL cylindrical lens (L5) which focuses the beam into a thin line with the same width of the expanded Gaussian beam. The lens is placed approximately 100 mm away from the front (input) side of the VIPA. The distance of this lens with respect to the VIPA is determined by the maximum output power from the VIPA, which is an indicator of optimal coupling into and out of the VIPA. As the beam inside the VIPA reflects back onto the high-reflective coating at a very shallow angle, the incoming beam line has to be placed as close to the intersection of the two coatings as possible, but not to clip the beam on the HR coating. The VIPA is vertically translated to achieve this, where the optimised power out of the VIPA (as recorded with a power meter) is roughly 2 mW (incoming power is close to 3 mW).

As the output of the VIPA is a series of lines, the size of the beam can be considered as a square with the same width as the incoming beam and a height determined by the number of reflections achieved in the VIPA. This square beam then reflects off the diffraction grating, at its first diffraction order angle (approximately 70°). As previously mentioned in section 2.2.6.1, the more grooves illuminated on the diffraction grating, the better the resolution of the horizontal diffraction pattern. The previous beam expansion means the beam covers a large area of the diffraction grating. Therefore, many grooves are illuminated on the grating, which achieves a good contrast ratio on the imaging camera.

Before the final lenses into the IR camera, two square mirrors are implemented to direct the comb. While the use of these two mirrors might seem odd, their positioning means less physical space on the optical table is needed to image the comb onto the camera. In addition, these two mirrors are used to change which frequencies are imaged onto the camera in any one "window" (further explained in section 3.1) without changing the diffraction grating angle and thus does not change the number of grooves illuminated and also does drastically change the imaging resolution.

Finally, two lenses are needed for the imaging of the 2D array of comb teeth onto the camera, as one focusing lens does not allow for the full coverage of the camera. However, this alignment is counter-intuitive, as the final lens (L7) is aligned before the penultimate lens (L6), therefore the description of the lenses and the alignment process will be written in chronological order. Firstly, a 1" achromatic lens with a short focal length of +50 mm (L7, Edmund Optics), is placed directly before the camera input to ensure the laser light fills the entire imaging detector. The short focal length is needed as there is a small aperture between the camera input and the focal plane array (FPA). Although not including the achromatic lens in the full imaging alignment would still give useable images for analysis, the beam would not fill the full detector array and only a small circular 2D array would be acquired. This means more images would need to be collected in order to create a full spectrum (more information on this can be found in section 3.1). In addition, a short focal length achromatic lens has the added advantage does not contribute any beam astigmatism or spherical aberrations, which would result in slightly different focal lengths for different wavelengths. [222] For the following alignment description, the *y*-direction corresponds to the height of the lens, the *x*-direction is parallel to the camera face, and the *z*-direction is perpendicular to the camera face along the beam propagation axis. When the lens is the furthest from the camera (approximately 50 mm away along the *x*-direction), the entire mount is moved in the *z*- and *y*-directions to centre the beam on the camera. When the lens is the closest to the camera (approximately 10 mm away), fine adjustments are made to move the lens along the *z*- and *y*-directions to centre a small black reflection seen on the image. These two processes are repeated until the beam is fully centred on the camera, at which point the lens translated along the *x*-direction to a position such that the circular beam just fills the full detector array of the camera.

For focusing the beam onto the camera array, a 2” +440 mm FL uncoated CaF_2 plano-convex lens (L6) is used (*Crystran)*. This lens is complicated to align for optimal imaging conditions, and so the lens must be translated in the *x*-, *y*- and *z*- directions along with changing the tilt of the lens: As the with previous lens: the *y*-direction corresponds to the height of the optic, the *x*-direction is parallel to the camera face, and the *z*-direction is perpendicular to the camera face along the beam propagation axis. When changing the frequencies imaged on the camera, this requires changes to the left-right direction of the two mirrors (M7 and M8), however in response to this change, the *z*-direction and occasionally the tilt of the +440 mm FL plano-convex lens needs to be altered to restore the resolution of the image.

The evolution of the alignment process can be easier to understand through the use of actual images taken from the infrared camera, as seen in Figure 2-17. Within this image, the colours are representative of the intensity of light on the camera, where the pink is highest intensity of light and the black is lowest intensity of light. Image A, shows the beam being imaged as the direct output from the VIPA. This is a single vertical stripe where the comb modes have been separated out by the vertical diffraction. However the comb modes are horizontally superimposed on top of each other and so no spectral information can currently be obtained. Image B, also shows the direct output from the VIPA, however, both of the imaging lenses are now in place, so the single stripe can be seen more clearly. For both of these images the diffraction grating is in place, however the alignment is at the zero-order position, and so the diffraction grating optic is acting as a simple mirror. Image C has the VIPA and grating, now at the first order diffraction angle with respect to the incident beam, aligned onto the camera and no imaging lenses in place. The circle within the image shows how the beam is ‘clipping’ on the aperture of the camera. Image D is after the +440 mm FL lens has been aligned. The vertical dispersion and horizontal diffraction are now visible, however, once again, due to the aperture of the camera the beam is not filling the full detector array. Image E shows the VIPA and grating (first order) aligned, with only the +50 mm FL achromatic lens in place, this is shown in the ‘far’ position. The beam is centred in this alignment, as the 4 dark corners (where the beam is starting to ‘clip’ the lens) are evenly distributed. Image F, is the same as image E but this time the +50 mm FL achromatic lens is in the ‘near’ position and the back reflection, which is used for alignment at this position, is labelled.

Image G shows a complete image after the full alignment procedure has taken place. The beam is filling the full detector array and there is minimal ‘clipping’ of the laser beam. This image contains a 40 cm^{-1} wide window of spectral information with over 5,000 individual comb modes. The final image H, shows a zoomed in portion of the full image (as indicated on image G), where the individual comb modes can be seen clearly. To reiterate, the vertical dispersion is caused by the VIPA optic and the horizontal diffraction is caused by the diffraction grating. This means that the wavenumber difference between adjacent vertical teeth is 0.008 cm^{-1} and the difference between horizontal comb teeth is 0.408 cm^{-1}.

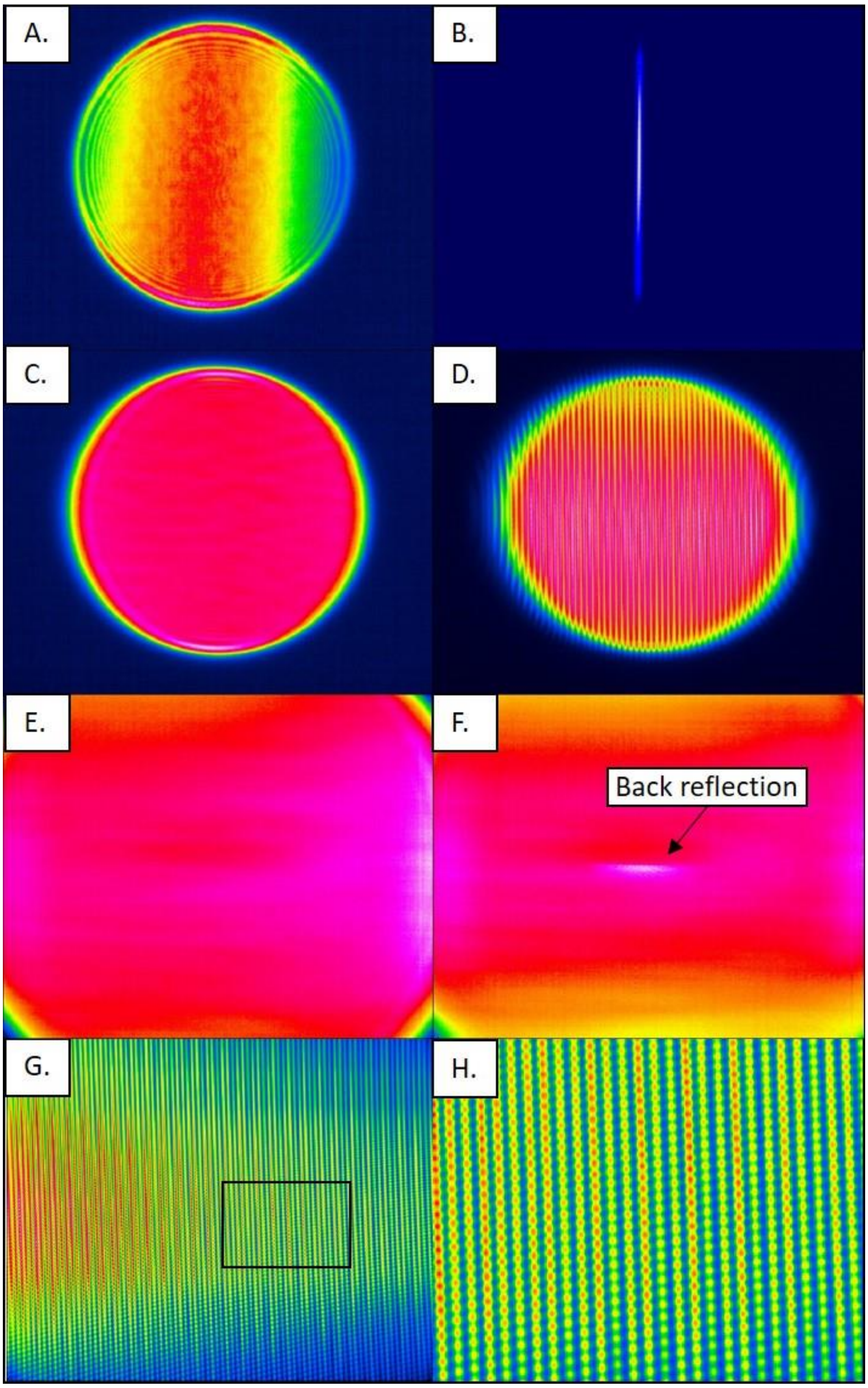

Figure 2-17 Camera Alignment Images. A. VIPA imaged onto camera with no lenses in place. B. VIPA imaged onto camera, with both lenses in place. C. VIPA and grating (first order) imaged onto the camera, no imaging lenses are in place. D. VIPA and grating (first order) are imaged onto the camera with only the +440 mm FL lens in place. E. VIPA and grating (first order), with only the +50 mm FL achromatic lens aligned (far position). F. VIPA and grating (first order), with only the +50 mm FL achromatic lens aligned (near position), with the back reflection labelled G. All four of the alignment optics are in place and aligned, this is the full camera image. H. Zoomed in portion of image G, the individual comb modes are visible as the small dots. The vertical difference between comb modes is 0.008 cm^{-1}, and the horizontal difference between comb modes is 0.408 cm^{-1}.

3. Commissioning and Characterising of a Frequency Comb Spectrometer

This chapter will discuss how the mid-IR images are recorded, processed from images into spectra, and how the final spectrum for each molecule is analysed to give information such as rotational constants and vibrational frequencies. The acquisition of data is achieved through the camera interface software (IRBIS® 3 program). Data processing is currently achieved through a combination of a home-written *MATLAB* script which automates the selection of the comb teeth, and the graphing software *Origin*, which requires manual input in order to wavenumber calibrate the acquired spectra. Finally, the spectra are analysed in the purpose designed program *PGOPHER,* [230] which is used for fitting rotational, vibrational, and electronic spectra. For the purposes of deeper understanding and illustration, this section uses various spectra recorded from a sample of methane, CH_4, in either the room temperature gas cell held at a constant pressure or as a pulsed sample in the free-jet expansion chamber. Furthermore, all wavenumber values within this chapter and the rest of the thesis are given in air measurements. Where necessary, for example comparing the HITRAN reference spectrum to the experimental spectrum for CH_4,

The rest of this chapter, from section 3.4 onwards, will then be dedicated to discussing the instrument line-shape function of the detection method, noise issues encountered during the initial stages of commissioning, and initialising the free-jet expansion apparatus.

3.1. Acquisition

3.1.1. Changing Imaging Frequencies

In order to acquire vibrational spectra of the molecules within the gaseous sample, images from the infrared camera are collected. However, collecting just one image is not sufficient. For a “full spectrum”, as in, a spectrum within the range of the laser mid-IR bandwidth, multiple images are taken across a range of different frequencies and at different repetition rates. Furthermore, as the core technique of this project is absorption spectroscopy, both background, I_0, and signal images, I, need to be taken to in order to calculate the absorbance using the Beer-Lambert law (see section 1.2.3 for further details).

First, focussing on the two types of images: background and signal. Figure 3-1 shows two averaged images where image A is the background image and image B is the signal image. (2000 images for each average, taken at a camera integration time of 50 µs, 125 Hz frame rate, for a total experiment time of 16 seconds for one averaged image). Recall that the horizontal diffraction of the VIPA FSR fringes are caused by the diffraction grating, and the vertical dispersion of the comb teeth is a result of the frequency comb being dispersed by the VIPA etalon. Fringes are defined as a vertical stripe of comb teeth which are separated from adjacent vertical stripes by an area of low intensity (dark blue). For the signal images, the darker spots within VIPA fringes are where absorption of specific frequencies by the sample molecule has attenuated the light. In this example, the absorptions are caused by the CH_4 ν_3 ($v = 1 \leftarrow 0$) vibrational transition. In addition, the absorption pattern seen here helps to determine where the start and end of one VIPA FSR (51 comb teeth) is located, which is required for converting the image into a spectrum. The orange circles within Figure 3-1 image B show the exact same frequency just separated vertically by 51 comb modes and on the adjacent vertical stripe.

However, this pair of images only contains 40 cm^{-1} of spectral information; whereas the frequency comb laser has a much larger range than this. Therefore, as previously mentioned in section 2.2.6.1, the diffraction grating angle can be changed with respect to the imaging camera in order to change which frequencies are being imaged. As each image contains up to 40 cm^{-1} of spectral information, different grating positions are needed to capture the full frequency range of the comb. To simplify the context, each different grating position is referred to as a “window”, hence multiple windows are needed to create a full spectrum.

For some of the sample molecules, changing the repetition rate is necessary in order to capture all the information for different rotational and vibrational transitions. The peaks observed in a spectrum are the molecular absorptions broadened by a FWHM of, for example, approximately 0.02 cm^{-1}, which is a combination of Doppler broadening, pressure broadening, and the instrument line-shape function contributions. With the spacing between adjacent frequency comb teeth of 0.0082 cm^{-1}, for a repetition rate of 250.000 MHz, using a single repetition rate may not be sufficient to accurately capture the shape or features of the peaks within the spectrum. This means that it can be necessary to change the repetition rate of the frequency comb in order to collect a sufficient number of data points over a peak.

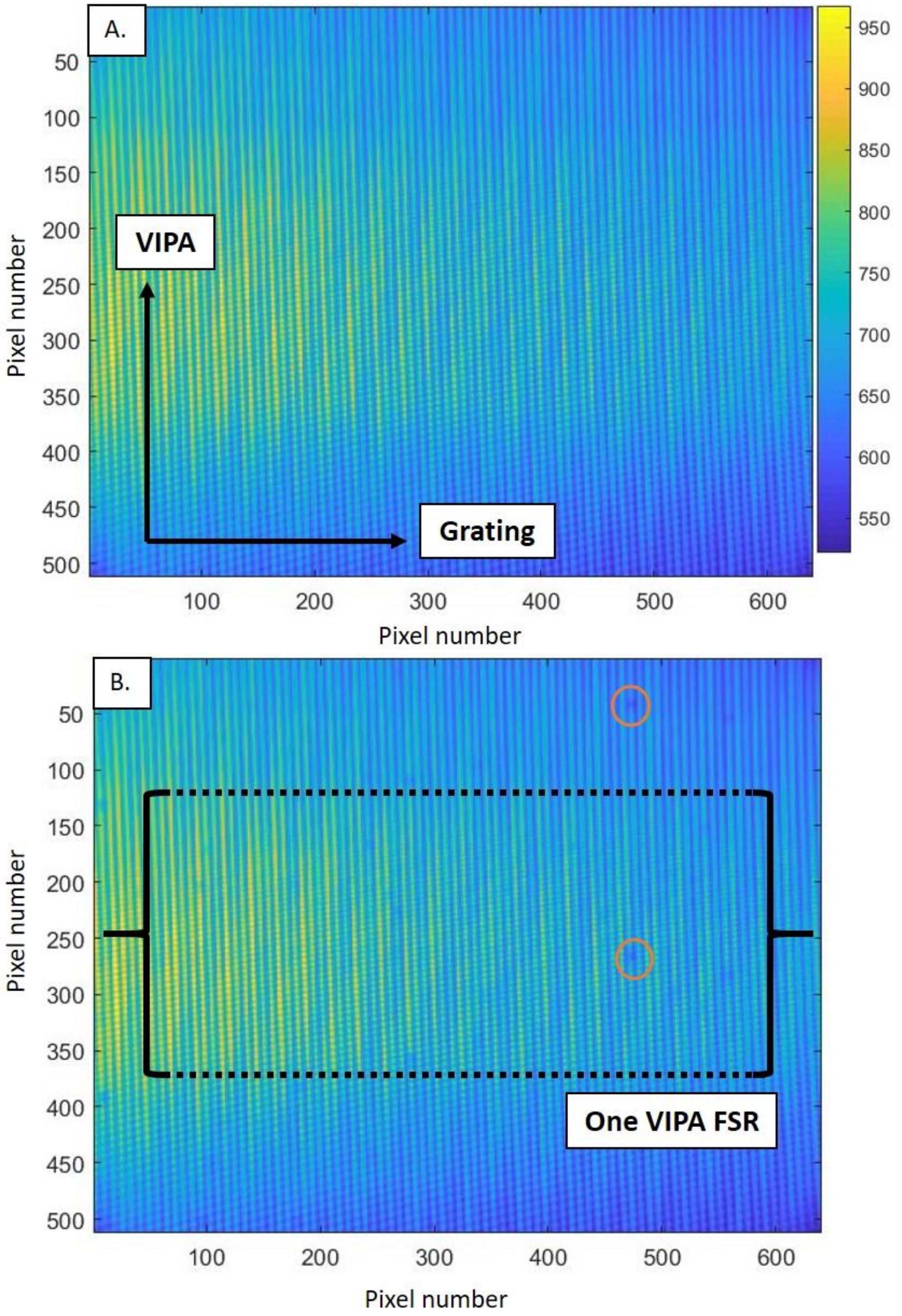

Figure 3-1 Acquired Images. A. Background image (50 μs, 2000 images averaged). The diffraction grating causes the horizontal dispersion, and the VIPA optics causes the vertical dispersion of the comb modes, as shown by the arrows. B. Signal image (50 μs, 2000 images averaged), with an approximate methane concentration of 1.44 × 10^{15} molecule cm^{-3}. The visible absorption pattern helps to identify where one VIPA FSR starts and finishes. The orange circle shows the same absorption peak, separated by 51 comb modes and on an adjacent vertical stripe. The colour map is shown on the left: Yellow is the highest intensity, green is mid-intensity, and dark blue is the lowest intensity.

While changing the repetition rate of the laser does not drastically change difference in the frequency between adjacent data points (comb teeth), for a given repetition rate, the absolute frequency of the comb teeth being observed does change. Recall from section 2.2.1, the repetition rate is set is set by the equation: (245 + DDS/4) MHz, where the frequency of the DDS is tuneable. The absolute frequency of the comb teeth, though, is given by $f_n = nf_{rep}$. Typically, the rate on the DDS is changed by 400 Hz which changes the laser repetition rate by 100 Hz. Changing the repetition rate from 250.0000 MHz to 250.0001 MHz changes the data point spacing (frequency difference between adjacent comb modes) by approximately 3×10^{-9} cm^{-1}. However, with typical n values of 350,000 to 370,000, the absolute frequency for n = 360,000 for these two repetition rates are 3002.00133 cm^{-1} and 3002.00614 cm^{-1}, respectively. By using multiple repetition rates, it allows for the acquisition of different frequencies and a finer grid of data points over the recorded spectrum. For example, instead of recording data points every 0.008 cm^{-1} for a single repetition rate, recording ten different repetition rates and interleaving the data gives a frequency difference between data points of 0.0017 cm^{-1}. Current conditions allow for the repetition rate to be scanned from 249.9995 to 250.0005 MHz.

While changing the window position and changing the repetition rate can be applied to both room temperature and cold temperature experiments, the data acquisition process for each experiment is different. In both instances, the IRBIS® 3 program controls the camera settings for data acquisition.

3.1.2. IRBIS Software Control

For the room temperature data, the signal and background images are taken as separate data sets, all set parameters are identical the only difference being whether there is sample in the gas cell or not. For each data set, typically 2000 images are collected, with a camera integration time of 50 μs, and a camera frame rate of 125 Hz, which is internally triggered. Each data set of 2000 images is then averaged together to form one image which can then be processed (see the next section for further information on averaging). However, for free-jet expansion data, more images are collected (typically 20,000 per data set), the camera integration time is longer at 200 μs, and the frame rate is set as externally to either 20 or 100 Hz. This external frame rate is controlled using a Berkley Nucleonics Corporation (BNC) digital delay generator, which also controls the jet-free expansion pulsed valve. The digital delay generator box is set up in such a way that the pulsed valve allows sample into the chamber every 10 Hz while the camera is recording an image every 20 or 100 Hz.

Therefore, for the 20 Hz frame rate, every other image is signal or background. This means the data set can then be processed using an active background subtraction method. This is further explained in section 3.6, along with the method employing the 100 Hz frame rate.

The way the camera saves images, such as file names and extensions, along with how many frames are recorded per data set is also set through the IRBIS® program. For each data set, the pressure inside the respective sample apparatus, the repetition rate, and the file names are all manually recorded.

3.2. Processing

This section discusses how the collected images for each data set are transformed into a vibrational spectrum. This is done in three steps: convert the camera digital values to intensity values, use a *MATLAB* script to convert the images into a spectrum, and then further processing in *Origin* to determine the frequency *x*-axis. Within this processing section, the images and graphs are from a single data set of signal (CH_4 concentration of 1.44×10^{15} molecule cm^{-3} in a bath gas of N_2 with a total pressure of 9.1 mbar) and background images, so any given information stands true throughout.

3.2.1. Dark Counts on Camera

As the detection camera is fundamentally a thermal imaging camera, the images obtained from the camera technically reports temperature in the form of digital values. However, these thermal digital values are nonsensical when it comes to understanding the intensity of the light, which is needed for the Beer-Lambert Law. Therefore, the digital values undergo conversion to light intensity.

In order to figure out the conversion from digital values to intensity, the noise of the camera must be understood. For any CCD (charged-coupled device), of which the thermal imaging camera is, there are multiple sources of noise arising from the temporal and spatial variation in the measured signal. [231, 232] First, the photon flux and the background flux noise (σ_S) arises from the variation in the arrival time of the photons on the camera. As it is the photons arriving at the camera that determines the signal response, the photon noise is equivalent to the square root of the signal level (as determined by Poisson statistics). However, the photon noise is independent of the camera temperature, but does have a wavelength dependence. Secondly, there is a fixed pattern noise (σ_F) which is caused by spatial differences of the camera pixels. This fixed pattern noise is independent of the signal level and camera temperature, and thus will be ignored in calculating the total noise of the camera. Thirdly, there is a read level noise (σ_R), which is the noise produced when the electronic signal is made. This noise is individual for each camera and is independent of the signal level and the camera temperature. Finally, there is dark noise (σ_D), which is based on a dark current. This dark current is essentially a count of the electrons spontaneously generated within the sensor that occurs even when there are no photons striking the detector. This noise is independent of signal level, and is the only noise contribution dependent on temperature of the sensor. Furthermore, the dark count noise will change as a function of integration time of the camera.

All of the three types of noise (ignoring the contribution of σ_F), can be combined to obtain the total effective noise:

$$\sigma_{Eff} = \sqrt{\sigma_D^2 + \sigma_R^2 + \sigma_S^2} \qquad \textbf{\textit{Equation 3-1}}$$

As the read out noise and photon flux noise does not change as a function of camera temperature or camera integration time, only the dark noise needs to be calculated. As the dark noise is based on the number of spontaneously generated electrons, the current (I_D) can be measured by summing the electrons. As this summing process observes the Poisson statistics, the dark noise is proportional to the square root of the number of electrons during exposure time, *t*:

$$\sigma_D = \sqrt{I_D t} \qquad \textbf{\textit{Equation 3-2}}$$

Thus, increasing the exposure time of the camera, or the integration time, will increase the dark noise. However, for a thermal camera, it is almost impossible to manually count the number of electrons spontaneously generated, therefore a different method is found to calculate the dark current. Using the SNR, the dark current value (*D*) can be calculated:

$$\mathrm{SNR} = \frac{PQ_e t}{\sqrt{(P-B)Q_e t + Dt + N_r^2}} \qquad \textbf{\textit{Equation 3-3}}$$

where Q_e is the quantum efficiency, *P* is the incident photon flux, *B* is the background photon flux, and N_r is the read out noise. Equation 3-3 can be interpreted as the total signal generated during the integration time divided by the total noise during the integration time. Furthermore, the bottom of the division is equal to the intensity (*I*) measured on the detector camera:

$$\mathrm{I} = (P - B)Q_e t + Dt + N_r^2 \qquad \textbf{\textit{Equation 3-4}}$$

In addition, the intensity needed for the Beer-Lambert law can be equated to the ratio between P_s/P_0, where P_0 is the background photon flux and P_S is the photon flux when a sample is present, and should remain constant for all integration times. Therefore, in order to keep the ratio of P_S/P_0 at a constant value for each integration time, an offset value must be subtracted from the intensity to account for the noise.

In order to calculate this offset value, CH_4 and background images are acquired from the camera using the processes described in section 3.1. These images are identical for the concentration of CH_4, and the number of images per average, but differ in their camera integration time. The acquisition of these images is referred to as “time series data”, due to their dependence on the integration time. For a typical time series data set, integration times of 50 µs, 10 µs, and 5 µs are used. The images are then analysed using the *MATLAB* script (as described in the next section). However, instead of obtaining a final spectrum, the array containing the intensity as a function of pixel number for each image is selected.

For each array, the corresponding signal and background array for each integration time are “paired together”, and a minimum of three pixel locations are found for where there is a CH_4 absorption. The corresponding six intensity values (3 for signal, 3 for background at each integration time) for each pixel location are then used to evaluate P_S/P_0 for each integration time using Equation 3-4, where the signal pixel intensity is used as P, the background pixel intensity is used as B, and initial values for QB, D, and N are used. If three pixel locations are used, there is a total of nine P_S/P_0 are calculated, and these nine ratios are then converted to transmission. The *Solver* program within *EXCEL* can then be used. This solver requires Equation 3-4 to be defined, and the program finds a combination of QB, D, and N which ensures that the sum of all nine P_S/P_0 values reaches a minimum value. The outcome of this solution gives the offset value for the pixel intensities. For ($QB + D$) this value is zero, and for N this value is approximately 18315 ± 3 (this value can fluctuate, but is regularly checked).

3.2.2. MATLAB

In order to analyse the recorded images, a *MATLAB* script was developed. Although the images from the two apparatus are analysed in a slightly different method, the fundamental workings of the code is still the same. Therefore, the general code for the room temperature images will be discussed first, then the relevant changes needed for the free-jet expansion images will be discussed. The core goal of the *MATLAB* code is to obtain a value for each comb tooth intensity for each acquired image. This is done by summing the intensity of the pixels which corresponds to one comb tooth. Currently one comb tooth corresponds to 5 pixels in width and between 3 and 5 pixels in height (the height of the comb tooth increases towards the bottom of the image).

The initial *MATLAB* script works in four main stages: 1. Find the minimum intensities between the vertical fringes to sum the intensities horizontally; 2. Find the minimum intensities between the separate comb teeth to sum the intensities vertically; 3. Total summed intensity comb teeth are then collected by counting 51 comb teeth down a vertical stripe before moving one vertical fringe to the right and reading another 51 comb teeth down; and 4. Transform the data to an absorption spectrum for one specific image data set as a function of pixel number. Currently, the *MATLAB* code is ill-equipped to automatically convert from array number to wavenumber, so this process is done manually using *Origin* (discussed in the next section). Unfortunately the code is too long to reproduce here, (at over 300 lines of code) however, the basic procedure is detailed below.

After the signal and background images have been imported into *MATLAB*, the offset value determined during the time series data sets is subtracted (see section 3.2.1). Then, the signal image is cropped to incorporate slightly more than one FSR of the VIPA (see Figure 3-1 for an example of a VIPA FSR). This cropped section defines where the image analysis is undertaken, and therefore must include a minimum of 51 comb modes in the vertical direction to ensure a continuous spectrum is processed and analysed. The same crop parameters are then used to crop the background image to ensure the specific comb modes match between the two images. In addition, the specified cropped section is kept constant for the analysis of a specific window, as the wavenumber range and the mode number, *n*, needs to remain consistent for the multiple data sets and multiple repetition rates within that specific window.

After both the signal and background images have been cropped, the *MATLAB* script finds the local minima between the vertical fringes to create an array detailing these locations. Figure 3-2 shows an overlay of the background image with the positions of the lowest intensity pixels. Due to the slightly diagonal nature of the vertical fringes, incomplete fringes are possible on the left- and right-hand sides of the cropped images. However, the

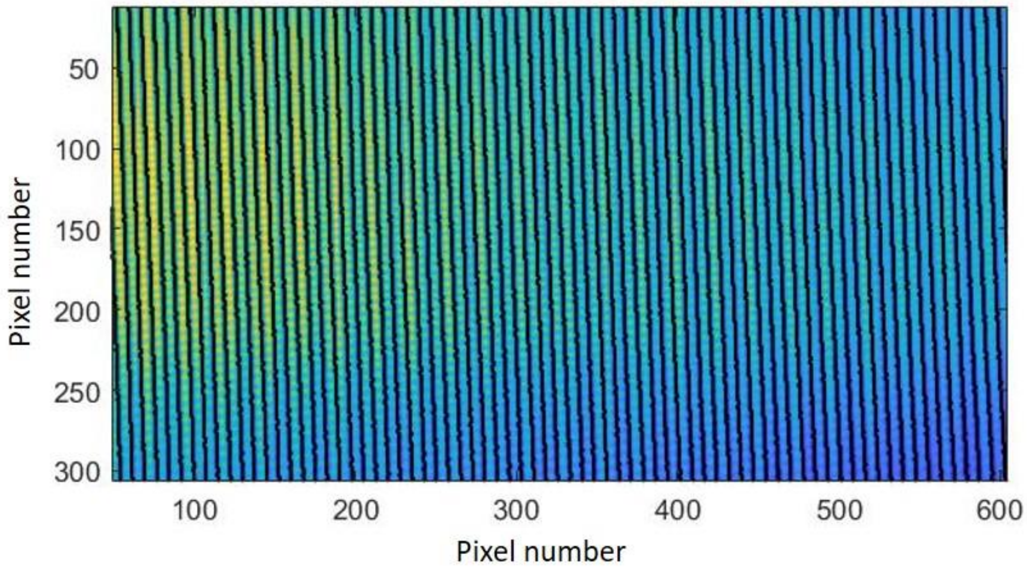

Figure 3-2 Local Minima Between Fringes. The cropped background image with an overlay showing where the local minima between vertical fringes are located (black dots appearing like lines). Both the *x*- and *y*-axes are given as array number.

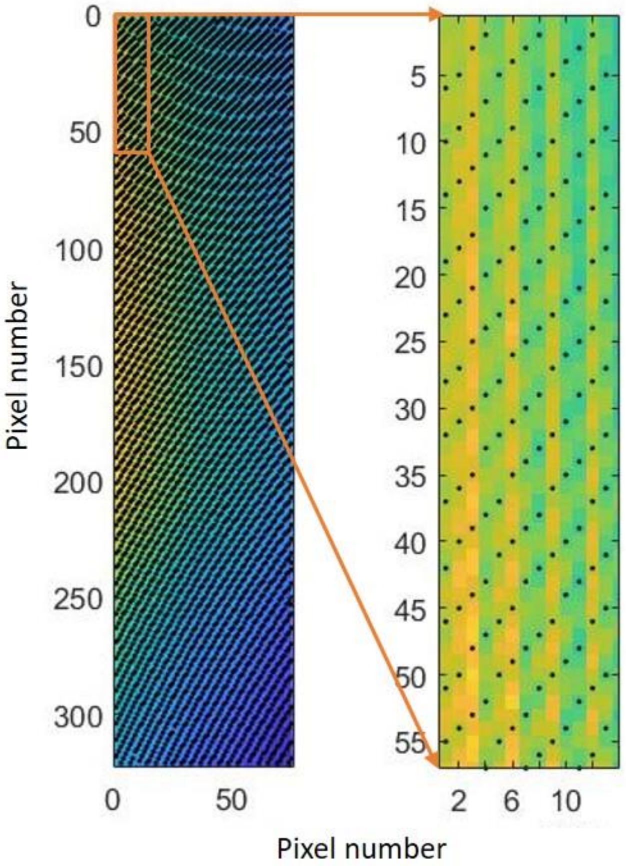

Figure 3-3 Local Minima Between Comb Modes. Background image, after the comb modes have been averaged horizontally, with an overlay of the local minimum locations between vertical comb modes (black dots). The zoomed in region of interest better shows the location of these dots and the uniformity of them.

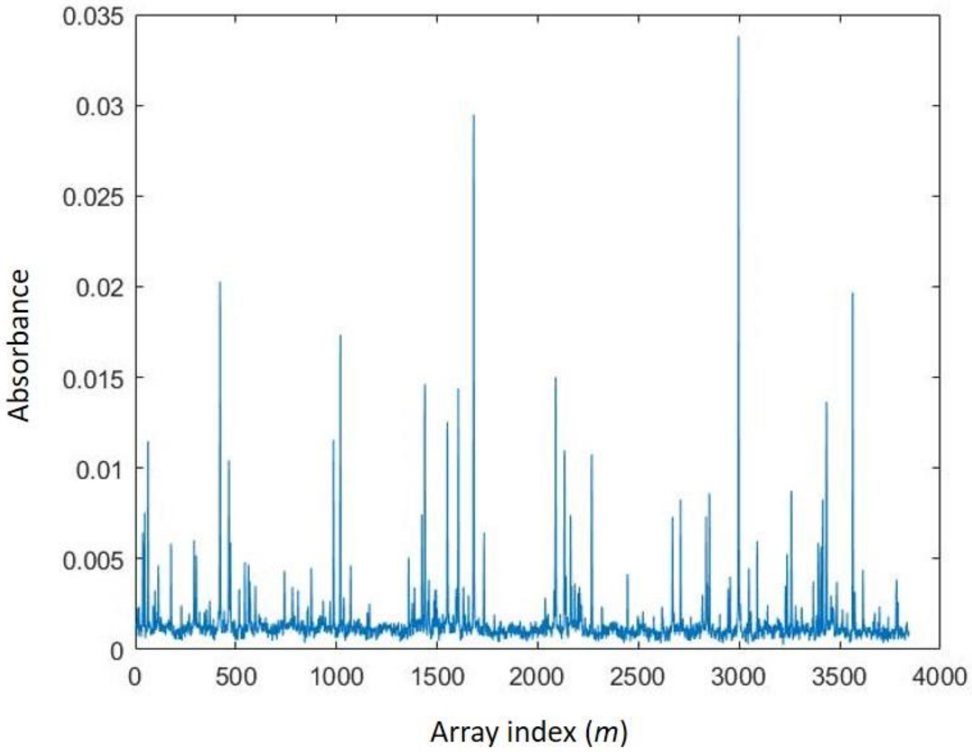

Figure 3-4 MATLAB Spectrum. One window worth of spectral data containing the ν_3 v = 1 ← 0 transition of CH_4. The *x*-axis is in wavenumber order within the array, but the *y*-axis is now in absorption as $\log_{10}(I/I_0)$.

script is written in such a way that these fringes are ignored when the intensities are summed horizontally across the vertical fringes on each line. For this example, 78 fringes are acquired from the cropped image, however, as there are two incomplete fringes on the left and the right, only 74 fringes are used in the rest of the script. The pixel intensities are summed horizontally across each fringe, and corrected for the number of pixels in each fringe.

The next step is to use the local minima function again, but this time to find the minimum intensity points between the comb modes along the same fringe. Figure 3-3 shows the location of these minimum points on top of the horizontally summed signal image. In some cases, manual adjustment of the locations of the minima is necessary to ensure all frequency data points are collected. Then, similar to above, the intensities between the local minima are summed down the fringes. The combination of the horizontal and vertical summation gives an intensity which is the summed area of each comb tooth. These summed values are then placed into an array where each intensity corresponds to a different wavenumber. As the full script is applied to both the signal and background images, the two are divided in accordance with the Beer-Lambert law, giving a $log_{10}(I/I_0)$ relationship (see section 1.2.3). The final absorption spectrum is then plotted as a function of array number, which allows for visual confirmation of the expected vibrational absorbance pattern for the sample molecule (Figure 3-4). For the spectra shown in later chapters, the *y*-axis has been converted to $log_e(I/I_0)$ instead.

Currently there are some drawbacks to using the summing method to obtain the intensity of the individual comb teeth. Most notably, the inclusion of “ghost” peaks in the final spectrum. These “ghost” peaks arise from problems with the resolution of the images where the intensity of a comb tooth bleeds into adjacent vertical stripes. This intensity bleeding then manifests itself in the spectrum as small satellite peaks which appear to the left and right of the real peak. These satellite peaks appear at exactly 51 mode numbers away from the main peak and can vary in intensity (asymmetric about the main peak), or multiple ghost peaks can appear for one main peak, for example two additional peaks on either side of the main peak. An example of these ghost peaks can be seen in Figure 3-14 in section 3.6.1, where each of the absorption peaks at 3038 cm^{-1}, 3047 cm^{-1}, and 3056 cm^{-1} present smaller peaks on either side of the “main” peak. While this intensity bleeding does not affect the intensity of the main peak, the “ghost” peaks can artificially increase the integrated σ_ν calculated from the spectrum. Or more seriously, if the “ghost” peaks are close to another main peak, i.e. in a congested spectrum, then the intensity can impact the intensity of the main peak.

In order to move away from observing “ghost” peaks in the acquired spectra, the processing code must be altered. Instead of summing the pixels to obtain the intensity of the comb tooth, the same pixel area can instead be treated as 2D Gaussians functions and integrated to give the overall intensity. This alternative method removes the ghost peaks, but at great computational expense. It also narrows the observed peak FWHM, due to narrowing the instrument line-shape function induced by incompletely resolving adjacent comb modes in the vertical (VIPA) direction.

Initially, the analysis for the free-jet expansion data can be achieved in two ways depending on how the data are collected. Data acquired using the 20 Hz method (explained in section 3.6) use the same version of the code for the room temperature data.

However, data taken using the 100 Hz method, instead uses a variation of the code. Instead of running a few averaged images through the code, all acquired images are run as a sequence through the code and populated into an array as a time series of intensity vs array number data sets. The final step of using the Beer-Lambert law is not used in this method. This is due to the acquisition method, where it is unknown which images coincide with the firing of the jet-free expansion at 10 Hz (the sample) and which contain the background (see section 3.6). To extract the infrared spectrum, a Fourier transform is performed on the time sequenced data for each individual comb tooth. In other words, the Fourier transform of time series for each comb tooth intensity yields an array of intensity as a function of frequency for each comb tooth. The intensity of the 10 Hz frequency component is extracted from the Fourier transformed time series for each comb tooth, yielding the infrared spectrum of the sample from the 10 Hz free-jet expansion. However the *y*-axis is now in arbitrary units. (Section 3.6.1 describes the outcomes of this method further)

3.2.3. Origin

As previously mentioned, in order to convert the *x*-axis from array number to wavenumber the graphical program *Origin* is used. The absorbance data from *MATLAB* is exported into *Origin*, and the array number, m, is converted to wavenumber, ν:

$$\nu \ = \frac{(-m + n_0)(\frac{f_{DDS}}{4} + f_{245})}{c} \qquad \textbf{\textit{Equation 3-5}}$$

where n_0 is the initial comb mode number, and $m + n_0$ gives the n mode number for a specific comb tooth, f_{DDS} is the repetition rate set by the DDS electronic (ranges from 19.9976 to 20.0020 MHz), f_{245} is the standard 245 MHz, and c is the speed of light. In order to match each window and repetition rate to the correct mode number, the different repetition rates used to collect the spectrum of calibration gas CH_4 are plotted as a scatter plot overlaid on *HITRAN* reference data (Figure 3-5). [216] The initial mode number is then manually chosen to ensure all absorption peaks within the window match the reference data. The initial mode numbers for one repetition rate should stay consistent across the different repetition rates, however the value may change by ± 1 due to the comb modes moving position within the cropped region.

As the calibration CH_4 spectrum is referenced against another experimental spectrum, the accuracy of both frequency axes must be discussed. In general, the accuracy of the frequency axis in the *HITRAN* CH_4 reference spectrum is much smaller than the repetition rate of the frequency comb laser. Thus, assuming the repetition rate of the comb is well determined since it is referenced to a Rb frequency standard, the starting mode number, and therefore the remaining ascending integer mode numbers in the image, can be determined without any uncertainty. An upper limit on the uncertainty of the experimental frequency axis can be determined by a worst case scenario of 0.005 ppm error in the Rb frequency standard, which is based on a 20-year aging. This would result in an uncertainty on the order of 450 kHz in the mid-infrared wavelength range.

Once the data has been wavenumber calibrated, the different repetition rates undergo baseline subtraction, which is sometimes necessary due to the laser intensity of the spectrum drifting over the course of an experiment. This intensity drift can manifest itself as an uneven baseline. In addition, sometimes noise filtering is needed, although this is explained further in section 4.2.1. Then, the full data set for each window is then interleaved for the different repetition rates, as seen in Figure 3-6. Finally, once all the different windows have been analysed in the exact same way, the windows are concatenated together and where parts of the spectra overlap in adjacent windows, the absorption data points are averaged together to give one data point for that particular frequency.

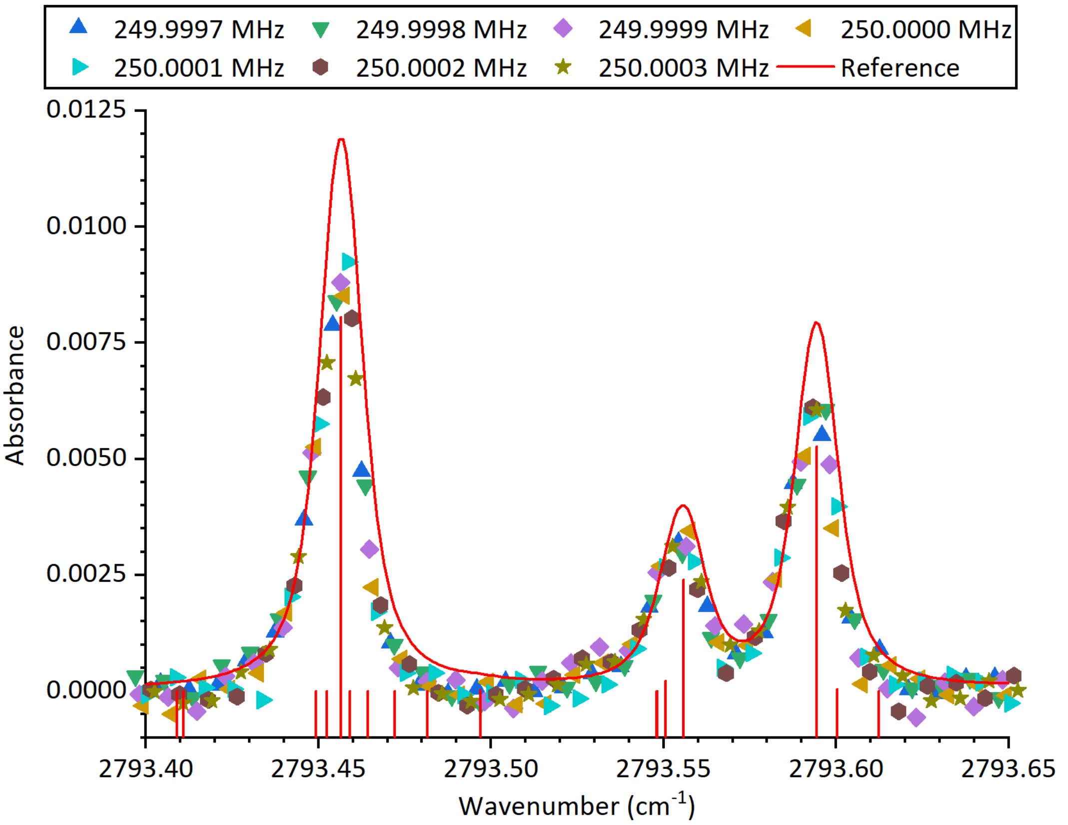

Figure 3-5 Multiple Repetition rates. A 0.25 cm^{-1} wide portion of a spectrum within the ν_3 fundamental vibrational transition of CH_4. Each symbol represents a different repetition rate of the frequency comb laser (the interleaved spectrum is shown in Figure 3-6). The red stick lines are from the reference spectrum in *HITRAN* and the red continuous line is a convolution of the reference spectrum using the HAPI program. [216, 233] This figure is reproduced with permission from reference [137].

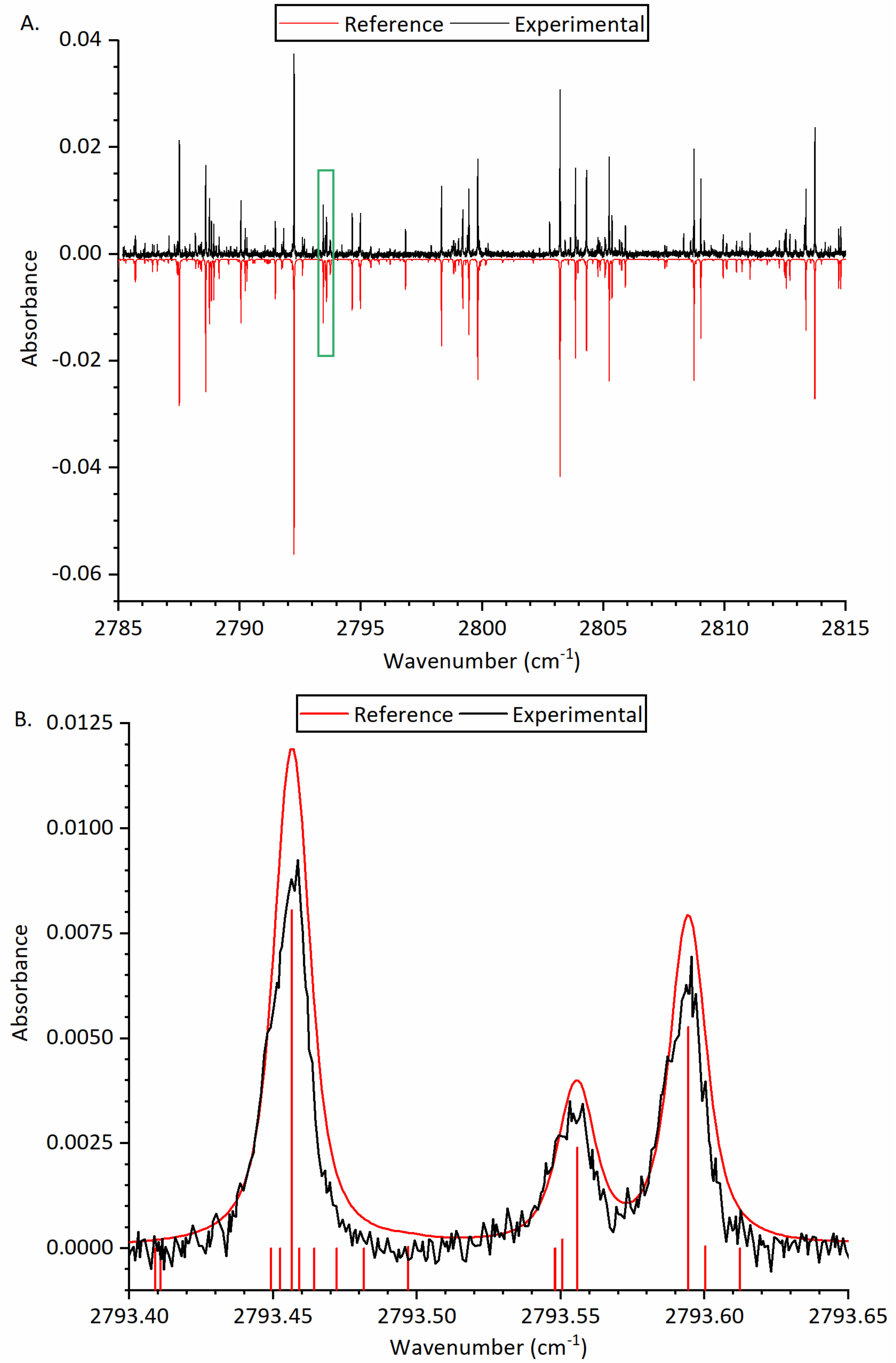

Figure 3-6 Example Spectrum. A. One 30 cm^{-1} wide spectral window containing the ν_3 vibrational mode of CH_4. Black trace is the experimental spectrum with a concentration of 1.44 × 10^{15} molecule cm^{-3}, total pressure 9.1 mbar. Red trace is the *HITRAN* reference spectrum. Green box is the region shown in part B. B. 0.25 cm^{-1} wide window, is the same as Figure 3-5 but with 10 repetition rates interleaved to give one spectrum. This figure is reproduced with permission from reference [137].

3.3. Analysis

3.3.1. PGOPHER

PGOPHER is an open-access program created by Colin M. Western (University of Bristol) and used by the research community for simulating and fitting spectra, [230] including rotational, vibrational, and electronic spectra. The program is freely available from http://pgopher.chm.bris.ac.uk/, where appropriate documentation and walkthroughs for the program can be found. For the analysis of molecules in this project, *PGOPHER* was used to simulate rovibrational spectra of asymmetric top molecules in order to determine the wavenumbers of the observed vibrational transitions and determine the rotational constants of each observed vibrational state. As this project only deals with the analysis of asymmetric top molecules, specifically CH_2I_2 and CH_2Br_2, this section will only cover how an asymmetric top file is created, and the two fitting procedures which are undertaken as part of the analysis: band-head fitting and contour fitting. In addition, this walkthrough/discussion uses version 11 of *PGOPHER* (released December 2020), so some features may not be available in previous versions of the program.

To start, a new asymmetric top file can be created (file → new → asymmetric top), which creates a basic spectrum as shown in Figure 3-7. The tool bar along the top of the program (orange box) can be used to navigate the spectrum, such as move from lower to higher wavenumber, zoom into a specific part of the spectrum, or change how the spectrum and any corresponding overlays are shown. Along this same tool bar, 3 parameters of the spectrum can be altered (green box): temperature, Gaussian broadening, and Lorentzian broadening. While the set temperature is self-explanatory, the values for the Gaussian broadening and Lorentzian broadening need to be changed in order to make the simulated spectrum resemble the experimental spectrum. To recall from section 1.2.4 the Gaussian broadening parameter is calculated from the Doppler broadening (typical values are around 0.002 cm^{-1} for a molecule at room temperature), and the Lorentzian broadening parameter is the sum of the instrument line-shape function and any pressure broadening effects. Finally, under the 'view' menu (blue box), the constants list, fit log, line list, and overlay windows can be opened. Other windows within the program are available, but this walkthrough only focuses on the 4 windows listed.

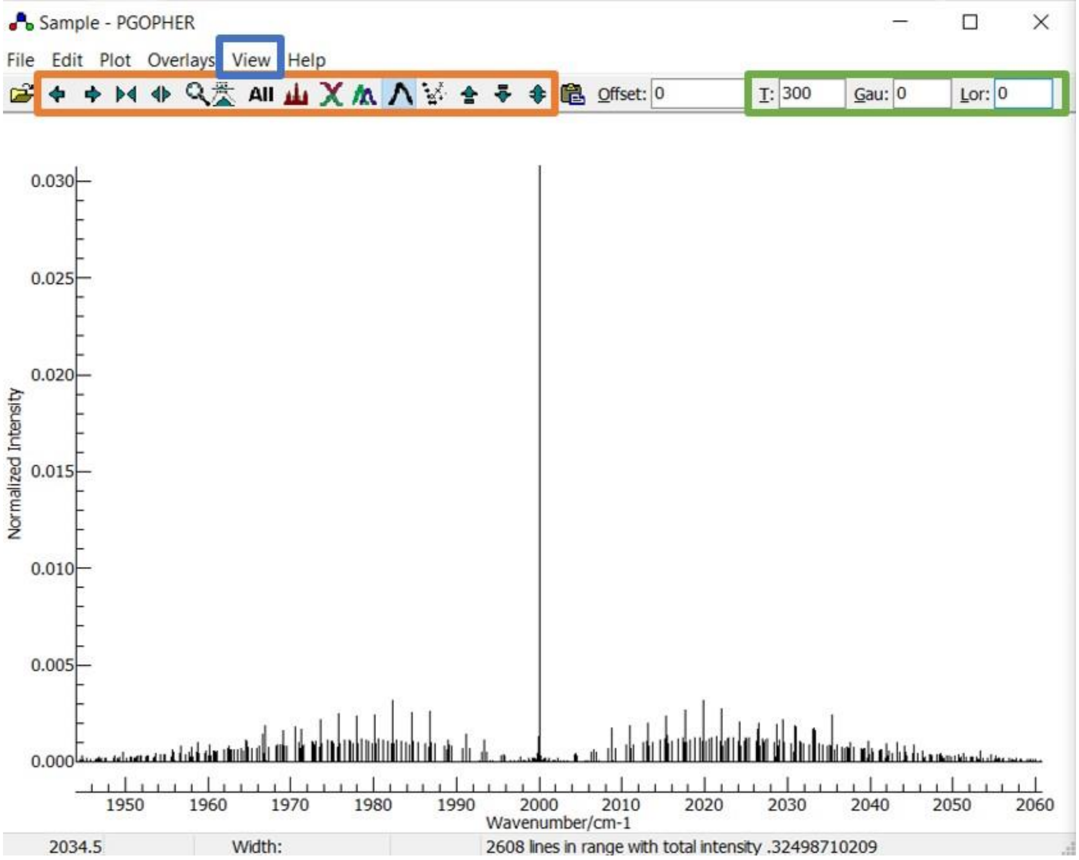

2608 lines in range with total intensity .32498710209

Figure 3-7 PGOPHER Starter File. How the file looks upon creation of an asymmetric top molecule. Blue box is the view menu where the different windows can be accessed. Orange box shows all the options for controlling the main window plot. Green box shows three of the parameters which effect the spectrum: temperature, Gaussian broadening parameter, and Lorentzian broadening parameter.

From the constants window, the simulation can be finely controlled. Within the window, different parameters and constants can be set depending on which level of the menu is selected. For example, under ‘simulation’, further simulation parameters can be set such as frequency range and plot units. When first setting up an asymmetric top file, the point group and symmetry axes must be selected under the asymmetric top manifold (Figure 3-8 part A, red boxes). For CH_2I_2 and CH_2Br_2, the point group is C_{2v} and the C_{2z} axis is set to *b* and the C_{2x} axis is set to *c*. A different asymmetric top manifold can be created for different isotopologues of the same molecule (CH_2Br_2 has 3 such isotopologues), and the relative abundance of the isotopologues can be set (grey box).

Within each asymmetric top manifold, the ground/lower vibrational states and the excited/upper vibrational states can be added. As many vibrational states as needed can be added at this stage. In addition, new transition moments can be added. For the example shown in Figure 3-8 part B, there is one ground state, one excited state, and one transition moment between the ground and excited state. For each vibrational state, the band origin and rotational constants can be defined (yellow boxes), and the symmetry label changed (purple box). For the ground state, rotational constants can sometimes be sourced within appropriate microwave spectroscopy literature. For the excited state, a few approaches can be made to finding appropriate rotational constants: previous literature, copying the ground state rotational constants as a starting, or employing a semi-empirical method to determine rotational constants from *ab initio* calculations (this method is discussed in section 3.3.2).

For rotational constants of either the ground or excited states, the bare minimum to include in a simulation are the A, B, and C rotational constants. It is also good practice to include distortion constants (D_K, D_{JK}, D_K, d_K, and d_J) as these constants become important as the rotational quantum numbers increase. For a few cases, higher level distortion constants are also included in the simulation (H_K, H_{KJ}, H_{JK}, and H_J), however these constants are not normally included in the fitting procedure, and are kept the same between the ground and excited states.

In order to determine the rotational constants, the experimental spectrum is imported to *PGOPHER* as an overlay. From the "view" menu, the overlay window can be inspected (Figure 3-8, part C). From here, the both the *y*- and *x*-axis units of the overlay can be altered. In addition, the baseline and scale of the overlay (Part C, aqua box) can be altered to ensure the overlay matches the simulation on the *y*-axis, however this is not a necessary step unless the contour fitting procedure is undertaken. This contour fitting process is explained later in this section. As many overlays as needed can be imported, where each overlay is assigned a different colour. In addition, the plot style of the simulation and overlay can be changed from the main plotting window, such that the two spectra are either staggered vertically or completely overlapping (other layouts are also available).

Once initial parameters and rotational constants have been set, a process termed band-head fitting can be undertaken. If the ground state constants are known or assumed to be fixed at specific values, then this fitting process alters the excited state constants to match the position and shape of the simulated and experimental peaks. This band-head fitting procedure is a simpler version of the line position fitting procedure, as recommended in the *PGOPHER* online literature. The line position fitting is best used where transitions are well-resolved, whereas band-head fitting is best used when many absorption transitions convolve into one peak.

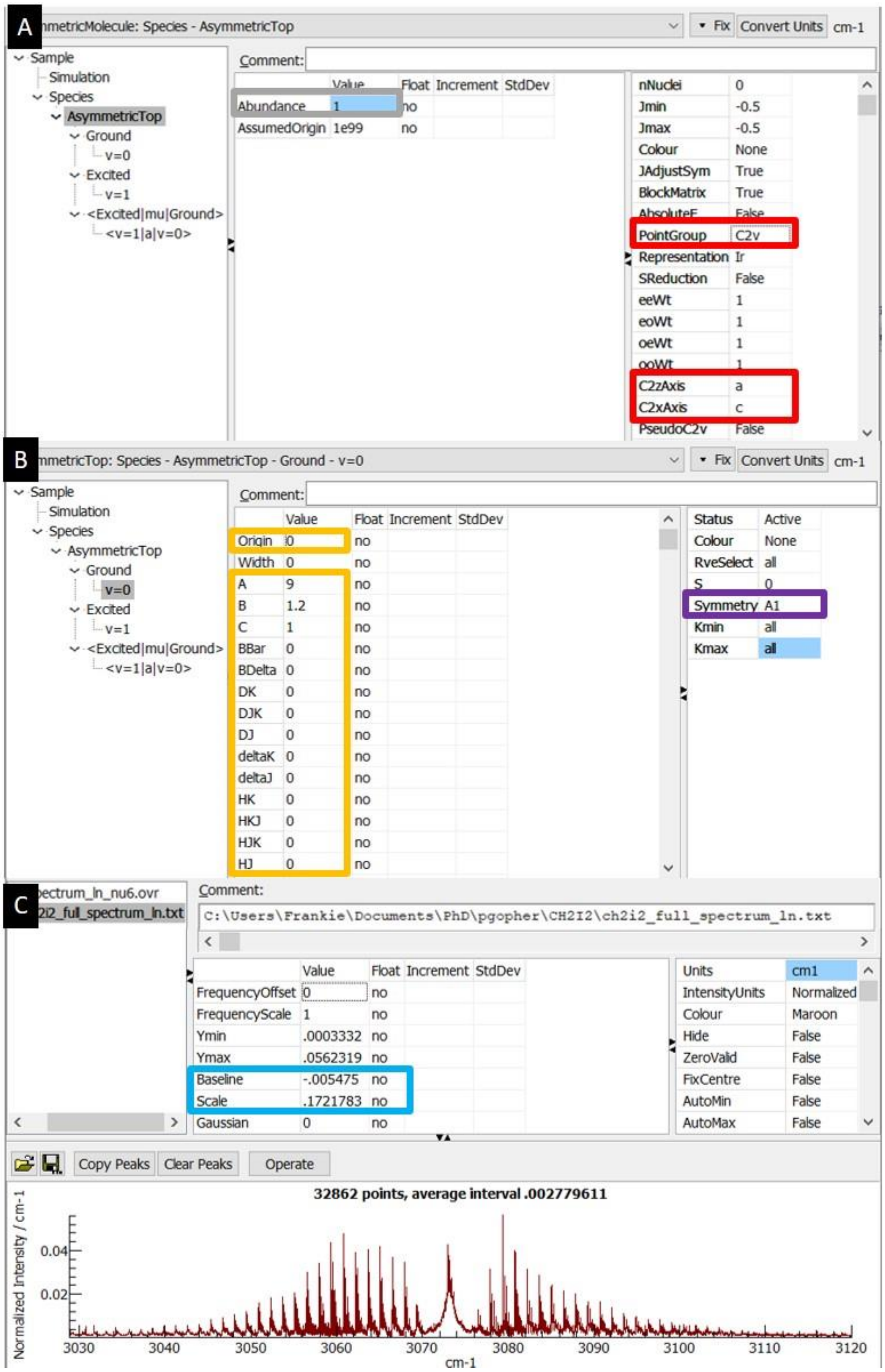

	Value	Float	Increment	StdDev
Abundance	1	no		
AssumedOrigin	1e99	no		

nNuclei	0
Jmin	-0.5
Jmax	-0.5
Colour	None
JAdjustSym	True
BlockMatrix	True
AbsoluteE	False
PointGroup	C2v
Representation	Ir
SReduction	False
eeWt	1
eoWt	1
oeWt	1
ooWt	1
C2zAxis	a
C2xAxis	c
PseudoC2v	False

	Value	Float	Increment	StdDev
Origin	0	no		
Width	0	no		
A	9	no		
B	1.2	no		
C	1	no		
BBar	0	no		
BDelta	0	no		
DK	0	no		
DJK	0	no		
DJ	0	no		
deltaK	0	no		
deltaJ	0	no		
HK	0	no		
HKJ	0	no		
HJK	0	no		
HJ	0	no		

Status	Active
Colour	None
RveSelect	all
S	0
Symmetry	A1
Kmin	all
Kmax	all

```
C:\Users\Frankie\Documents\PhD\pgopher\CH2I2\ch2i2_full_spectrum_ln.txt
```

	Value	Float	Increment	StdDev
FrequencyOffset	0	no		
FrequencyScale	1	no		
Ymin	.0003332	no		
Ymax	.0562319	no		
Baseline	-.005475	no		
Scale	.1721783	no		
Gaussian	0	no		

Units	cm1
IntensityUnits	Normalized
Colour	Maroon
Hide	False
ZeroValid	False
FixCentre	False
AutoMin	False
AutoMax	False

Figure 3-8 Constants and Overlay Window. A. Asymmetric top manifold window. Grey box shows the relative abundance of the molecule, and the red boxes shows the symmetry group of the molecule and the C_{2v} axes. B. Vibrational state window, showing the ground state. Yellow boxes show the origin and rotational constants, purple box shows the symmetry of the particular vibrational mode C. Overlay window, showing an example of a CH_2I_2 spectrum. The aqua box shows the baseline and scale which need to be altered in order for the experimental spectrum to match the simulated spectrum in the *y*-axis.

The first step of the band-head fitting procedure is to generate a line list. To start, right click on the simulation close to where the “band-head” of the peak is: on one side of the peak close to the base of the peak (see blue arrow on Figure 3-9). This gives list of the nearest 10 rovibrational transitions associated with that peak. Then select two transitions which have wavenumber assignments close to the most intense part of the peak. While the two transitions are selected, right click and drag over the corresponding peak in the experimental overlay. This will assign the two simulation transitions with the selected peak in the experimental spectrum. Upon clicking the ‘test’ button, a small window showing a plot of observed-calculated vs wavenumber, and also a little green line appears over the peaks which shows the difference between the two positions of the selected transition (see Figure 3-9). This process can be continued to build up a line list of the band-heads. Once the line list is created, the fitting of constants can occur.

For fitting the various constants, it is easier to start with the origin, then move onto A, B, and C, then move onto distortion constants. Simply “float” the constant, and press fit in the line list window, until the value of the origin/rotational constant remains consistent. For each fit, the fit-log window becomes visible, which shows the original value of the constant, the new value of the constant, and the standard deviation of the fit. Meanwhile, observe the spectrum to ensure that the constants are not drastically changing and causing the simulation to become vastly different from the experimental spectrum. For asymmetric top molecules, it can be beneficial to convert the B and C constants to $\bar{\mathrm{B}}$ and δ (where $\bar{\mathrm{B}} = \frac{1}{2}(B + C)$ and $\delta = (B - C)$). The fitting of the constants is an iterative process, where after an initial fit of constants, the line list can be re-made and the origin/rotational constants fitted for a second round. For the second try, it can be useful to combine which constants are being fitted i.e. origin and A, $\bar{\mathrm{B}}$ and δ.

The second procedure used in this thesis is contour fitting, which uses a residual plot to fit constants. However, this process is not best used for fitting the origin or rotational constants as any slight deviation between the simulation and experimental spectra can cause the values to become drastically wrong. The contour fitting procedure is instead used to fit the Lorentzian broadening factor. This factor is a combination of the instrument line-shape function (see section 3.4) and pressure broadening (see section 1.2.4.3). As one set of experiments investigates the effect of pressure on the spectra, the Lorentzian broadening factor is determined in *PGOPHER* for each spectrum. The procedure is as follows: each spectrum is imported into the program and the baseline and scale of the overlay is changed such that the experimental and simulated spectra match in the y-axis. The

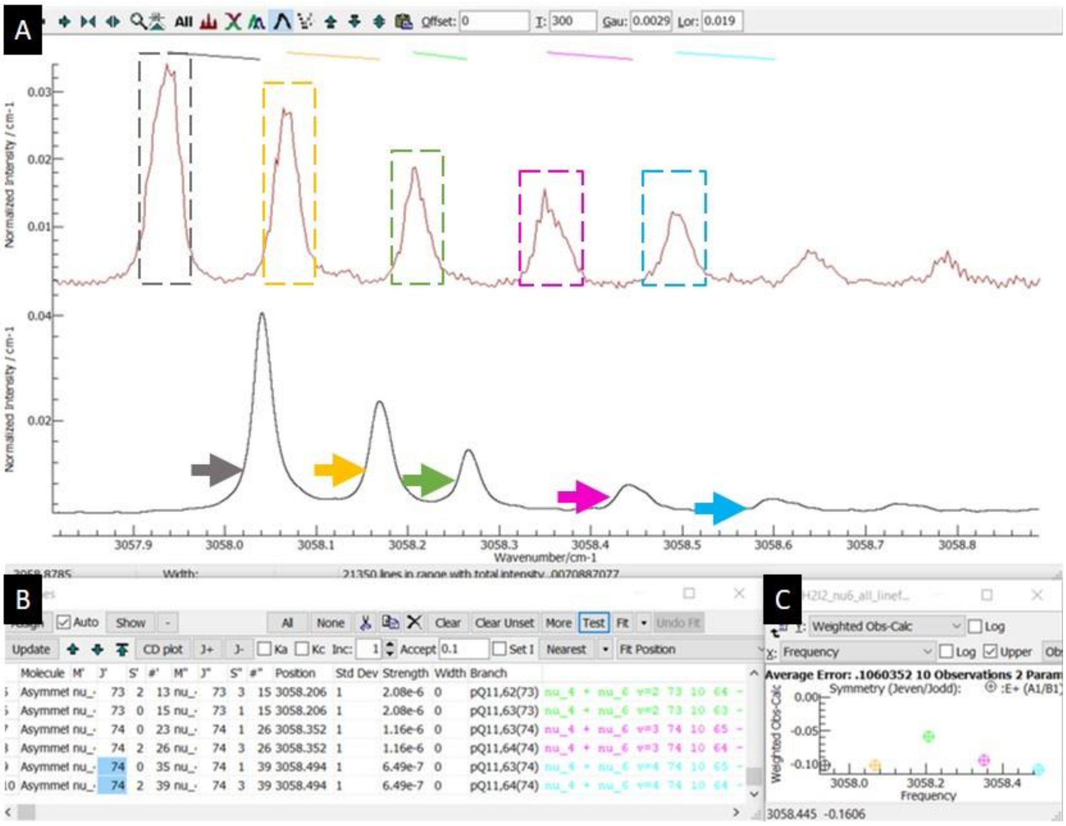

21350 lines in range with total intensity .0070887077

	Molecule	M'	J'	S'	#'	M"	J"	S"	#"	Position	Std Dev	Strength	Width	Branch	
	Asymmet	nu_	73	2	13	nu_	73	3	15	3058.206	1	2.08e-6	0	pQ11,62(73)	nu_4 + nu_6 v=2 73 10 64 -
	Asymmet	nu_	73	0	15	nu_	73	1	15	3058.206	1	2.08e-6	0	pQ11,63(73)	nu_4 + nu_6 v=2 73 10 63 -
	Asymmet	nu_	74	0	23	nu_	74	1	26	3058.352	1	1.16e-6	0	pQ11,63(74)	nu_4 + nu_6 v=3 74 10 65 -
	Asymmet	nu_	74	2	26	nu_	74	3	26	3058.352	1	1.16e-6	0	pQ11,64(74)	nu_4 + nu_6 v=3 74 10 64 -
	Asymmet	nu_	74	0	35	nu_	74	1	39	3058.494	1	6.49e-7	0	pQ11,63(74)	nu_4 + nu_6 v=4 74 10 65 -
10	Asymmet	nu_	74	2	39	nu_	74	3	39	3058.494	1	6.49e-7	0	pQ11,64(74)	nu_4 + nu_6 v=4 74 10 64 -

Average Error: .1060352 10 Observations 2 Param

Figure 3-9 Band-head Fitting Line List Creation. A. Simulation in black, experimental overlay in red. Arrows show where the band-head of each simulated peak is. Dotted boxes in the corresponding colour are the experimental peak which are assigned to the simulated peak. The lines along the top of the spectra show the difference in positions between the experimental and simulated spectra. B. Generated line list C. Residual plot, weighted observed − calculated vs wavenumber.

Lorentzian broadening factor is then “floated”, and a small portion section of the two experimental and simulated spectra are selected: right click on the overlay and “select visible”, otherwise the program will try to contour fit the whole spectrum rather than only the region visible on the screen. Within the fit-log window, the “contour” option can be selected and the contour fit can be undertaken. As with the band-head fitting, the fit-log window shows the old and new value for the broadening factor, the standard deviation of the fit, and the contour fit is undertaken until the factor converges.

3.3.2. Semi-Empirical Method

Due to the nature of research, spectroscopic rotational constants of different vibrational states are not always available within the published literature. Therefore, before meaningful analysis can be undertaken in *PGOPHER*, it can be useful to calculate rotational constants through *ab initio* methods. In addition to calculating rotational constants, the semi-empirical method can be used to calculate isotopic shifts and vibrational transition frequencies. For all computational results in this thesis, *Gaussian 09* was utilised to compute constants using various Density Function Theory (DFT) methods and different basis sets (specifics are discussed within the experimental sections: 4.2.3 and 5.2.3). [234] However, the direct outputs of the computational files are not used in the simulated spectra. Instead, a semi-empirical approach is undertaken. Within this thesis, all Gaussian calculations were undertaken by Dr Lehman, and only the output files were used for the analysis here. In addition, the semi-empirical method presented in the next paragraph was adapted from work published by Sadiek and Friedrichs. [93]

From within the *Gaussian 09* output files, the appropriate *A*, *B*, and *C* ground state (v = 0) and upper state (v = 1 for a certain vibrational mode) rotational constants are extracted. The difference between the ground and upper state constant is then calculated, to give the Δ_i value (always given as ground − upper). Then the Δ_i value for each of the *A*, *B*, and *C* constants is added to the corresponding experimentally determined ground state constant, which are again typically found in microwave spectroscopy literature. For example, if the calculated *A* constant for the ground state and upper state is 0.10 cm^{-1} and 0.09 cm^{-1}, respectively, then the Δ_i is −0.01 cm^{-1}. If the experimentally determined ground state *A* constant is 0.05, then the new semi-empirically determined upper state constant is now 0.04. This process can be repeated for as many vibrational states as needed. The new semi-empirically determined rotational constants for the upper states can then be utilized within *PGOPHER* for initial simulations.

3.4. Instrument Line-shape Function

In order to analyse the acquired spectra, the instrument line-shape function of the VGC set up needs to be determined. This is particularly important for analysing the spectra acquired for pressure broadening analysis as the instrument line-shape function needs to be removed from the broadened spectra. In order to measure the line-shape function, a spectrum of CH_4 with a known concentration and a known Herriott cell path length is used.

Firstly, a 4.85% CH_4 in nitrogen certified mix (BOC gas), is introduced into the flow cell using the 30 sccm MFC and then further diluted with nitrogen to a 0.1% mix. For the instrument line-shape function characterization, a 1.44(5) x 10^{13} molecule cm^{-3} sample of methane was used with approximately 0.5 mbar total pressure. A methane spectrum was collected using the frequency comb spectrometer over the wavenumber range of approximately 3037 to 3080 cm^{-1} (Figure 3-10, part A).

From the methane spectrum, the observed total line-shape function is a combination of collisional (pressure) broadening, Doppler broadening, and the instrument line-shape function. As the spectrum was acquired under low-pressure conditions, the pressure broadening is assumed to be negligible compared to other sources of broadening. The specific broadening coefficients based on the *HITRAN* reference database are: $b_{self} = 7 \times 10^{-5}$ cm^{-1} mbar^{-1} and $b_{air} = 4 \times 10^{-5}$ cm^{-1} mbar^{-1}. [216] Using these two coefficients, the total pressure broadening for the CH_4 spectrum will be 2×10^{-5} cm^{-1}. The Doppler broadening for CH_4 at room temperature is a Gaussian contribution to the line-shape function, with a FWHM of 0.0095 cm^{-1} at 3060 cm^{-1}. The remaining broadening of the observed vibrational spectrum is the instrument line-shape function, which is a Lorentzian function. This function is due to the combination of the VIPA line-shape function [227] and the diffraction grating line-shape function. [222] As both of these are Lorentzian line-shape functions, the product of two Lorentzian line-shapes is still a Lorentzian.

Using a *MATLAB* code, the *HITRAN* line positions for CH_4 are convolved with a Voigt line-shape function yielding a reference σ_ν as a function of wavenumber. A Voigt function was chosen as this is the product of the Doppler (Gaussian) and instrument (Lorentzian) linewidths. Then these reference cross sections were multiplied by the experimental methane concentration and Herriott cell path length to yield a reference absorption spectrum. The *MATLAB* code then fit the reference spectrum to the experimental spectrum using a nonlinear least squares fitting procedure. This allowed the Lorentzian contribution to the Voigt line-shape function to be fit, while the Gaussian contribution was held constant (at 0.0095 cm^{-1}). Assuming the pressure broadening of methane is an insignificant contribution to the Lorentzian line-shape, the instrument line-shape function HWHM was determined to be 0.0142 cm^{-1}.

As the instrument line-shape function does not change from experiment to experiment, due to not changing the core optical components in the apparatus, this process does not need to be repeated even if the full alignment of the VGC detector is altered. However, the instrument line-shape function is the limitation of the VGC resolution, assuming that Doppler broadening and pressure broadening are negligible. At higher pressures, the pressure broadening would then become the limiting factor, as seen in sections 4.3.2 and 5.3.2. If there was no instrument line-shape function from the VGC detector, then the theoretical limit of the spectral resolution would be the linewidth of each comb tooth from the frequency comb laser.

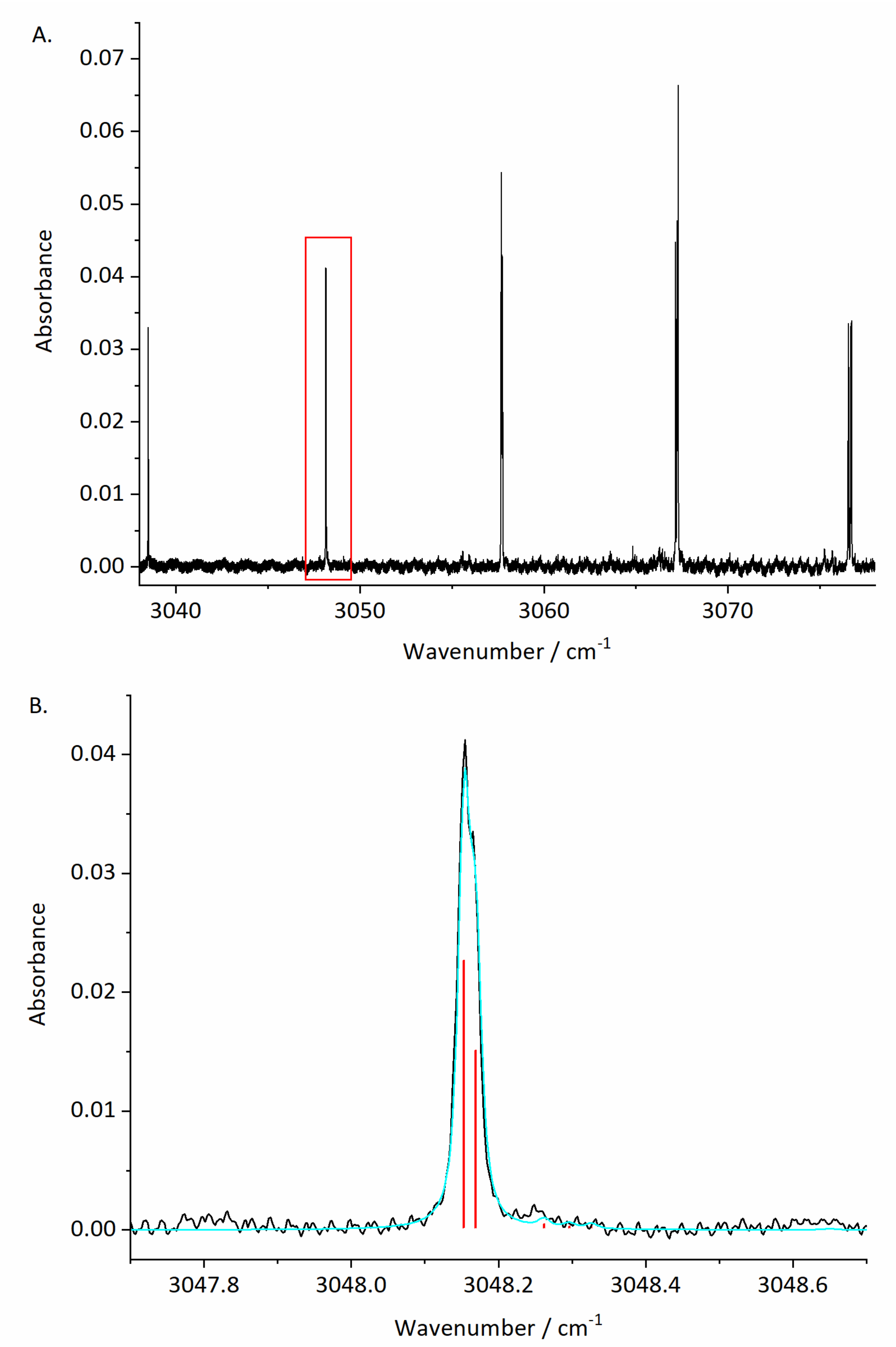

Figure 3-10 CH_4 Instrument Line-shape Function. A. Methane absorption spectrum at a concentration of 1.44(5) x 10^{13} molecule cm^{-3}, 0.5 mbar total pressure, in the Herriott flow cell with a path length of 570(60) cm. The red box is the smaller portion of the spectrum shown in part B. B. 1 cm^{-1} portion of the spectrum, overlaid with the Voigt fit (blue line) and *HITRAN* “stick” spectrum (red lines). The final parameters for the Voigt function are 0.0142 cm^{-1} FWHM for the Lorentzian contribution (ILS function) and 0.0095 cm^{-1} FWHM for the Gaussian contribution (Doppler broadening).

3.5. Noise

In order to understand the limitations of the spectrometer, the level of baseline noise within the acquired spectra needs to be quantified. Within this thesis, the baseline noise is taken to be the standard deviation of the baseline where no sample is present, such that the value should represent the average background noise of the instrument free of any real absorptions. A conservative rule of thumb within spectroscopy, is that any peak which has an intensity of 3 × σ above the baseline noise, where σ is the value of the baseline noise is a "real peak". This rule of thumb is a simple estimate to help pick out peaks by eye, however, rigorous methodologies in determining when an event is not considered noise can be achieved with statistical methodologies. [235] The baseline noise is not a constant value in the VGC apparatus, and changes with a variety of factors: number of images collected and averaged together, integration time of the detector camera, and there is also a difference in baseline noise for data collected from the flow cell or free-jet expansion and the analysis method of the free-jet expansion (this latter point is covered in the next section).

First, increasing the number of images that are collected and averaged together brings down the baseline noise level significantly. For a single CH_4 spectrum, where 190 signal images and 190 background images are averaged together, taken at a camera integration time of 50 μs and a frame rate of 125 Hz, total integration time of 9.5 ms, the σ is approximately 5.79×10^{-4}. For the same set of conditions, however this time, 2000 signal images are collected and averaged together, and 2000 background images are collected and averaged together, a σ of approximately 1.20×10^{-4} is achieved. Collecting a total of 2000 images, for either signal or background, at a camera integration time of 50 μs and a frame rate of 125 Hz, corresponds to a total experiment time of 16 seconds and a total integration time of 100 ms. Therefore increasing the number of collected images and hence increasing the total integration time, by a factor of 10 improves the σ by a factor of 4.8. Furthermore, a comparison can be made for the minimum observed concentration of CH_4, for 190 images acquired for the sample, the $[CH_4]_{min} \approx 8.0 \times 10^{11}$ molecule cm^{-3}, whereas for 2000 images acquired for the sample, the $[CH_4]_{min} = 1.7 \times 10^{11}$ molecule cm^{-3}. These minimum values assumes an average methane absorption line intensity value of 1×10^{-19} cm^2 cm^{-1} $molecule^{-1}$ and that the detectable absorption peaks are 3 × σ above the baseline noise.

Secondly, the camera integration time for a single frame also has an effect on the baseline noise. The camera described in section 2.2.6 is capable of operating at an integration time between 1 and 10,000 μs. For experiments using the flow cell, a camera integration time of 50 μs is used, whereas for the free-jet expansion experiments 200 μs is used. Using the exact same imaging conditions (190 signal images averaged together, 190 background images averaged together, 125 Hz camera rep rate), two spectra of CH_4 are shown in Figure 3-11 were collected, where the black trace has a camera integration time of 50 μs and the grey trace has a camera integration time of 5 μs. Included in the figure is also a red simulated spectrum of CH_4 and red sticks indicating the spectral line intensities which are obtained from *HITRAN*. Using a portion of the spectra for where there are no vibrational peaks assigned to CH_4, the baseline noise for each camera integration time is determined to be: $\sigma_{50\mu s} = 5.79 \times 10^{-4}$ and $\sigma_{5\mu s} = 1.28 \times 10^{-3}$. Therefore, increasing the total camera integration time, for the same number of total images, by a factor of 10, gives a decrease in baseline noise by a factor of 2.2. The decrease in baseline noise as the camera integration time is increased also means the minimum observed concentration of CH_4 is decreased. For a 50 μs integration time, where the total integration time is 9.5 ms, the $[CH_4]_{min} \approx 8.0 \times 10^{11}$ molecule cm^{-3}. On the other hand, for a 5 μs integration time, where the total integration time is 950 μs, the $[CH_4]_{min} \approx 2.5 \times 10^{12}$ molecule cm^{-3}.

In addition to looking at the baseline noise level, the noise equivalent absorption (NEA) can be calculated which is useful when comparing different detection systems. The NEA is a function of the baseline noise level (σ) measured over an integration time (T) for a specific path length (L, which for this instance is 430 cm):

$$NEA = \frac{\sigma}{L}\sqrt{T} \qquad \textbf{Equation 3-6}$$

Therefore, for the given $\sigma_{50\mu s}$ above of 5.79×10^{-4} the NEA^{1s} is 9.8×10^{-8} cm^{-1} $Hz^{-1/2}$, and for $\sigma_{5\mu s} = 1.28 \times 10^{-3}$, the NEA^{1s} is 2.2×10^{-7} cm^{-1} $Hz^{-1/2}$ (both NEA values have been normalised to 1 s). The instrument NEA^{1s} values are on-par with the system performance values listed in Table 5 of ref. [236], which compares a variety of spectrometers using incoherent and coherent light sources for broadband spectroscopy. For example, a Fourier transform spectrometer using a frequency comb laser with a centre wavenumber of 2660 cm^{-1} (3760 nm) in a high finesse cavity has a $NEA^{1s} = 5.5 \times 10^{-9}$ cm^{-1} $Hz^{-1/2}$. [237] Similarly, for a frequency comb laser centred near 2680 cm^{-1} (3730 nm) coupled to a high finesse cavity and detected using a VGC spectrometer, $NEA^{1s} = 4.8 \times 10^{-8}$ cm^{-1} $Hz^{-1/2}$. [185]

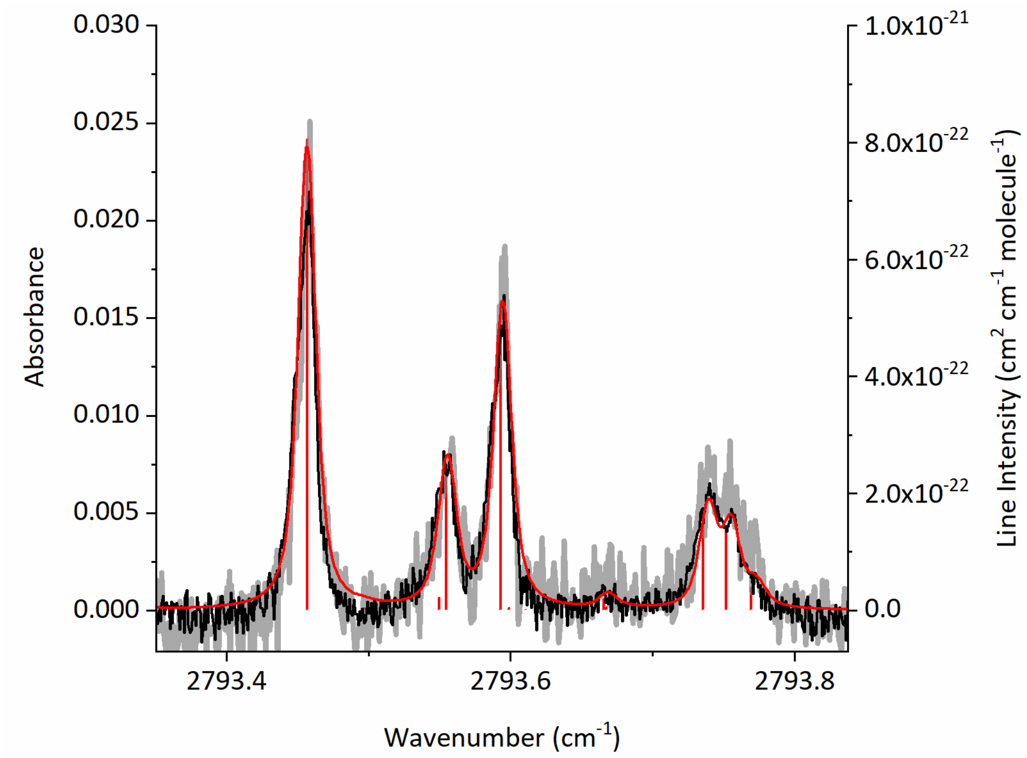

Figure 3-11 50 µs vs 5 µs Camera Integration Times. A 0.5 $\mathrm{cm^{-1}}$ portion of the CH_4 spectrum, where the concentration of the sample is 1.44(5) x 10^{13} molecule $\mathrm{cm^{-3}}$, 0.5 mbar total pressure, in the Herriott flow cell with a path length of 570(60) cm. The black spectrum is the data recorded with camera integration time of 50 µs, and the grey spectrum is the data recorded with a camera integration time of 5 µs, both using the left-hand *y*-axis of absorption. The red spectrum is a simulated overlay, also using the left-hand *y*-axis. The red sticks are the spectral line intensities from *HITRAN* and are plotted against the right-hand *y*-axis. This figure is reproduced with permission from reference [137].

3.5.1. Uninterruptable Power Source

During the course of initialising and characterising the frequency comb detection system, it became apparent there was an external source causing an intermittent sine wave in the baseline of acquired spectra. An example of this noise can be seen in Figure 3-12, part A. This figure shows three spectra taken on the same day, where all six averaged images were taken with the following parameters: 2000 images averaged together, no sample present, and a 50 µs integration time. The lack of sample ensured that only a baseline spectrum was recorded, and the only difference between the spectra was the time of day at which the images were acquired. However, each image pair needed to create the spectrum were taken within 2 minutes of each other. As the legend in Figure 3-12 part A shows, the black spectrum was taken at 9:30 am, the blue spectrum at 9:40 am, and the red spectrum at 2:30 pm. Looking at the three spectra, it is evident that the sine wave within the baseline is inconsistent in amplitude, and although not shown here, the noise was not always guaranteed to be present. This inconsistency meant it was difficult to generate a method to remove the noise during the post-processing procedures. Therefore, efforts were made to locate the source of the noise.

Initial investigations into the noise focussed on the different types of noise: a property of the lasing system, vibrational, or electronic. First, the noise was deemed to not be an inherent property of the lasing system due to the inconsistency of the noise. Secondly, inducing vibrations on the optical table through the use of a vacuum pump showed that while there was an increase in noise amplitude from the pump, the noise was still present when there was no possible vibrational source. This narrowed the source of the noise down to electrical, however the specific source of the electrical noise was still undetermined.

As the source of noise could not be identified, efforts were instead focused on how to nullify the electrical noise effects on the acquired spectra. The solution was found in employing a 3-phase uninterruptible power supply (UPS). Fundamentally, a UPS is a battery system which will ensure that a piece of equipment remains powered in the event the mains power is no longer supplying a voltage. A 3-Phase UPS works by “cleaning” the electricity supplied from the mains power source, before the voltage is supplied to the equipment. This “cleaning” process works by converting the electrical voltage from AC (alternating current) to DC (direct current) and then back to AC. In this case, the piece of equipment being supplied the “cleaned” electrical voltage is the frequency comb lasing system. Figure 3-12 part B, shows two spectra taken on the same day, where the green spectrum is from the lasing system being supplied voltage directly from the mains, and the purple spectrum is from the lasing system being supplied voltage via the 3-phase UPS. Both spectra were taken with the same parameters: four total averaged images, where 2000 images were used in each average, no sample present, and a 50 μs integration time. In addition, the imaging pairs were recorded within a two minute time frame, and the two spectra were recorded within a 60 minute time frame. Although Figure 3-12 shows a decrease in amplitude of the baseline noise when implementing the 3-Phase UPS, it is useful to compare σ values, where the σ is determined to be the standard deviation of the spectra shown in Figure 3-12: for no 3-Phase UPS in use $\sigma = 2.4 \times 10^{-3}$, and for the 3-Phase UPS in use, $\sigma = 1.2 \times 10^{-4}$.

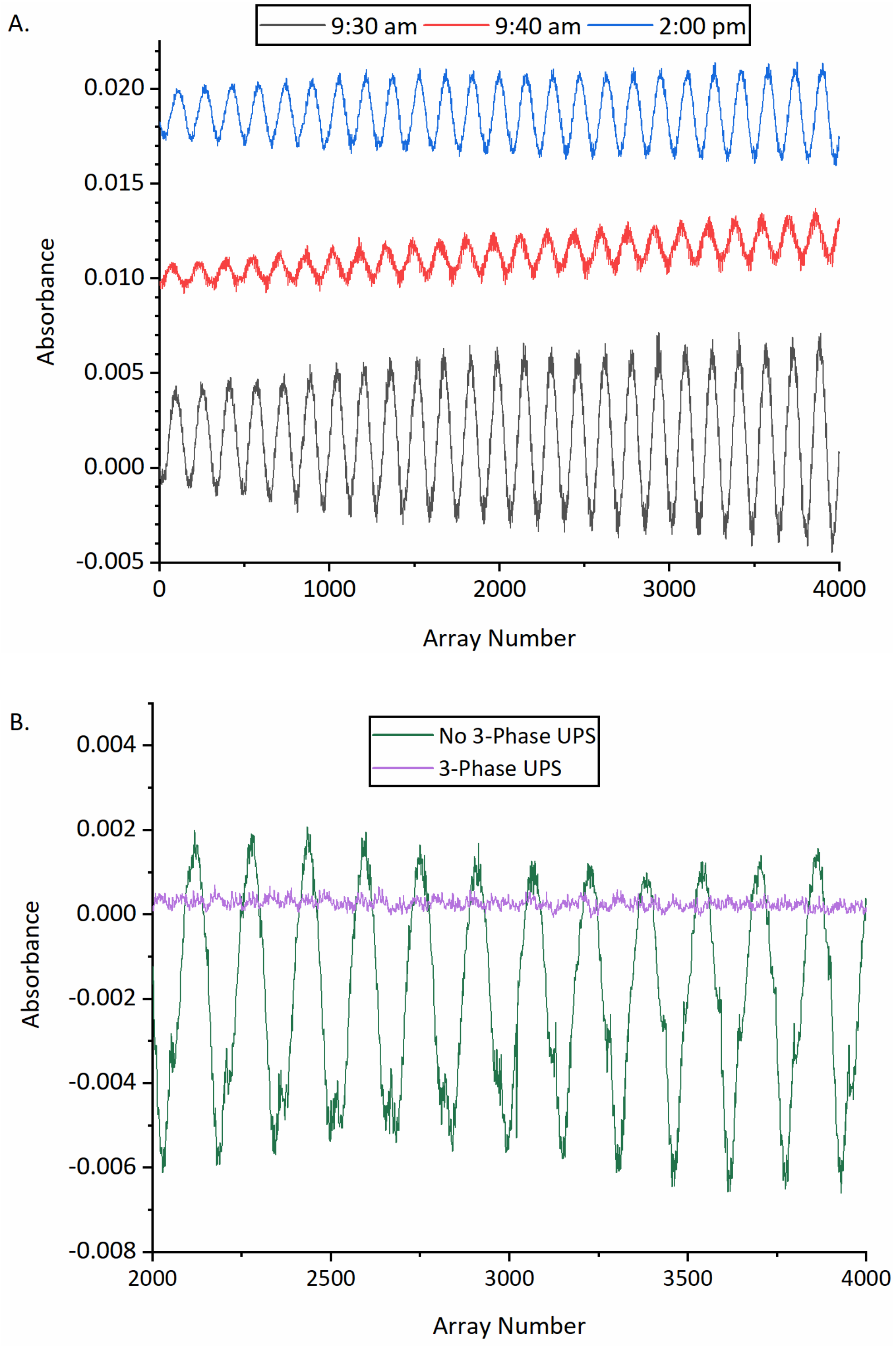

Figure 3-12 Electrical Baseline Noise. A. Three stacked baseline spectra plotted as a function of array number, with the same acquisition parameters and on the same day: 2000 images averaged together, no sample present, and a 50 µs integration time. The only difference between the three spectra is the time of acquisition: blue = 2:00 pm, red = 9:40 am, grey = 9:30 am. Lots of noise, taken on the same day, but at different times. B. Two overlaid baseline spectra plotted as a function of array number, with the same acquisition parameters and on the same day: 2000 images averaged together, no sample present, and a 50 µs integration time. The green spectrum was acquired with no 3-Phase UPS in use, and the purple spectrum was acquired with the 3-Phase UPS in use.

3.6. Initialisation of the Free-Jet Expansion Experiment

As previously mentioned in the acquisition section, the free-jet expansion data are acquired through an active background method. This means that rather than acquire signal and background images as two separate data files with the background dataset collected before or after the signal dataset, as is the method for data using the flow cell, one data file is collected where signal and background images are collected concurrently, with either every other image being a signal image, or every tenth image being a signal image. Active background subtraction is a useful method, especially for long acquisition times as any intensity drift of the frequency comb is negated. Furthermore, any external noise fluctuations such as vibrations or thermal effects on the frequency comb source are also nullified as the background and sample images would effectively undergo the same effects.

The first method developed for acquiring free-jet expansion data involved collecting images with a camera frame rate of 20 Hz and an integration time of 200 µs. As mentioned in section 3.1, the frame rate is set externally by a digital delay generator, and the pulsed valve operates at 10 Hz. This means that for every two images collected, one image contains the signal information, and the next image contains the background information. The data can then be processed using the initial *MATLAB* script in one of two methods: “pseudo” background subtraction or “proper” background subtraction. The pseudo subtraction method works by averaging together all of the odd numbered images and then averaging together all of the even numbered images. This gives average signal and average background images which can be analysed within the already written *MATLAB* code to give one spectrum. The proper subtraction method involves exporting the whole set of images (typically 20,000 in one set) and analysing pairs of acquired images through the *MATLAB* code e.g. image 1 and 2 together as signal and background images, then 3 and 4 together, and so on. This creates 10,000 spectra which can be averaged. However, this method is very time consuming as it takes approximately 4 hours to create one averaged spectrum comprising of 10,000 individual spectra, and as seen below, has negligible benefits to the level of noise.

With either method of analysis, the same amount of data was acquired, just analysed in a different way. In order to analyse which method gives better baseline noise (σ), many data sets of increasing size were collected. Figure 3-13 shows the plot of the baseline standard deviation as a function of total integration time. The baseline standard deviation was acquired by performing a standard deviation calculation on the baseline of the acquired spectra such that there were no absorptions from signal in the calculation. The grey squares are data that were analysed using the proper active background subtraction method, and the red circles and blue triangles were analysed using the pseudo-background subtraction method. The two data sets for the pseudo method were obtained with the same experimental parameters, just on consecutive days. As the graph shows, a total integration time of 8 seconds is necessary to reach the baseline noise limit: 40,000 images total at an integration time of 200 μs. In addition, the laboratory time for acquiring 40,000 images at a 20 Hz acquisition rate corresponds to a laboratory time of 33.3 minutes. Across the three sets of data presented in Figure 3-13, σ reaches a similar value: 6.71×10^{-6} for the proper background subtraction method, 6.72×10^{-6} for the first pseudo background subtraction method data, and 6.51×10^{-6} for the second pseudo background method subtraction. Therefore, the analysis method did not make a significant difference to the observed baseline noise level. Hence, in order to reduce processing time, the pseudo-background subtraction method is used when collecting images at the 20 Hz camera frame rate.

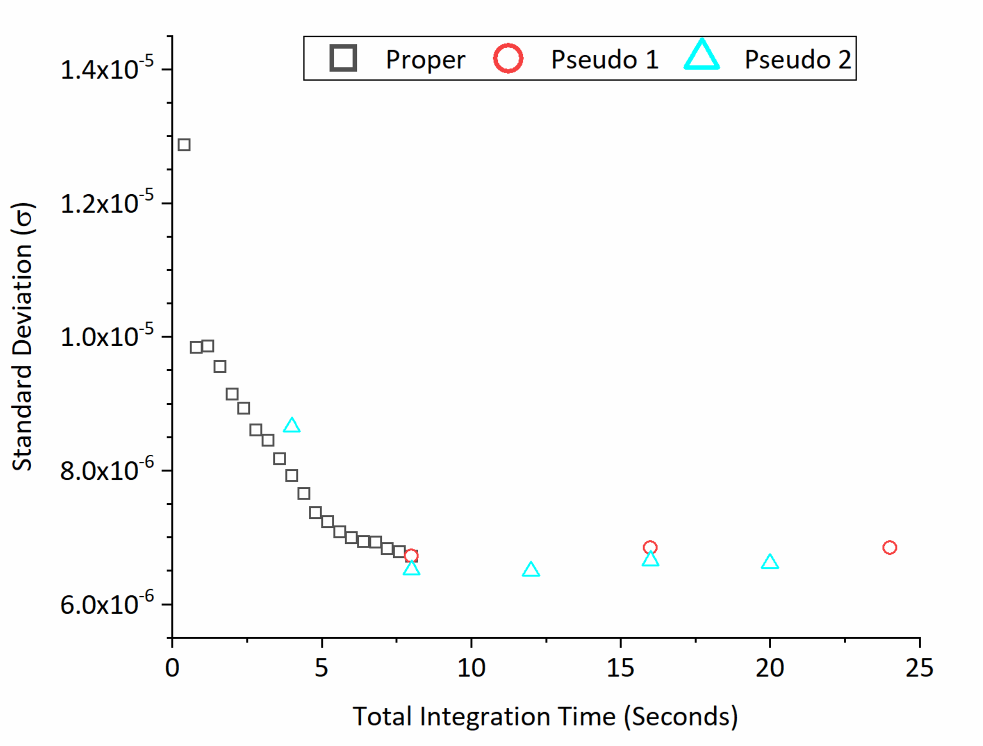

Figure 3-13 Standard Deviation vs Total Integration Time. Three sets of data analysed by two separate methods: "pseudo" background subtraction (red circles and blue triangles), and "proper" background subtraction (grey squares). All data sets were acquired using the same experimental parameters across multiple days, with an increasing number of acquired images which increases the total integration time. To combine the notion of number of images to integration time, 0.4 seconds corresponds to 1000 spectra or 2000 images.

3.6.1. Initial Results

Initial spectra acquired using the 20 Hz data camera frame rate and pseudo background subtraction method outline above can be compared to data collected from the flow cell apparatus (Figure 3-14). The grey spectrum was taken at room temperature (300 K) and the red spectrum was taken in the free-jet expansion apparatus (temperature estimated to be approximately 40 K based on a *HITRAN* simulation). Within Figure 3-14 there is clear evidence of "ghost peaks" (as discussed in section 3.2), and minimisation of these peaks relies on a good optical alignment of the detection set-up. However, these "ghost peaks" do not affect the intensity of the main peak. For the spectra presented in Figure 3-14, room temperature spectrum has a CH_4 concentration of approximately 0.1 mbar and with a path length of 1130 cm, and the cold temperature spectrum has an unknown CH_4 concentration and an unknown path length. However, despite the unknown CH_4 concentration within the free-jet expansion, the sample parameters are known before the CH_4 is pulsed through the jet: 4.5% mix of CH_4 in N_2 with an approximate total pressure of 4000 mbar.

The two experimental spectra match well but with an obvious shift in the intensity patterns due to the change in population distribution of the rotational levels at cold temperatures. As each peak in the vibrational spectra of CH_4 (3_0^1 vibrational transition) is attributed to a different rovibrational transition, increasing wavenumber transitions are linked to increasing the J quantum number. Therefore, as the rotational temperature of CH_4 decreases, the available J levels for rovibrational transitions also decrease, and the intensity of the transitions shifts towards the central Q-branch at 3018 cm^{-1}.

As the level of absorption for the cold temperature spectra is very low, even with the very intense peaks of CH_4, a different analysis method was developed. As discussed in section 3.2.1, the Fourier transform method uses the 10 Hz frequency component containing the signal information. However, this method cannot be used with the 20 Hz camera frame rate. This is due to the Nyquist frequency concept which states that the highest frequency must be greater than twice the sampling rate. In this case, as 10 Hz is the sampling rate, the 20 Hz camera frame rate is at the Nyquist frequency. Therefore, the camera frame rate is increased to 100 Hz, as this is straightforward to program into the digital delay generator box. Figure 3-15 shows the final spectral results of the two acquisition methods: the red CH_4 spectrum is acquired using the active background subtraction method (identical to the data in Figure 3-14, images acquired at a 20 Hz frame rate), and the green spectrum is acquired using the Fourier transform method (images

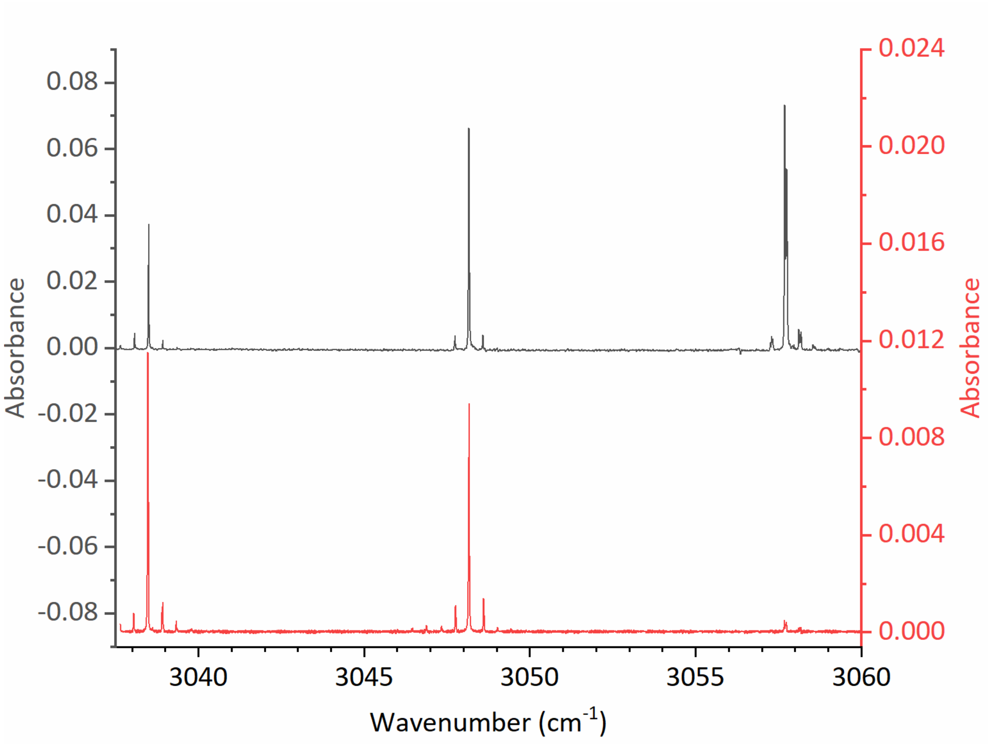

Figure 3-14 CH_4 300 K and ~40 K Comparison Spectra. A 25 cm^{-1} portion of the CH_4 fundamental ν_3 vibrational spectrum, incorporating three rovibrational transitions. The grey spectrum was acquired at 300 K with a CH_4 concentration of approximately 0.1 mbar and a path length of 1130 cm, and corresponds to the left *y*-axis. The red spectrum was acquired at approximately 40 K with an unknown CH_4 concentration and an unknown path length, and corresponds to the right *y*-axis.

acquired at a 100 Hz frame rate). Between both spectra, the path length of the cell was kept constant, and the sample concentration of the CH_4 was kept approximately the same. Once again, the actual concentration of CH_4 cannot be determined, but a 4.5% mix of CH_4 in N_2 with an approximate pressure of 4000 mbar was used to supply the free-jet expansion pulse value. Although the Fourier transform processing method results in a *y*-axis that is arbitrary in absorption, the SNR is greatly increased compared to the spectra obtained using the normal processing method (Figure 3-15). For example, for the absorption peak at 3038.5 cm^{-1}, the SNR for the 20 Hz method is 278.3, and the corresponding value for the 100 Hz method is 803.5. Furthermore, the FWHM of identical absorption peaks remains the same: for the 20 Hz method the peak at 3038.5 cm^{-1} has a FWHM of 0.02700 cm^{-1} and the corresponding peak for the 100 Hz method has a FWHM of 0.02695 cm^{-1}.

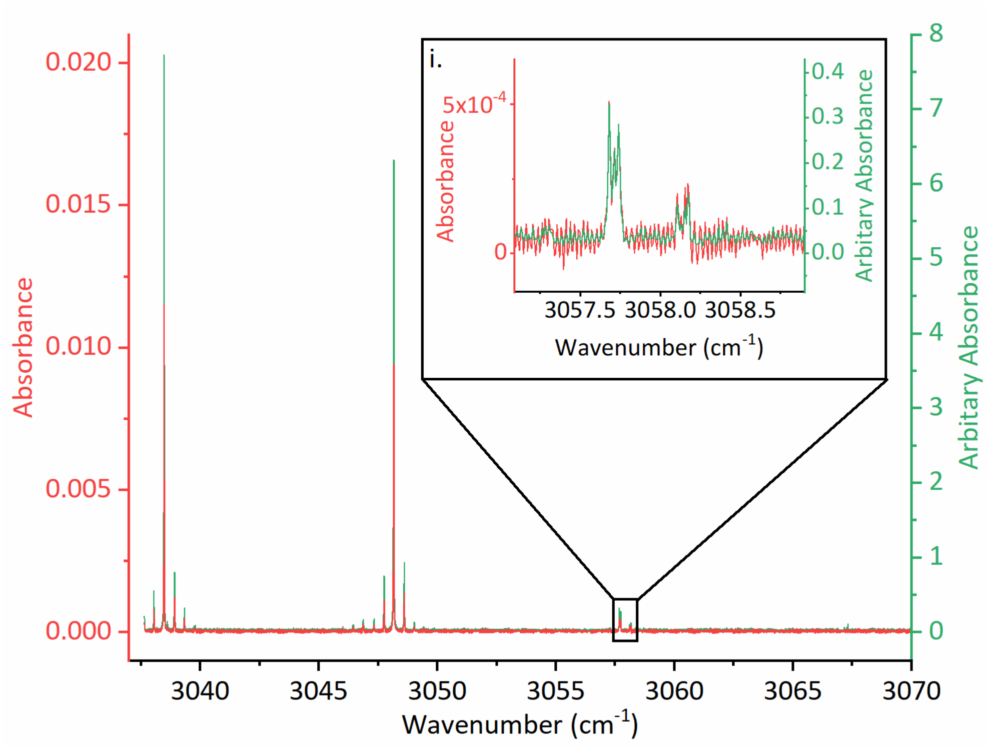

Figure 3-15 20 Hz vs 100 Hz Acquisition Method. CH_4 fundamental ν_3 vibrational spectrum from 3033 to 3070 cm^{-1} incorporating three rovibrational transitions. The red spectrum, and the left *y*-axis, corresponds to the spectrum acquired with the 20 Hz method. The green spectrum, and the right *y*-axis, corresponds to the spectrum acquired with the 100 Hz method. Inset i, shows a small 1.75 cm^{-1} window of the spectra.

However, when attempting to obtain cold temperature spectra for different molecules, the results were poor. An example of this is shown in Figure 3-16, for the infrared spectrum of the small molecule bromoform, $CHBr_3$, from 3042.5 to 3055.0 cm^{-1} incorporating the fundamental 1_0^1 vibrational transition. The room temperature spectrum (grey, left *y*-axis) has a strong absorption peak value of 8.5×10^{-3} at approximately 3048 cm^{-1} and with an approximate FWHM of 1 cm^{-1} which incorporates many rovibrational transitions. However, the corresponding peak in the cold spectrum (red, right *y*-axis, taken with the 20 Hz acquisition method) is weaker with an absorption peak of 3.58×10^{-5}, and an approximate FWHM of 0.03 cm^{-1}. This smaller FWHM is due to the decrease in rotational states in the ground state of $CHBr_3$, causing there are fewer rovibrational transitions at colder temperatures. In addition, the SNR of the two spectra can be compared, where the room temperature data has a value of 128.6 and the cold temperature has a value of 3. Within Figure 3-16 the red peaks along the baseline of the spectrum are attributed to noise. The low SNR for the cold spectra means that the peak can only just be classified as an absorption peak, if the assumption is made that the peak intensity must be three times greater than the baseline noise, σ. However it is difficult to fully compare the two spectra as they are acquired with varying concentration and path lengths: room temperature data have a concentration of approximately 24.5 mbar and a path length of 430 cm, cold temperature data have an unknown concentration and an unknown path length. However, information is known about the sample used to supply the free-jet expansion pulse valve. A liquid sample of $CHBr_3$ was soaked in an approx. 20 cm^3 piece of glass wool, which was placed directly before the pulsed valve in a sample cup holder. At room temperature, the saturated vapour pressure of $CHBr_3$ is approximately 6.7 mbar at room temperature. A flow of pure N_2 at a pressure of approximately 2000 mbar was passed over the glass wool, giving a 0.3 % mix of $CHBr_3$ in N_2.

Using the $CHBr_3$ spectrum as a guide for other molecules, predications can be made for the cold spectra of CH_2I_2 and CH_2Br_2 based on their respective absorption cross sections, σ_ν. Although, as the temperature of the molecule decreases the maximum σ_ν for a particular vibrational transition will change, literature σ_ν values for CH_2I_2 and CH_2Br_2 at lower temperatures (< 298 K) do not exist. Therefore, assumptions will be made in the following analysis. For the main peak at 3048 cm^{-1} in the $CHBr_3$ fundamental ν_1 vibrational spectrum, the maximum σ_ν at room temperature is approximately 2.5×10^{-19} cm^2 $molecule^{-1}$. However, the peak observed in the cold spectra, is just above the minimum we can observe, assuming the peak has a minimum absorption of 3σ above the baseline noise. For CH_2I_2 and CH_2Br_2, the room temperature maximum σ_ν values are 2×10^{-20} cm^2 $molecule^{-1}$ and 1×10^{-20} cm^2 $molecule^{-1}$, respectively. Therefore, if similar experimental conditions are applied, we do not anticipate seeing any peaks in the spectrum for the 20 Hz acquisition method of either molecule. This held true when initial experiments were performed. Furthermore, moving to the 100 Hz acquisition method for CH_2I_2 and CH_2Br_2 did not yield any observable peaks. Efforts where then made to attempt to increase the % concentration of both samples before the free-jet expansion. Using the same glass wool method as used for the $CHBr_3$ spectrum, heating tape was applied around the outside of the sample cup containing the sample. Heating the sample with the tape increase the saturated vapour pressure of the sample and thus increases the % mix of the sample within the bath gas flow. However, this method proved futile and did not yield any observable peaks. Hence, the future work of moving to an enhancement cavity. It is impossible to increase the σ_ν of the molecules, the total concentration within the free-jet cannot be held higher than the average of 2×10^{-4} mbar (due to how the free-jet expansion apparatus operates), and so we the path length needs to be significantly increased. This enhanced cavity is further discussed in section 7.1.1.

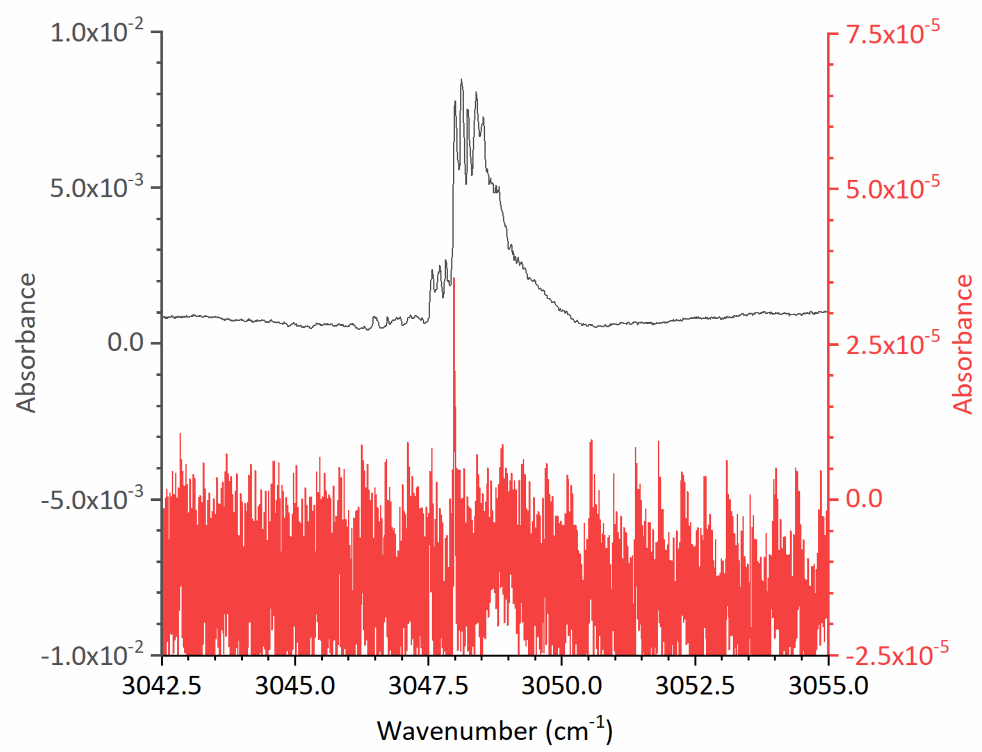

Figure 3-16 $CHBr_3$ 300 K and ~40 K Comparison Spectra. $CHBr_3$ fundamental C-H vibrational spectrum from 3042.5 to 3055.0 cm^{-1}. The grey spectrum was acquired at 300 K with a $CHBr_3$ concentration of approximately 24.5 mbar and a path length of 430 cm, and corresponds to the left *y*-axis. The red spectrum was acquired at approximately 40 K with an average $CHBr_3$ concentration of 2×10^{-4} mbar and an unknown path length, and relates to the right *y*-axis.

3.7. Conclusion

This chapter, alongside the previous chapter, has shown the work undertaken to build, characterise and commission a new frequency comb spectrometer. Such building of the spectrometer included aligning the VGC detector set-up, developing the analysis *MATLAB* code, and understanding the contribution of noise to the spectrometer. For the spectrometer presented in this thesis, the ILS is calculated to be 0.0142 cm^{-1}. Furthermore, considering the specifics of the spectrometer and analysis method, the average baseline noise for 2000 images averaged together is 1.20×10^{-4}, whereas for 190 images the baseline noise is 5.79×10^{-4}. In addition, based on these baseline noises, the minimum observable concentration for methane is $[CH_4]_{min} = 1.7 \times 10^{11}$ molecule cm^{-3}. Finally, the NEA^{1s} for 190 images is 9.8×10^{-8} cm^{-1} Hz$^{-1/2}$, which is comparable to other spectrometers. Furthermore, efforts were made to build a free-jet expansion apparatus in order to record cold temperature mid-IR spectra. However, although the current cold spectra results showed promise, they currently not useable due to poor SNR and an inability to observe low concentrations of the sample molecules.

4. Rovibrational Absorption Spectroscopy of CH_2I_2 from 2960 to 3125 cm^{-1}

This chapter covers the work undertaken to record a mid-IR spectrum of CH_2I_2 from 2960 to 3125 cm^{-1} and determine the spectroscopic constants of the two measured vibrational states, ν_6 (v = 1) and ν_1 (v = 1). In addition further spectroscopic constants for measured for the combination states ν_6 (v = 1) + ν_4 (v ≤ 5) and ν_1 (v = 1) + ν_4 (v ≤ 4) which arise from population in the ν_4 (v ≤ 5) vibrational states. The effects of pressure broadening on the observed rovibrational transitions are also reported here. In addition, computational studies of CH_2I_2 are undertaken to allow comparison between semi-empirical simulated spectra and the experimental spectrum. The majority of the work presented in this chapter has already been published: Roberts, F.C. and J.H. Lehman, *Infrared frequency comb spectroscopy of CH_2I_2: Influence of hot bands and pressure broadening on the ν_1 and ν_6 fundamental transitions.* The Journal of Chemical Physics, 2022. **156**(11): p. 114301, and any figures and results are reproduced here with the permission of AIP Publishing.

4.1. Background of CH_2I_2

In recent years, the understanding of CH_2I_2 contributing to the global iodine budget has grown in significance. In particular, CH_2I_2 is known to be a significant contributor to the global iodine budget at coastal locations and in the marine boundary layer, with average mixing ratios ranging from 0.1 pptv around the west coast of Ireland, [27] to 0.001 pptv around Cape Verde in the North Atlantic Ocean. [28] By itself, diiodomethane in the atmosphere has limited impact due to its short atmospheric lifetime of 2 to 10 minutes. [80, 238] This short lifetime is due to the rapid photolysis of the molecule to form CH_2I and I. It is these products, in particular the iodine radical, that then react in the atmosphere and interrupt important processes such as the tropospheric HO_x and NO_x cycles, whilst also contributing to stratospheric ozone depletion and aerosol formation: [239-243]

$$CH_2I_2 + h\nu\ (< 320\ nm) \rightarrow CH_2I + I$$ **Reaction 4-1**

$$I + O_3 \rightarrow IO + O_2$$ **Reaction 4-2**

$$IO + HO_2 \rightarrow HOI + O_2$$ **Reaction 4-3**

$$IO + NO_2 \rightarrow IONO_2$$ **Reaction 4-4**

In addition to its atmospheric influence, CH_2I_2 is commonly used in laboratory experiments to generate the simplest Criegee intermediate CH_2OO. This is achieved through the reaction of CH_2I and O_2. [244] However, despite its atmospheric and laboratory experimental importance, fundamental spectroscopic studies of CH_2I_2 are scarce, particularly in the infrared. Justifiably, there is a plethora of studies surrounding the electronic spectroscopy and photolysis pathways of CH_2I_2 (for example, references [80, 82, 101-104] and references therein). However, due to the dissociative nature of the excited electronic states, most of these studies do not contain much spectral information outside of absorption cross section values. For rotational spectroscopy, there have only been two significant studies by the same research group. [105, 106] Despite there only being two studies, useful rotational constants have been reported for the ground state (v = 0) and the ICI bending mode ν_4 (where v ≤ 4), all of which were necessary to include in the analysis of the rovibrational spectrum reported in this thesis.

Moving onto vibrational spectroscopy, there has been one recent (2006) published study on the gas-phase IR spectrum of CH_2I_2. [95, 107] In addition, the work of Ford [108] reported some gas-phase vibrational frequencies, however only five out of the nine fundamental transitions were recorded (ν_9, ν_7, ν_8, ν_2, and ν_6, see Table 4-1). However, there are other studies covering solid state, [75, 109, 110] liquid, [108, 111, 112] and computational results [113] for vibrational spectroscopy. A comprehensive table collecting all the vibrational frequencies for the nine different fundamental modes of CH_2I_2 is presented here (Table 4-1). Focusing firstly on the gas-phase IR literature, there have been two recorded spectra at temperatures 298.15 K and 323.15 K, [95, 107] and measured σ_ν from 530 to 7100 cm^{-1}. These two spectra are included in the *HITRAN* database. [216] The spectrum recorded at 298.15 K is used as a reference spectrum for this work and is referred to as such in this chapter. However, both of the spectra in the *HITRAN* database were recorded at atmospheric pressure, meaning the observed peaks are broadened due to the high pressure. This broadening means no upper vibrational state rotational constants can be confidently measured, and the reported information is limited to band origins and σ_{ν}. A third study has been found, [245] in which the IR spectrum of gas phase CH_2I_2 was recorded from 2250 to 3400 cm^{-1} with a spectral resolution of 0.002 cm^{-1}. However, this study remains unpublished (and thus not peer-reviewed) and the only information available is from presentation slides where rotational constants for the ν_6 (v = 1) and ν_1 (v = 1) vibrational states were extracted.

Theoretical studies are fairly limited on CH_2I_2 vibrational spectroscopy, however, one particular study [113] used the internal coordinate model to calculate anharmonic vibrational frequencies of fundamental and overtone bands, which did show good agreement between theory and observations. Some vibrational information for CH_2I_2 can be found within references that focus on the influence of vibrational relaxation and redistribution within electronic energy levels. However, these types of studies do not list rotational constants of specific vibrational states. [102, 246] Solid state IR spectra, mainly involving the adsorption of CH_2I_2 onto a surface, have demonstrated two different phase forms of the molecule is possible on surfaces. [75, 109, 110] These works then led to two different observed frequencies for each observed normal mode. However, while these studies are broadband, and so report transition wavenumbers for many normal modes, the studies are typically of low resolution (4 cm^{-1}) and therefore does not contribute largely to understanding the more minute points of the IR spectra. In addition, while there have been more studies of CH_2I_2 in the solution phase than solid phase, this did not results in significant improvement to the understanding of the fundamental vibrational modes. The work of Plyler [112] and of Voelz [111] simply report low resolution spectra alongside a list of the fundamental transition wavenumbers. Furthermore, many liquid IR experiments only utilise IR based techniques to observe vibrational relaxation and energy transfer in solution after electronic excitation rather than focusing on the fundamental IR spectroscopy. [247-251]

Considering all the previous spectroscopic studies of CH_2I_2, predictions can be made for the high resolution spectrum we wish to obtain. As CH_2I_2 is a monoisotopic molecule, the spectrum and consequent rovibrational assignment should remain simple. Furthermore, there is a trend amongst the di-halogenated molecules that coupling and resonances are weaker with increasing weight of the molecule, such that spectra of CH_2F_2 molecules observe strong coupling and resonances, whereas the opposite should be true for CH_2I_2. [73] Therefore, the two expected observed fundamental bands, ν_1 and ν_6, of CH_2I_2 should be free of couplings and resonances.

Table 4-1 Literature CH_2I_2 Fundamental Vibrational Band Origins. Collection of available all fundamental normal vibration transitions in cm^{-1}.

	Symmetry	Gas Phase	Liquid Phase	Solid State	Computational
ν_4	a_1	….	121[a] 125[b]	….	127[c]
ν_3	a_1	493.01[a]	485[a] 481[b] 445[c] 486[d]	484[e] 484[f]	494[h] 487[c]
ν_9	b_2	584.21[a] 585[b]	571[a] 564[b] 577[c] 572[d]	570[e] 574[f]	584[h] 567[c]
ν_7	b_1	718.08[a] 717[b]	717[a] 714[b] 717[c] 717[d]	716[e] 733[f] 719[g*], 729[g†]	716[c]
ν_5	a_2	1041.99[a]	1033[a] 1033[b] 1034[c] 1035[d]	1031[e] 1036[f]	1028[c]
ν_8	b_2	1113.87[a] 1113.5[b]	1106[a] 1104[b] 1105[c] 1182[d]	1105[e] 1104[f] 1100[g*], 1082[g†]	1164[h] 1105[c]
ν_2	a_1	1373.61[a] 1230[b]	1352[a] 1351[b] 1350[c] 1351[d]	1350[e] 1349[f]	1351[c] 1348[c]
ν_1	a_1	3002.00[a]	2968[a] 2961[b] 2967[c] 2967[d]	2967[e] 2964[f] 2959[g*], 2953[g†]	2993[h] 2968[c]
ν_6	b_1	3073.01[a] 3074[b]	3046[a] 3036[b] 3051[c] 3049[d]	3047[e] 3044[f] 3041[g*], 3035[g†]	3072[h] 3050[c]

a. Ref. [107]
b. Ref. [108]
c. Ref. [111]
d. Ref. [112]
e. Ref. [110], Crystal Form I
f. Ref. [75]
g. Ref. [109], * is Phase I, † is Phase II
h. Ref. [113]

4.2. Experiments

4.2.1. 300 K Rovibrational Spectrum

For the room temperature spectrum of CH_2I_2, the apparatus described in chapter 2.2 was used. The Herriott multipass flow cell was aligned to a path length of 570 ± 60 cm, as determined using a known concentration of CH_4. The full mid-IR spectrum was recorded from 2960 to 3125 cm^{-1} using six different diffraction grating positions (also known as windows). For each window, three different repetition rates of the frequency comb laser were selected: 249.9999 MHz, 250.0000 MHz, and 250.0001 MHz. This yields a data point separation of 0.0028 cm^{-1} once the three individual spectra are interleaved. The three different repetition rates are useful for seeing some finer structure within individual peaks, but it was not wholly necessary to acquire. For each window, and for each repetition rate, 10,000 images (collected with a 50 µs integration time, 125 Hz camera frame rate) were averaged together for both the signal (CH_2I_2 sample present plus Ar buffer gas) and background (N_2 only). Comparable data was collected to obtain a CH_4 spectrum for each window and repetition rate in order to frequency calibrate the CH_2I_2 spectrum. This comparable data comprises of 2000 images averaged together for both signal (CH_4 present) and background (N_2 only), with a camera integration time of 50 µs and a 125 Hz camera frame rate.

For each background acquisition, a pure flow of N_2 is used with a total pressure in the flow cell of approximately 10 mbar. This background pressure was kept similar to the sample pressure in order to minimise scattering effects. For each sample acquisition, a mixture of Ar and CH_2I_2 is used: a low pressure of Ar is passed over a liquid sample of CH_2I_2 (Sigma Aldrich, 99% pure) and an MFC and vacuum pump controls the flow into the cell for a total pressure of 11.3 ± 0.3 mbar. As the vapour pressure of CH_2I_2 is low at room temperature (1.6 mbar at 298 K), [252] the sample was heated within the sample container (Teflon PTFE coated), to approximately 313 K yielding a vapour pressure of 6.15 mbar. However, this method lead to a high level of uncertainty in the vapour pressure of CH_2I_2 and the specific partial pressure of the sample within the flow mixture. Firstly, as the Teflon lined sample container is not an effective thermal conductor, the temperature of the water bath (313 K) is not an accurate indication of the temperature of the liquid sample within the sample cup. Secondly, the distance between the flow cell and the sample cup is approximately 2 m of Teflon tubing, so the probability of losing sample to deposition on the walls is high. Supposing that the sample temperature is known exactly and that there is no loss to the walls, the concentration of CH_2I_2 would be $(2.29 \pm 0.05) \times 10^{16}$ molecule cm^{-3}.

However, comparing the reported σ_ν from the reference spectrum available in *HITRAN* [216] to the experimental spectrum gives a factor of approximately 3.7 difference between the $\int\sigma_\nu$ (integrated absorption cross section) in the region 2965.1 to 3025.0 cm^{-1}: 1.81×10^{-20} cm^2 molecule^{-1} for our work and 6.74×10^{-20} cm^2 molecule^{-1} for the reference spectrum. Moreover, the factor is increased to 4.5 for the full spectrum (from 2936.3 to 3125.4 cm^{-1}), with the experimental spectrum giving a total $\int\sigma_\nu$ of 1.08×10^{-19} cm^2 molecule^{-1} and 4.87×10^{-19} cm^2 molecule^{-1} for the reference spectrum. The difference between these two factors can be attributed to a combination of recording the wrong concentration of CH_2I_2 or having the wrong path length of the Herriot flow cell. In addition, a few negative absorption values which occur in the baseline of the experimental spectrum could contribute to the differences. As the path length of Herriott flow cell in our apparatus is determined to a high level of uncertainty (as calculated through spectral analysis of a known concentration of CH_4), it is unlikely this is the cause of the large difference in $\int\sigma_\nu$. Therefore, the biggest contributor to the reported difference is the uncertainty in the concentration of CH_2I_2.

For the reference spectrum, [107] there was a strong attention to detail when designing the delivery method to ensure little sample loss between the syringe pump and the measurement cell used in the experiment. [253] Although this study uses 2-propanol instead of CH_2I_2 to study the effectiveness of the delivery method, the logic remains. This method involved heating the connecting parts between the sample and the measurement cell, and using a disseminator head. This delivery method then led to a less than 1% difference between the calculated and measured concentrations for 2-propanol. Therefore, the reported σ_ν can be considered as significantly accurate, and can be used to "correct" the concentration of CH_2I_2 used in this experiment. Using an average of the two factors reported above (3.7 and 4.5), the concentration of CH_2I_2 in the experimental spectrum can be corrected to give a lower limit of $(6.8 \pm 1.3) \times 10^{15}$ molecule cm^{-3}. Use the ideal gas law, this would correspond to a sample temperature of 297 K. However, as we observe an increase in peak intensity with the IR spectrum when using the water bath method, the uncertainty of the temperature of the liquid sample would not account for the four factor difference. Therefore, loss of sample to the walls is also contributing to the discrepancy, however this cannot be quantitatively determined. Thus, the right *y*-axis (σ_ν in cm^2 molecule^{-1}) for the spectrum shown in Figure 4-1 has been calculated using the corrected CH_2I_2 concentration. The error of the σ_ν has also been calculated, using the error in the concentration and the error in the cell path length, yielding an overall error of 11.6% (seen as the grey trace in Figure 4-2 inset i).

As discussed in chapter 3.2, the images collected for each window are transformed into spectra using the *MATLAB* code and then frequency calibrated using the acquired CH_4 spectra. Before the individual experimental spectra for each repetition is interleaved, each spectrum underwent a fast Fourier transform band-pass filtering at 840 MHz. This 840 MHz noise manifested itself in the baseline of the spectra (no dependence on sample being present), and is caused by unknown source, but is generally used for broadcasting and mobile services. [254] Removing the 840 MHz noise reduced the baseline noise from 4.92×10^{-4} to 2.35×10^{-4}. Next, the individual spectra are baseline subtracted due to the drift in laser intensity across the course of an experiment. After the baseline subtraction, the three different spectra corresponding to the three different repetition rates for each window are interleaved. Finally, the six interleaved spectra are concatenated together to give one full and final spectrum from 2960 to 3125 cm^{-1}. Where different windows of spectra overlap, the spectra are averaged together to give an average of 7 cm^{-1} overlap between adjacent windows.

4.2.2. Pressure Broadening

To investigate the effect of pressure broadening on the observed peaks within the CH_2I_2 spectrum, two experiments were performed, both within the flow cell. In these experiments a sample of CH_2I_2, with the concentration kept approximately constant at $(2.7 \pm 0.5) \times 10^{14}$ molecule cm^{-3}, was recorded in a mixture with either N_2 or Ar at various pressures from 20 to 1000 mbar. For each total pressure mixture, the concentration of CH_2I_2 was controlled by the 30 sccm MFC and the bath gas was controlled by either the 500 or 1000 sccm MFC. In addition, to reach pressures beyond 100 mbar, the needle valve after the gas cell was slowly closed in order to increase the pressure within the flow cell. Each different total pressure was recorded from 3052 to 3070 cm^{-1}, however the analysis was only performed from 3056.5 to 3069.0 cm^{-1}, which incorporated 9 different Ka transitions within the ν_6 vibrational band. To keep the analysis simple, only one repetition rate, 250.0000 MHz, was used.

After the spectra were acquired, the overall Lorentzian broadening parameter for each bath gas was determined using contour fitting in *PGOPHER* (as described in section 3.3.1). Further analysis was then undertaken which is described in section 4.3.2 alongside the final results.

4.2.3. Computational Calculations

In order to validate the proposed assignment of the full spectrum (see section 5.3.1), computational calculations were undertaken to acquire anharmonic vibrational frequencies and spectroscopic rotational constants. Due to the lack of appropriate basis sets which can handle the heavy element iodine, only two suitable basis sets were used: a Karlsruhe Def2QZVPP [255] and MidiX. [256] In particular, the Def2QZVPP basis set is one of the most extended basis sets, can be used with a wide range of atoms (H to La, and Hg to Rn), and can nearly reach the DFT basis set limit, but is computationally faster than coupled-cluster basis sets which are generally considered to be the best basis set. In addition, the use of effective core potentials within this basis set helps to reduce the number of basis functions and ensures heavier atoms are sufficiently accounted for within the electronic structure calculation. On the other hand, MidiX is a Slater-Type orbital basis set and can only be used with a handful of atoms (H, C to F, S to Cl, Br, and I). However, this basis set was specifically created to produce optimized results for non-metal atoms, with a specific emphasis on biological functional groups. Despite being a small basis set, the results can be considered highly accurate, especially when comparing the results to other basis sets. [256] Although they are typically used as an initial calculation step as they are efficient and cheap, no Pople basis sets were able to be utilized for the electronic structure calculations of CH_2I_2. This is due to the Pople basis sets not being optimised for heavier atoms, and the highest level basis set of 6-311G is only valid for atoms H to Kr. [257]

However, several levels of theory have been shown to work well with iodine-containing molecules, so 5 different methods were selected: wB97X, M062X, B3P86, B3LYP, and MP2. This gave the calculation pairs: wB97X/Def2QZVPP, M062X/Def2QZVPP, B3P86/Def2QZVPP, B3LYP/Def2QZVPP, and MP2/MidiX. All calculations were performed in Gaussian 09 using a tight anharmonic setting. [234] In addition, all Gaussian calculations were undertaken by Dr Lehman, and only the output files were used for the analysis here. The appropriate semi-empirical rotational constants were calculated using the method described in section 3.3.2. Briefly, the Δ_i value between the upper and lower calculated rotational constants is determined, and this Δ_i can be added to the experimentally determined rotational constants. This semi-empirical method was adapted from work published by Sadiek and Friedrichs. [93]

4.3. Results and Discussions

4.3.1. 300 K Rovibrational Spectrum

Figure 4-1 shows the full acquired rovibrational spectrum for CH_2I_2 from 2960 to 3125 cm^{-1} incorporating two fundamental vibrational transitions: ν_1 and ν_6. The left-hand *y*-axis of the spectrum is absorption, as measured in this experiment, defined as $\ln(I/I_0)$. The right-hand *y*-axis is given in $\sigma_{\tilde{\nu}}$ (cm^2 $molecule^{-1}$), as defined in the *HITRAN* database:

$$\sigma_{\tilde{\nu}} = \frac{\ln(\tau_{\tilde{\nu}})}{\rho L}$$ ***Equation 4-1***

where $\sigma_{\tilde{\nu}}$ is the absorption cross section (cm^2 $molecule^{-1}$) at wavenumber $\tilde{\nu}$, τ is the spectral transmittance at $\tilde{\nu}$, and ρ is the concentration (molecule cm^{-3}) along an optical path of length, L (cm). [216] In addition, Figure 4-1 inset (i) shows a 3 cm^{-1} portion of the spectrum, and inset (ii) shows the CH_2I_2 molecule superimposed on the rotational axis system used during the analysis. CH_2I_2 is a near prolate asymmetric top molecule with C_{2v} symmetry, with a κ value of −0.9986, using Equation 1-91, as calculated using the ground vibrational state rotational constants, measured in reference. [106]

As stated above, the acquired spectrum covers two fundamental vibrational transitions: ν_1 from 2967 to 3032 cm^{-1} and ν_6 from 3032 to 3115 cm^{-1}. The ν_1 normal mode can be described as the symmetric C-H stretch and the ν_6 normal mode is the anti-symmetric C-H stretch, both of which involve the CH_2 moiety. Firstly, the ν_1 band is a *b*-type transition with a_1 symmetry, which manifests itself with well-defined ${}^{P/R}Q_{Ka}(J)$ branches and no central Q branch. Conversely, the ν_6 band is a *c*-type transition with b_1 symmetry and has a strong, central Q branch alongside well-defined ${}^{P/R}Q_{Ka}(J)$ branches. To determine the band strength ratio between the two modes, the $\int\sigma_\nu$ areas are calculated. For ν_1 this value is 7.32×10^{-20} cm^2 $molecule^{-1}$ (from 2970.003 to 3028.001 cm^{-1}), and for ν_6 this value is 3.21×10^{-19} cm^2 $molecule^{-1}$ (from 3045.003 to 3099.999 cm^{-1}). These regions do not cover the whole of the bands in order to exclude water impurity peaks and avoid the overlapping region of the two bands around 3032 cm^{-1}. Therefore, the band strength ratio is 1:0.23 for ν_6:ν_1 which agrees well with the reference data. In the case of the reference data, [95, 107] for ν_1 (from 2970.00 to 3028.03 cm^{-1}) the $\int\sigma_\nu$ is 7.03×10^{-20} cm^2 $molecule^{-1}$, and for ν_6 (from 3045.02 to 3099.98 cm^{-1}) the integrated value is 3.63×10^{-19} cm^2 $molecule^{-1}$. This gives a band strength ratio of 1:0.19 for ν_6:ν_1.

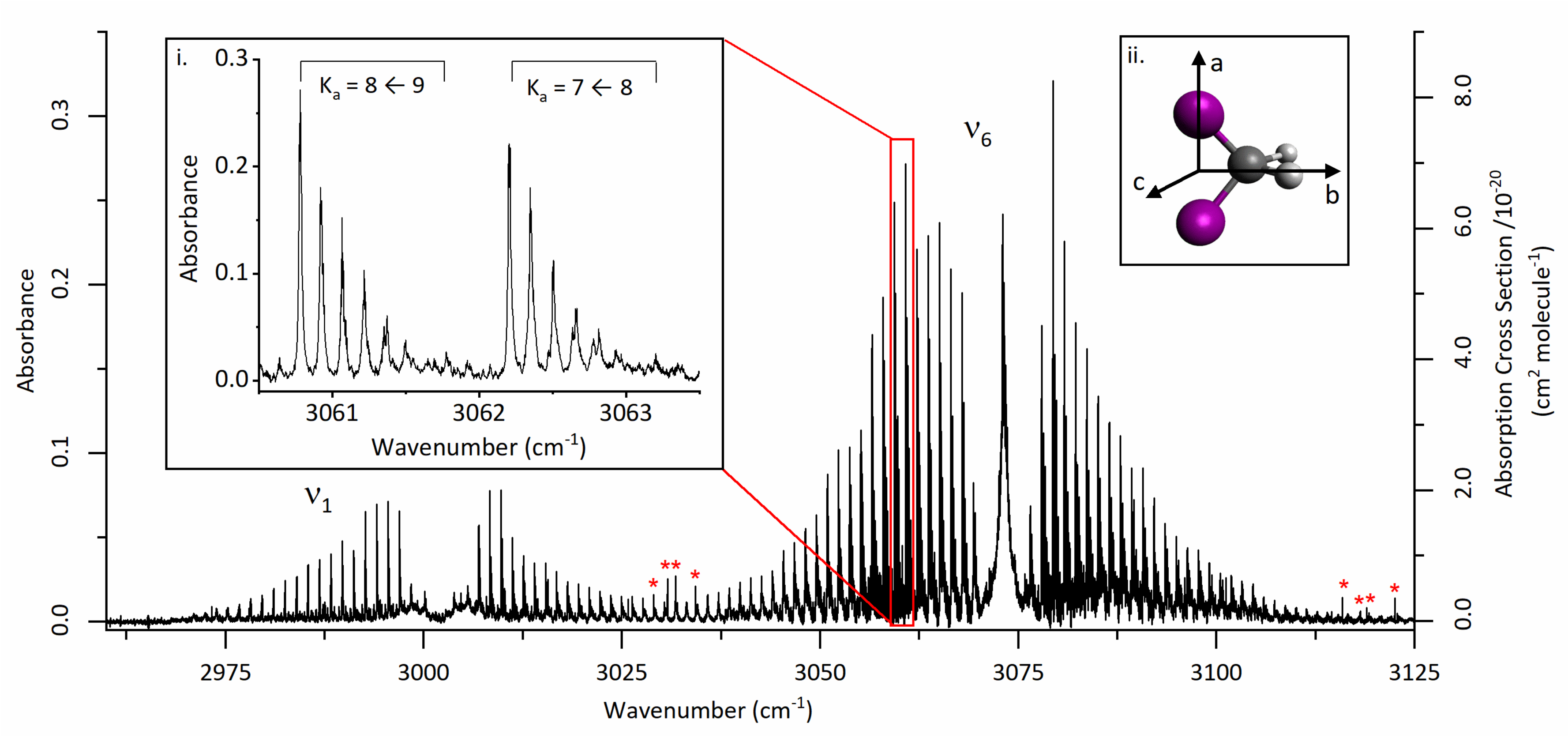

Figure 4-1 Full Experimental CH_2I_2 Spectrum. The full experimental vibrational spectrum from 2960 to 3125 cm^{-1}, acquired under the conditions: 298 K, path length of 570 ± 60 cm, CH_2I_2 partial pressure of 0.28 ± 0.05 mbar, total pressure of 11.3 ± 0.1 mbar. Red asterisks indicate water impurities within the spectrum. The left *y*-axis shows the absorbance measured in this thesis, and the right *y*-axis shows absorption cross section (cm^2 molecule^{-1}). (i) Zoomed in portion of the ν_6 spectrum from 3060.5 to 3063.5 cm^{-1}, showing two K_a transitions (8 ← 9 and 7 ← 8). (ii) Molecular structure of CH_2I_2 (iodine = purple, carbon = grey, hydrogen = white). The axes show the labels used for this analysis: the ν_6 asymmetric stretch causes a transition dipole moment (TDM) along the *c*-axis and the ν_1 symmetric stretch causes a TDM along the *b*-axis. This figure is reproduced from ref. [258] with the permission of AIP Publishing.

As seen in Figure 4-1 inset (i), there are many peaks within a vibrational transition. Each peak consists of many rotational transitions, which due to Doppler, pressure, and instrument line-shape broadening appear as one peak. The majority of this broadening is likely to be pressure broadening. However, there are too many peaks in the full spectrum which can be attributed to either of the fundamental vibrational transitions, even when considering the amount of possible rovibrational transitions. Looking at inset (i), this shows two different K_a transitions, where $K_a = 8 \leftarrow 9$ and $K_a = 7 \leftarrow 8$. While there should only be two peaks, one for each K_a transition, there are at least 6 peaks near each K_a transition. Hereafter, the repeating stacks of peaks within a K_a transition are referred to as progressions. For the reference data, [107] as the spectrum was recorded at atmospheric pressure, the individual peaks in the progressions are not visible. This is due to the peaks convolving into one single broad peak (average FWHM of 0.3 cm^{-1}), albeit with an asymmetrical line-shape. This is further visible in Figure 4-2, where the reference spectrum (red line) is overlaid on the experimental spectrum (black line).

However, the peak progressions have been seen before in a previous high resolution study of CH_2Br_2. [93] In this case, at least 4 peaks are visible within each K_a progression. For this study, the progressions are attributed to the three isotopologues of CH_2Br_2. However, this argument fails for CH_2I_2, due to the monoisotopic nature of iodine. Consequently, a different hypothesis is needed to explain the peak progressions seen in the experimental spectrum. The two following sections describe the fitting of each fundamental vibrational band, and offers an explanation as to the source of the additional peaks within the peak progressions.

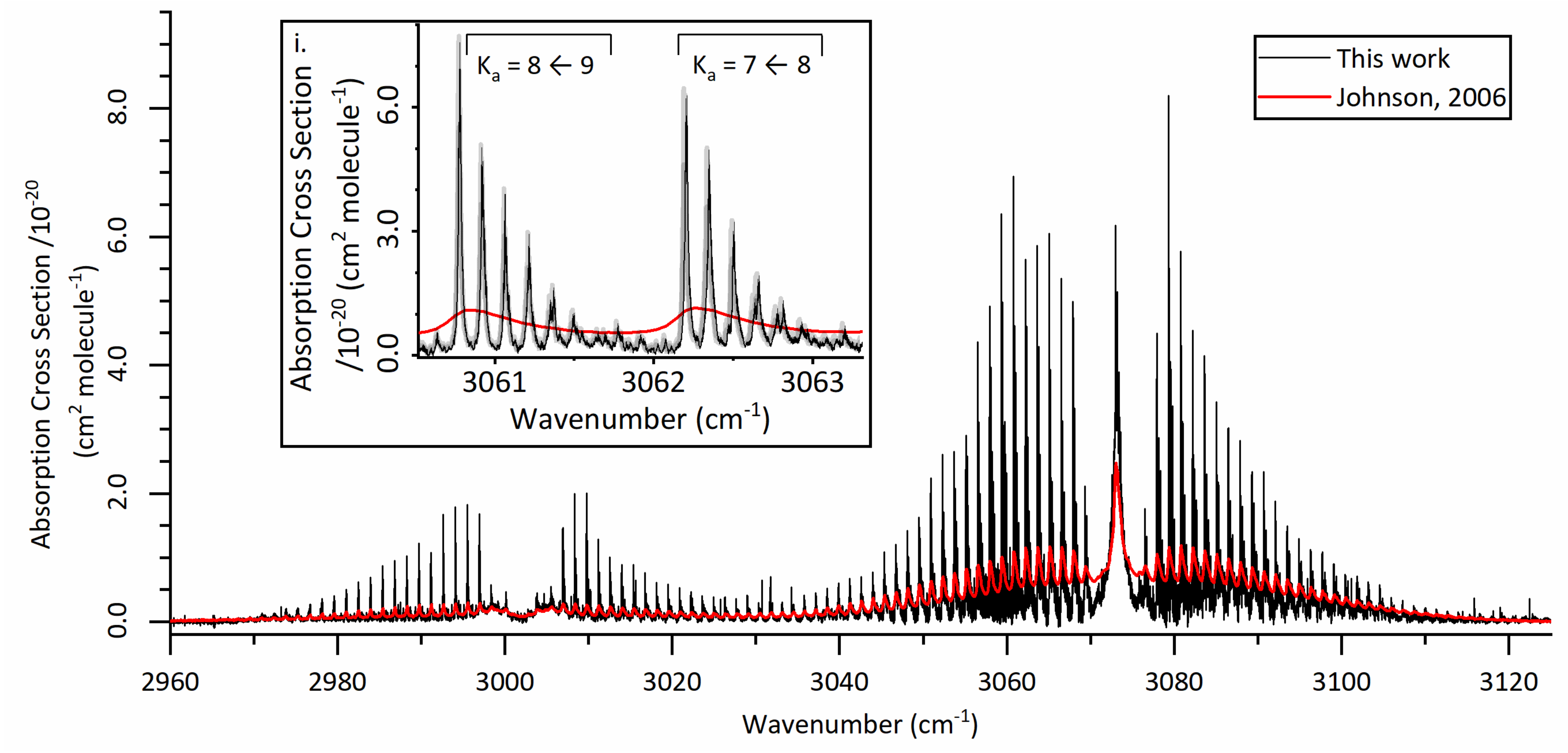

Figure 4-2 Comparison of Experimental and Reference Spectra of CH_2I_2. Experimental spectrum in black from 2960 to 3125 cm^{-1}, and corresponding portion of the reference spectrum in red. [107] (i) Zoomed in portion of the two spectra from 3060.5 to 3063.3 cm^{-1}, showing two K_a transitions (8 ← 9 and 7 ← 8). The grey shading shows the error of the black experimental spectrum as determined by the path length and concentration of the sample. This figure is reproduced from ref. [258] with the permission of AIP Publishing.

4.3.1.1. Fitting results of the ν_6 band

For the ν_6 vibrational band, the discernible peaks span 3032 up to 3115 cm^{-1}, with the band origin at 3072.906(3) cm^{-1}. Approximately 210 peaks in this band are detectable, which assumes a minimum detectable absorption of 3σ above the baseline noise ($\sigma = 2.4 \times 10^{-4}$). These peaks involve a strong central Q branch and $^{P/R}Q_{Ka}(J)$ branches which are spaced by approximately $2(A-\overline{B})$. For a *c*-type transitions such as this, and using the inertial axes as labelled in Figure 4-1 inset (ii), the rotational selection rules are: $\Delta J = 0, \pm1$, $\Delta K_a = \pm1$, and $\Delta K_c = 0, \pm2$. Due to broadening of the observed transitions, each peak is a combination of many transitions, where there are different J and K_c transitions, but the same K_a transition occurs for each peak. For example, the peak at 3068 cm^{-1} is attributed to the $K_a = 3 \leftarrow 4$ transition in the P branch, which is made up of rotational transitions from different J and K_c rotational states but still have the same $K_a = 3 \leftarrow 4$ transition.

In order to fit the experimental spectrum and determine the rotational constants of the ν_6 (v = 1) vibrational state, *PGOPHER* was used as described in section 3.3.1. For this fitting procedure, the origin, A, $\overline{B}$, δ, D_J, D_{JK}, and D_k constants for the ν_6 (v = 1) state were fitted using the band-head fitting procedure (as described in section 3.3.1) and using Watson's *S* reduction Hamiltonian. Within some literature, the alternative Watson's *A* reduction Hamiltonian is used. However, investigations of the two different Hamiltonians on the fitted spectrum, produced no significant differences. [259] Higher level distortion constants (d_k, d_J, H_K, H_{KJ}, H_{JK}, H_J) were also included in the simulations for the lower and excited vibrational states. However, these constants were not fitted due to a lack of appropriate higher K_a transitions. While values of these higher level constants are only shown in Table 4-2 for the ground (v = 0) state and the ν_6 (v = 1) state, the constants are held the exact same for all vibrational states included in the simulation. For the simulation presented in Figure 4-3, the temperature was set to 300 K, the Gaussian broadening parameter was 0.0029 cm^{-1}, and the Lorentzian broadening parameter was set to 0.0149 cm^{-1}. For the 6_0^1 band, the results of the fitted rotational constants for each vibrational state are produced in Table 4-2.

While the initial simulation of the 6_0^1 band produced a good similarity between the highest intensity peak in each peak progression between the experimental spectrum and corresponding peaks in the simulation, the additional peaks within the K_a progressions were not captured. Therefore, further analysis was needed to understand which vibrational transitions were causing the additional extra peaks within the progressions. Taking into account all nine fundamental normal mode vibrations of CH_2I_2 (see Table 4-1), there are no obvious overtone or combination bands which would cause visible absorption peaks from 2960 up to 3115 cm^{-1}. However, the lowest energy fundamental vibrational transition is the ν_4 ICI bending mode, with a transition wavenumber of 121 cm^{-1} for liquid IR studies. [107] Unfortunately, the fundamental ν_4 vibrational transition is yet to be observed in the gas phase. The energy of this fundamental vibrational transition is lower than the available thermal energy at room temperature ($k_BT \approx 200$ cm^{-1}). Therefore, it is reasonable to assume that the ν_4 (v = 1) state has population during the course of the experiment. Higher vibrational states of the ν_4 could also be populated due to the available thermal energy being a distribution of values, rather than a fixed energy. This theory is further bolstered as the initial rotational spectroscopy experiment [105], witnessed peaks within their microwave spectrum which could be attributed to the first four vibrational states of ν_4. This lead to their second work, in which the rotational constants of the first four ν_4 states were calculated. [106]

PGOPHER automatically calculates the Boltzmann population distribution for the population residing in the ground state and the excited ν_4 states. However, the expected ratio for the ground state and the ν_4 v ≤ 4 states are: 1:0.56:0.32:0.18:0.10. The population residing in the ν_4 (v > 0) can then be excited with a transition frequency similar to that of the fundamental ν_6 transition. This means that the additional observed transitions are denoted $6^1_0 4^1_1$ for population initially in ν_4 (v = 1). These types of transitions are referred to as hot-bands as it requires the initial population to reside in a vibrational state other than the ground state, but are not considered combination bands, as only one vibrational quantum number is changed with the transition. However, cross anharmonicity terms are still present.

Using the rotational constants as determined in the microwave spectroscopy paper [106] for the ν_4 (v ≤ 4) states, and extrapolating to calculate the ν_4 (v = 5) state, the inclusion of the $6_0^1 4_n^n$ (n > 0) transitions (where the notation "n" is used in order to not be confused between ν and v, however n and v can be used interchangeably) shows a very good to the overall experimental spectrum (Figure 4-3). As for the ν_6 (v = 1) state, the origin, A, $\bar{B}$, δ, D_J, D_{JK}, and D_k constants were fitted for the ν_6 (v = 1) + ν_4 (v ≤ 5) vibrational states using the band-head fitting procedure. And as previously mentioned, the higher level distortion constants were held constant to match those in the ground state. The spectroscopic rotational constants for each vibrational state determined in the fitting procedure are shown in Table 4-2.

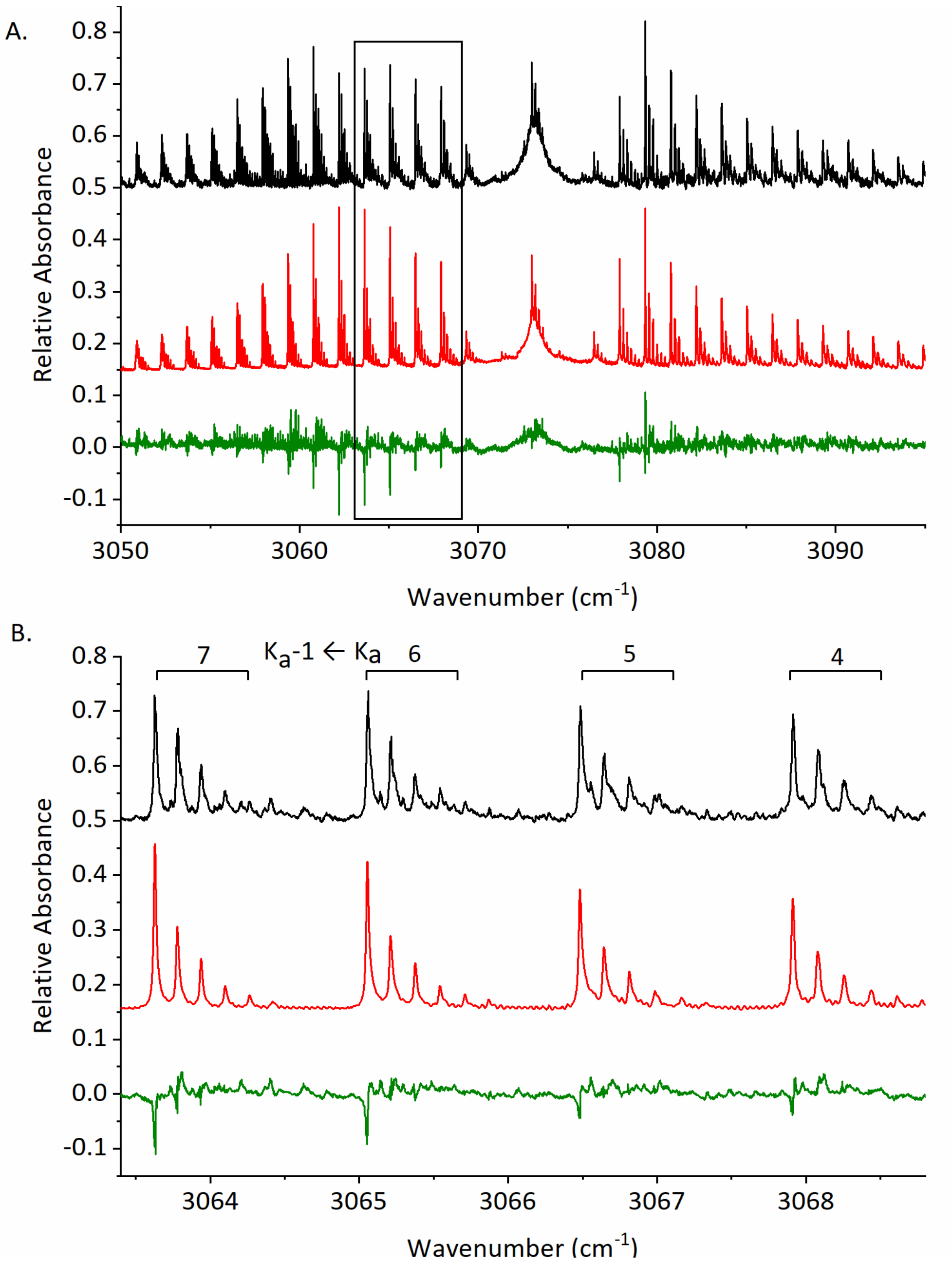

Figure 4-3 Comparison of CH_2I_2 ν_6 Simulation to Experimental Spectrum. A. Comparison of the experimental spectrum (black) and the overall simulation (red), as determined in *PGOPHER*, for the ν_6 band from 3050 to 3095 cm^{-1}. The overall simulation is comprised of the different simulated transitions for the fundamental 6^1_0 band and the $6^1_0\ 4^n_n$ hot bands, where $n \leq 5$. *Y*-axis shows relative absorbance of the experimental and simulation spectra, where the simulation has been scaled up to match the experimental. The green line is the residual plot of experimental minus the overall simulation. B. Zoomed in portion of the three spectra, from 3062.4 to 3068.7 cm^{-1} showing 4 different K_a transitions in the ^PQ branch. This figure is reproduced from ref. [258] with the permission of AIP Publishing.

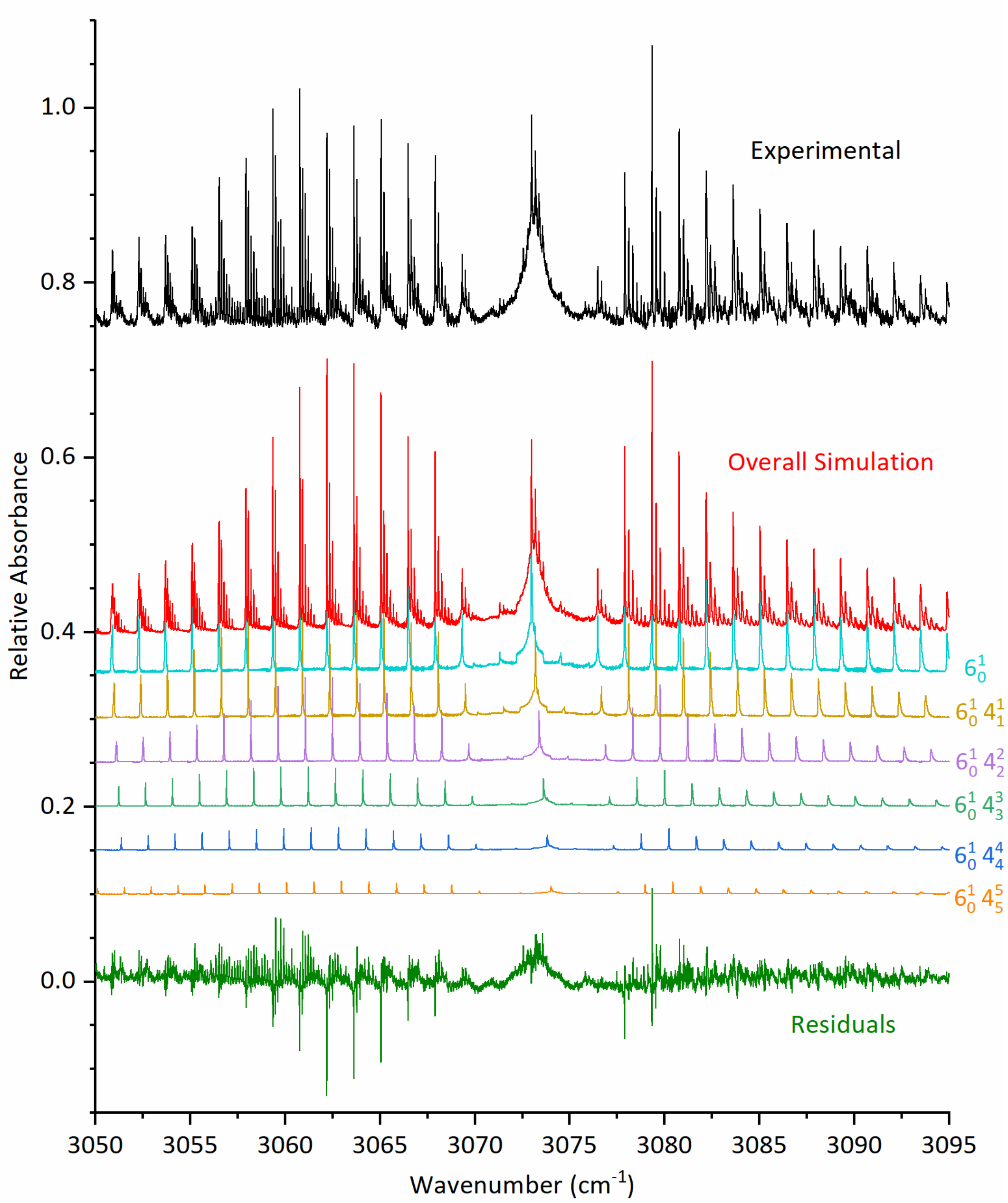

Figure 4-4 CH_2I_2 ν_6 Simulation Breakdown. Breakdown of the 6 different vibrational transitions which make up the *PGOPHER* simulation shown from 3050 to 3095 cm^{-1}: 6_0^1 (light blue), $6_0^1 4_1^1$ (yellow), $6_0^1 4_2^2$ (purple), $6_0^1 4_3^3$ (light green), $6_0^1 4_4^4$ (dark blue), $6_0^1 4_5^5$ (orange). Experimental spectrum (black), overall simulation (red), and residual plot (dark green) are also shown. This figure is reproduced form ref. [258] with the permission of AIP Publishing.

While Figure 4-3 shows the complete simulation, Figure 4-4 shows the breakdown of the different $6_0^1 4_n^n$ transitions included in the simulation. For the case of the ν_6 analysis, there are 6 vibrational transitions which can attributed to either the 6_0^1 fundamental transition or the $6_0^1 4_n^n$ up to n = 5 hot-band transitions. Both figures also show the residual plot (green line) between the experimental spectrum and the full simulation. While there is a general good agreement between the two spectra, there is a small mismatch in the observed relative intensities. The shape of the residuals indicate that the discrepancy is largely attributed to the peak intensity rather than a peak position or width mismatch. This is particularly noticeable in the ${}^{P}Q_{Ka}(J)$ branch between 3060 and 3070 cm^{-1}, and most notably for the 6_0^1 transitions as opposed to any of the hot-band transitions. As this region in particular region was also used for the pressure broadening analysis, many spectra were recorded in this range and the different spectra did not show significant difference in the relative intensities between peaks, specifically in the peak progressions. As the simulation is over-predicting the intensity, this indicates that there is a possible perturbation in the system that is not currently included in the simulation. Such perturbations could be arising from intensity borrowing by other vibrational transitions or by not correctly accounting for the spin of the iodine atoms.

Unfortunately, there are no current gas-phase studies which have observed the ν_4 ($v = 1 \leftarrow 0$) fundamental transition, so the transition energy for 4_0^1 was approximated to 121 cm^{-1}, as determined from liquid IR studies. Subsequent transitions are then approximated as integer multiples of 121 cm^{-1}. These chosen values do not significantly impact the simulated spectrum, as the excited state origins for ν_6 ($v = 1$) + ν_4 ($v \leq 5$) are fitted during the band-head fitting procedure. Therefore, the Δ_{origin} between the ν_4 ($v \leq 5$) and the ν_6 ($v = 1$) + ν_4 ($v \leq 5$) states is correctly determined. The only impact from approximating the ν_4 ($v \leq 5$) band origins is the intensity of the transitions, since these are dependent on the *PGOPHER* calculated Boltzmann population distribution, based on a rotational temperature of 300 K and the calculated line strengths, S. However, it is anticipated that the actual origin value in the gas phase is not too dissimilar from the liquid value, and so the population distribution of the different observed vibrational transitions will not drastically change. Unfortunately, as the vibrational quantum number does not change for ν_4 in the observed transitions, the vibrational band origins for 4_0^n cannot be calculated. However, two different assumptions can be made in an attempt to derive further vibrational origin information, though this only leads to the constraint that the difference between the cross anharmonicity constants, x_{64} and x_{14}, must be equal to 0.188(4) cm^{-1}.

In order to calculate an anharmonicity constant, a general equation to describe a vibrational energy level is first needed (adapted from Equation 1-77):

$$\begin{aligned} G(v_1 v_2 \ldots v_{3N-6}) \\ &= \sum_r \nu_r (v_r + 1/2) \\ &+ \sum_{r \leq s} x_{rs} (v_r + 1/2)(v_s + 1/2) \end{aligned}$$

Equation 4-2

After calculating the transition energy, ΔG, the cross-anharmonicity terms could be calculated, however, this requires that the initial vibrational state energy for ν_4 is known. For example, the transition energy for the $6_0^1 4_n^n$ transition is:

$$\Delta G = \nu_6 + 2x_{66} + 1/2 \sum_{s \neq 4,6} x_{6s} + x_{64}(n + 1/2)$$

Equation 4-3

where x_{6s} are the cross anharmonicity constants for ν_6, where s $\neq$ 6, 4, and *n* denotes the vibrational quantum number for ν_4. As this transition energy is the difference between $6_0^1 4_n^n$ and 4_n^n, Equation 4-3 can be rewritten as;

$$6_0^1 4_n^n - 4_0^n = \nu_6 + 2X_{66} + 1/2 \sum_{s \neq 4,6} X_{6s} + X_{64}(n + 1/2)$$

Equation 4-4

Assuming the 4_0^n band origin is 121 cm^{-1}, as was the case in the analysis presented above, the x_{64} and x_{14} anharmonicity constants can be determined. However, if we assume we do not know the 4_0^n band origin value, then we can write an equation to describe the band origin but this relies on anharmonicity and cross anharmonicity terms:

$$4_0^n = n\nu_4 + x_{44} n(n + 1) + 1/2 \sum_{s \neq 4} x_{4s}$$

Equation 4-5

Note that the final term in the equation relies on the cross anharmonicity terms: x_{64} and x_{14}. Therefore, inserting Equation 4-5 into Equation 4-4 yields:

$$\begin{aligned} 6_0^1 4_n^n &= \nu_6 + 2x_{66} + 1/2 \sum_{s \neq 4,6} x_{6s} + x_{64}(n + 1/2) + n\nu_4 \\ &+ x_{44} n(n + 1) + 1/2 \sum_{s \neq 4} x_{4s} \end{aligned}$$

Equation 4-6

Which has the following unknowns: ν_4, ν_6, x_{66}, x_{44}, x_{64}, and all other cross anharmonicity constants. Therefore two different assumptions can be made in order to determine the 4_0^n

band origins or anharmonicity constants: assume all anharmonicity and cross anharmonicity constants are zero, or assume x_{64} and x_{14} are non-zero but all other anharmonicity and cross anharmonicity constants are zero.

For the first assumption that all anharmonicity and cross anharmonicity constants are zero, Equation 4-4 can be rewritten as:

$$6_0^1 4_n^n = \nu_6 + n\nu_4$$ ***Equation 4-7***

$$1_0^1 4_n^n = \nu_1 + n\nu_4$$ ***Equation 4-8***

A linear fit of the origins given in Table 4-2 as a function of *n* would yield a slope of ν_4 and an intercept of ν_6 and ν_1 for the two different linear fits. However, this method yields two different values of ν_4: 121.1949(9) cm^{-1} and 121.076(3) cm^{-1}. Therefore, this assumption is incorrect, which is further proved when considering the experimental observation that the $6^1{}_0 4^n{}_n$ peak progressions are further apart (better resolved) than the $1^1{}_0 4^n{}_n$ peak progressions.

The second assumption, that the x_{64} and x_{14} are non-zero but all other anharmonicity and cross anharmonicity constants are zero, means that Equation 4-6 can be rewritten as:

$$6_0^1 4_n^n = \nu_6 + x_{64}(n + 1/2) + n\nu_4 + 1/2\, x_{64} + 1/2\, x_{14}$$ ***Equation 4-9***

$$1_0^1 4_n^n = \nu_1 + x_{14}(n + 1/2) + n\nu_4 + 1/2\, x_{64} + 1/2\, x_{14}$$ ***Equation 4-10***

These two equations can then be subtracted to yield the following:

$$6_0^1 4_n^n - 1_0^1 4_n^n = \nu_6 + x_{64}(n + 1/2) - \nu_1 - x_{14}(n + 1/2)$$ ***Equation 4-11***

Or in other words, a linear equation with the form:

$$6_0^1 4_n^n - 1_0^1 4_n^n = constants + (x_{64} - x_{14})(n + 1/2)$$ ***Equation 4-12***

However, Equation 4-12 puts a constraint on the difference between x_{64} and x_{14}. Using the measured band origins from Table 4-2, this constraint has the value of 0.188(4) cm^{-1}.

Equation 4-9 and Equation 4-10 can be further rearranged to give the following:

$$6_0^1 4_n^n \ = \nu_6 + x_{64} + n(\nu_4 + \ x_{64}) \ + 1/2\, x_{14}$$ ***Equation 4-13***

$$1_0^1 4_n^n \ = \nu_1 + x_{14} + n(\nu_4 + \ x_{14}) \ + 1/2\, x_{64}$$ ***Equation 4-14***

Further linear fits can be made using these two equations. However, the slope becomes $\nu_4 + x_{64}$ (or $\nu_4 + x_{14}$) and the intercept becomes $\nu_6 + x_{64} + 1/2 x_{14}$ (or $\nu_1 + x_{14} + 1/2 x_{64}$), meaning there are more unknown values than equations. Hence, the values of ν_4, x_{64}, and x_{14} cannot be derived.

4.3.1.1. Fitting results of the ν_1 band

For the ν_1 vibrational band, the discernible peaks span 2967 up to 3032 cm^{-1}, with the band origin at 3001.9407(4) cm^{-1}. Again, assuming a minimum detectable absorption of 3σ above the baseline noise (σ = 2.4 x 10^{-4}), approximately 100 peaks in this band are detectable. These peaks involve $^{P/R}Q_{Ka}(J)$ branches which are spaced by approximately $2(A-\bar{B})$. For a *b*-type transitions such as this, and using the inertial axes as labelled in Figure 5-1 inset (ii), the rotational selection rules are: $\Delta J = 0, \pm1$, $\Delta K_a = \pm1$, and $\Delta K_c = \pm1$. Once again, due to broadening of the observed transitions, each peak is a combination of many transitions, each with a different J and K_c, but with the same K_a transition.

Once again, in order to fit the experimental spectrum and determine the rotational constants of the ν_1 (v = 1) vibrational state, *PGOPHER* was used as described in section 3.3.1. In this situation, the origin, A, $\bar{B}$, δ, D_J, D_{JK}, and D_k constants were fitted using the band-head fitting procedure using Watson's *S* reduction Hamiltonian. Higher level distortion constants (d_k, d_J, H_K, H_{KJ}, H_{JK}, H_J) were also included in the simulations for the ground and excited vibrational states, however, the constants were not fitted due to a lack of appropriate higher K_a transitions. For the simulation presented in Figure 4-5, the temperature was set to 300 K, the Gaussian broadening parameter was 0.0029 cm^{-1}, and the Lorentzian broadening parameter was set to 0.0149 cm^{-1}. For the 1_0^1 band, the results of the fitted rotational constants are produced in Table 4-2.

Table 4-2 Experimentally determined rotational constants for CH_2I_2 for the vibrational modes ν_1 (v = 1), ν_6 (v = 1), ν_1 (v = 1) + ν_4 (v ≤ 4), and ν_6 (v = 1) + ν_4 (v ≤ 5). All constants in cm^{-1}. Standard deviation in brackets. Constants for ν_4 (v ≤ 4) vibrational states are from ref. [106], and the rotational constants for ν_4 (v = 5) are calculated from the reference constants. This table is reproduced from ref. [258] with the permission of AIP Publishing.

	Ground state (v = 0)[a]	ν_6 (v = 1)	ν_1 (v = 1)
Origin	···	3072.906(3)	3001.9407(4)
A	0.734994042	0.735004(2)	0.733603(3)
$\bar{B}$	0.020453481	0.0204549(4)	0.0204527(1)
δ	0.000493192	0.000493(6)	0.000498(3)
$D_K \times 10^{-5}$	1.18601	1.201(2)	1.180(1)
$D_{JK} \times 10^{-7}$	−2.14926	−2.13(2)	−2.103(7)
$D_J \times 10^{-9}$	2.29197	2.23(6)	2.26(2)
$d_k \times 10^{-13}$	−8.339	−8.339[a]	−8.339[a]
$d_J \times 10^{-11}$	−9.553	−9.553[a]	−9.553[a]
$H_K \times 10^{-10}$	2.769	2.769[a]	2.769[a]
$H_{KJ} \times 10^{-12}$	−8.442	−8.442[a]	−8.442[a]
$H_{JK} \times 10^{-15}$	−7.705	−7.705[a]	−7.705[a]
$H_J \times 10^{-16}$	2.825	2.825[a]	2.825[a]

	ν_6 (v = 1) + ν_4 (v = 1)	ν_6 (v = 1) + ν_4 (v = 2)	ν_6 (v = 1) + ν_4 (v = 3)	ν_6 (v = 1) + ν_4 (v = 4)	ν_6 (v = 1) + ν_4 (v = 5)
Origin	3194.0936(9)	3315.291(1)	3436.489 (1)	3557.691(1)	3678.876(1)
A	0.737785(7)	0.740639(8)	0.74345(1)	0.74634(1)	0.74940(2)
$\bar{B}$	0.0204485(1)	0.0204404(1)	0.0204333(1)	0.0204251(1)	0.0204168(1)
δ	0.0004951(5)	0.0004950(7)	0.0004950(9)	0.000495(2)	0.0004940(7)
$D_K \times 10^{-5}$	1.216(2)	1.219(2)	1.222(2)	1.226(4)	1.224(9)
$D_{JK} \times 10^{-7}$	−2.158(9)	−2.19(1)	−2.225(9)	−2.29(1)	−2.33(2)
$D_J \times 10^{-9}$	2.241(2)	2.23(1)	2.18(2)	2.17(2)	2.13(2)

	ν_1 (v = 1) + ν_4 (v = 1)	ν_1 (v = 1) + ν_4 (v = 2)	ν_1 (v = 1) + ν_4 (v = 3)	ν_1 (v = 1) + ν_4 (v = 4)	ν_1 (v = 1) + ν_4 (v = 5)
Origin	3123.0288(8)	3244.1060(7)	3365.185(2)	3486.246(1)	···
A	0.736356(8)	0.739179(6)	0.742023(2)	0.744904(1)	···
$\bar{B}$	0.0204458(1)	0.0204383(1)	0.0204308(3)	0.0204241(1)	···
δ	0.0000490(2)	0.00050(1)	0.00051(1)	0.00052(1)	···
$D_K \times 10^{-5}$	1.201(3)	1.2251(2)	1.2663(8)	1.299(6)	···
$D_{JK} \times 10^{-7}$	−2.22(1)	−2.19(1)	−2.18(3)	−2.17(2)	···
$D_J \times 10^{-9}$	2.28(2)	2.25(2)	2.23(4)	2.21(2)	···

a. Constants from ref. [106]

As seen in the ν_6 band, the ν_1 band also exhibits the peak progressions (evident in Figure 4-5, part B). Once again, these progressions are attributed to the ν_4 hot-bands, and transitions up to v = 4 are visible in the ν_1 band. The breakdown of the individual vibrational transitions are shown in Figure 4-6. However, the hot-band peaks converge into one peak at lower K_a values unlike in the ν_6 band. This is due to the difference in anharmonicity and cross-anharmonicity constants between the ν_6, ν_1, and ν_4 vibrational bands. Using the vibrational origins in Table 4-2, some of the anharmonicity constants can be calculated: $x_{11} = -0.009(4)$ cm^{-1} and $x_{66} = -0.052(4)$ cm^{-1}, with the added relationship of $x_{64} - x_{14} = 0.118(4)$ cm^{-1}. As the anharmonicity constant is a numerical description of the anharmonic oscillator potential energy surface, x values close to zero describe an energy surface that is close to a harmonic oscillator. Whereas, x values not close to zero describe an anharmonic oscillator. With the x_{11} being close to zero and the x_{66} being more negative than x_{11}, this pattern is expected for symmetric versus asymmetric stretching vibrations. Therefore, the symmetric stretching vibration closely resembles a harmonic oscillator, and the asymmetric stretching vibration is an anharmonic oscillator.

For both the ν_6 (v = 1), ν_1 (v = 1) and the combination vibrational states, there is a difference in the degree of uncertainty of the experimentally determined rotational constants. For example, the origins for ν_6 (v = 1) and ν_1 (v = 1) differ in uncertainty by a factor of 10, with the ν_1 constant being the more accurate value. This is mainly due to the how the *PGOPHER* band-head fitting procedure calculates the uncertainties given in Table 4-2. When undergoing the band-head fitting procedure, the uncertainty in a constant is the calculated standard deviation based on the quality of the fit. This quality of the fit can be physically described as the difference between the experimental transition peak and the assigned simulation peak. This uncertainty will be impacted by the number of transitions included in the fitting procedure. Therefore, as more peaks are incorporated into the fit from higher K_a transitions, as is the case for the ν_6 fitting compared to the ν_1 fitting, higher level distortion constants need to be included in the simulation to ensure these peaks match the experimental spectrum. Not including these higher level constants within the fitting procedure (as is the case here) means the quality of fit for the origin constant and other rotational constants will have a higher uncertainty.

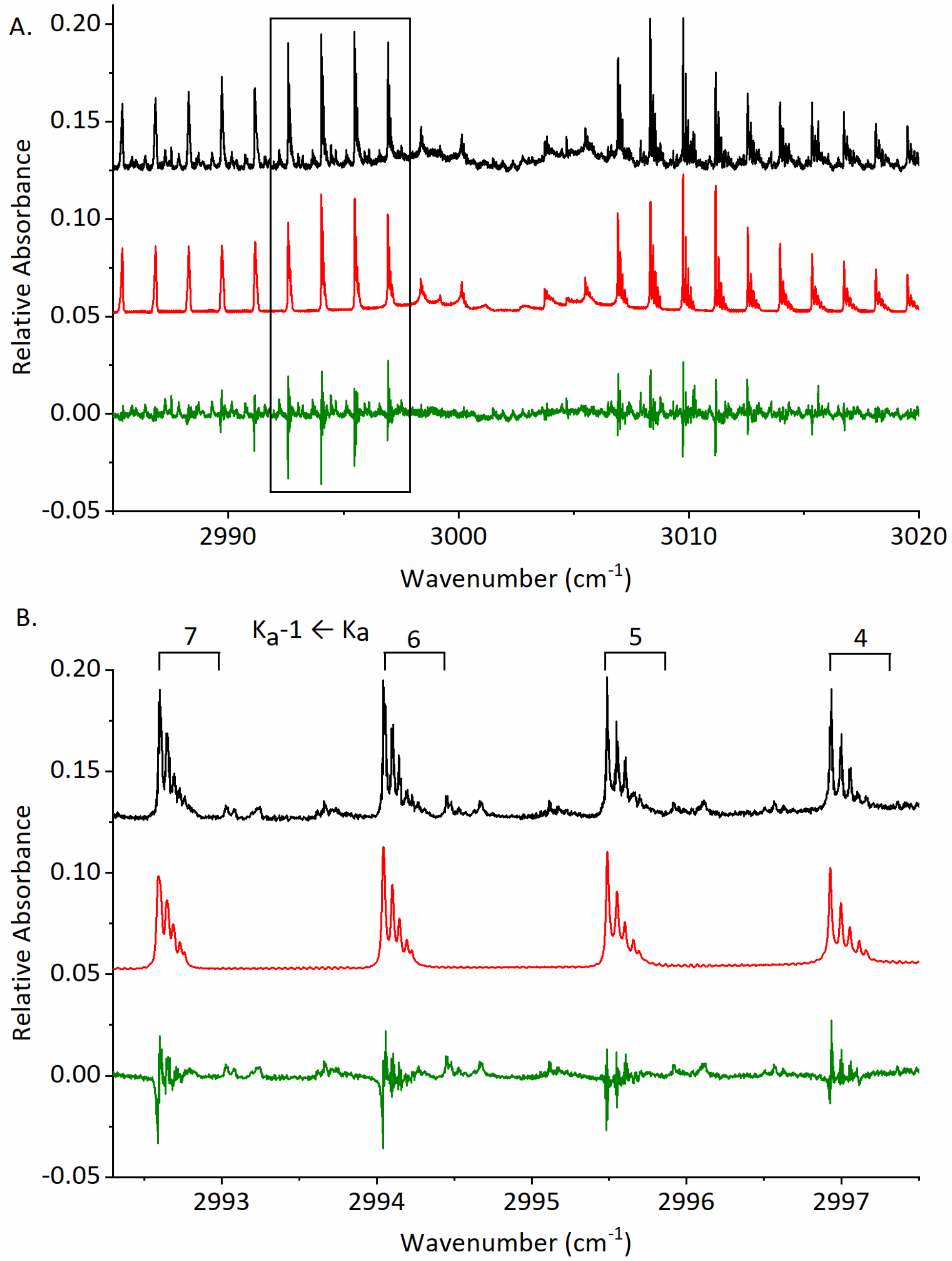

Figure 4-5 Comparison of CH_2I_2 ν_1 Simulation and Experimental Spectra. A. Comparison of the experimental spectrum (black) and the overall simulation (red), as determined in *PGOPHER*, for the ν_1 band from 2985 to 3020 cm^{-1}. The overall simulation is comprised of the different simulated transitions for the fundamental 1^1_0 band and the $1^1_0\,4^n_n$ hot bands, where $n \leq 4$. *Y*-axis shows relative absorbance of the experimental and simulation spectra, where the simulation has been scaled up to match the experimental. The green line is the residual plot of experimental minus the overall simulation. B. Zoomed in portion of the three spectra, from 2992.3 to 2997.5 cm^{-1} showing 4 different K_a transitions in the ^PQ branch. This figure is reproduced from ref. [258] with the permission of AIP Publishing.

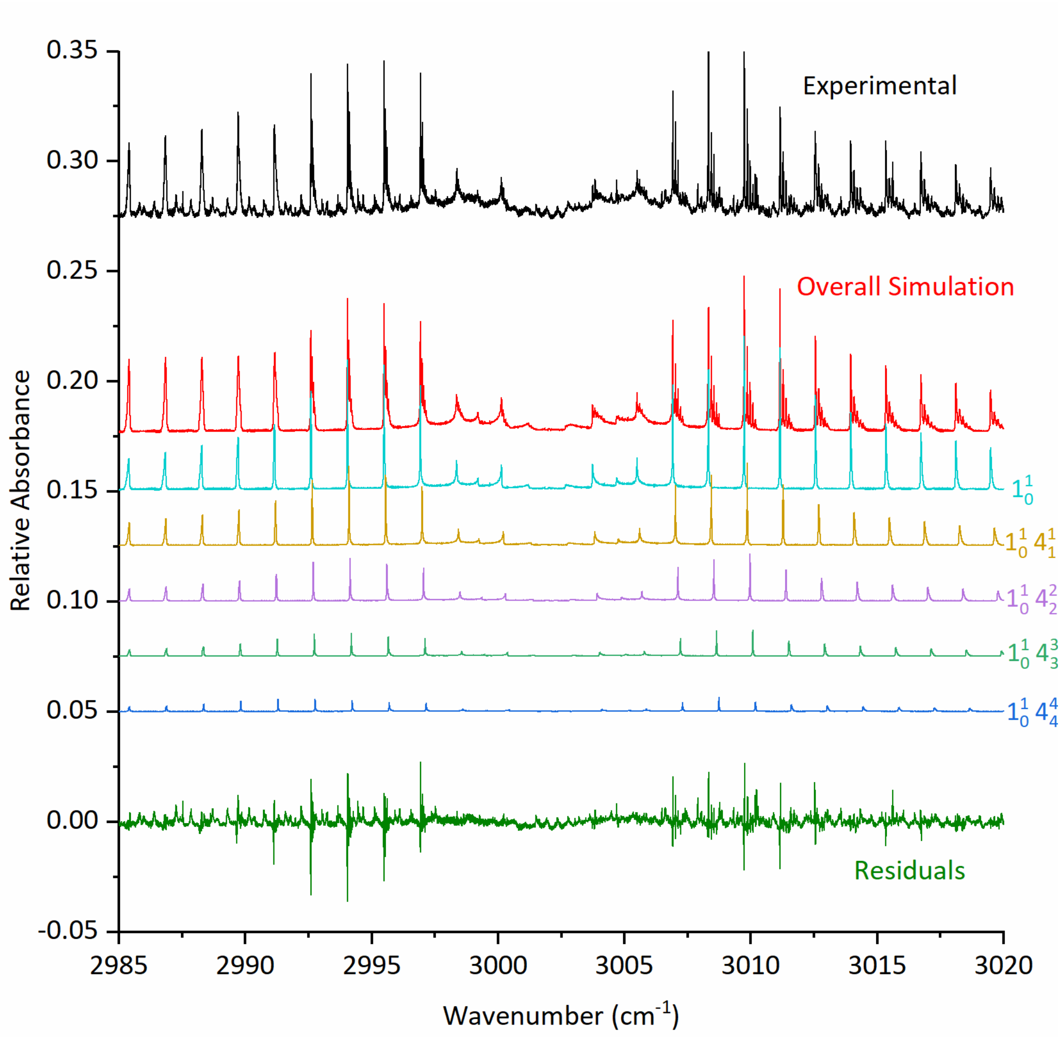

Figure 4-6 CH_2I_2 ν_1 Simulation Breakdown. Breakdown of the 5 different vibrational transitions which make up the *PGOPHER* simulation shown from 2985 to 3020 cm^{-1}: 1_0^1 (light blue), $1_0^1 4_1^1$ (yellow), $1_0^1 4_2^2$ (purple), $1_0^1 4_3^3$ (light green), $1_0^1 4_4^4$ (dark blue). Experimental spectrum (black), overall simulation (red), and residual plot (dark green) are also shown. This figure is reproduced from ref. [258] with the permission of AIP Publishing.

4.3.1.2. Additional Peaks

Although the inclusion of the ν_4 hot-bands in the *PGOPHER* simulations helps to capture the majority of the observed peaks in the experimental spectrum, there are still some low intensity peaks that have not been simulated. This is mainly visible in the ν_1 band (Figure 4-5, part B), where there are multiple peaks near to 2993.3 cm^{-1}, 2994.5 cm^{-1}, and 2996.0 cm^{-1}. The first possible source of these peaks is CH_2I_2 dimers, as the presence of the peaks are dependent on CH_2I_2 being present. These dimers have been calculated to be stable by circa 4 kcal mol^{-1} (1400 cm^{-1}), so it is possible they exist over the course of the experiment. However, when keeping the total pressure of the cell constant but increasing the concentration of CH_2I_2 from 0.1 to 10%, the relative intensity of the additional peaks to the known peaks (i.e. those caused by the fundamental or hot-band transitions) did not increase. This indicates that it is unlikely the dimers are present during the experiments and they are not responsible for the additional peaks.

The most likely source of the additional peaks is other overtones, combination bands or hot-band transitions. Looking at Table 4-1, there are no obvious combinations or overtones of the vibrational modes that can contribute to visible peaks within the 2960 to 3125 cm^{-1} region. Therefore, further hot-band transitions are considered. Since the simulation shows there is population in the ν_4 vibrational states up to and including the ν_4 (v = 5), which has a transition frequencies close to 605 cm^{-1} (estimated from the liquid IR studies), any other vibrational mode with a transition frequency lower than 605 cm^{-1} could be populated as well. This includes the ν_3 (v = 1) state at 493.01 cm^{-1} and the ν_9 (v = 1) state at 584.21 cm^{-1}. [107] However, a lack of microwave data for these states means simulating these hot-band transitions would introduce a large degree of uncertainty. In addition, as there are two potential hot-band transitions (population from ν_3 and ν_9), it is difficult to know which low intensity peak corresponds to which transition. An effort was made to simulate the ν_3 and ν_9 bands within *PGOPHER* using the results from the wB97X/Def2QZVPP calculations (section 4.3.3). While the simulation did prove that the $6_0^1 3_1^1$ and $6_0^1 9_1^1$ would be possible in terms of intensity, the uncertainty in the band origins and cross-anharmonicity terms meant the results were difficult to quantify in terms of peak assignment.

4.3.2. Pressure Broadening Coefficients

Each peak in the spectrum of CH_2I_2 is comprised of many different rovibrational transitions which are broadened due to a variety of factors. Firstly, the expected Doppler broadening for the transitions at room temperature is 0.0023 cm^{-1}, which is observed as a Gaussian line-shape. Secondly, there is the Lorentzian line-shape due to the instrument line-shape function (as discussed in section 3.4), which has a FWHM of 0.0142 cm^{-1}. When including both of these values in the *PGOPHER* simulations, the experimental spectrum shows additional broadening which is not captured using 0.0023 cm^{-1} as the Gaussian contribution and 0.0142 cm^{-1} Lorentzian contribution to the linewidth. The remainder of this linewidth is most likely due to pressure broadening. [260-262] This is further confirmed by considering the reference spectrum (Figure 4-2). Here, the observed peaks are broadened due to the atmospheric pressure experimental conditions.

As stated in the experimental section, the spectra for the pressure broadening analysis was collected from 3052 to 3070 cm^{-1}, within the ν_6 band, for two different bath gases, N_2 and Ar. Contour fitting (as described in section 3.3.1) was then undertaken in *PGOPHER* to fit an overall Lorentzian broadening parameter (as a FWHM) between 3056.5 to 3069 cm^{-1} which incorporated 51 peaks across nine different K_a transitions. This region was chosen as it has well-defined transitions and high intensity peaks. The overall parameter includes the contribution from the instrument line-shape function, so this is removed before further analysis is undertaken. Then, the remaining FWHM is converted to a half-width-at-half-maximum (HWHM) for the rest of the analysis. For each HWHM, the pressure broadening contribution can be split into two parts:

$$\Gamma_{broadening} = p_1 \times b_{self} + p_2 \times b_x$$ ***Equation 4-15***

Where, b_{self} is the self-broadening parameter for CH_2I_2, b_x is the broadening parameter for each bath gas, (x = N_2 or Ar), and p_1 and p_2 are the partial pressures of the respective gases.

Unfortunately, the concentration of CH_2I_2 varies slightly between 0.003 to 0.05 mbar for each acquired spectrum. This variation is due to the experimental conditions and the MFC configurations. However, as this variation is only small and experiments were not undertaken to vary the concentration of CH_2I_2, b_{self} was not determined. Since the concentration of CH_2I_2 does vary slightly, the variance must be removed from each overall HWHM Lorentzian parameter in order to accurately determine the broadening coefficient for each bath gas. This process requires a few steps. Firstly, an initial plot of $\Gamma_{broadening}$ vs bath gas partial pressure (one each for N_2 and Ar) is created, and a linear slope is fitted. The intercepts from the fits represent the average self-broadening parameter (one each for N_2 and Ar). The average parameters are then removed from the individual HWHM parameters to give a new Lorentzian value.[263] This new value can then be plotted against the partial pressure of the appropriate bath gas. Once again, a linear slope can be fitted, where the slope corresponds to the b_x parameter. The results of these two linear fits are shown in Figure 4-7.

For N_2, the $\Gamma_{broadening}$ parameter ranged from 0.003 cm^{-1} at 26.3 mbar to 0.18 cm^{-1} at 1000 mbar. This corresponds to a b_x value of 1.41(6) × 10^{-4} cm^{-1} mbar or 0.143(6) cm^{-1} atm^{-1}. Conversely, for Ar the $\Gamma_{broadening}$ parameter ranged from 0.003 cm^{-1} at 24.0 mbar to 0.11 cm^{-1} at 980 mbar. This corresponds to a b_x value of 1.14(6) × 10^{-4} cm^{-1} mbar or 0.116(6) cm^{-1} atm^{-1}. These values are also recorded in Table 4-3.

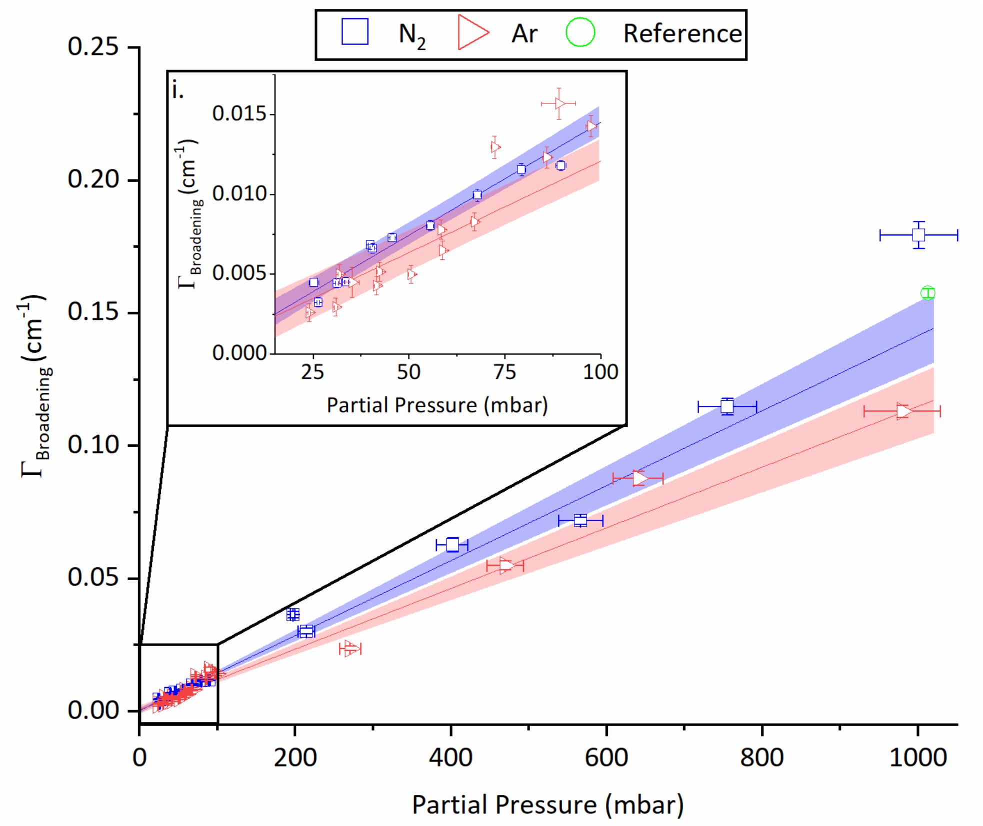

Figure 4-7 CH_2I_2 Pressure Broadening Linear Fit. $\Gamma_{broadening}$ (cm^{-1}) as a function partial pressure of either N_2 or Ar from 0 to 1000 mbar. Blue squares are the N_2 data with a corresponding blue linear line-fit and a 95% confidence limit. Red triangles are the Ar data with a red linear line-fit and a 95% confidence limit. The reference data is also shown as a green circle. Inset (i) shows the same data but between 20 and 100 mbar. This figure is reproduced from ref. [258] with the permission of AIP Publishing.

Table 4-3 CH_2I_2 Pressure Broadening Coefficients. Broadening coefficients from this work for N_2 and Ar with the error fit of the linear line-fit given in brackets. Average J-dependent broadening coefficients from available literature for CH_3I, CH_2F_2 and CH_3F, with the standard deviation in brackets.

Collision Partner	CH_2I_2 *b* (cm^{-1} atm^{-1})	CH_3I *b* (cm^{-1} atm^{-1})	CH_2F_2 *b* (cm^{-1} atm^{-1})	CH_3F *b* (cm^{-1} atm^{-1})
N_2	0.143(6)^a	0.107(14)^b	0.087^c	0.101(14)^d
Ar	0.116(6)^a	…	…	0.063(6)^e

a. This work
b. Ref. [264]
c. Ref. [263]
d. Ref. [265]
e. Ref. [266]

Comparisons can now be made between the two broadening parameters. While the two values are of similar magnitude, they differ in absolute value and are just outside the margins of error to be considered the same value. For the two coefficients, b_{Ar} is approximately 1.25 times smaller than the b_{N2} value. The magnitude of the b_{N2} value also means that any atmospheric observations of CH_2I_2 vibrational transitions will be broad.

Attempting to compare the experimental values reported here to other available values is difficult due to the lack of appropriate pressure broadening studies for CH_2X_2 molecules (were X = F, Cl, Br, or I). For b_{N2} there is only one study for the CH_2F_2 molecule. For this molecule the b_{N2} parameter ranges from 0.061 to 0.125 cm^{-1} atm^{-1}, with an average value of 0.087 cm^{-1} atm^{-1}. [263]

However, there have been more studies for the CH_3X molecules, where each of the four halogen-substituted methane molecules has an observed b_{N2} parameter. Calculating average values for different CH_3X molecules yields an average of 0.105 cm^{-1} atm^{-1}, and specifically for CH_3I, the average is b_{N2} parameter = 0.107(14) cm^{-1} atm^{-1}. [264] These two values are averages over J-dependent values, where such values for CH_3I ranged from 0.072(2) cm^{-1} atm^{-1} to 0.148(4) cm^{-1} atm^{-1}. In addition, there is only study in total for a b_{Ar} parameter, which is for the CH_3F molecule. For both of the studies involving the CH_3F molecule, the b_{N2} parameter ranges from 0.087 to 0.123 cm^{-1} atm^{-1}, with an average value of 0.101(14)cm^{-1} atm^{-1}, [265] and the b_{Ar} parameter ranges from 0.050(3) cm^{-1} atm^{-1} to 0.080(5) cm^{-1} atm^{-1} with an average of 0.063(6) cm^{-1} atm^{-1}. [266] Comparing to the CH_2I_2 broadening coefficients in Table 4-3, both of the experimental values in this thesis are much higher than those reported for CH_3F. However, the general trend of b_{N2} being higher than b_{Ar} still stands true.

While the value reported in this thesis is higher than the average b_{N2} value, it is within the upper range of the J-dependent value for CH_3I. Therefore, the observed b_{N2} and b_{Ar} parameters are potentially higher than expected. The most probable explanation for this is that the contribution of the bath gas to the pressure broadened transitions has been over-predicted. Simultaneously, the contribution from the self-broadening by CH_2I_2 might be under-predicted. Full comparisons between the CH_2X_2 and CH_3X molecules will be made in section 6.2.

Comparisons can also be made to the reference spectrum. The experimental conditions for that study uses N_2 as a bath gas with a total pressure of 1013 mbar (atmospheric pressure). Using the same *PGOPHER* contour fitting method, the $\Gamma_{\mathrm{broadening}}$

value is determined to be 0.158 cm^{-1}. Using the linear fit results shown in Figure 4-7, a prediction $\Gamma_{broadening}$ value can be calculated to be 0.14(1) cm^{-1} at the same 1013 mbar pressure. While the predicted $\Gamma_{broadening}$ is lower than the fitted $\Gamma_{broadening}$ value, the reference data still incorporates any ILS function and does not account for any self-broadening contributions.

4.3.3. Computational Calculations

Table 4-4 and Table 4-5 show the results of the semi-empirical computational values for the five different levels of theory and the corresponding basis sets. Table 4-4 gives the values for the ground state (v = 0), ν_6 (v = 1), ν_4 (v = 1), and ν_6 (v = 1) + ν_4 (v = 1) vibrational states, whereas Table 4-5 gives the corresponding values for the ν_1 containing vibrational states. The band origin values within the tables are the calculated values, however the band origin values used within the *PGOPHER* simulations (shown in Figure 4-8 part A for ν_6 and part B for ν_1), are adjusted in order to match the experimental spectrum. Out of the five simulated spectra, the results for wB97X/Def2QZVPP calculations matched the closest to the experimental spectrum in terms of peak position, so a comparative analysis is given between these two simulations. However, the results from the other four stimulated spectra were not too dissimilar from the experimental spectrum. In addition, the results for MP2/MidiX gave the most accurate band origins when comparing with the experimental band origins. For example, for the experimental ν_6 (v = 1) vibrational state, the band origin = 3072.906 cm^{-1}, and for the MP2/MidiX ν_6 (v = 1) vibrational state, the band origin = 3072.330 cm^{-1}. However the simulation for the MP2/MidiX results does not match qualitatively with the experimental spectrum and struggles to capture the hot-band transitions with the peak progressions accurately.

Initially looking at the values for wB97X/Def2QZVPP within Table 4-4, the calculated rotational values are different to the microwave ground state and the experimentally determined rotational constants by 0.02 cm^{-1}. In addition, the Δ_i between the *A* rotational constant for the calculated ground state and ν_6 (v = 1) is much larger than the equivalent difference between the experimental ground state and ν_6 (v = 1), −46.3 cm^{-1} compared to 9.8 cm^{-1} respectively. On the other hand, the Δ_i value for the *B* and *C* constants match well to experimental Δ_i values. However, for the ν_1 results (Table 4-5), the Δ_I values for the *A* rotational constant are better matched between the experimental results and the wB97X/Def2QZVPP results, −139 cm^{-1} and −144 cm^{-1} respectively.

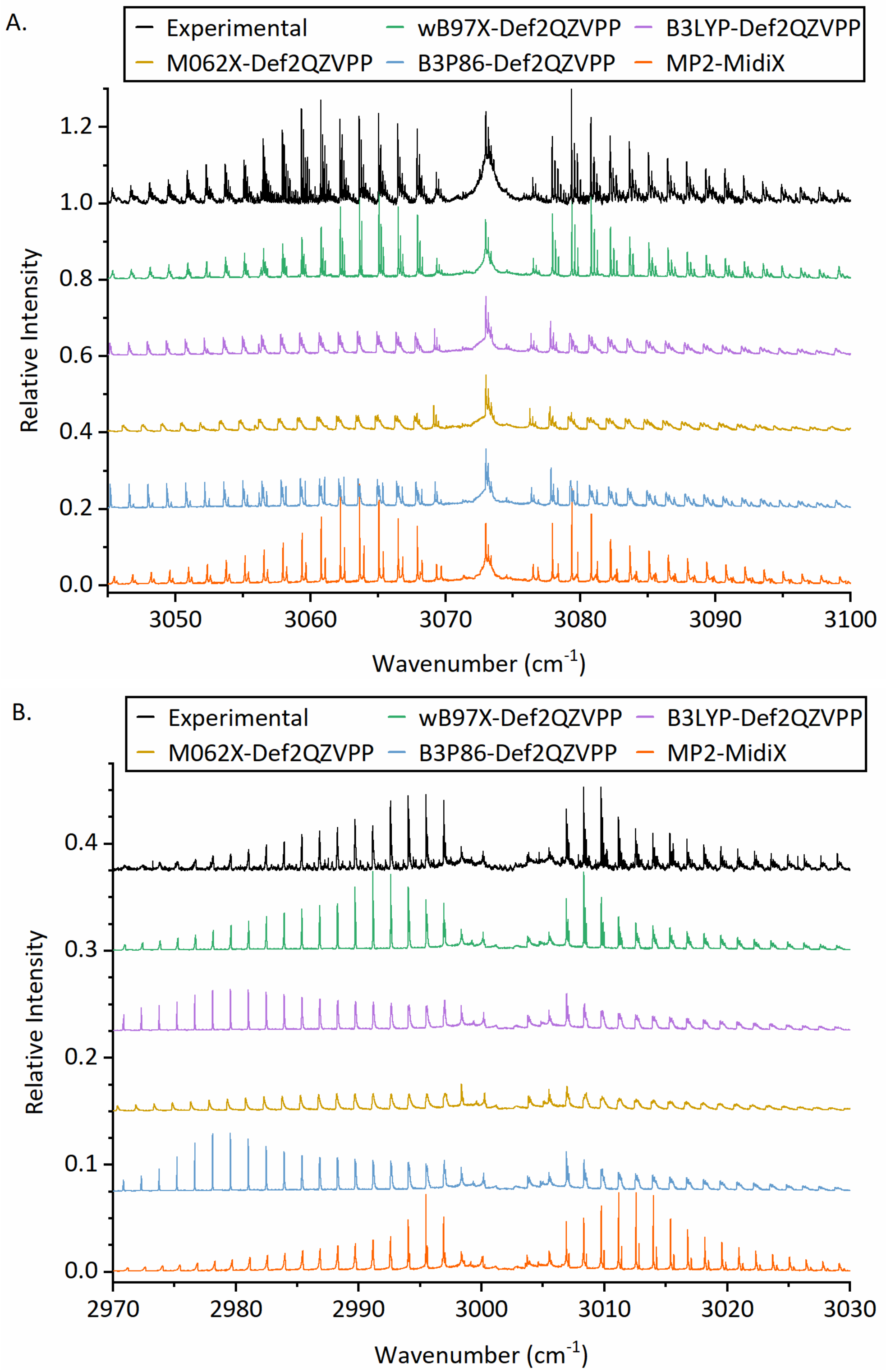

Figure 4-8 CH_2I_2 Computational Simulated Spectra. A. Comparison of the experimental spectrum and the five computational spectra from 3045 to 3100 cm^{-1} showing the ν_6 band. B. Comparison of the experimental and the five computational spectra from 2097 to 3030 cm^{-1} showing the ν_1 band. The colours of the spectra are: Experimental (black), wB97X/Def2QZVPP (green), B3LYP/Def2QZVPP (purple), M062X/Def2QZVPP (yellow), B3P86/Def2QZVPP (blue), and MP2/MidiX (orange). This figure is reproduced ref. [258] with the permission of AIP Publishing.

However, this large difference (56.1) for the Δ_i between the *A* rotational constants does not manifest itself in the simulated spectra. Figure 4-9 shows the results of the experimental spectrum (black), the simulated results from section 4.3.1.1 (red), and the wB97X/Def2QZVPP results (blue) for the ν_6 band. The general shape of each peak is well matched, which is dependent on the *B* and *C* constants. But there is a slight 0.03 cm^{-1} difference in the peak locations between the experimental and the wB97X/Def2QZVPP simulation, which is due to the *A* rotational constant. Similar results can be seen for the ν_1 simulations. Figure 4-10 shows the results of the experimental spectrum (black), the simulated results from section 4.3.1.1 (red), and the wB97X/Def2QZVPP results (blue) for the ν_1 band. Once again, the general shape of the peaks is well matched and the peak locations are better matched for the ν_1 band than the ν_6 band, with a difference of only 0.01 cm^{-1} between the experimental and wB97X/Def2QZVPP simulation.

Alongside the fundamental transitions, the hot-band transitions were also calculated and simulated. As shown in both Figure 4-9 and Figure 4-10, the inclusion of these hot-bands qualitatively match well to the experimental simulation, which helps to confirm the hot-band theory and analysis as presented in section 4.3.1.

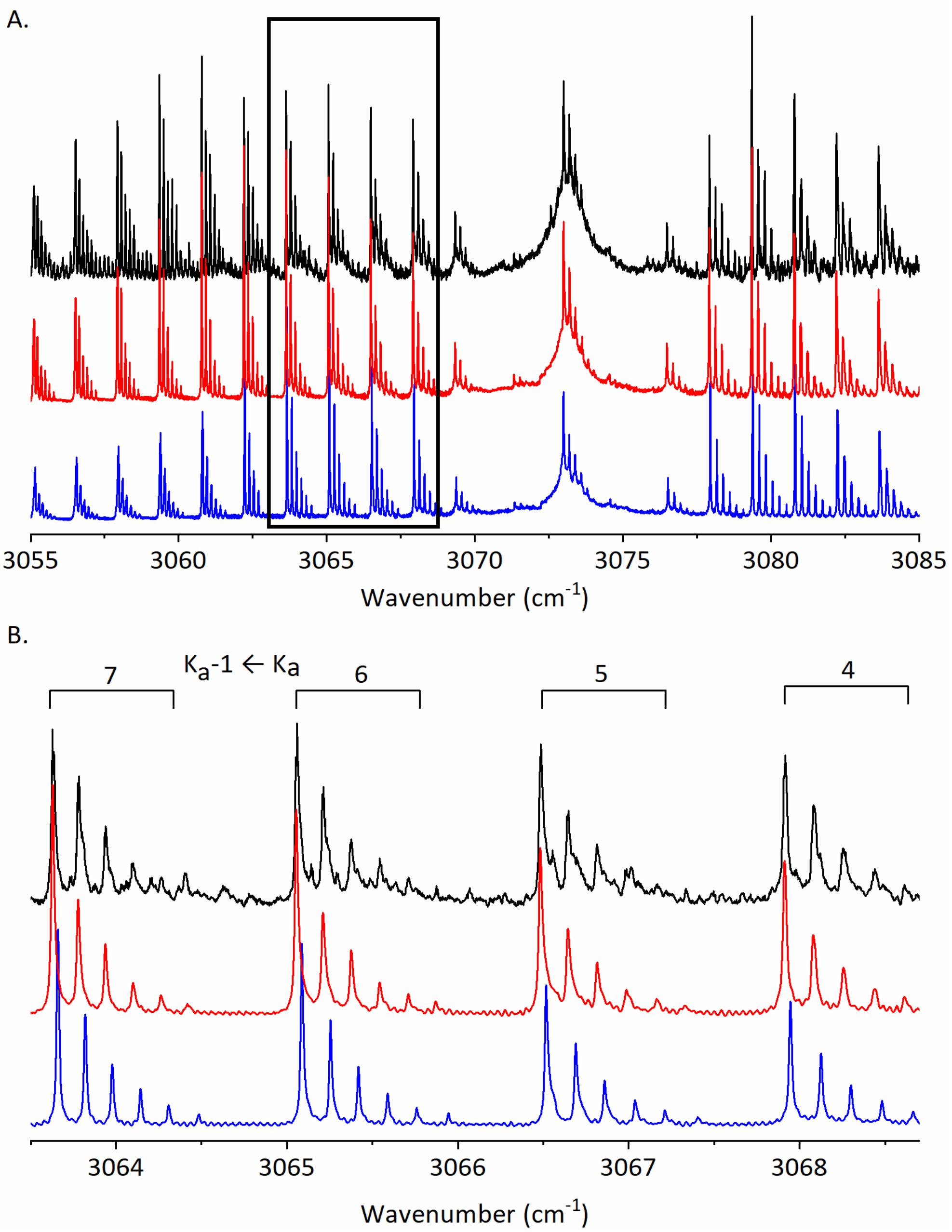

Figure 4-9 CH_2I_2 ν_6 wB97X/Def2QZVPP Simulation Comparison Results. Comparison of the experimental spectrum (black), the line-fitted simulation (red), and the semi-empirical simulation based on the results of the wB97X/Def2QZVPP calculations (blue). A. Sub-section of all three spectra, from 3055 to 3085 cm^{-1} covering the 6^1_0 band (including the $6^1_0\ 4^n_n$ transitions where n ≤ 5) band. B. Zoomed in portion of the three spectra, from 3063.5 to 3068.6 cm^{-1} showing four different K_a transitions in the ^PQ branch. This figure is reproduced from ref. [258] with the permission of AIP Publishing.

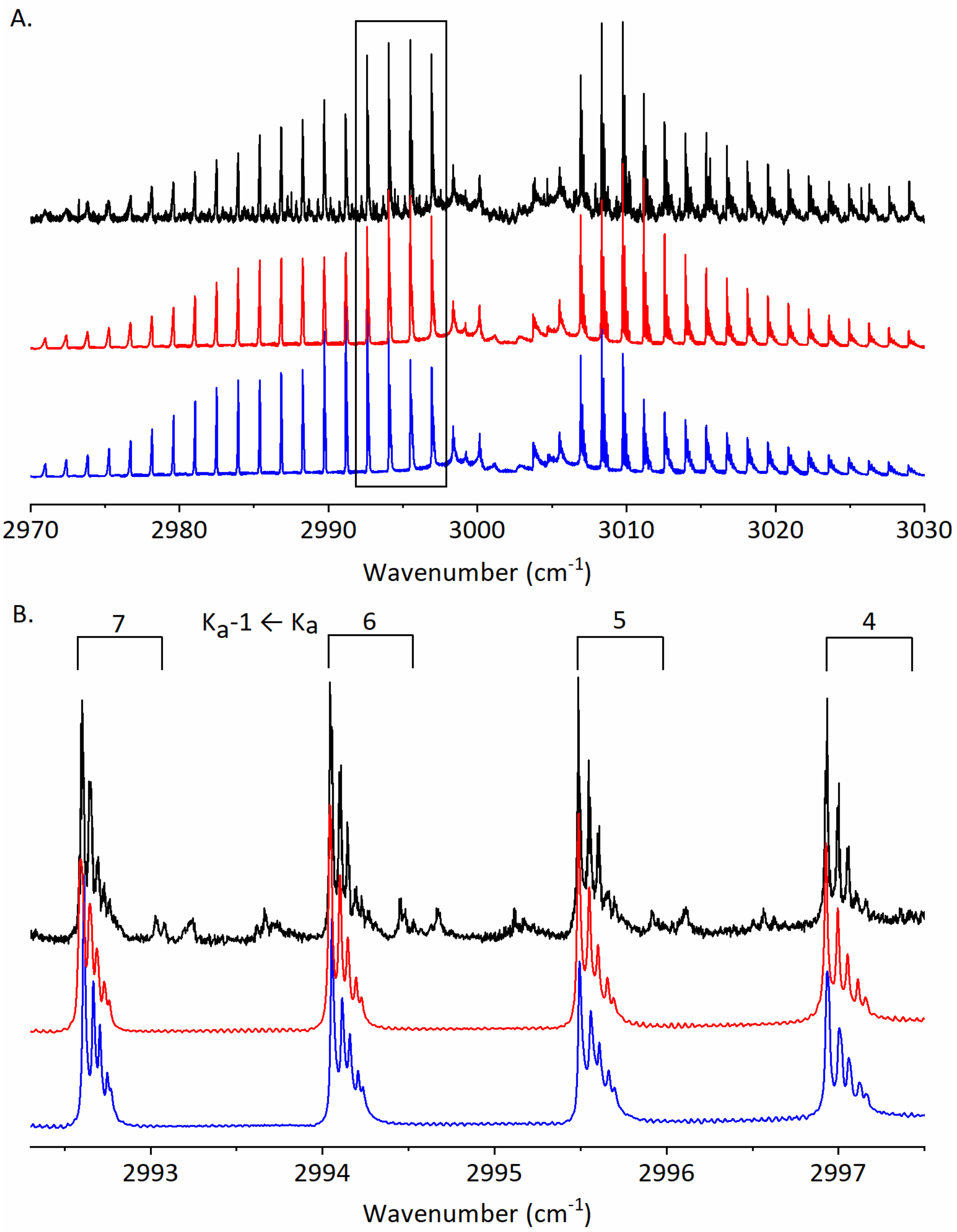

Figure 4-10 CH_2I_2 ν_1 wB97X/Def2QZVPP Simulation Comparison Results. Comparison of the experimental spectrum (black), the line-fitted simulation (red), and the semi-empirical simulation based on the results of the wB97X/Def2QZVPP calculations (blue). A. Sub-section of all three spectra, from 2970 to 3030 cm^{-1} covering the 1^1_0 band (including the $1^1_0 4^n_n$ transitions where n ≤ 4) band. B. Zoomed in portion of the three spectra, from 2992.4 to 2997.5 cm^{-1} showing four different K_a transitions in the ^PQ branch. This figure is reproduced from ref. [258] with the permission of AIP Publishing.

Table 4-4 CH_2I_2 ν_6 Semi-empirical Computational Values. Comparison of calculated and experimentally determined anharmonic frequencies and rotational constants for CH_2I_2 for the vibrational ground state (v = 0), ν_6 (v = 1), ν_4 (v = 1), and the first hot band ν_6 (v = 1) + ν_4 (v = 1). All values given in cm^{-1}, error bars for experimental values are given above in Table 4-2. This table is reproduced from ref. [258] with the permission of AIP Publishing.

		Ground state (v=0)	ν_6 (v=1)	Δ_i /10^{-6}	ν_4 (v = 1)	ν_6 (v = 1) + ν_4 (v = 1)	Δ_j /10^{-6}
Experimental	ν	0	3072.906	···	121.0	3194.0936	…
	A	0.734994[a]	0.735500	9.8	0.737856[a]	0.737784	−70.1
	B	0.020700[a]	0.207014	1.3	0.020694[a]	0.020696	2.5
	C	0.020206[a]	0.020208	1.5	0.020198[a]	0.020201	2.5
wB97X / Def2QZVPP	ν	0	3196.503	···	122.802	3319.646	···
	A	0.756904	0.756858	−46.3	0.758381	0.758335	−46.0
	B	0.020722	0.020723	0.9	0.020741	0.020742	1.0
	C	0.020248	0.020250	1.2	0.020265	0.020266	1.0
B3LYP / Def2QZVPP	ν	0	3084.591	···	113.560	3198.268	···
	A	0.754299	0.754001	−298.1	0.755808	0.755509	−299
	B	0.019928	0.01994	11.4	0.019947	0.019958	11.0
	C	0.019490	0.019501	11.3	0.019506	0.019517	11.0
M062X / Def2QZVPP	ν	0	2824.927	···	116.988	2940.409	···
	A	0.746255	0.744737	−1518	0.747667	0.746149	−1518
	B	0.020673	0.020692	19.2	0.020692	0.020711	19
	C	0.020198	0.020215	17.4	0.020215	0.020232	17
B3P86 / Def2QZVPP	ν	0	3091.403	···	114.929	3206.442	···
	A	0.758783	0.758516	−267.3	0.760348	0.760081	−267
	B	0.020428	0.020437	9.0	0.020447	0.020456	9.0
	C	0.019970	0.019979	8.7	0.019987	0.019996	9.0
MP2 / MIDIX	ν	0	3072.330	···	118.861	3191.309	···
	A	0.715676	0.715986	309.8	0.718191	0.718501	310
	B	0.019623	0.019624	1.5	0.019662	0.019617	−44.5
	C	0.019172	0.019174	2.0	0.019164	0.019166	2.0

a. Constants from ref. [106]

Table 4-5 CH_2I_2 ν_1 Semi-empirical Computational Values. Comparison of calculated and experimentally determined anharmonic frequencies and rotational constants for CH_2I_2 for the vibrational ground state (v = 0), ν_1 (v = 1), ν_4 (v = 1), and the first hot band ν_1 (v = 1) + ν_4 (v = 1). All values given in cm^{-1}, error bars for experimental values are given above in Table 4-2. This table is reproduced from ref. [258] with the permission of AIP Publishing.

		Ground state (v=0)	ν_1 (v=1)	Δ_i /10^{-6}	ν_4 (v = 1)	ν_1 (v = 1) + ν_4 (v = 1)	Δ_j /10^{-6}
Experimental	v	0	3001.939	…	121.0	3123.029	…
	A	0.734994[a]	0.733606	−139	0.737856[a]	0.736355	−150
	B	0.020700[a]	0.020698	−1.9	0.020694[a]	0.020691	−2.7
	C	0.020206[a]	0.020210	3.1	0.020198[a]	0.020201	2.3
wB97X / Def2QZVPP	v	0	3133.216	…	122.802	3256.026	…
	A	0.756904	0.755465	−144	0.758381	0.756941	−144
	B	0.020722	0.020724	18.9	0.020741	0.020743	2.0
	C	0.020248	0.020251	16.2	0.020265	0.020268	3.0
B3LYP / Def2QZVPP	v	0	3017.650	…	113.560	3131.131	…
	A	0.754299	0.752528	−177	0.755808	0.754036	−177
	B	0.019928	0.019937	8.4	0.019947	0.019955	8.0
	C	0.019490	0.019498	8.3	0.019506	0.019514	8.0
M062X / Def2QZVPP	v	0	2774.860	…	116.988	2890.359	…
	A	0.746255	0.743240	−301	0.747667	0.744676	−299
	B	0.020673	0.020692	19.2	0.020692	0.020711	19.0
	C	0.020198	0.020215	17.4	0.020215	0.020232	17.0
B3P86 / Def2QZVPP	v	0	3022.180	…	114.929	3136.833	…
	A	0.758783	0.757036	−175	0.760348	0.758601	−175
	B	0.020428	0.020435	7.0	0.020447	0.020711	8.0
	C	0.019970	0.019977	6.7	0.019987	0.020232	7.0
MP2 / MIDIX	v	0	3008.467	…	118.861	3127.338	…
	A	0.715676	0.714785	−89.1	0.718191	0.717300	−89.1
	B	0.019623	0.019620	−2.5	0.019662	0.019613	−48.5
	C	0.019172	0.019170	−2.0	0.019164	0.019162	−2.0

a. Constants from ref. [106]

4.4. Conclusion

Firstly, the room temperature rovibrational absorption spectrum of CH_2I_2 has been measured from 2960 to 3125 cm^{-1}. Within this region, two fundamental transitions of CH_2I_2 were observed, belonging to the ν_6 and ν_1 normal modes. However, further analysis of these two bands revealed contributions from hot-band transitions arising from population in the ν_4 vibrational states. Within the ν_6 band, there were six assigned vibrational transitions: 6_0^1 and $6_0^1 4_n^n$ (where n ≤ 5). Within the ν_1, there were five assigned vibrational transitions: 1_0^1 and $1_0^1 4_n^n$ (where n ≤ 4). In addition, within both bands there were unassigned transitions which could be attributed to $6_0^1 3_1^1$ or $6_0^1 9_1^1$ within the ν_6 band, or $1_0^1 3_1^1$ within the ν_1 band. A *PGOPHER* simulation was generated to experimentally determine the spectroscopic rotational constants of all 11 vibrational states observed in the experimental spectrum. Some of the cross anharmonicity constants were determined: x_{11} is −0.009(4) cm^{-1} and x_{66} is −0.052(4) cm^{-1} and the added constraint that $x_{64} - x_{14}$, must be equal to 0.188(4) cm^{-1}.

Secondly, the pressure broadening coefficients of N_2 and Ar have also been measured for CH_2I_2, with b_{N2} = 0.143(6) cm^{-1} atm^{-1} and b_{Ar} = or 0.116(6) cm^{-1} atm^{-1}. Both of these experimental values are much higher than corresponding values for CH_3X and CH_2X_2 molecules. However, the general trend of b_{N2} being higher than b_{Ar} is observed here. The most probable explanation for the high values is that the contribution of the bath gas to the pressure broadened transitions has been over-predicted. Simultaneously, the contribution from the self-broadening by CH_2I_2 might be under-predicted.

Lastly, the results of five different computational calculations were used to predict the spectra of the ν_1 and ν_6 bands in order to confirm the hot-band theory. The computational basis set and method pairs were: wB97X/Def2QZVPP, M062X/Def2QZVPP, B3P86/Def2QZVPP, B3LYP/Def2QZVPP, and MP2/MidiX. Out of the ten simulation spectra, five for the ν_6 and five for the ν_1 band, the semi-empirical simulated spectra for the wB97X/Def2QZVPP computational calculation were qualitatively the best match for the experimental spectrum for both vibrational bands.

5. Rovibrational Absorption Spectroscopy of CH_2Br_2 from 2925 to 3125 cm^{-1}

This chapter covers the experimental work undertaken to record a mid-IR spectrum of CH_2Br_2 from 2925 to 3125 cm^{-1} and the attempts to determine the spectroscopic constants of the two measured vibrational states, ν_6 (v = 1) and ν_1 (v = 1). In addition, further spectroscopic constants are measured for the combination states ν_6 (v = 1) + ν_4 (v ≤ 3) which arise from population in the ν_4 (v ≤ 3) vibrational states. The effects of pressure broadening on the observed rovibrational transitions are also reported here. In addition, computational studies of CH_2Br_2 are undertaken to guide the fitting process and allows for comparison between semi-empirical simulated spectra and experimental spectrum. The majority of the work presented in this chapter is currently being prepared for a manuscript, including the full recorded spectrum, the ν_6 fitting analysis, and the pressure broadening analysis.

5.1. Background of CH_2Br_2

Dibromomethane, CH_2Br_2 is a known contributor to the global bromine budget and, as seen for CH_2I_2, is mostly found in coastal regions as it is produced in seawater by macroalgae. [81] A number of studies have observed the mixing ratio of CH_2Br_2 in the atmosphere to be around 1 pptv: 0.88 pptv over the western Pacific Ocean,[24] 0.85 to 1.75 pptv over the East China Sea, [25] and 1.08(17) pptv at Cape Point, South Africa. [26] Atmospheric studies have also shown that CH_2Br_2 has a moderate tropospheric lifetime of approximately 120 days [80, 267] and an ozone depletion potential (ODP) of 0.17. [267] This ODP is the relative amount of degradation to the ozone layer a molecule can cause, with CCl_3F being fixed at 1.0. Within the atmosphere CH_2Br_2 undergoes two main reactions, namely photolysis and reaction with the OH radical:

$$CH_2Br_2 + h\nu\ (<\ 320\ nm)\ \rightarrow\ CH_2Br + Br$$ ***Reaction 5-1***

$$CH_2Br_2 + OH\ \rightarrow\ CHBr_2 + H_2O$$ ***Reaction 5-2***

The generation of the bromine radical contributes to the ozone depletion cycle in the upper stratosphere (as discussed in section 1.1.1). [10] As was the case with CH_2I_2, CH_2Br_2 has also been used in laboratory settings to generate Criegee intermediates. [268] However, unlike CH_2I_2, there is more available gas-phase spectroscopy literature for CH_2Br_2. For electronic spectroscopy, there have been many studies into the UV-Vis spectrum of CH_2Br_2, in particular understanding its photolysis rates as a function of UV light, which acts as a simulation for solar radiation. [79-85] While some of these studies did observe vibrational overtone and combination bands, only band-origin information can be gleaned from these studies. [81] For rotational spectroscopy studies, there are six studies probing the ground vibrational state. [86-91] Furthermore, one of these studies also determines rotational constants for the ν_4 (v = 1) vibrational state but only for the 79/81 isotopologue. [90] Understanding the vibrational and rotational spectroscopy of CH_2Br_2 can be complex due to the introduction of isotopologues. As the bromine molecule has two stable isotopes, with mass 78.91834 and mass 80.91629, three isotopologues are stable for CH_2Br_2: $CH_2{}^{79}Br^{79}Br$, $CH_2{}^{79}Br^{81}Br$, and $CH_2{}^{81}Br^{81}Br$. For the purpose of this thesis, the written masses are simplified to 79 and 81. These have an abundance ratio of 1:2:1, and for simplicity reasons (and where appropriate) the isotopologues will be referred to as 79/79, 79/81, and 81/81. For the analysis presented later, the rotational constants for the ground vibrational state are taken from ref. [88] for the 79/79 and 81/81 isotopologues and from ref. [90] for the 79/81 isotopologue.

Moving onto vibrational studies, there have been four studies focusing on the IR gas phase spectrum of CH_2Br_2. [92-95] Only two of these papers cover a broad range of the IR spectrum, from 400 to 4000 cm^{-1}, and measures eight of the nine possible normal vibrational fundamental transitions. Unfortunately, ν_4 could not be measured as its transition wavenumber (approximately 171 cm^{-1}) is lower in energy than the available light source, however the transition wavenumber was calculated. [92] Furthermore, this study does not reproduce the full IR spectrum so it is unknown if the authors witnessed any rovibrational structure. The other two studies, however, focus on specific vibrational bands and do observe rovibrational structure and hyperfine splitting. Brumfield *et al.* [94] use cavity ring-down spectroscopy coupled to a supersonic jet expansion to record a very high resolution spectrum of the fundamental vibrational transition of ν_8 from 1196.14 to 1197.92 cm^{-1}. From this spectrum, rotational constants for the ν_8 (v = 1) state are determined for each of the three isotopologues. Furthermore, complex hyperfine splitting at low-J values (for both the P and R branches) was observed, which is attributed to the presence of the two bromine nuclei within the molecule. Lastly, Sadiek *et al.* [93] acquired a Doppler limited spectrum from 2955 to 3086 cm^{-1} which incorporated the ν_6 and ν_1 vibrational bands. Within this study, they also saw the peak progressions which are observed for CH_2I_2 (see section 4.3.1). However, these progressions are attributed to the three isotopologues. This study will be furthered discussed in section 5.3.1, in comparison to the results obtained in this thesis.

In addition to these three gas phase studies, there are further liquid IR, [97] solid state IR, [76, 98] and computational studies, [99, 100] for CH_2Br_2. While the majority of these papers do not provide additional information that cannot be gleaned from other studies, one computational paper does attempt to calculate rotational constants (*A*, *B*, and *C*) and vibrational frequencies for the (v = 1) vibrational states of the all nine normal modes. [100] However, the calculated anharmonic frequencies do not match the experimental values, where differences range from the calculated energy being 7 cm^{-1} lower in energy (ν_4) to being 141 cm^{-1} higher in energy (ν_1) (see Table 5-1). Furthermore, the calculated spectroscopic rotational constants are also different than available in given literature, at 400 MHz or 0.013 cm^{-1} higher.

Table 5-1 Literature CH_2Br_2 Fundamental Vibrational Band Origins. Collection of available all fundamental normal vibration transitions in cm^{-1}.

	Symmetry	Gas Phase	Liquid Phase	Solid State	Computational
ν_4	a_1	171.1[i]	….	….	172[a] 165[g] 165[h]
ν_3	a_1	588[a]	577[a] 580[e]	577[e] 576.5[f]	577[a] 558[g] 559[h]
ν_9	b_2	653[a]	635[a] 639[e]	645[e] 636[f]	638[a] 640[g] 608[h]
ν_7	b_1	812[a]	812[a] 810[e]	810[e] 807[e]	813[a] 809[g] 812[g]
ν_5	a_2	….	1095[a] 1090[e]	1089[e] 1090[f]	1095[a] 1105[g] 1111[h]
ν_8	b_2	1195[a] 1196.957[b†]	1192[a] 1191[e]	1182[e] 1179[f]	1193[a] 1219[g] 1215[h]
ν_2	a_1	1382[a]	1387[a] 1388[e]	1385[e] 1385[f]	1388[a] 1423[g] 1434[h]
ν_1	a_1	3009[a]	2989[a] 2994[d] 2988[e]	2987.5[e] 2990[f]	2987[a] 3004[g] 3150[h]
ν_6	b_1	3073[a] 3077.126[c*]	3061[a] 3067[d] 3063[e]	3064[e] 3063[f]	3063[a] 3089[g] 3240[h]

a. Ref. [92]
b. Ref. [94], † is the 79/81 isotope, although all 3 are given.
c. Ref. [93], * is the 79/81 isotope, although all 3 are given.
d. Ref. [97], C_6D_6 solvent used (there are others)
e. Ref. [98]
f. Ref. [76]
g. Ref. [99]
h. Ref. [100], DFT results, assignments changed to match other literature chosen
i. Ref. [90], microwave spectroscopy

5.2. Experiments

5.2.1. 300 K Rovibrational Spectrum

For the room temperature spectrum of CH_2Br_2, the apparatus described in chapter 2.2 was used. The Herriott multipass flow cell was aligned to a path length of 1130 ± 30 cm, as determined using a known concentration of CH_4. The full mid-IR spectrum was recorded from 2921.85 to 3123.78 cm^{-1} using 13 different diffraction grating positions (different windows). For each window, only one repetition rate of the frequency comb laser was used: 250.0000 MHz. This yields a data point separation of 0.0083 cm^{-1}. Due to the broader nature of the peaks within the spectrum, additional repetition rates were not necessary. Each window was recorded multiple times, where each acquisition contained 2000 images (collected with a 50 μs integration time, 125 Hz camera frame rate) and were averaged together for both the signal (CH_2Br_2 sample present) and background (N_2 only). This meant across the 13 windows, 48 spectra were acquired. For each window, comparable data were collected to obtain a CH_4 spectrum in order to frequency calibrate the CH_2Br_2 spectrum. However, only one spectrum was obtained for each window, so only 13 CH_4 spectra total were used for the frequency calibration.

For each background acquisition, a pure flow of N_2 is used. For each sample acquisition pure CH_2Br_2 is used: a liquid sample of CH_2Br_2 (Sigma Aldrich, 99% pure) within the sample container (Teflon PTFE coated) is allowed to reach equilibrium at a vapour pressure of 59.2 mbar (at 298 K). Then an MFC and the vacuum pump controls the flow into the flow cell for a total pressure of 0.7 ± 0.03 mbar. Unlike the measurements for CH_2I_2, no bath gas was used for the full spectrum measurements as the vapour pressure was sufficient enough to allow the MFC to flow the gas. As with the CH_2I_2 experimental, the concentration was verified against the reference spectrum. [95, 216] A factor of 1.48 was calculated as the difference between the $\int \sigma_\nu$ of the reference and experimental spectra: reference = 1.4×10^{-19} cm^2 $molecule^{-1}$ and experimental = 1.00×10^{-19} cm^2 $molecule^{-1}$ (from 2921.8 to 3002.6 cm^{-1}). Using this factor, a final concentration of $(1.69 \pm 0.08) \times 10^{16}$ molecule cm^{-3} is determined. This factor is much less than the factor for CH_2I_2 due to the elimination of the water bath, therefore the only major component to the difference in concentration is loss to the Teflon walls.

As discussed in chapter 3.2, the images for each window are transformed into spectra using the *MATLAB* code and then frequency calibrated using the acquired CH_4 spectra. For an unknown reason, the 840 MHz noise is no longer present in the baseline of the 48 individual spectra, so no fast Fourier transform band-pass is applied. Furthermore, no baseline subtraction was applied to the individual spectra due to improvements in the stability of the laser intensity. Finally, the 48 spectra are concatenated together to give one full and final spectrum from 2921.85 to 3123.78 cm^{-1}. Where adjacent windows overlapped, the spectra was averaged together. In addition, due to the overlapping nature of the windows, each frequency data point was recorded in at least two different windows. The final absorption spectrum can also be converted to σ_ν (in cm^2 molecule^{-1}), as seen as the right *y*-axis for the spectrum shown in Figure 5-1. The error of the σ_ν has also been calculated, using the error in the concentration and the error in the cell path length, yielding an overall error of 5.7%. This is a lower error bar than the measurements for CH_2I_2 due the lack of water bath (no heating of the sample).

5.2.2. Pressure Broadening

To investigate the effect of pressure broadening on the observed peaks within the CH_2Br_2 spectrum, two experiments were performed, both within the flow cell. In these experiments a sample of CH_2Br_2 (concentration kept approximately constant at $(1.60 \pm 0.08) \times 10^{16}$ molecule cm^{-3}) was recorded in a mixture with either N_2 or Ar at various pressures from 10 to 350 mbar. Unfortunately, the pressure reader capable of reading up to atmospheric pressure broke before measurements could be made, so the upper limit of measurements was 350 mbar. Each different total pressure spectrum was recorded from 3048 to 3070 cm^{-1}, however the analysis was performed from 3054 to 3063 cm^{-1} which incorporated 5 different K_a transitions within the ν_6 vibrational band. To keep the analysis simple, only one repetition rate at 250.0000 MHz was used.

After all of the spectra were acquired, the overall Lorentzian broadening parameter was determined using contour fitting in *PGOPHER* (as described in section 3.3.1). Further analysis is then undertaken which is described in section alongside the final results.

5.2.3. Computational Calculations

Due to the increased complexity of the CH_2Br_2 spectrum, especially the introduction of three isotopologues, computational results are needed to guide the spectra fitting process. In addition, a lack of reported rotational constants for ν_4 ($v \leq 3$) vibrational states meant that meaningful calculations were needed in order to begin to simulate the extra peaks within the peak progressions.

Even though there are more basis sets that can be used with bromine-containing molecules, the same basis sets and theory methods that were utilised for CH_2I_2 are also used for CH_2Br_2: wB97X/Def2QZVPP, M062X/Def2QZVPP, B3P86/Def2QZVPP, B3LYP/Def2QZVPP, and MP2/MidiX. All calculations were performed in Gaussian 09 using a tight anharmonic setting. [234] All Gaussian calculations were undertaken by Dr Lehman, and only the output files were used for the analysis here. The appropriate semi-empirical rotational constants were calculated using the method described in 3.3.2. This semi-empirical method was adapted from work published by Sadiek and Friedrichs. [93]

5.3. Results and Discussions

5.3.1. 300 K Rovibrational Spectrum

Figure 5-1 shows the full acquired rovibrational spectrum for CH_2Br_2 from 2925 to 3125 cm^{-1} incorporating two fundamental vibrational transitions: ν_1 and ν_6. Just as in the previous chapter: the left-hand *y*-axis of the spectrum is absorbance, as measured in this experiment, defined as $\ln(I/I_0)$. The right-hand *y*-axis is given in σ_ν (cm^2 $molecule^{-1}$), as defined in the *HITRAN* database and discussed in the previous chapter (Equation 4-1). [216] In addition, Figure 5-1 inset (i) shows a 3 cm^{-1} portion of the spectrum, and inset (ii) shows the CH_2Br_2 molecule superimposed on the rotational axis system used during the analysis. Furthermore, CH_2Br_2 is a near prolate asymmetric top molecule with C_{2v} symmetry, an average κ value of −0.996, using Equation 1-91, as calculated using the ground vibrational state rotational constants from references [88] and [90].

As stated above, the acquired spectrum covers two fundamental vibrational transitions: ν_1 from 2935 to 3040 cm^{-1} and ν_6 from 3040 to 3125 cm^{-1}. The ν_1 normal mode can be described as the symmetric C-H stretch and the ν_6 normal mode is the asymmetric C-H stretch, both of which involve the CH_2 moiety. Firstly, the ν_1 band is a *b*-type transition with a_1 symmetry, which manifests itself with ${}^{P/R}Q_{Ka}(J)$ branches and no central Q branch. Conversely, the ν_6 band is a *c*-type transition with b_1 symmetry and has a strong, central Q branch alongside well-defined ${}^{P/R}Q_{Ka}(J)$ branches. To determine the band strength ratio between the two modes, the $\int\sigma_\nu$ areas are calculated. For ν_1 this value is 3.49×10^{-19} cm^2 $molecule^{-1}$ (from 2935.001 to 3034.998 cm^{-1}), and for ν_6 this value is 2.02×10^{-19} cm^2 $molecule^{-1}$ (from 3040.001 to 3123.783 cm^{-1}). These regions cover the majority of the two

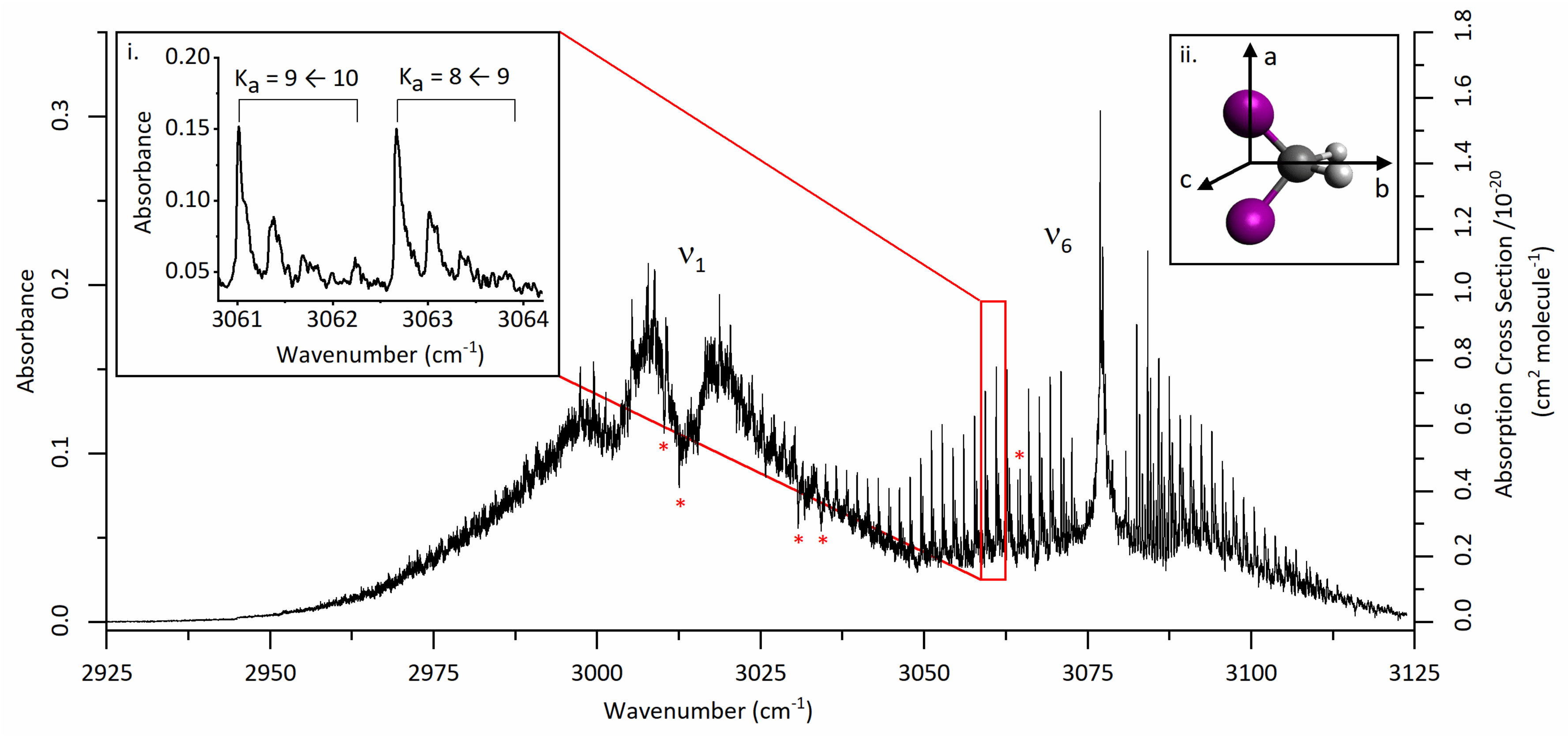

Figure 5-1 Full Experimental CH_2Br_2 Spectrum. The full experimental vibrational spectrum from 2925 to 3125 cm^{-1}, acquired under the conditions: 298 K, path length of 1130 ± 30 cm, CH_2Br_2 pressure of 0.7 ± 0.03 mbar. Red asterisks indicate water impurities within the spectrum. The left *y*-axis shows the absorbance measured in this thesis, and the right *y*-axis shows absorption cross section (cm^2 molecule^{-1}). (i) Zoomed in portion of the ν_6 spectrum from 3060.7 to 3064.2 cm^{-1}, showing two K$_a$ transitions (9 ← 10 and 8 ← 9). (ii) Molecular structure of CH_2Br_2 (bromine = purple, carbon = grey, hydrogen = white). The axes show the labels used for this analysis: the ν_6 asymmetric stretch causes a transition dipole moment (TDM) along the *c*-axis and the ν_1 symmetric stretch causes a TDM along the *b*-axis.

bands, however, they avoid the overlapping region of the two bands around 3035 to 3040 cm^{-1}. Therefore, the band strength ratio is 1:1.73 for ν_6:ν_1 which agrees well with the reference data. In the case of the reference data, [95] for ν_1 (from 2935.00 to 3035.00 cm^{-1}) the $\int\sigma_\nu$ is 3.58 × 10^{-19} cm^2 molecule^{-1}, and for ν_6 (from 3040.00 to 3125.00 cm^{-1}) the integrated value is 1.93 × 10^{-19} cm^2 molecule^{-1}. This gives a band strength ratio of 1:1.86 for ν_1:ν_6.

As seen in Figure 5-1 inset (i), there are many peaks within each vibrational transition band. Each peak consists of many J transitions, which due to Doppler, pressure, and instrument line-shape broadening appear as one peak. The majority of this broadening is likely to be pressure broadening. However, there are too many peaks in the spectrum which can be attributed to the fundamental vibrational transitions, even considering the amount of rovibrational transitions. Looking at inset (i), this shows two different K_a transitions, where $K_a = 9 \leftarrow 10$ and $K_a = 8 \leftarrow 9$. While there should only be two peaks, one for each K_a transition, there are at least 4 peaks near each K_a transition. Hereafter, the repeating stacks of peaks within a K_a transition are referred to as progressions. For the reference data, [95] as the spectrum was recorded at atmospheric pressure, the individual peaks do begin to convolve into one broad peak, (average FWHM of 0.6 cm^{-1}) however the top of each peak is still visible. This is further visible in Figure 5-2 and inset (i), where the reference spectrum (red line) is overlaid on the experimental spectrum (black line).

The progressions seen in this spectrum were previously seen in the work of Sadiek *et al.* [93]. However in this instance, the progressions were attributed to the three isotopologues of CH_2Br_2. The most intense peak in each progression was assigned to the 81/81 isotopologue, followed by 79/81 and finally, 79/79. While this theory is justifiable, it does have its limitations. Firstly, this theory ignores the 4th peak in the progressions. Secondly, the relative intensity of the peaks in the progressions do not match the expected abundance ratio of 1:2:1 (for 81/81:79/81:79/79), and instead follows a pattern of approximately 1:0.5:0.25. Finally, the isotopic shift between the isotopologues has to be 0.28 cm^{-1} between the 79/79 and 79/81 molecules, and 0.395 cm^{-1} 79/81 and 81/81 molecules. This is much higher than any of the calculated isotopic shifts, which are typically on the order of 0.01 cm^{-1}.

Therefore, this thesis proposes that the observed peak progressions are due to hot-bands transitions from the ν_4 vibrational states. The following section describes the fitting results for ν_6 band in which the hot-band transitions are included.

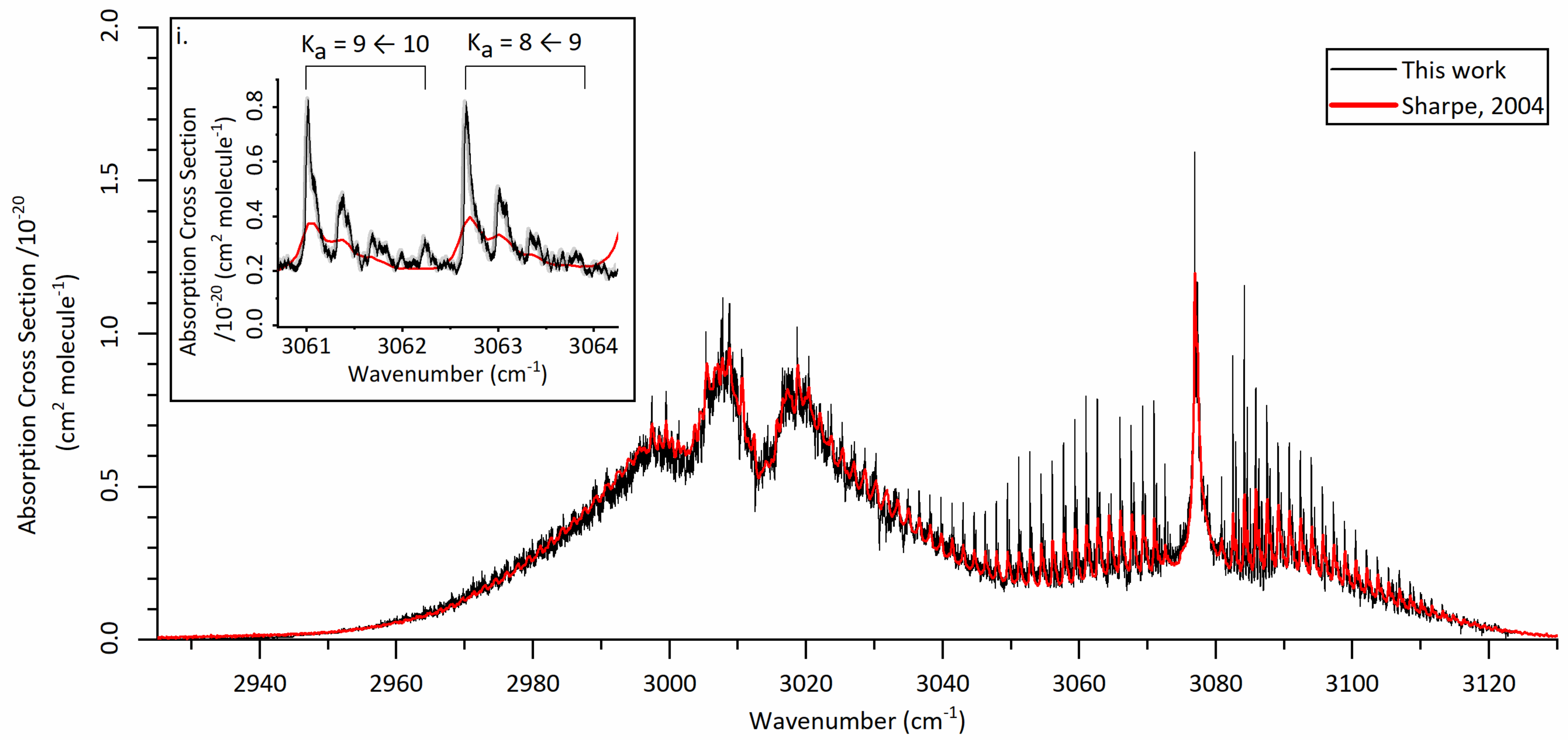

Figure 5-2 Comparison of Experimental and Reference Spectra of CH_2Br_2. Experimental spectrum in black from 2925 to 3130 cm^{-1}, and corresponding portion of the reference spectrum in red. [95] (i) Zoomed in portion of the two spectra from 3060.6 to 3064.3 cm^{-1} incorporating two K_a transitions (9 ← 10 and 8 ← 9). The grey shading shows the error of the black experimental spectrum as determined by the path length and concentration of the sample.

5.3.1.1. Fitting results of the ν_6 band

For the ν_6 vibrational band, the discernible peaks span from 3035 up to 3120 cm^{-1}, with the band origin at 3076.7205(5) cm^{-1}. Approximately 150 peaks in this band are detectable, which assumes a minimum detectable absorption of 3σ above the baseline noise ($\sigma = 1.5 \times 10^{-4}$). As was the case for CH_2I_2, these peaks involve a strong central Q branch and $^{P/R}Q_{Ka}(J)$ branches which are spaced by approximately $2(A-\bar{B})$. Once again, for a *c*-type transition and using the inertial axes as labelled in Figure 5-1 inset (ii), the rotational selection rules are: $\Delta J = 0, \pm1$, $\Delta K_a = \pm1$, and $\Delta K_c = 0, \pm2$. Due to broadening of the observed transitions, each peak is a combination of many transitions, where there are different J and K_c transitions, but the same K_a transition for each peak.

In order to fit the experimental spectrum and determine the rotational constants of the ν_6 (v = 1) vibrational state, *PGOPHER* was used as described in section 3.3.1. This fitting procedure was undertaken by Dr Sadiek (*Leibniz Institute for Plasma Science and Technology)* as part of an ongoing collaboration. For this fitting procedure, the origin, *A*, *B*, and *C* constants for each isotopologue ν_6 (v = 1) state were fitted using the band-head fitting procedure (as described in section 3.3.1) and using Watson's *A* reduction Hamiltonian. The initial starting point for each rotational constant in each vibrational state (apart from the ground state), were taken from the semi-empirical results of the wB97X/Def2QZVPP computational results. Unlike for CH_2I_2, higher level distortion constants (Φ_K, Φ_{KJ}, Φ_{JK}, Φ_J) were not included in the simulations due to a lack of appropriate constants within available literature. However, the distortion constants, D_J, D_{JK}, D_k, δ_k, and δ_J were included in the simulations, but were not fitted due to a lack of appropriate higher K_a transitions. While values of these distortion constants are only shown in Table 5-2 for the ground (v = 0) state and the ν_6 (v = 1) state for each isotopologue, the constants are held the same for all vibrational states included in the simulation. For the simulation presented in Figure 5-3, the temperature was set to 300 K, the Gaussian broadening parameter was 0.0029 cm^{-1}, and the Lorentzian broadening parameter was set to 0.0281 cm^{-1}.

For the ν_6 band, the results of the fitted spectroscopic rotational constants for each isotopologue ν_6 (v = 1) vibrational state are stated in Table 5-2. The degree of uncertainty given in Table 5-2 (and Table 5-3) is the calculated standard deviation based on the quality of the fit and the difference between the experimental transition peak and the assigned simulation peak. These errors are of similar magnitude to the errors seen for the CH_2I_2 vibrational state rotational constants. However, it is notable that the three isotopologue band origins for ν_6 (v = 1) are more accurate than the equivalent band origin for CH_2I_2. This difference is due to the reduction in the number of higher K_a transitions which need to be included within the band-head fitting procedure.

Once again, in order to ensure the simulation of all three isotopologues matches the experimental spectrum, the hot-band transitions arising from the ν_4 vibrational states are included. However, as CH_2Br_2 has a higher transition frequency for the fundamental ν_4 transition with a transition wavenumber of 171.1 cm^{-1}, [90] there are fewer visible hot-bands. Calculating the Boltzmann population distribution for the population residing in the ground state and the ν_4 ($v \leq 3$) states yields of ratio of: 1:0.44:0.19:0.08.

However, unlike for CH_2I_2, there is a lack of literature citing spectroscopic rotational constants for the ν_4 vibrational states. There is one study which cites ν_4 (v = 1) rotational constants for the 79/81 isotopologue, [90] however it is impossible to extroplate the constants for the two other isotopologues based on one set of results. Therefore, the semi-empirical results of the wB97X/Def2QZVPP (see section 5.3.3) for the origin, *A*, *B*, and *C* rotational constants, were utilized as a starting point for the ν_4 ($v \leq 3$) vibrational states. In order to ensure the fitting results are accurate, both the lower vibrational states (ν_4 ($v \leq 3$)) rotational constants were fitted alongside the excited vibrational states (ν_6 (v = 1) + ν_4 ($v \leq 3$)) rotational constants for each isotopologue. The results of the fitting can be seen in Table 5-3.

While there is literature citing the 4_0^1 transition energy for CH_2Br_2, this is only one value at 171.1 cm^{-1} and which is for the 79/81 isotopologue. [90] Once again however, as the vibrational quantum number does not change for ν_4 in the observed transitions, the vibrational band origins for 4_0^n cannot be calculated. However, the band-head fitting procedure did attempt to fit the 4_0^n band origins, alongside the $6_0^1 4_n^n$ band origins (Table 5-3). Furthermore, the value for the x_{64} cannot be calculated, but the x_{66} anharmonicity constant for the 79/81 isotopologue is calculated to be −0.747(4) cm^{-1}.

While Figure 5-3 shows the complete simulation for the ν_6 band, Figure 5-4 part A shows the breakdown of the different $6_0^1 4_n^n$ transitions included in the simulation. For the ν_6 band, there are 4 different vibrational transitions which can be attributed to either the 6_0^1 vibrational transition or the $6_0^1 4_n^n$ up to v = 3. In addition, there are the three different isotopologues for CH_2Br_2, which means there is a total of 12 different vibrational transitions within the full simulation. Both figures also show the residual plot (green line) between the experimental spectrum and the full simulation. While there is a good agreement between

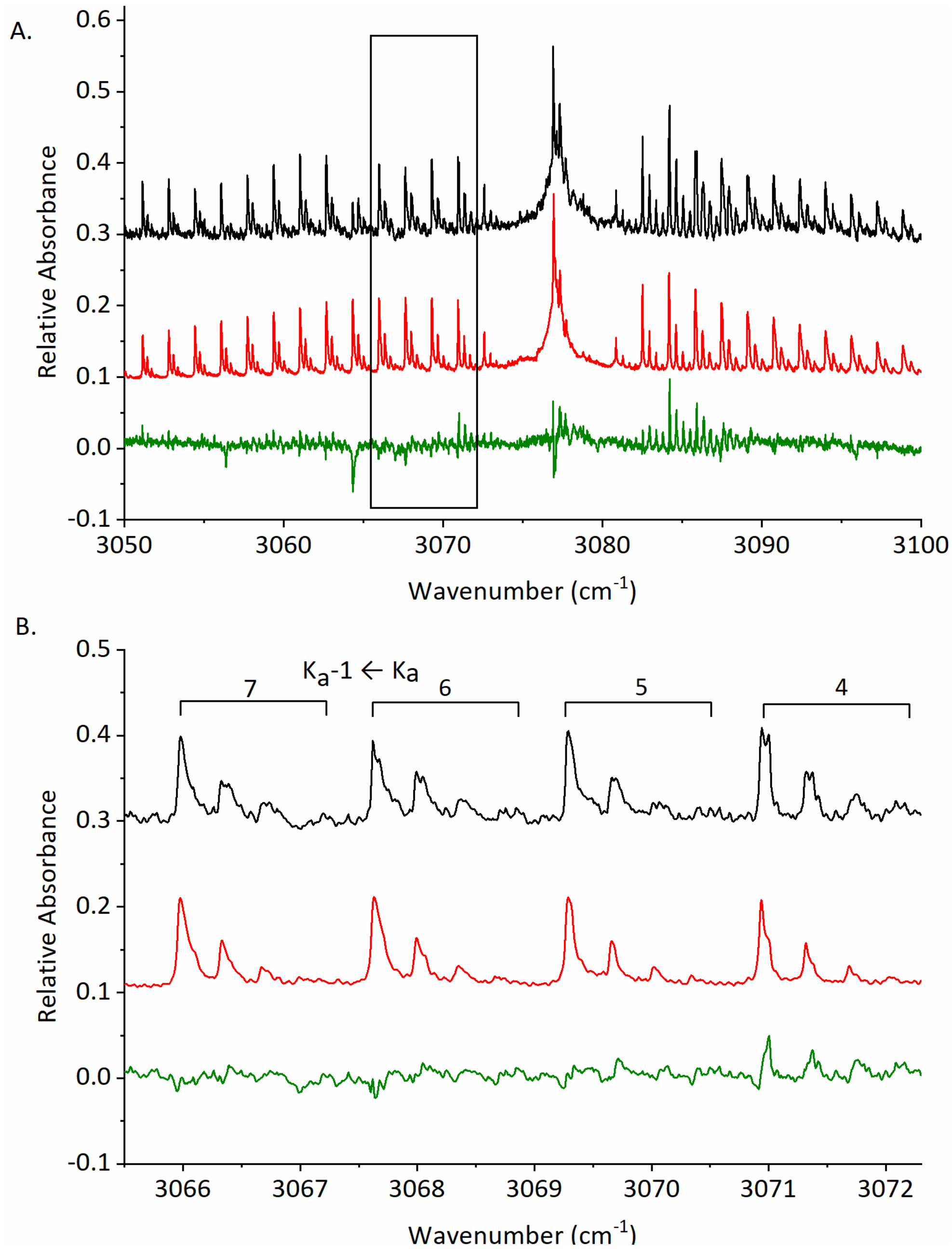

Figure 5-3 Comparison of CH_2Br_2 ν_6 Simulation to Experimental Spectrum. A. Comparison of the experimental spectrum (black) and the overall simulation (red), as determined in *PGOPHER*, for the ν_6 band from 3050 to 3100 cm^{-1}. The overall simulation is comprised of the different simulated transitions for the fundamental 6^1_0 band and the $6^1_0\,4^n_n$ hot bands, where $n \leq 5$. *Y*-axis shows relative absorbance of the experimental and simulation spectra, where the simulation has been scaled up to match the experimental. The green line is the residual plot of experimental minus the overall simulation. B. Zoomed in portion of the three spectra, from 3065.5 to 3072.2 cm^{-1} showing 4 different K_a transitions in the ^PQ branch.

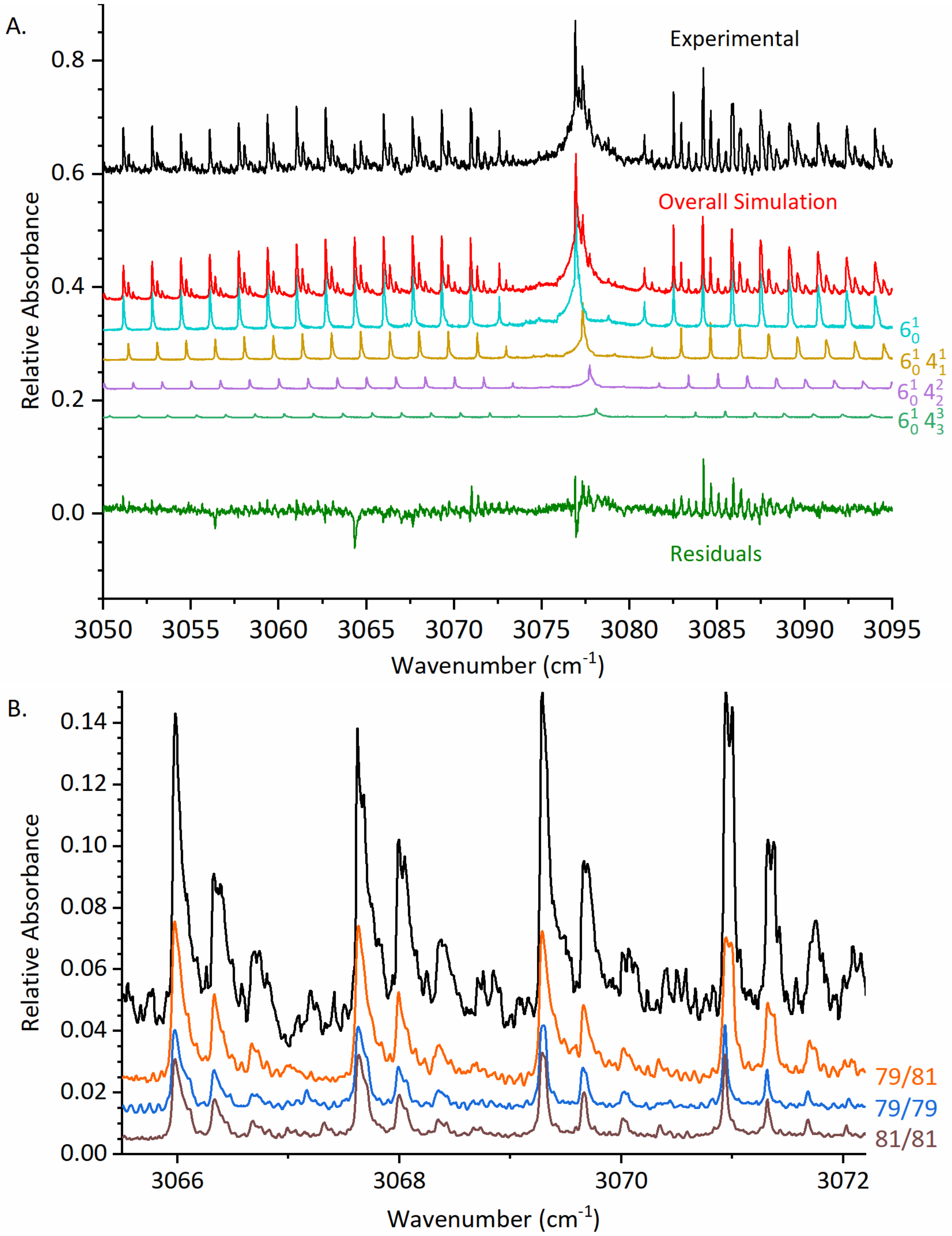

Figure 5-4 CH_2Br_2 ν_6 Simulation breakdown. A. Breakdown of the 6 different vibrational transitions which make up the *PGOPHER* simulation shown from 3050 to 3095 cm^{-1}: 6_0^1 (light blue), $6_0^1 4_1^1$ (yellow), $6_0^1 4_2^2$ (purple), $6_0^1 4_3^3$ (light green). Experimental spectrum (black), overall simulation (red), and residual plot (dark green) are also shown. B. Breakdown of the three different isotopologues which make up the *PGOPHER* simulation shown from 3065.5 to 3072.2 cm^{-1}: 79/81 (orange), 79/79 (dark blue), 79/81 (brown). The experimental spectrum is also shown in black.

the two spectra, there is a small mismatch in the observed relative intensities. Most notably, at 3064 cm^{-1} there is a large discrepancy between the two spectra. However, this discrepancy can be attributed to a water absorption within the experimental spectrum which is causing the observed peak to be lower in intensity than expected (red asterisks in Figure 5-1). This is due to a water contamination within the background images that was not present in the signal images. Fortunately, this did not cause any significant issues with the fitting of any of the spectroscopic rotational constants. There is a further difference in intensity in the R branch of the spectra, where the simulated spectrum is under predicting the intensities of the absorption peaks. Notably, this is the opposite of the effect seen in CH_2I_2 (refer to section 4.3.1).

Furthermore, part B shows the breakdown of the three different isotopologues: grey is the experimental spectrum, yellow is the 79/81 isotopologue, blue is 79/79 isotopologue, and purple is the 81/81 isotopologue. While the isotope shift has been governed by the wB97X/Def2QZVPP semi-empirical results, the breakdown shows there is a small difference in the isotope shift, so much so it is practically negligible. The bigger difference between the isotopologues is the relative intensities, which follows the pattern of 1:2:1 for the 79/79:79/81:81/81 isotopologues.

5.3.1.2. Fitting results of the ν_1 band

For the ν_1 vibrational band, the overall band spans from 2935 to 3040 cm^{-1}, however unlike for the ν_6 band, there is no defined structure. In addition, the few visible peaks around 3005 cm^{-1} are difficult to assign. As will be discussed in section 5.3.3, the semi-empirical results could not simulate the experimental spectrum correctly, even though all three isotopologues and hot-bands transitions from ν_4 ($v \leq 3$) were included in the simulations. As such, there are no fitting results for this band.

Possible explanations for the crowded spectrum can be sought in the work of CH_2F_2 and CH_2Cl_2. For CH_2Cl_2, there has been evidence of Fermi coupling between the 1_0^1 and 2_0^2 transitions, which have transition wavenumbers of 2997.3 cm^{-1} and 2853 cm^{-1}, respectively. [73] However, for CH_2Br_2 the same transitions have wavenumbers of approximately 3009 cm^{-1} and 2764 cm^{-1}, so any possible Fermi coupling would be very weak. For CH_2F_2, there has been evidence of coupling between 6 different transitions between 2800 and 3100 cm^{-1}: 1_0^1, 6_0^1, 2_0^2, 8_0^2, and $2_0^1 8_0^1$. [46] However, for CH_2Br_2 the 8_0^2 and $2_0^1 8_0^1$ transition wavenumbers are 2390 cm^{-1} and 2577 cm^{-1}, which are much too low in energy to consider coupling to the 1_0^1 transition. This is further explored later on in the context of the other

Table 5-2 Experimentally determined rotational constants for CH_2Br_2 for the vibrational ν_6 (v = 1) state for each isotopologue. All constants in cm^{-1}. Standard deviation in brackets.

79/79	Ground state (v = 0)[a]	ν_6 (v = 1)
Origin	···	3076.7205(5)
A	0.86831117	0.867759(6)
B	0.041313137	0.0413355(6)
C	0.039725549	0.0397480(3)
$D_K \times 10^{-5}$	1.2922	1.2922
$D_{JK} \times 10^{-7}$	−3.8403	−3.8403
$D_J \times 10^{-9}$	7.932	7.932
$d_k \times 10^{-8}$	3.936	3.936
$d_J \times 10^{-10}$	5.228	5.228
79/81	Ground state (v = 0)[b]	ν_6 (v = 1)
Origin	···	3076.7187(5)
A	0.867519156	0.866907(5)
B	0.040804716	0.040827(6)
C	0.039253679	0.0392753(5)
$D_K \times 10^{-5}$	1.290	1.288
$D_{JK} \times 10^{-7}$	−3.806	−3.750
$D_J \times 10^{-9}$	7.749	7.566
$d_k \times 10^{-8}$	−6.438	3.783
$d_J \times 10^{-10}$	−1.034	4.877
81/81	Ground state (v = 0)[a]	ν_6 (v = 1)
Origin	···	3076.7177(4)
A	0.866756	0.866122(4)
B	0.040297	0.0403195(3)
C	0.038782	0.0388033(3)
$D_K \times 10^{-5}$	1.288	1.290
$D_{JK} \times 10^{-7}$	−3.750	−3.806
$D_J \times 10^{-9}$	7.566	7.749
$d_k \times 10^{-10}$	3.783	−6.438
$d_J \times 10^{-9}$	4.877	−1.034

a. Constants from ref. [88]
b. Constants from ref. [90]

Table 5-3 Experimentally determined rotational constants for CH_2Br_2 for the vibrational states ν_4 (v ≤ 3) and ν_4 (v ≤ 3) + ν_6 (v = 1) for each isotopologue. All constants in cm^{-1}. Standard deviation in brackets.

79/79	ν_4 (v = 1)	ν_6 (v = 1) + ν_4 (v = 1)	ν_4 (v = 2)	ν_6 (v = 1) + ν_4 (v = 2)	ν_4 (v = 3)	ν_6 (v = 1) + ν_4 (v = 3)
Origin	172.078(3)	3249.204(3)	343.859(1)	3421.381(3)	515.4599(6)	3593.360(7)
A	0.87187(5)	0.87123(6)	0.87543(1)	0.87472(1)	0.879395(7)	0.87843(2)
B	0.041315(7)	0.041337(7)	0.041275(8)	0.041303(8)	0.041257(2)	0.041328(2)
C	0.039711(4)	0.039731(4)	0.039711(7)	0.039729(6)	0.039666(7)	0.039673(7)
79/81	ν_4 (v = 1)	ν_6 (v = 1) + ν_4 (v = 1)	ν_4 (v = 2)	ν_6 (v = 1) + ν_4 (v = 2)	ν_4 (v = 3)	ν_6 (v = 1) + ν_4 (v = 3)
Origin	171.1008(3)	3248.229(3)	341.6389(3)	3419.16(3)	512.5325(4)	3590.406(1)
A	0.871208(2)	0.870566(6)	0.874895(3)	0.87421(1)	0.87850(2)	0.878058(2)
B	0.040788(1)	0.04081(1)	0.040747(8)	0.040773(8)	0.040747(2)	0.040778(2)
C	0.039227(5)	0.039246(4)	0.039247(7)	0.039265(7)	0.039195(7)	0.039211(7)
81/81	ν_4 (v = 1)	ν_6 (v = 1) + ν_4 (v = 1)	ν_4 (v = 2)	ν_6 (v = 1) + ν_4 (v = 2)	ν_4 (v = 3)	ν_6 (v = 1) + ν_4 (v = 3)
Origin	170.1369(2)	3247.264(2)	340.0197(3)	3417.538(3)	509.649(4)	3587.537(4)
A	0.870371(6)	0.869715(6)	0.874255(9)	0.873564(9)	0.87892(2)	0.87866(3)
B	0.039961(7)	0.03998(7)	0.040262(7)	0.040287(8)	0.040081(2)	0.040118(2)
C	0.038468(4)	0.038487(4)	0.038731(6)	0.03875(6)	0.038794(7)	0.038802(7)

CH_2X_2 molecules (see section 6.1).

However, liquid Raman studies of CH_2Br_2 shows evidence of Fermi coupling between the 1_0^1 fundamental transition and several forbidden transitions. [269] These transitions appear when an allowed transition is close in energy to the forbidden transition, and intensity is borrowed between the transitions giving a Fermi doublet. Such forbidden transitions were theorised to be $2_0^1 7_0^2$, $3_0^2 8_0^1 9_0^1$, $2_0^1 4_0^2 9_0^2$, and $3_0^3 9_0^2$. Although these transitions were observed in liquid Raman studies, they are also allowed IR transitions, with symmetry labels of a_1, and have approximate gas-phase transition wavenumbers of approximately 3006 cm^{-1}, 3024 cm^{-1}, 3026 cm^{-1}, and 3070 cm^{-1}, respectively. Further work in the study used the modified Winther method to calculate the Fermi coupling constant, *W*, of the perturbed transitions. This calculated coupling constant gave imaginary values for the $3_0^2 8_0^1 9_0^1$ and $3_0^3 9_0^2$ transitions, meaning that the $2_0^1 7_0^2$ and $2_0^1 4_0^2 9_0^2$ are the most probable transitions causing the observed Fermi-doublet coupling. Considering the normal modes and symmetry of these combination bands where ν_2 (a_1) is the CH_2 scissor motion, ν_7 (b_2) is the CH_2 rocking motion, ν_4 (a_1) is the CX_2 scissor motion and ν_9 (b_2) is the CX_2 asymmetric stretch, it is possible these different normal modes could combine into different combination band. In the case of the $2_0^1 7_0^2$ and $2_0^1 4_0^2 9_0^2$ both of these states have an a_1 symmetry, which allows for coupling to the ν_1 (a_1) vibrational mode. Furthermore, although these complex combination bands could be the cause of the congested ν_1 band, it would be difficult to confirm this in practice, both experimentally and computationally.

5.3.2. Pressure Broadening Coefficients

Just as for the CH_2I_2 spectrum, each peak within the CH_2Br_2 spectrum is comprised of many rovibrational transitions which are broadened due to a variety of factors. The expected Doppler broadening for the transitions around 3000 cm^{-1} at room temperature is 0.0029 cm^{-1}, which is observed as a Gaussian line-shape. There is also the Lorentzian line-shape contribution from the instrument line-shape function, which as discussed in section 3.4, is 0.0142 cm^{-1}. However, when including both of these broadening values in the *PGOPHER* simulations, the experimental spectrum shows additional broadening which is not captured. In order to match the simulation to the experimental spectrum (as shown in Figure 4-3), the Gaussian contribution is set to 0.0029 cm^{-1} and the Lorentzian contribution is 0.0281 cm^{-1}. Therefore, the increase of the Lorentzian contribution from 0.0142 cm^{-1} to 0.0281 cm^{-1} is most likely due to pressure broadening. This is further confirmed by considering the reference spectrum (Figure 5-2). Here, the observed absorption peaks are broadened due to the atmospheric experimental conditions.

As stated in the experimental section, the spectra for the pressure broadening analysis was collected from 3048 to 3070 cm^{-1}, which incorporated the ν_6 band, for two different bath gases; N_2 and Ar. Contour fitting was then undertaken in *PGOPHER* to fit an overall Lorentzian broadening parameter (as a FWHM) between 3054 to 3063 cm^{-1}. This region incorporated 6 different K_a transitions. This region was chosen as it has well-defined absorption transition peaks with high intensity, and does not incorporate any overlap with the complicated ν_1 band. The overall fitted Lorentzian parameter includes the contribution from the instrument line-shape function, so this is removed before further analysis is undertaken. Then, the remaining FWHM is converted to a HWHM for the remainder of the analysis. For each HWHM, the pressure broadening can be split into two contributions; self-broadening and bath gas-broadening (Equation 4-15).

Unfortunately, due to the configuration of the gas delivery set up, the concentration of CH_2Br_2 varies slightly for each acquired spectrum. Within the N_2 spectra the CH_2Br_2 concentration varies from 0.37 to 1.10 mbar, and for Ar spectra the CH_2Br_2 concentration varies from 0.32 to 0.61 mbar. However, as this variation is only small compared to the variation in the pressure of the bath gases, experiments were not undertaken to vary the concentration of CH_2Br_2, and b_{self} was not determined. Since there is a small variation in the concentration of CH_2Br_2, the variance must be removed from each overall HWHM Lorentzian parameter. This removal ensures the broadening coefficient for each bath gas is accurately determined. The process follows the same as described in the previous chapter (section 4.3.2), where an initial plot of $\Gamma_{\text{broadening}}$ vs bath gas partial pressure (one each for N_2 and Ar) is created, and the intercept from a linear slope represents the average self-broadening parameter. The average parameter is them removed from the individual HWHM parameters to give a new Lorentzian value. [263] The new HWHM values are then plotted against the partial pressure of the appropriate bath gas, and linear slopes are fitted to the data, where the slope corresponds to the b_x parameter. The results of the two linear fits are shown in Figure 5-5.

For N_2, the $\Gamma_{\text{broadening}}$ parameter ranged from 0.0004 cm^{-1} at 10.3 mbar to 0.049 cm^{-1} at 326.7 mbar (after correcting for the self-broadening). This corresponds to a b_x value of $1.44(6) \times 10^{-4}$ cm^{-1} mbar or 0.145(7) cm^{-1} atm^{-1}. Conversely, for Ar the $\Gamma_{\text{broadening}}$ parameter ranged from 0.0002 cm^{-1} at 11.4 mbar to 0.033 cm^{-1} at 336.9 mbar (after correcting for the self-broadening). This corresponds to a b_x value of $1.04(5) \times 10^{-4}$ cm^{-1} mbar or 0.105(5) cm^{-1} atm^{-1}. These values are also recorded in Table 5-4. For all given values, the error values given in brackets correspond to the fit of the slope.

Comparisons can then be made between the two broadening parameters. Just as for CH_2I_2, the two values are of similar magnitude, but they differ in absolute value and are outside the margins of error to be considered the same value. For the two coefficients, b_{N2} is 1.38 times bigger than the b_{Ar} value. This means as the molecules collide with nitrogen, this result in 1.38 times broader CH_2Br_2 transitions. In addition, this means that any atmospheric observations of CH_2Br_2 vibrational transitions will be significantly broad.

Attempting to compare the experimental values reported here to other available values is difficult due to the lack of appropriate pressure broadening studies for CH_2X_2 molecules (were X = F, Cl, Br, or I). For b_{N2} there is only one study for the CH_2F_2 molecule.

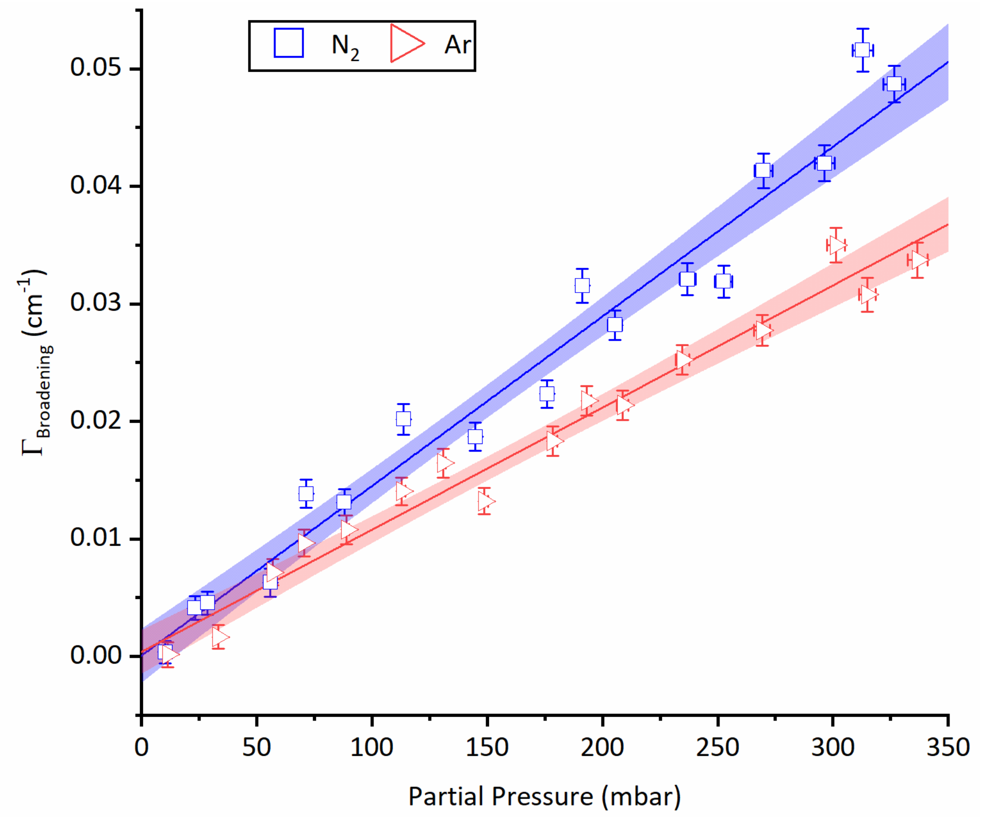

Figure 5-5 CH_2Br_2 Pressure Data. $\Gamma_{\text{broadening}}$ (cm^{-1}) as a function partial pressure of either N_2 or Ar from 0 to 350 mbar. Blue squares are the N_2 data with a corresponding blue linear line-fit and a 95% confidence limit. Red triangles are the Ar data with a red linear line-fit and a 95% confidence limit.

Table 5-4 CH_2Br_2 Pressure Broadening Coefficients. Broadening coefficients from this work for N_2 and Ar with the error fit of the linear line-fit given in brackets. Average J-dependent broadening coefficients from available literature for CH_3Br, CH_2F_2 and CH_3F, with the standard deviation in brackets.

Collision Partner	CH_2Br_2 *b* (cm^{-1} atm^{-1})	CH_3Br *b* (cm^{-1} atm^{-1})	CH_2F_2 *b* (cm^{-1} atm^{-1})	CH_3F *b* (cm^{-1} atm^{-1})
N_2	0.145(7)^a	0.103(11)^b	0.087^c	0.101(14)^d
Ar	0.105(5)^a	…	…	0.063(6)^e

a. This work
b. Ref. [270]
c. Ref. [263]
d. Ref. [265]
e. Ref. [266]

For this molecule the b_{N2} parameter ranges from 0.061 to 0.125 cm^{-1} atm^{-1}, with an average value of 0.087 cm^{-1} atm^{-1}. [263]

However, there have been more studies for the CH_3X molecules, where each of the four halogen-substituted methane molecules has an observed b_{N2} parameter. Calculating average values for different CH_3X molecules yields an average of 0.105 cm^{-1} atm^{-1}, and specifically for CH_3Br, the average is b_{N2} parameter = 0.103(11) cm^{-1} atm^{-1}. [270] These two values are averages over J-dependent values, where values for CH_3Br ranged from 0.0737 cm^{-1} atm^{-1} to 0.1284 cm^{-1} atm^{-1}. In addition, there is only study in total for a b_{Ar} parameter, which is for the CH_3F molecule. For both of the studies involving the CH_3F molecule, the b_{N2} parameter ranges from 0.087 to 0.123 cm^{-1} atm^{-1}, with an average value of 0.101(14) cm^{-1} atm^{-1}, [265] and the b_{Ar} parameter from 0.050(3) cm^{-1} atm^{-1} to 0.080(5) cm^{-1} atm^{-1} with an average of 0.063(6) cm^{-1} atm^{-1}. [266] Comparing to the CH_2Br_2 values in Table 5-4, both of the experimental values are much higher than those reported for CH_3F. However, the general trend of b_{N2} being higher than b_{Ar} still stands true. Furthermore, the experimental value in this thesis for the b_{N2} parameter is much higher than the highest J-dependent b_{N2} value for CH_3Br. Therefore, the observed b_{N2} and b_{Ar} parameters are potentially higher than expected. The most probable explanation for this difference in the literature and experimental parameters is that the contribution of the bath gas to pressure broadened transitions has been over-predicated. Furthermore, the contribution of self-broadening by CH_2Br_2 might be under-predicted. Further comparisons between the CH_2X_2 and CH_3X molecules will be made in chapter and section 6.2.

Comparisons can also be made to the reference spectrum. [95] The experimental conditions for that study uses N_2 as a bath gas with a total pressure of 1013 mbar (atmospheric pressure). Using the same *PGOPHER* contour fitting method, the $\Gamma_{broadening}$ value is determined to be 0.231(5) cm^{-1}. Using the linear fit results shown in Figure 4-7, a prediction $\Gamma_{broadening}$ value can be calculated to be 0.146(1) cm^{-1} at the same 1013 mbar pressure. While the predicted $\Gamma_{broadening}$ is lower than the fitted $\Gamma_{broadening}$ value, the reference data still incorporates any ILS function and does not account for the self-broadening of CH_2Br_2.

5.3.3. Computational Calculations

While the computational results for CH_2I_2 were used to confirm the hot-band theory, the corresponding computational results for CH_2Br_2 were acquired in order to guide the fitting procedure. The computational results were especially necessary as there was limited literature available for the spectroscopic rotational constants of the ν_4 (v ≤ 3) vibrational states. In addition, computational results for involving the ν_1 (v = 1) vibrational state may allow for some understanding of the observed congested band.

Table 5-5 to Table 5-10 give the semi-empirical computational values for the four different levels of theory and the corresponding basis sets. Unfortunately, the computational results for the MP2/MidiX combination produced nonsensical results which were impossible to interpret, and so they not reproduced within this thesis. Table 5-5, Table 5-6, and Table 5-7 give the values for the ground state (v = 0), ν_6 (v = 1), ν_4 (v = 1), and the first hot band ν_6 (v = 1) + ν_4 (v = 1), for each of the three isotopologues: 79/79, 79/81, and 81/81, respectively. Table 5-8, Table 5-9, and Table 5-10 give the values for the ground state (v = 0), ν_1 (v = 1), ν_1 (v = 1), and the first hot band ν_1 (v = 1) + ν_4 (v = 1), for each of the three isotopologues: 79/79, 79/81, and 81/81, respectively. Initially looking at all the semi-empirical values within Table 5-5 (and also Table 5-6 and Table 5-7), the rotational constants for the ground state do differ from the literature ground state values. However, the Δ_i between the three rotational constants for the calculated ground state and upper vibrational states are all on the same magnitude and value: typically 5×10^{-3} cm^{-1} for the *A* rotational constant, and -2.0×10^{-5} cm^{-1} for the *B* and *C* constants.

For the ν_6 band, once again the wB97X/Def2QZVPP results matched the closest to the experimental spectrum (black spectrum), as seen in Figure 5-6 part A, so a comparative analysis is given for this semi-empirical simulation. However, the results from the other four stimulated spectra were not dissimilar from the experimental spectrum.

Alongside calculating rotational constants of the different vibrational states, the computational results were also used to understand the isotopic shift between the band origins of the three different isotopologues. For each of the computational results the isotope shift was calculated. For wB97X/Def2QZVPP: Δ(79/81 − 79/79) = 0 cm^{-1} and Δ(79/81 − 81/81) = −0.003 cm^{-1}. For B3LYP/Def2QZVPP: Δ(79/81 − 79/79) = −0.019 cm^{-1} and Δ(79/81 − 81/81) = 0.043 cm^{-1}. For M062X/Def2QZVPP: Δ(79/81 − 79/79) = 0.134 cm^{-1} and Δ(79/81 − 81/81) = 0.237 cm^{-1}. Lastly, for B3P86/Def2QZVPP: Δ(79/81 − 79/79) = 0.02 cm^{-1} and Δ(79/81 − 81/81) = −0.103 cm^{-1}. The first thing to note is that the isotope shifts are not identical between the three isotopologues for each computational result. Secondly, the expected pattern that the band origins decrease in wavenumber with increasing isotope weight is not exhibited by every computational result. In addition the overall pattern of band origin energies is inconsistent, such that the 79/79 isotope pair should exhibit the highest

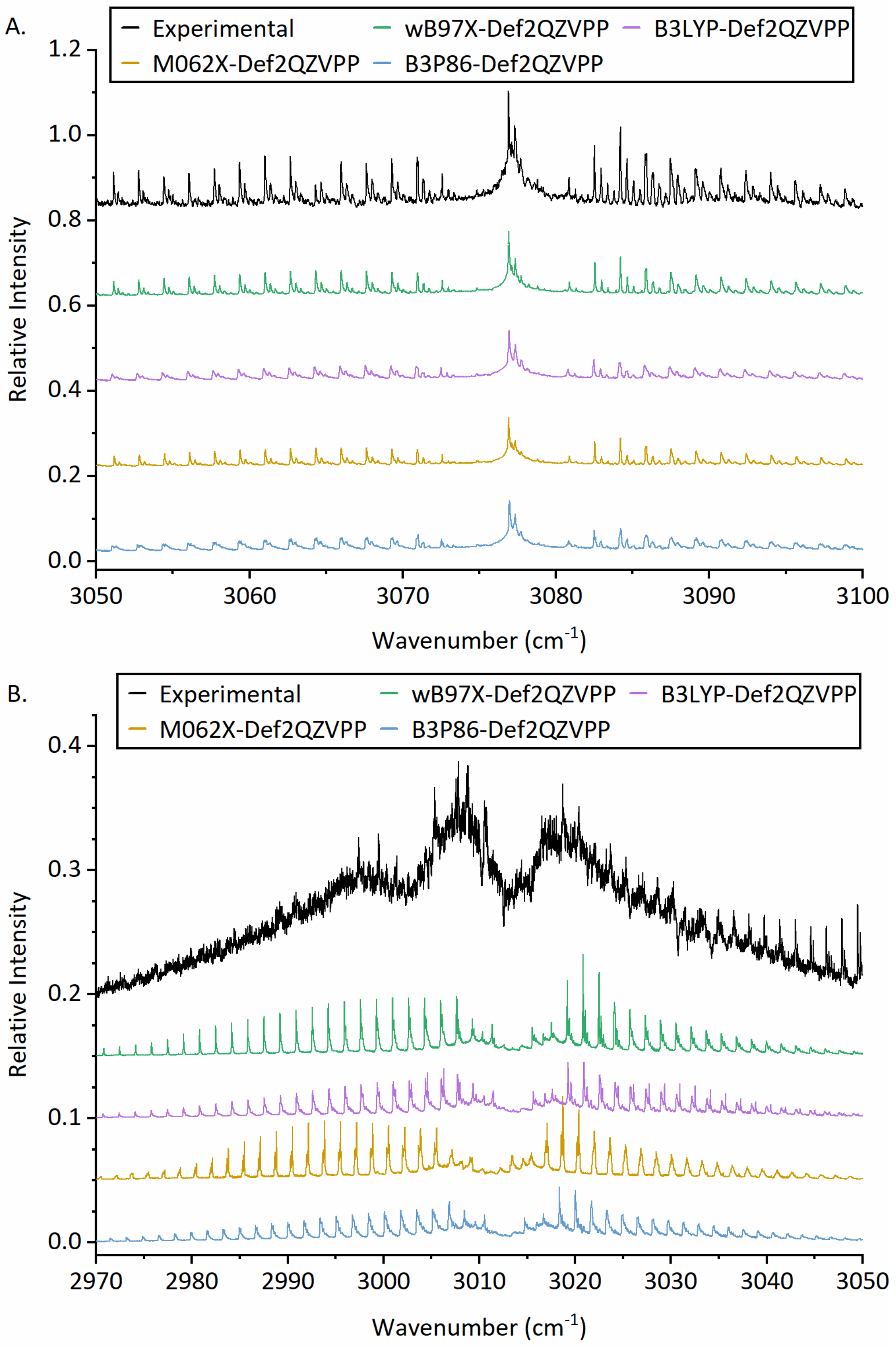

Figure 5-6 CH_2Br_2 Computational Simulated Spectra. A. Comparison of the experimental spectrum and the 5 computational spectra from 3050 to 3100 cm^{-1} showing the ν_6 band. B. Comparison of the experimental and the 5 computational spectra from 2970 to 3050 cm^{-1} showing the ν_1 band. For both panels the colours of the spectra are: Experimental (black), wB97X/Def2QZVPP (green), B3LYP/Def2QZVPP (purple), M062X/Def2QZVPP (yellow), B3P86/Def2QZVPP (blue), and MP2/MidiX (orange).

wavenumber band origin and the 81/81 isotope pair should have the lowest wavenumber band origin, with the 79/81 isotope pair having a band origin in the middle of the other two isotope pairs. However, these calculated isotopic shift values do further help to confirm the hot-band theory presented in this thesis. The highest isotopic shift is calculated to be 0.237 cm^{-1}, however the separation between adjacent peaks within a peak progression, for example $K_a = 6 \leftarrow 7$ is 0.35 cm^{-1}. This separation stays constant within a progression but the peak separation decreases as K_a increases. Therefore, the frequency separation between peaks within a progression is greater than the highest isotopic shift value, and the three isotopologues cannot be reason for the multiple peaks within the progressions.

While the origin values within all six of the tables are the calculated values, the origin values used with the *PGOPHER* simulations (Figure 5-6 part A for ν_6 and part B for ν_1) are adjusted in order to match the experimental spectrum. However, the calculated isotopic shifts between the three isotopologues are kept constant within each of the simulations.

Figure 5-7 shows the results of the experimental spectrum (black), the simulated results from section 5.3.1.1 (red), and the wB97X/Def2QZVPP results (blue) for the ν_6 band. Both simulations include contributions from the three isotopologues and include 6^1_0 transitions and $6^1_0\ 4^n_n$ transitions where $n \leq 3$. The general shape of each peak is well matched, which is dependent on the *B* and *C* constants. There is a 0.02 cm^{-1} difference in the peak locations between the experimental and the wB97X/Def2QZVPP simulation, which is due to the *A* rotational constant. Furthermore, the inclusion of the hot-bands qualitatively matches well to the experimental simulation, which helps to confirm the hot-band theory and analysis as presented in this chapter, and the previous chapter.

On the other hand, none of the computational results were able to accurately simulate the ν_1 band, even though over 12 different vibrational transitions across the three isotopologues were included in the simulations. Figure 5-6, part B highlights the stark differences between the computational simulated spectra and the experimental spectrum (black spectrum). Therefore, the possibility of Fermi resonances, as discussed in section 5.3.1.2, is highly probable.

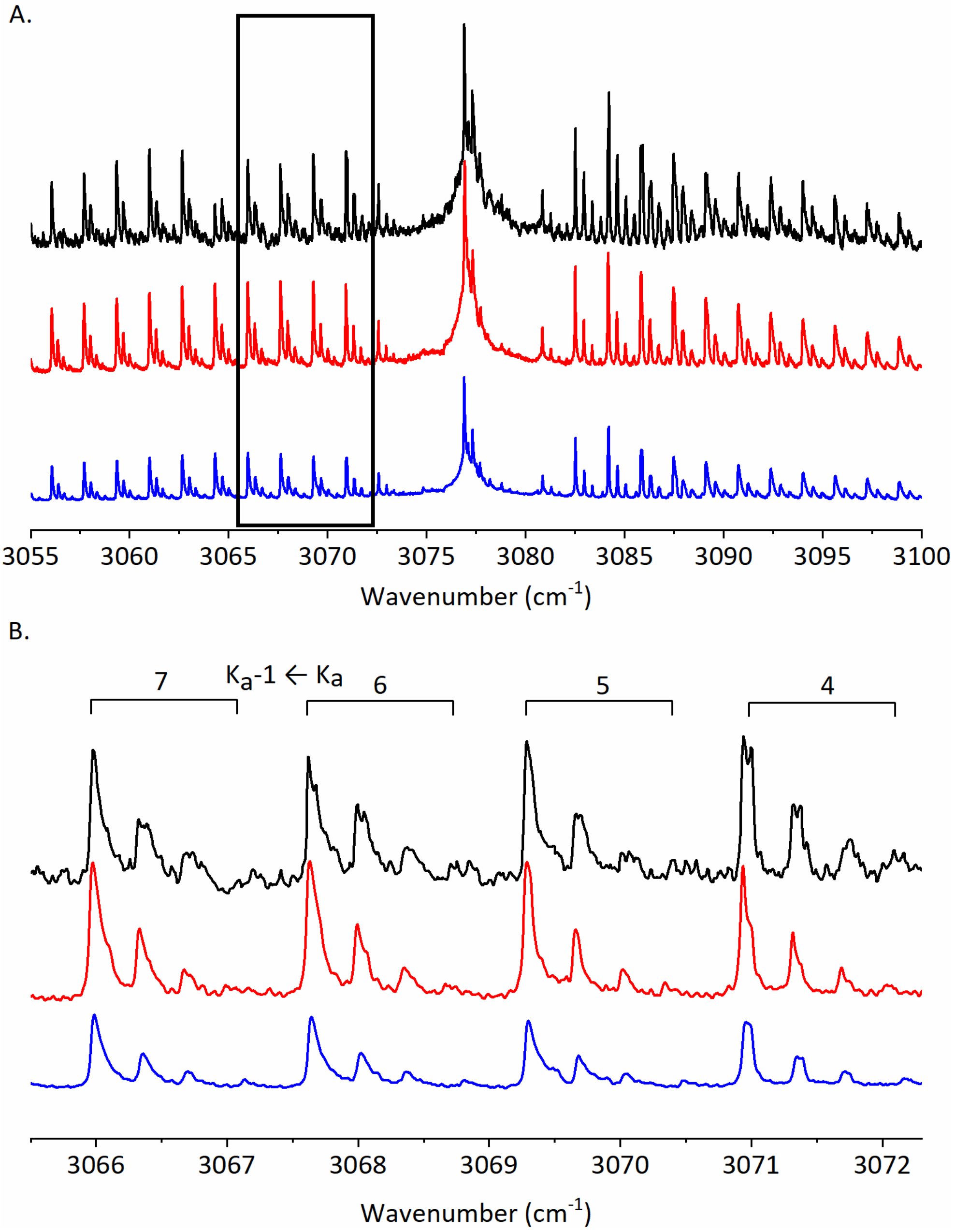

Figure 5-7 CH_2Br_2 ν_6 wB97X/Def2QZVPP Simulation Comparison Results. Comparison of the experimental spectrum (black), the line-fitted simulation (red), and the semi-empirical simulation based on the results of the wB97X/Def2QZVPP calculations (blue). A. Sub-section of all three spectra, from 3055 to 3100 cm^{-1} covering the 6^1_0 band (including the $6^1_0\,4^n_n$ transitions where n ≤ 3) band. B. Zoomed in portion of the three spectra, from 3065.5 to 3072.2 cm^{-1} showing four different K_a transitions in the ^PQ branch.

Although, the ν_1 simulation results were not as expected, the wB97X/Def2QZVPP results are still shown in depth here. Figure 5-8 shows the results of the experimental spectrum (black) and the wB97X/Def2QZVPP results (blue) for the ν_1 band. The computational simulation includes contributions from the three isotopologues and includes 1^1_0 transitions and $1^1_0\ 4^n_n$ transitions where $n \leq 3$. Although an effort was made to choose a band origin that placed the centre of the band around 3007 cm^{-1}, this did not help in being able to assign an experimental peak to a simulated peak. Furthermore, it is difficult to match experimental absorption peaks to those in the simulation, as there is no reoccurring pattern to the visible peaks, specifically the peaks visible around 3005 cm^{-1}. The peaks that are noticeable between 3020 and 3050 cm^{-1} are assigned to the ν_6 band.

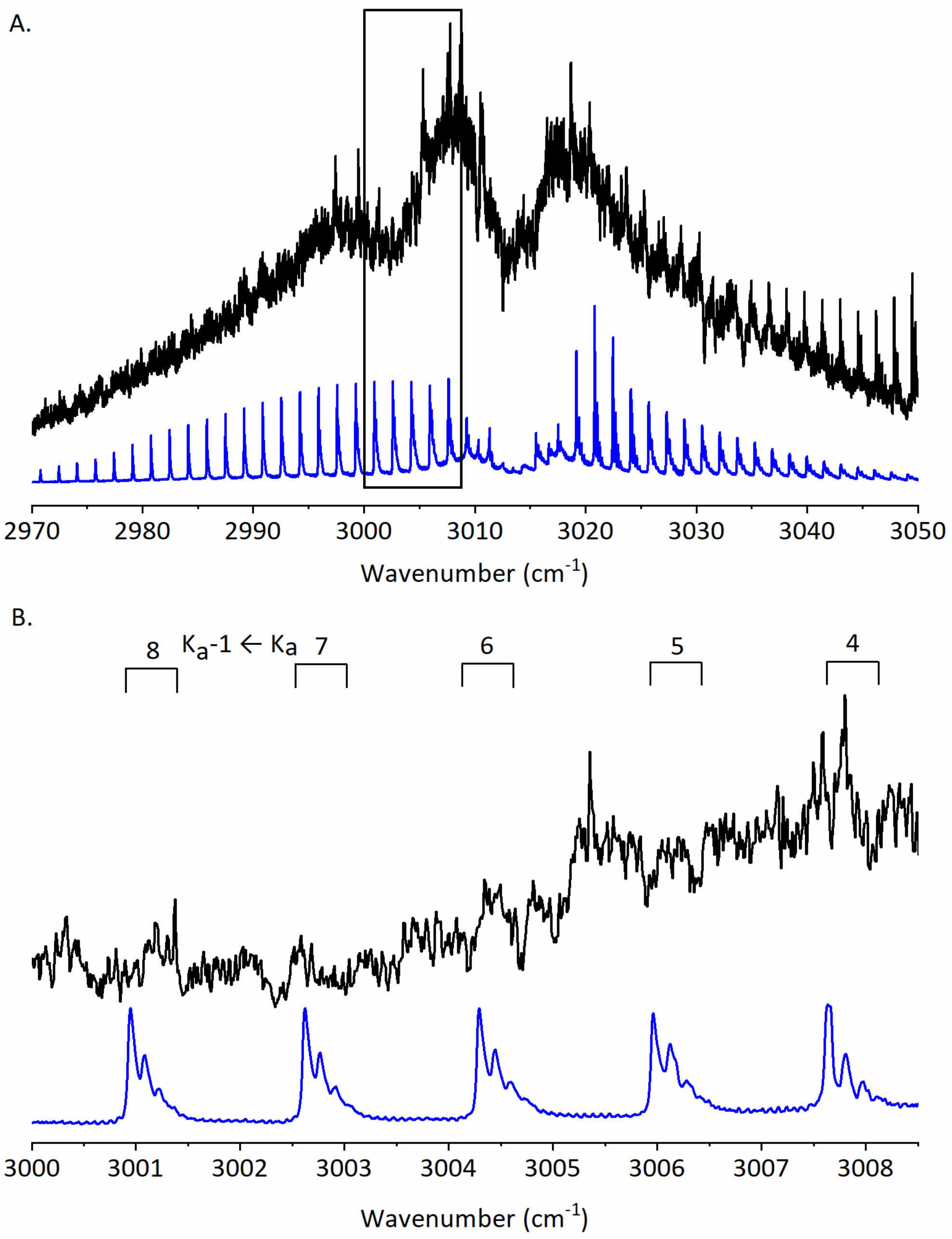

Figure 5-8 CH_2Br_2 ν_1 wB97X/Def2QZVPP Simulation Comparison Results. Comparison of the experimental spectrum (black), and the semi-empirical simulation based on the results of the wB97X/Def2QZVPP calculations (blue). A. Sub-section of both spectra, from 2970 to 3050 cm^{-1} covering the 1^1_0 band (including the $1^1_0 4^n_n$ transitions where $n \leq 3$) band. B. Zoomed in portion of the two spectra, from 3000.0 to 3008.5 cm^{-1} showing five different K_a transitions in the ^PQ branch, which are based on the simulation, not the experimental spectrum.

Table 5-5 $CH_2{}^{79}Br^{79}Br$ ν_6 Semi-empirical Computational Values. Comparison of calculated and experimentally determined anharmonic frequencies and rotational constants for $CH_2{}^{79}Br^{79}Br$ for the vibrational ground state (v = 0), ν_6 (v = 1), ν_4 (v = 1), and the first hot band ν_6 (v = 1) + ν_4 (v = 1). All values given in cm^{-1}, error bars for experimental values are given above in Table 5-2 and Table 5-3, along with the full value.

$CH_2{}^{79}Br^{79}Br$		Ground state (v=0)	ν_6 (v=1)	Δ_i /10^{-6}	ν_4 (v = 1)	ν_6 (v = 1) + ν_4 (v = 1)	Δ_j /10^{-6}
Experimental *	ν	…	3076.721	…	172.078	3249.204	…
	A	0.86831[a]	0.8677590	552	0.87187	0.871230	640
	B	0.04131[a]	0.0413355	−22.0	0.041315	0.041337	−22
	C	0.03973[a]	0.0397480	−22.0	0.039711	0.039731	−20
wB97X / Def2QZVPP	ν	…	3178.091	…	176.549	3354.850	…
	A	0.883522	0.882879	643	0.887190	0.886546	644
	B	0.041172	0.041193	−21.0	0.041155	0.041176	−21
	C	0.039641	0.039660	−19.0	0.039621	0.039640	−19
B3LYP / Def2QZVPP	ν	…	3081.965	…	165.961	3248.5	…
	A	0.875877	0.875043	834	0.879677	0.878843	834
	B	0.039747	0.039790	−43.0	0.039724	0.039767	−43.0
	C	0.038308	0.038347	−39.0	0.038283	0.038323	−40.0
M062X / Def2QZVPP	ν	…	2833.362	…	175.563	3009.197	…
	A	0.875347	0.874930	417	0.878321	0.877904	417
	B	0.040890	0.040911	−21.0	0.040872	0.040893	−21.0
	C	0.039368	0.039388	−20.0	0.039348	0.039367	−19.0
B3P86 / Def2QZVPP	ν	…	3087.553	…	168.100	3256.095	…
	A	0.885051	0.884181	870	0.888854	0.887984	870
	B	0.040603	0.040641	−38.0	0.040485	0.040622	−37.0
	C	0.039119	0.039154	−35.0	0.039098	0.039133	−35.0

a. Constants from ref. [88]

** Not the full value due to table constraints*

Table 5-6 $CH_2{}^{79}Br^{81}Br$ ν_6 Semi-empirical Computational Values. Comparison of calculated and experimentally determined anharmonic frequencies and rotational constants for $CH_2{}^{79}Br^{81}Br$ for the vibrational ground state (v = 0), ν_6 (v = 1), ν_4 (v = 1), and the first hot band ν_6 (v = 1) + ν_4 (v = 1). All values given in cm^{-1}, error bars for experimental values are given above in Table 5-2 and Table 5-3, along with the full value.

$CH_2{}^{79}Br^{81}Br$		Ground state (v=0)	ν_6 (v=1)	Δ_i /10^{-6}	ν_4 (v = 1)	ν_6 (v = 1) + ν_4 (v = 1)	Δ_j /10^{-6}
Experimental	ν	…	3076.719	…	171.101	3248.299	…
	A	0.86752[a]	0.866907	613	0.871208	0.870566	642
	B	0.04080[a]	0.0408270	-27.0	0.040788	0.040810	−22.0
	C	0.03925[a]	0.0392753	-25.3	0.039227	0.039246	−19.0
wB97X / Def2QZVPP	ν	…	3178.091	…	175.338	3353.638	…
	A	0.882735	0.882093	642	0.886373	0.885731	642
	B	0.046660	0.040686	−20.0	0.040649	0.040669	−20.0
	C	0.039170	0.039189	−19.0	0.03915	0.039169	−19.0
B3LYP / Def2QZVPP	ν	…	3081.946	…	165.336	3247.778	…
	A	0.875095	0.874262	833	0.878865	0.878031	834
	B	0.039258	0.039300	−42.0	0.039236	0.039278	−42.0
	C	0.037852	0.037891	−39.0	0.037827	0.037867	−40.0
M062X / Def2QZVPP	ν	…	2833.496	…	174.508	3008.258	…
	A	0.874567	0.874151	416	0.877518	0.877102	416
	B	0.040387	0.040408	−21.0	0.040369	0.040390	−21.0
	C	0.038900	0.038920	−20.0	0.038880	0.038900	−20.0
B3P86 / Def2QZVPP	ν	…	3087.573	…	167.591	3255.645	…
	A	0.884262	0.883394	868	0.888034	0.887166	868
	B	0.040104	0.040141	−37.0	0.040086	0.040123	−37.0
	C	0.038654	0.038688	−34.0	0.038633	0.038668	−35.0

a. Constants from ref. [90]

Table 5-7 $CH_2{}^{81}Br^{81}Br$ ν_6 Semi-empirical Computational Values. Comparison of calculated and experimentally determined anharmonic frequencies and rotational constants for $CH_2{}^{81}Br^{81}Br$ for the vibrational ground state (v = 0), ν_6 (v = 1), ν_4 (v = 1), and the first hot band ν_6 (v = 1) + ν_4 (v = 1). All values given in cm^{-1}, error bars for experimental values are given above in Table 5-2 and Table 5-3, along with the full value.

$CH_2{}^{81}Br^{81}Br$		Ground state (v=0)	ν_6 (v=1)	Δ_i /10^{-6}	ν_4 (v = 1)	ν_6 (v = 1) + ν_4 (v = 1)	Δ_j /10^{-6}
Experimental *	v	…	3076.718	…	170.137	3247.264	…
	A	0.866756	0.866122	634	0.870371	0.869715	656
	B	0.040297	0.0403195	-22.5	0.039961	0.039980	−19.0
	C	0.038782	0.0388033	-21.3	0.038468	0.038487	−19.0
wB97X / Def2QZVPP	v	…	3178.094	…	174.527	3352.829	…
	A	0.881945	0.881305	640	0.885554	0.884914	640
	B	0.040160	0.040181	−21.0	0.040143	0.040164	−21.0
	C	0.038699	0.038718	−19.0	0.038680	0.038699	−19.0
B3LYP / Def2QZVPP	v	..	3081.903	…	163.340	3245.778	…
	A	0.874311	0.873480	831	0.878049	0.877218	831
	B	0.038770	0.038812	−42.0	0.038748	0.038790	−42.0
	C	0.037396	0.037435	−39.0	0.037373	0.037412	−39.0
M062X / Def2QZVPP	v	…	2833.259	…	173.227	3006.682	…
	A	0.873784	0.873371	413	0.876712	0.876298	414
	B	0.039885	0.039905	−20.0	0.039867	0.039888	−21.0
	C	0.038433	0.038452	−19.0	0.038413	0.038432	−19.0
B3P86 / Def2QZVPP	v	…	3087.676	…	166.783	3255.000	…
	A	0.883471	0.882605	866	0.887214	0.886348	866
	B	0.039605	0.039642	−37.0	0.039588	0.039624	−36.0
	C	0.038189	0.038223	−32.0	0.038169	0.038203	−34.0

a. Constants from ref. [88]

** Not the full value due to table constraints*

Table 5-8 $CH_2{}^{79}Br^{79}Br$ ν_1 Semi-empirical Computational Values. Comparison of calculated and experimentally determined anharmonic frequencies and rotational constants for $CH_2{}^{79}Br^{79}Br$ for the vibrational ground state (v = 0), ν_1 (v = 1), ν_1 (v = 1), and the first hot band ν_1 (v = 1) + ν_4 (v = 1). All values given in cm^{-1}.

$CH_2{}^{79}Br^{79}Br$		Ground state (v=0)	ν_1 (v=1)	Δ_i /10^{-6}	ν_4 (v = 1)	ν_1 (v = 1) + ν_4 (v = 1)	Δ_j /10^{-6}
Experimental *	v	…	…	…	172.078	…	…
	A	0.86831[a]	…	…	0.87187	…	…
	B	0.04131[a]	…	…	0.041315	…	…
	C	0.03973[a]	…	…	0.039711	…	…
wB97X / Def2QZVPP	v	…	3116.302	…	176.549	3923.051	…
	A	0.883522	0.881525	2000	0.887190	0.885192	2000
	B	0.041172	0.041188	−16.0	0.041155	0.041170	−15.0
	C	0.039641	0.039655	−14.0	0.039621	0.039635	−14.0
B3LYP / Def2QZVPP	v	…	3017.138	…	165.961	3183.437	…
	A	0.875877	0.873580	2300	0.879677	0.877380	2300
	B	0.039747	0.0397750	−28.0	0.039724	0.039753	−29.0
	C	0.038308	0.038334	−26.0	0.038283	0.038309	−26.0
M062X / Def2QZVPP	v	…	2778.998	…	175.563	2954.645	…
	A	0.875347	0.873705	1640	0.878321	0.876679	1640
	B	0.040890	0.040901	−11.0	0.040872	0.040883	−11.0
	C	0.039368	0.039348	−11.0	0.039348	0.039358	−10.0
B3P86 / Def2QZVPP	v	…	3021.327	…	168.100	3189.645	…
	A	0.885051	0.882743	2310	0.888854	0.886546	2310
	B	0.040603	0.040629	−26.0	0.040485	0.040611	−26.0
	C	0.039119	0.039143	−23.0	0.039098	0.039122	−24.0

a. Constants from ref. [88]

** Not the full value due to table constraints*

Table 5-9 $CH_2{}^{79}Br^{81}Br$ ν_1 Semi-empirical Computational Values. Comparison of calculated and experimentally determined anharmonic frequencies and rotational constants for $CH_2{}^{79}Br^{81}Br$ for the vibrational ground state (v = 0), ν_1 (v = 1), ν_4 (v = 1), and the first hot band ν_1 (v = 1) + ν_4 (v = 1). All values given in cm^{-1}.

$CH_2{}^{79}Br^{81}Br$		Ground state (v=0)	ν_1 (v=1)	Δ_i /10^{-6}	ν_4 (v = 1)	ν_1 (v = 1) + ν_4 (v = 1)	Δ_j /10^{-6}
Experimental	v	…	…	…	171.101	…	…
	A	0.86752[a]	…	…	0.871208	…	…
	B	0.04080[a]	…	…	0.040788	…	…
	C	0.03925[a]	…	…	0.039227	…	…
wB97X / Def2QZVPP	v	…	3116.299	…	175.338	3291.823	…
	A	0.882735	0.880741	1990	0.886373	0.8854379	1990
	B	0.046660	0.040681	−15.0	0.040649	0.0406640	−15.0
	C	0.039170	0.0396184	−14.0	0.039150	0.0391640	−14.0
B3LYP / Def2QZVPP	v	…	3017.127	…	165.336	3182.778	…
	A	0.875095	0.872800	2290	0.878865	0.876698	2170
	B	0.039258	0.039286	−28.0	0.039236	0.039197	39.0
	C	0.037852	0.037878	−26.0	0.037827	0.037854	−27.0
M062X / Def2QZVPP	v	…	2779.106	…	174.508	2953.679	…
	A	0.874567	0.872928	1640	0.877518	0.875878	1640
	B	0.040387	0.040398	−11.0	0.040369	0.040380	−11.0
	C	0.038900	0.038911	−11.0	0.038880	0.038891	−11.0
B3P86 / Def2QZVPP	v	…	3021.354	…	167.591	3189.206	…
	A	0.884262	0.881957	2310	0.888034	0.885730	2300
	B	0.040104	0.040129	−25.0	0.040086	0.040112	−26.0
	C	0.038654	0.038678	−24.0	0.038633	0.038657	−24.0

a. Constants from ref. [90]

Table 5-10 $CH_2{}^{81}Br^{81}Br$ ν_1 Semi-empirical Computational Values. Comparison of calculated and experimentally determined anharmonic frequencies and rotational constants for $CH_2{}^{81}Br^{81}Br$ for the vibrational ground state (v = 0), ν_1 (v = 1), ν_4 (v = 1), and the first hot band ν_1 (v = 1) + ν_4 (v = 1). All values given in cm^{-1}.

$CH_2{}^{81}Br^{81}Br$		Ground state (v=0)	ν_1 (v=1)	Δ_i /10^{-6}	ν_4 (v = 1)	ν_1 (v = 1) + ν_4 (v = 1)	Δ_j /10^{-6}
Experimental *	ν	…	…	…	170.137	…	…
	A	0.866756	…	…	0.870371	…	…
	B	0.040297	…	…	0.039961	…	…
	C	0.038782	…	…	0.038468	…	…
wB97X / Def2QZVPP	ν	…	3116.307	…	174.527	3291.033	…
	A	0.881945	0.879954	1990	0.885554	0.883563	1990
	B	0.040160	0.040175	−15.0	0.040143	0.040158	−15.0
	C	0.038699	0.038713	−14.0	0.038680	0.038694	−14.0
B3LYP / Def2QZVPP	ν	..	3017.074	…	163.340	3190.701	…
	A	0.874311	0.872020	2290	0.878049	0.875758	2290
	B	0.038770	0.038798	−28.0	0.038748	0.038776	−15.0
	C	0.037396	0.037422	−26.0	0.037373	0.037399	−14.0
M062X / Def2QZVPP	ν	…	2778.902	…	173.227	2952.147	…
	A	0.873784	0.872149	1640	0.876712	0.875076	1640
	B	0.039885	0.039896	−11.0	0.039867	0.039878	−11.0
	C	0.038433	0.038443	−10.0	0.038413	0.038432	−19.0
B3P86 / Def2QZVPP	ν	…	3021.460	…	166.783	3188.567	…
	A	0.883471	0.881170	2300	0.887214	0.884913	2300
	B	0.039605	0.039631	−26.0	0.039588	0.039613	−25.0
	C	0.038189	0.038213	−24.0	0.038169	0.038193	−24.0

a. Constants from ref. [88]

** Not the full value due to table constraints*

5.4. Conclusion

Firstly, the room temperature rovibrational absorption spectrum of CH_2Br_2 has been measured from 2920 to 3125 cm^{-1}. Within this region, two fundamental transitions of CH_2Br_2 were observed, belonging to the ν_6 and ν_1 normal modes. However, further analysis of the ν_6 band revealed contributions from hot-band transitions arising from population in the ν_4 vibrational states. Within the ν_6 band, there were six assigned vibrational transitions: 6_0^1 and $6_0^1 4_n^n$ (where n ≤ 3). For the ν_6 band, the x_{66} anharmonicity constant for the 79/81 isotopologue is calculated to be −0.747(4) cm^{-1}. Furthermore, the three isotopologues of CH_2Br_2: 79/79, 79/81, and 81/81, are considered and their effect on the spectrum is discussed. A *PGOPHER* simulation was generated to experimentally determine the spectroscopic rotational constants of all 12 vibrational states across the three isotopologues observed in the experimental spectrum. However, the portion of the spectrum attributed to the ν_1 band was too complicated and congested to have specific rovibrational states assigned or spectroscopic rotational constants determined.

Secondly, the pressure broadening coefficients of N_2 and Ar have also been measured for CH_2I_2, with b_{N2} = 0.145(7) cm^{-1} atm^{-1} and b_{Ar} = or 0.105(5) cm^{-1} atm^{-1}. Both of these experimental values are much higher than corresponding values for CH_3X and CH_2X_2 molecules. However, the general trend of b_{N2} being higher than b_{Ar} is observed here. The most probable explanation for the high values is that the contribution of the bath gas to the pressure broadened transitions has been over-predicted. Simultaneously, the contribution from the self-broadening by CH_2Br_2 might be under-predicted.

Lastly, the results of four different computational calculations were used to predict the spectra of the ν_1 and ν_6 bands in order to confirm the hot-band theory and help with peak assignment in regards to the three isotopologues. The computational basis set and method pairs were: wB97X/Def2QZVPP, M062X/Def2QZVPP, B3P86/Def2QZVPP, and B3LYP/Def2QZVPP. Out of the eight simulation spectra, four for the ν_6 and four for the ν_1 band, the semi-empirical simulated spectra for the wB97X/Def2QZVPP computational calculation were qualitatively the best match for the ν_6 band of the experimental spectrum. However, none of the semi-empirical simulated spectra for the ν_1 band could reproduce the complicated and congested structure observed experimentally.

6. Comparison of CH_2X_2 Molecules

This chapter will cover the similarities and differences between the results presented in the previous two chapters of this thesis. First, the difference between the two acquired spectra for CH_2I_2 and CH_2Br_2 will be discussed, followed by comparisons to previous works for CH_2F_2 and CH_2Cl_2. Secondly, the observed pressure broadening coefficients will be evaluated against similar literature values for CH_3X, CH_2X_2, and CHX_3 molecules (where X = F, Cl, Br, or I).

6.1. Room Temperature Mid-IR Spectra

As CH_2I_2 and CH_2Br_2 are both asymmetric top molecules, comparisons can be made with their respective infrared spectra. Figure 6-1 shows the two spectra overlaid on top of each other, where green is CH_2I_2 and blue is CH_2Br_2. While both spectra are shown in units of σ_ν (cm^2 molecule^{-1}), they have to be plotted with their own separate *y*-axis due to the large differences in magnitude of their absorption cross section. The peak absorption cross section for CH_2I_2 is 4 times larger than the peak of the CH_2Br_2 absorption cross section. In the case of Figure 6-1, the left *y*-axis corresponds to CH_2I_2 and the right *y*-axis corresponds to CH_2Br_2.

Firstly, the rigorous approach of calculating the integrated σ_ν for both spectra can be used to compare the two spectra. For CH_2I_2, the integrated σ_ν is 7.32×10^{-20} cm^2 molecule^{-1} for ν_1 (from 2970.003 to 3028.001 cm^{-1}), and for ν_6 this value is 3.21×10^{-19} cm^2 molecule^{-1} (from 3045.003 to 3099.999 cm^{-1}). For CH_2Br_2, the corresponding value for ν_1 is 3.49×10^{-19} cm^2 molecule^{-1} (from 2935.001 to 3034.998 cm^{-1}), and for ν_6 the value is 2.02×10^{-19} cm^2 molecule^{-1} (from 3040.001 to 3123.783 cm^{-1}). This gives a ratio for ν_1:ν_6 of 0.28:1 for CH_2I_2 and 1.73:1 for CH_2Br_2. However, looking at the overall spectra, it is obvious that CH_2Br_2 has lower cross section peaks overall than CH_2I_2, approximately a four times difference between the two most intense peaks. Furthermore, the relative differences between the ν_1 and ν_6 bands are different for both molecules, where we are looking at the overall peak heights rather than comparing integrated σ_ν. For CH_2I_2 the ratio of ν_1:ν_6 is 0.25:1, whereas for CH_2Br_2 the ratio of ν_1:ν_6 is 1:1. In addition, the general intensity of the ν_1 band for CH_2I_2 is similar to both the ν_1 and ν_6 bands for CH_2Br_2, approximate intensity for the peaks is between 1 to 2×10^{-21} cm^2 molecule^{-1}.

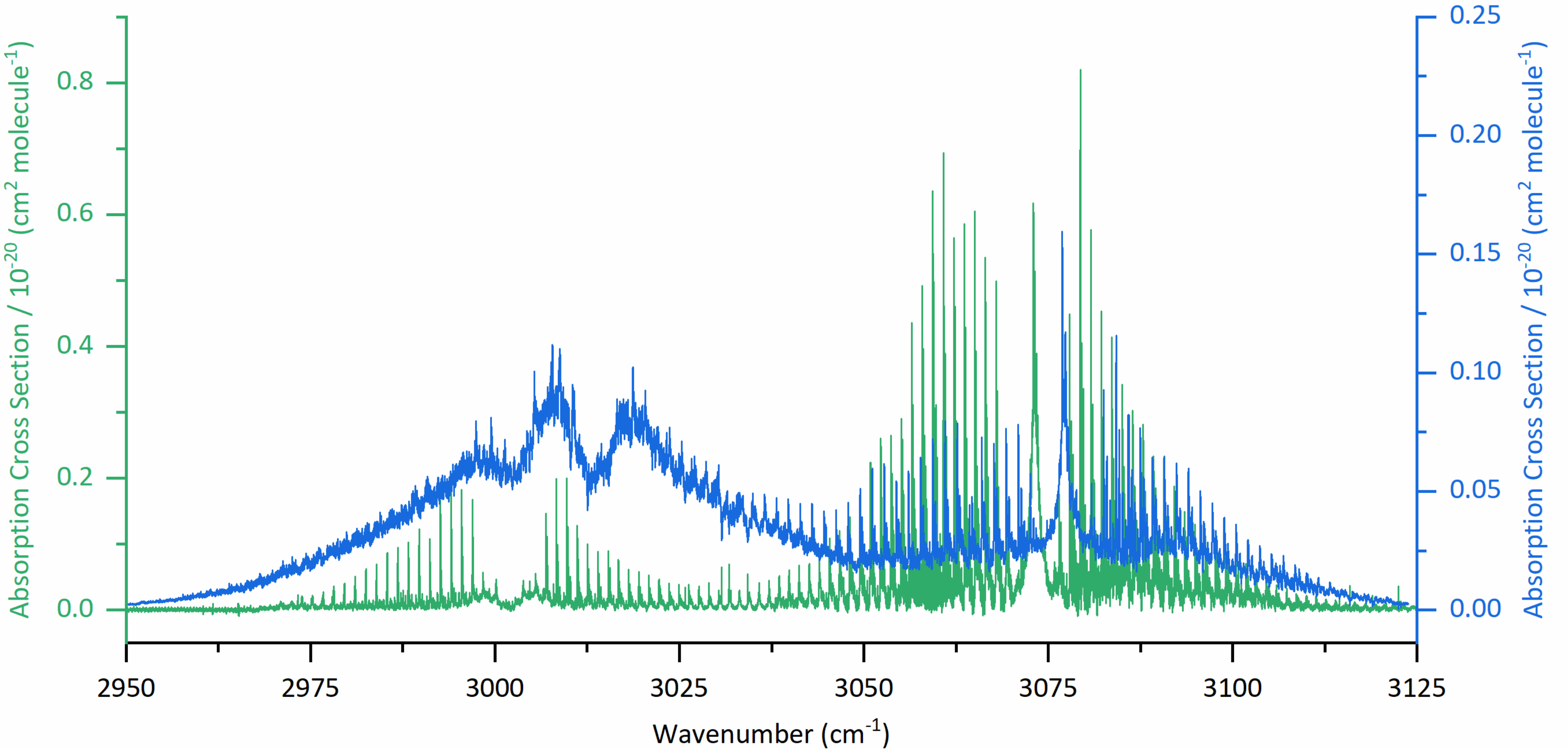

Figure 6-1 Comparison of Room Temperature CH_2I_2 and CH_2Br_2 Spectra. Full spectrum for both CH_2I_2 (green) and CH_2Br_2 (blue) from 2950 to 3125 cm^{-1} as presented in Chapters 4 and 5. The left *y*-axis in green corresponds to the absorption cross section of CH_2I_2 in units of cm^2 molecule^{-1}. The right *y*-axis in blue corresponds to the absorption cross section of CH_2Br_2 in units of cm^2 molecule^{-1}.

For both molecules, the ν_6 bands are very similar in overall shape and show the appearance of the peak progressions. Both bands have a strong central Q branch with $^{P/R}Q_{Ka}(J)$ branches, but with a different central peak wavenumber of 3073 cm^{-1} for CH_2I_2 and 3077 cm^{-1} for CH_2Br_2. However, for both molecules the ν_6 covers a similar range: the CH_2I_2 ν_6 band ranges from 3030 to 3120 cm^{-1} and the CH_2Br_2 ν_6 band ranges from 3030 to 3125 cm^{-1}. For the peak progressions within the ν_6 band, a different number of hot bands are visible for CH_2I_2 and CH_2Br_2. This difference is due to the difference in the transition wavenumber of ν_4 ($v = 1 \leftarrow 0$) between the two molecules and the effect this has the Boltzmann population for the subsequent vibrational states of ν_4. For CH_2I_2, there are a maximum of six visible peaks within the peak progressions, assuming that the ν_4 ($v = 1$) state has a transition wavenumber of 121 cm^{-1}, and subsequent vibrational states are integer multiples of this transition wavenumber, the Boltzmann population distribution (see Equation 1-2) of the ν_4 states is as follows: 1:0.56:0.31:0.17:0.1:0.05 (for v = 0:1:2:3:4:5 in the ν_4 state). Correspondingly, for CH_2Br_2, there are a maximum of four peaks within each peak progression, assuming that the ν_4 ($v = 1$) state has a transition wavenumber of 171 cm^{-1}, and subsequent vibrational states are integer multiples of this transition wavenumber. The Boltzmann population distribution of the ν_4 states is as follows: 1:0.44:0.19:0.08 (for v = 0:1:2:3 in the ν_4 state). Transitions arising from the ν_4 ($v = 4$) state have a Boltzmann population ratio of 0.04 (in comparison to the other states), and could potentially be discerned in the spectrum, however they are extremely weak and were not included in the final simulations.

However, the ν_1 band is visibly different between the two molecules. For CH_2I_2, the ν_1 band has a similar defined structure peak progression structure that the ν_6 band exhibits, with a key difference being there are less peaks attributed to the ν_4 hot-bands within each progressions and the absence of a central Q-type peak. On the other hand, for CH_2Br_2 there is no defined peak progressions or rovibrational peaks, so much so that there is no final simulation for the ν_1 band and theoretical calculations were not able to simulate the observed overall profile. The chapter for CH_2Br_2 covers the possible reasons for the congestion the ν_1 band (section 5.3.1.2).

Table 6-1 Fundamental Vibrational Frequencies of CH_2X_2 Molecules. Vibrational frequencies for nine fundamental vibrational transitions of the CH_2X_2 molecules, where X = F, Cl, Br, or I. Values in cm^{-1}.

Mode	Symmetry	CH_2F_2[a]	CH_2Cl_2[b]	CH_2Br_2[c]	CH_2I_2[d]
ν_4	a_1	528.34	281.5	172†	122*
ν_3	a_1	1111.61	712.9	588	493.01
ν_9	b_2	1089.9	759.82	653	584.21
ν_7	b_1	1178.74	898.66	812	718.08
ν_5	a_2	1256.8	1153	1095	1041.99
ν_8	b_2	1435.5	1268.86	1195	1113.87
ν_2	a_1	1509.6	1434.15	1382	1373.61
ν_1	a_1	2947.9	2997.66	3009	3002.00
ν_6	b_1	3014.45	3055	3073	3073.01

a. Ref. [36]
b. Ref. [73]
c. Ref. [92], † is calculated
d. Ref. [107], * Liquid IR

Further comparisons can also be made to the other two dihalomethane molecules, CH_2F_2 and CH_2Cl_2. Although the spectra of these two molecules have not been recorded within this thesis, there is previous literature available concerning the ν_1 and ν_6 bands for CH_2F_2 and CH_2Cl_2. [36, 46, 73, 95] Figure 6-2 shows a comparison of the four reference spectra for CH_2F_2 (black), CH_2Cl_2 (red), CH_2Br_2 (blue), and CH_2I_2 (green) from 2920 to 3125 cm^{-1}. Although these spectra were all recorded at atmospheric pressure (1013 mbar) and with a resolution of 0.112 cm^{-1}, some rotational structure can be seen within each band. However, the resolution is not sufficient enough to see the hot band structure. Strangely, for the CH_2Cl_2 the ν_6 band seems to be missing, according to the vibrational frequency list (see Table 6-1) the band should appear around 3055 cm^{-1}. The work of Liu *et al.* [73] however states that the ν_6 band is very weak in intensity and could be hidden under the very intense ν_1 band. Even stranger, the peaks attributed to the ν_1 band in the CH_2F_2 spectra does not follow the expected trend for a *b*-type transition as it has a central Q-type peak.

Considering the possibility of the ν_4 hot band structure for CH_2F_2 and CH_2Cl_2, it is unlikely the peak progressions would be seen to the same extent. Based on the CH_2I_2 peak progressions, a reasonable assumption can be made that a minimum population ratio of ground state to ν_4 state of 1:0.05 is needed to record a transition arising from that particular state, assuming the same experimental are used (~1 mbar of sample and a cavity path length of ~600 cm). For CH_2Cl_2, the ν_4 vibrational transition wavenumber is 281.5 cm^{-1}, [73] which

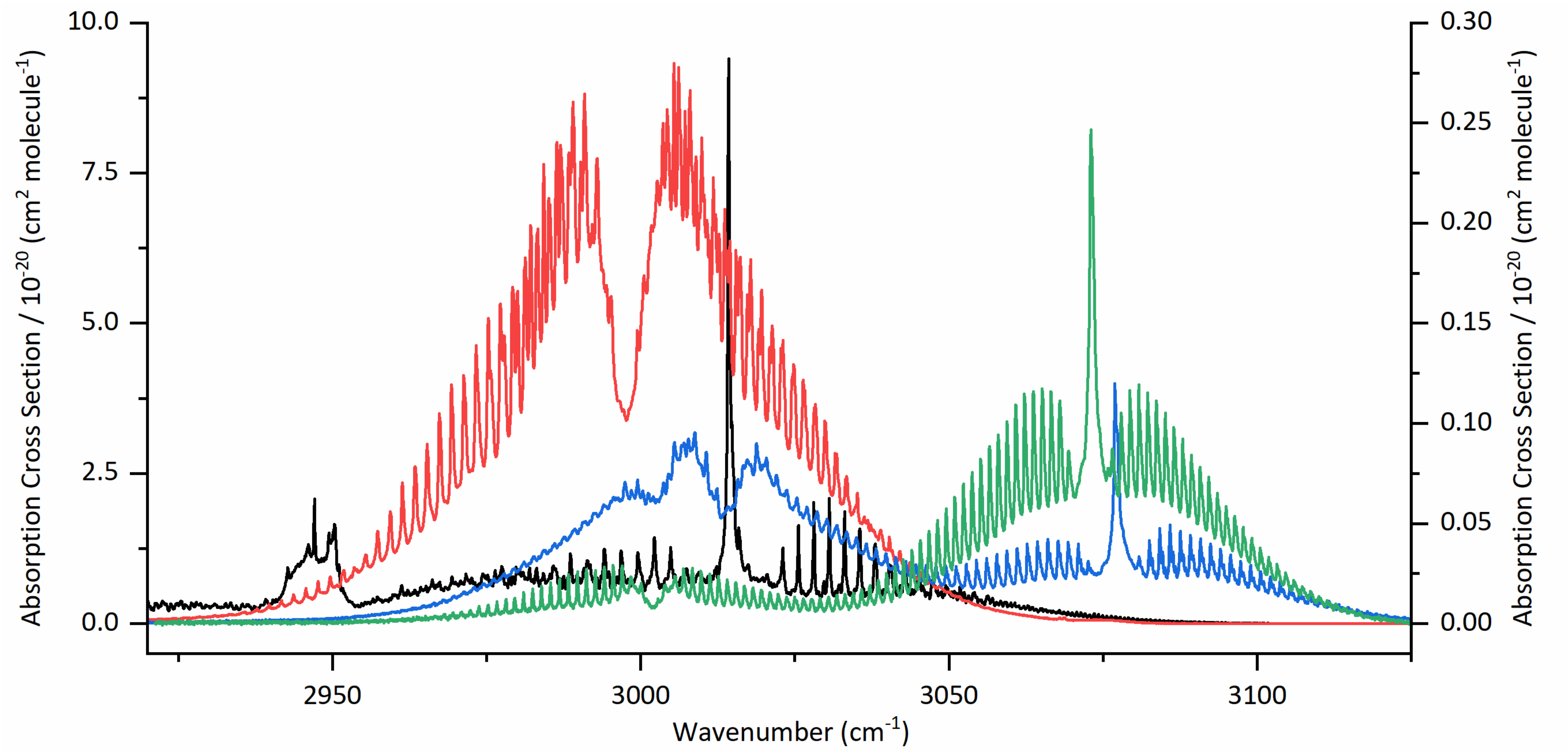

Figure 6-2 Reference Spectra Compare.Comparison of reference spectra for CH_2F_2 (black), CH_2Cl_2 (red), CH_2Br_2 (blue), and CH_2I_2 (green) from 2920 to 3125 cm^{-1}. Due to the differences in absorption cross section, the left *y*-axis corresponds to the CH_2F_2 spectrum, whereas the right *y*-axis corresponds to the CH_2Cl_2, CH_2Br_2, and CH_2I_2 spectra. All spectra are available from the *HITRAN* database. [95, 216]

gives rise a Boltzmann population distribution of 1:0.26:0.07 for ν_4 v = 0:1:2, meaning there would be potentially three peaks within the progression. For CH_2F_2 this is reduced to only two peaks in the progression as the transition wavenumber for ν_4 is much higher at 528.34 cm^{-1}, [45] giving rise to a Boltzmann population distribution of 1:0.08 for ν_4 v = 0:1.

Despite this lack of hot band structure for CH_2Cl_2 and CH_2F_2, their vibrational spectra in this region of the infrared show other interacting vibrational transitions that do not appear in the corresponding spectra for CH_2Br_2 and CH_2I_2. Figure 6-3 shows five different vibrational transitions, 1_0^1, 6_0^1, 2_0^2, 8_0^2, $2_0^1 8_0^1$, and their corresponding frequencies between 2700 and 3150 cm^{-1} for each of the four dihalomethane molecules. This figure also shows the different types of coupling between the different vibrational states. Although these types of couplings were previously discussed in more detail in section 1.3.5, a brief summary is covered here. Fermi resonances occur between a fundamental vibrational transition and an overtone vibrational transition of the same symmetry and similar energy. Darling-Dennison resonances occur between overtone and combination vibrational transitions which also have the same symmetry and are of similar energy. For Coriolis coupling, there are three different types: *a*-axis, *b*-axis, or *c*-axis. Between similar energy vibrational transitions an *a*-axis coupling occurs between two vibrational states with symmetries of a_1 and b_1. Conversely, *b*-axis coupling occurs between two vibrational states with symmetries of b_1 and b_2, and *c*-axis coupling between two vibrational states with symmetries of a_1 and b_2. Coupling to a vibrational state with the symmetry of a_2 is not possible in IR spectroscopy, as the a_2 modes are not IR active.

CH_2F_2 shows medium intensity overtone bands of 2_0^2 centred at 3026.23 cm^{-1} and 8_0^2 at 2838.64 cm^{-1}, alongside 1_0^1 at 2947.9 cm^{-1} and 6_0^1 at 3014.45 cm^{-1}. [46] Experiments have demonstrated an *a*-axis Coriolis interaction between the 2_0^2 and 6_0^1 bands. However, CH_2Cl_2 exhibits two overtone bands of 2_0^2 and 8_0^2 at 2853.66 cm^{-1} and 2526.58 cm^{-1} respectively, which are both somewhat nearby 1_0^1 at 2997.33 cm^{-1} and 6_0^1 at 3055 cm^{-1}. [73] Within the CH_2Cl_2 literature, Fermi resonances between 1_0^1 and 8_0^2 bands and 1_0^1 and 2_0^2 bands have been reported, alongside Darling-Denison resonances between 1_0^2 and 6_0^2, and 2_0^2 and 8_0^2. [46, 73]

The same transitions for CH_2I_2 and CH_2Br_2 are much lower in wavenumber than 1_0^1 and 6_0^1. For CH_2I_2, 2_0^2 is predicted near 2747 cm^{-1} and 8_0^2 at 2222.42 cm^{-1}, and for CH_2Br_2 the same transitions are expected near 2776 cm^{-1} and 2386 cm^{-1}, respectively. As the overtone band of 8_0^2 is at a much lower frequency than the transitions, we do not expect any coupling or resonances from this band with either ν₁ or ν₆. However, there may be a small Fermi resonance between 1_0^1 and 2_0^2 for either CH_2I_2 or CH_2Br_2. Furthermore, as stated in Chapter 5 for CH_2Br_2, there might be other overtones which give rise to the complicated structure seen for the ν₁ band. These may potentially arise from Fermi doublets between 1_0^1 and $2_0^1 7_0^2$ or $2_0^1 4_0^2 9_0^2$, which have vibrational transition frequencies of approximately 3006 and 3026 cm^{-1}, however these are not shown on Figure 6-3.

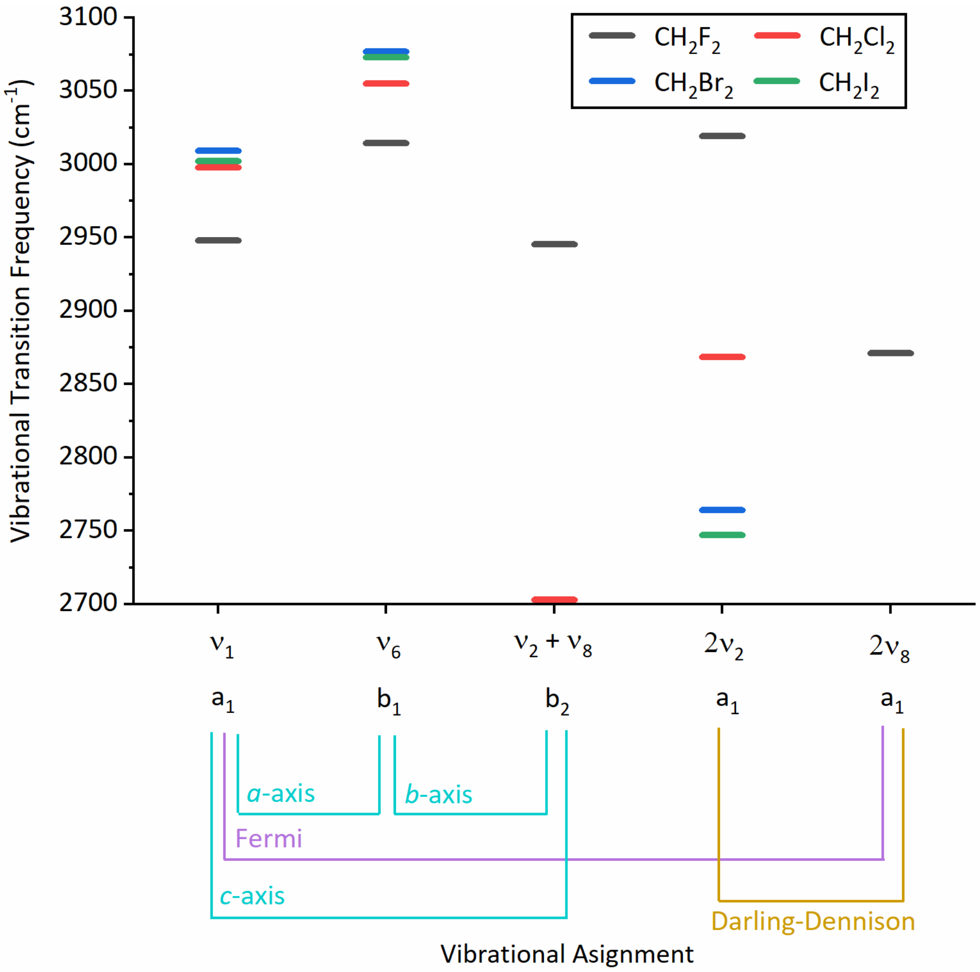

Figure 6-3 Vibrational Frequencies of CH_2X_2 Molecules and Types of Coupling Between the Vibrational States. Five different vibrational transition wavenumbers: 1_0^1, 6_0^1, $2_0^1 8_0^1$, 2_0^2, and 8_0^2, are shown for CH_2F_2 (black), CH_2Cl_2 (red), CH_2Br_2 (blue), CH_2I_2 (green) between 2700 and 3100 cm^{-1}. The different types of coupling between the vibrational states are shown along the bottom. One of each type of coupling is shown for simplicity. Fermi resonances (purple) between states of the same symmetry and similar energy, where one state must a fundamental transition. Darling-Dennison resonances (yellow) between states of the same symmetry and similar energy, where both states must be a combination or overtone state. All 3 types of Coriolis coupling are shown (aqua): *a*-axis is between states with symmetry a_1 and b_1, *b*-axis is between states with symmetry b_1 and b_2, and *c*-axis is between states with symmetry a_1 and b_2. States must still have similar energy for the Coriolis coupling to occur.

6.2. Pressure Broadening Coefficients

Although comparisons have been previously made between pressure broadening coefficients in the respective chapters for each molecule, this section will give a broader assessment of coefficients for all CH_3X and CH_2X_2 molecules, where X = F, Cl, Br, or I (CHX_3 molecule would have also been included, but no data was found for these molecules). Table 6-2 collates the pressure coefficients for the molecules. Although there is a plethora of data there the table only shows the coefficients for self-, N_2-, and Ar-broadening as these are most relevant to this thesis. In addition, within this table, any of the quoted literature values are either an average of J-dependent broadening coefficients, or the range of broadening coefficients is given due to the amount of individual coefficients given in the literature.

Firstly, for the N_2-broadening coefficients, all of the literature values are within a similar value ranging from 0.087 cm^{-1} atm^{-1} for CH_2F_2 to 0.133 cm^{-1} atm^{-1} for CH_3I. A general trend shows that the coefficient increases with significant increasing weight of the molecule, although the reported value for CH_2F_2 is smaller than that of CH_3F despite being heavier (52.02 amu compared to 34.03 amu). In addition, the two quoted values for Ar-broadening follow the same trend, with 0.072 cm^{-1} atm^{-1} for CH_3F and 0.092 cm^{-1} atm^{-1} for CH_3Cl. However, the N_2- and Ar-broadening coefficients reported in this thesis are larger than expected, although they are just outside the high value reported for each of the J-dependent broadening coefficients. While this was touched upon in the previous chapters, for continuity and clarity, some of the explanation will be reiterated here. The most probable explanation of the increase in broadening coefficient is that that the contribution of the bath gas to the pressure broadened transitions has been over-predicted. Simultaneously, the contribution from the self-broadening by CH_2I_2 and CH_2Br_2 might be under predicted.

For both CH_2I_2 and CH_2Br_2 a self-broadening contribution was removed from the overall Lorentzian broadening, these values are: for CH_2I_2, 0.0054 cm^{-1} for N_2 self-broadening and 0.0048 cm^{-1} for Ar self-broadening, and for CH_2Br_2, 0.0089 cm^{-1} for N_2 self-broadening and 0.0132 cm^{-1} for Ar self-broadening (with all four of these numbers representing a HWHM for an average pressure). For the self-broadening parameters of the CH_3X and CH_2F_2 molecule, these parameters are much higher than the coefficients attributed to N_2 and Ar. Furthermore, there is the opposite trend where increasing weight decreases the self-broadening coefficient. Using one of the average values for CH_3I, 0.284 cm^{-1} atm^{-1}, [264] for the data presented for CH_2I_2 a corresponding contribution of self-broadening would be 1.39×10^{-6} cm^{-1} based on an experimental CH_2I_2 concentration of

4.9×10^{-6} atm (or 0.005 mbar, as given in section 4.2.2). For CH_2Br_2, using an averaged value of 0.327 cm^{-1} atm^{-1} based on the self-broadening of CH_3Br, the corresponding self-broadening contribution would be 1.82×10^{-4} cm^{-1}, based on an experimental CH_2Br_2 concentration of 6.4×10^{-4} atm (or 0.66 mbar, as given in section 5.2.2). Comparing these values, shows the contribution of self-broadening has potentially been over predicted. However, this does not explain why the presented N_2- and Ar-broadening parameters are larger than expected.

Table 6-2 Pressure Broadening Coefficients of Various Halogenated Molecules. Broadening coefficients from this work for N2 and Ar, values quotes on their own are averages, values given in ranges are the lowest and highest measured value (a reasonable average could not be obtained).

Molecule	Self-Broadening b (cm^{-1} atm^{-1})	N_2 b (cm^{-1} atm^{-1})	Ar b (cm^{-1} atm^{-1})
CH_2F_2	0.493[a] 0.519[b]	0.087[b]	…
CH_3F	0.388 to 0.600[c]	0.094[d] 0.100[e]	0.072[f]
CH_3Cl	0.152 to 0.483[h]	0.100[g] 0.108[i] 0.105[j]	0.092[g]
CH_2Br_2	…	0.145(7)[k]	0.105(5)[k]
CH_3Br	0.180 to 0.481[L] 0.154 to 0.493[n]	0.089 to 0.135[L] 0.075 to 0.131[m] 0.103[n]	…
CH_2I_2	…	0.143(6)[o]	0.116(6)[o]
CH_3I	0.284[p] 0.221[q] 0.290 to 0.386[s]	0.107[p] 0.133[r] 0.089 to 0.130[s]	…

a. Ref. [271]
b. Ref. [263]
c. Ref. [272]
d. Ref. [273]
e. Ref. [265]
f. Ref. [274]
g. Ref. [275]
h. Ref. [276]
i. Ref. [277]
j. Ref. [278]
k. This work
L. Ref. [279]
m. Ref. [280]
n. Ref. [270]
o. This work
p. Ref. [264]
q. Ref. [281]
r. Ref. [282]
s. Ref. [283]

7. Final Remarks

This final chapter will cover the future work of this thesis and present an overall conclusion to the thesis. For the future work, this section will cover the attempts to move towards an enhanced optical cavity, which is needed for acquiring cold temperature spectra of CH_2I_2 and CH_2Br_2, and in general, more sensitive gas phase measurements. Furthermore, *PGOPHER* simulations are utilised to predict what will be observed for the cold temperature spectra.

7.1. Future Work

7.1.1. Enhanced Optical Cavity

Although a Herriott Cell was originally used for the free-jet expansion, as discussed in section 2.2.3.2, the path length through the cell was never long enough to observe the cold molecules. This is for two reasons: the free-jet expansion method gives a lower concentration of molecules in the cell, and the interaction region, where the molecules interact with the laser, is much smaller for this set-up than the room temperature Herriott cell (see section 2.2.3 and Figure 2-9 and Figure 2-10). Therefore, an enhanced cavity will be used to improve the path length for the cold temperature experiments.

As discussed in the introduction (see section 1.4.4.2), CE-DFCS is an established technique as the method improves the path length of the optical cavity from cm in length to kms, which allows for lower concentration detection limits. [140, 284] However, this technique significantly reduces the transmission power of the comb out of the cavity, which reduces the sensitivity of the acquired spectra and decreases the SNR. Thus the absorption peaks are harder to detect, which defeats the purpose of increasing the path length of the cavity. To improve the power of the comb out of the cavity, efficient comb-cavity coupling is needed, of which there are two methods to achieve this: tight locking scheme and swept coupling scheme. In the tight locking scheme, the comb modes and the cavity resonances are kept identical through feedback mechanisms such as the Pound-Drever-Hall (PDH) method or a dither lock. [284, 285] However, this scheme causes large dispersion issues with the comb frequencies which means less light is coupled into the cavity as a function of wavelength, so the entire bandwidth of the laser cannot be detected, and suffers from residual frequency noise which must be removed in post-processing to reach high signal-to-noise ratios. To negate these issues, the alternative swept coupling scheme can be implemented.

In the swept coupling scheme, the comb modes are swept through the cavity modes with the amplitude of the sweep larger than the FWHM linewidth of the cavity resonance. [284] Slow drifts between the comb and cavity modes can be nullified by stabilising the time interval between transmission peaks, plus dispersion issues are avoided as the resonance between modes happens rapidly. The easiest way to sweep the comb modes within the cavity is to change the length of the cavity, which can be done through the implementation of a piezo-electrical device. Piezo-electrical devices, as already discussed in section 2.1.3, change in length in response to an applied voltage. The new enhanced cavity is also matched closely in length to the lasing cavity (60 cm or 250 MHz), which ensures the comb modes are efficiently swept through the cavity modes. Unfortunately, the swept-coupling scheme is slower than a tight-locking scheme, meaning the experimental time rises. [285] Faster sweeps can speed up the collection time and reduce associated noise, but this comes at the loss of transmission power. Therefore, optimum settings can be achieved with reduces baseline noise while retaining a high transmission power and a good S/N ratio. As this swept coupling scheme for an enhanced cavity has been achieved previously, [284] we do not anticipate significant hurdles in its construction

Such construction has already commenced on moving towards the enhanced cavity. The necessary optics are two high finesse mirrors with focal lengths of +1000 mm (Layertec). In addition, the piezo-electrical device has already been identified and purchased. This is a hollow tubular 1" diameter piezo from Piezomechanik (part number HPSt 150/20-15/12), with a maximum stroke length of 16 μm.

7.1.2. Cold Spectra Prediction

In order to help confirm the hot-band theory presented in this thesis for the room temperature spectra of CH_2I_2 and CH_2Br_2, acquiring spectra take under colder conditions would be beneficial. As explained in previous chapters and the section above, the cold spectra will be acquired through the use of a free-jet expansion and an enhanced optical cavity. While the cold spectra have not yet been acquired due to experimental constraints, as explained in section 3.6, it can be useful to predict the expected spectra. The predictions can be achieved by changing the temperature within the ν_6 *PGOPHER* simulations for both molecules (ν_1 is not possible for comparison due to the lack of appropriate simulation for CH_2Br_2). However, while a free-jet expansion apparatus can be useful in reducing the rotational temperature of the molecule, vibrational temperature is not always reduced to the same extent. This difference is due to a non-Boltzmann distribution of population. Therefore, the non-statistical population distribution must be accounted for in the predicted spectra.

Figure 7-1 and Figure 7-2 show three different simulations for CH_2I_2 and CH_2Br_2, respectively. For both figures, the black is the simulation at a rotational and vibrational temperature of 300 K, the red is the simulation at a rotational temperature of 30 K and a vibrational temperature of 300 K, and the blue is the simulation at a rotational and vibrational temperature of 30 K. In order to keep the simulations accurate, all observed vibrational transitions and appropriate isotopologues are included in the simulations. For CH_2I_2, this includes $6_0^1\,4_n^n$, with n ≤ 5, and for CH_2Br_2 this includes $6_0^1\,4_n^n$, with n ≤ 4 and all three isotopologues.

The initial obvious difference, for both molecules, between the room temperature (black) and cold spectra (red or blue, for this section of analysis the two can be interchangeable) is the intensity and breadth of the peaks. In both cases, the peaks in cold temperature spectra only cover a circa 30 cm^{-1} span rather than an 80 cm^{-1} span as seen for the room temperature spectra. In addition, the cold spectra intensity increases almost ten-fold for the most intense peaks, assuming the concentration is the stays the same across both spectra. However, this does not mean the peaks in the experimental cold spectrum will be ten-fold in intensity than those seen in the room temperature spectrum. This is due to the difference in concentration and path length in the two experiments. For the room temperature experiments, the path length is well known (between 570 and 1130 cm) and the concentration of the sample molecules averages close to 1 mbar. However, for the cold temperature spectra the concentration for the sample molecules is close to 2×10^{-4} mbar (however this is just an average of the total pressure inside the free-jet expansion chamber), and the path length is currently undetermined. Considering the differences in concentration and path length, in order to see tangible peaks in the cold temperature spectra, the path length needs to be longer than 1,000 km. However, this is also dependent on the σ_ν which is dependent on the temperature of the sample.

Secondly, another obvious difference is the appearance of the central Q-band which is prominent for both molecules. This difference is due to the reduction of rotational levels being populated at low temperatures, as the majority of the central Q branch for the room temperature spectra consists of high K_a, J, and K_c rotational transitions.

Thirdly, there is a difference between all three spectra for each temperature in terms of the populated vibrational levels. Comparing the room temperature simulated spectrum (black) and the cold temperature spectrum where the rotational temperature is 30 K but the vibrational temperature is kept at 300 K (red), there is no difference in which vibrational states are populated. For both spectra, there is initial population in the ground state (v = 0) and the ν_4 ($v \leq 5$) states. In addition, there is no difference in the relative peak intensities between successive peaks within the peak progressions. However, there is obviously a large difference in the populated vibrational states between the two cold temperature spectra (red and blue spectra) in Figure 7-1 and Figure 7-2. This lower vibrational temperature for the red spectrum in both figures, reduces the population in the hot bands, as there is no longer sufficient thermal energy to excite the molecules to the ν_4 vibrational states. In addition, this means the peaks concerning the fundamental ν_6 vibrational band are more intense within the blue spectrum than the red spectrum.

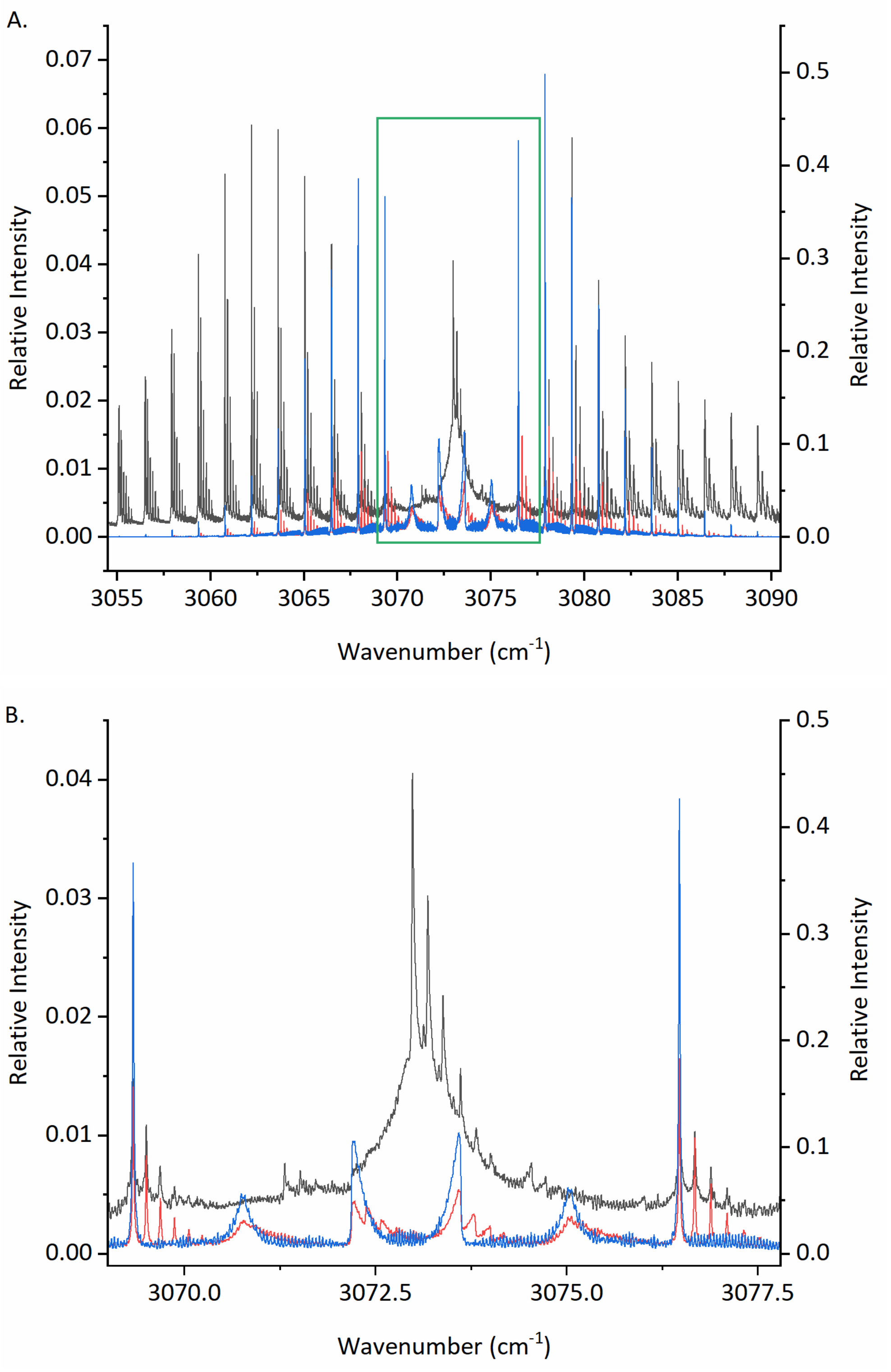

Figure 7-1 Comparison of CH_2I_2 Spectra at 300 K and 30 K. A. The simulated ν_6 vibrational band for CH_2I_2, from 3055 to 3090 cm^{-1}, the black = rotational and vibrational temperature of 300 K (relative intensity on the left *y*-axis), the red = rotational temperature of 30 K and vibrational temperature of 300 K (relative intensity of the right *y*-axis), and blue = rotational and vibrational temperature of 30 K (relative intensity of the right *y*-axis). B. Region of interest (green box in part A), from 3069.0 to 3077.6 cm^{-1}.

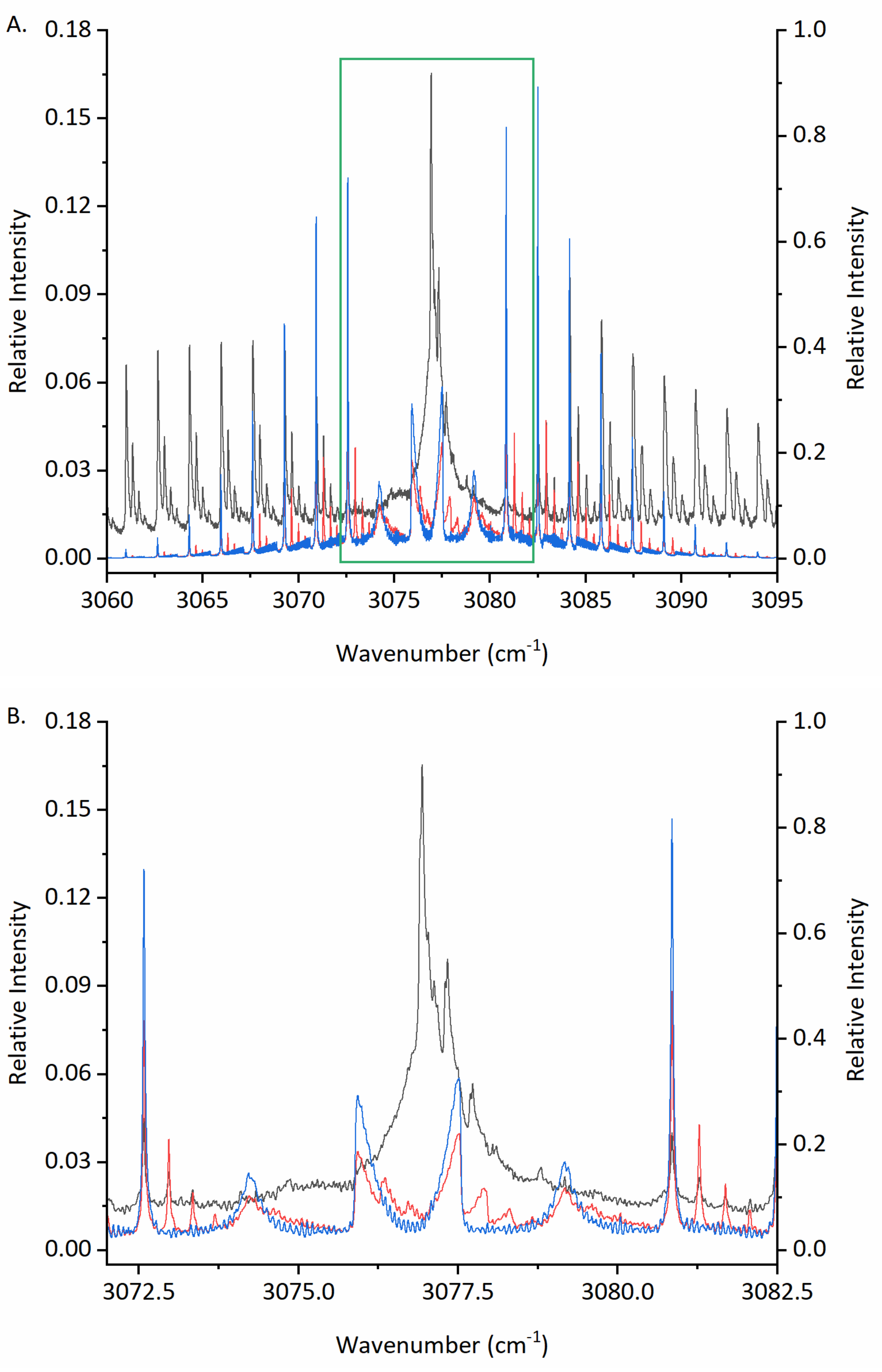

Figure 7-2 Comparison of CH_2Br_2 Spectra at 300 K and 30 K. A. The simulated ν_6 vibrational band for CH_2Br_2, from 3060 to 3095 cm^{-1}, the black = rotational and vibrational temperature of 300 K (relative intensity on the left *y*-axis), the red = rotational temperature of 30 K and vibrational temperature of 300 K (relative intensity of the right *y*-axis), and blue = rotational and vibrational temperature of 30 K (relative intensity of the right *y*-axis). B. Region of interest (green box in part A), from 3072.0 to 3082.5 cm^{-1}.

7.2. Conclusion

As stated in the introduction, halogen containing CH_2X_2 molecules are important species within the atmosphere as they contribute ozone depletion, interfere with the HO_x and NO_x cycles (CH_2Cl_2, CH_2Br_2, and CH_2I_2) or have a high global warming potential (CH_2F_2). While GC-MS techniques are currently used to measure concentrations of molecules in the atmosphere, however, this has shortcomings such as molecule degradation and fragmentation issues. Therefore, it is advantageous to move towards optical spectroscopy methods in order to observe molecules in the atmosphere. However, in order to use optical spectroscopy to observe the molecules, reference spectra and spectroscopic constants must be recorded within a laboratory setting before moving to outdoor measurements. After considering available literature, it was clear that research into mid-IR high resolution rovibrational spectra of CH_2I_2 and CH_2Br_2 was lacking. Therefore the majority of the work presented in this thesis was directed towards two different parts: 1. building a high resolution optical spectroscopy technique and 2. recording the rovibrational spectra of CH_2I_2 and CH_2Br_2.

Firstly, this thesis has demonstrated that mid-IR direct frequency comb spectroscopy is a powerful spectroscopic technique that can, and should, be implemented. This technique allows for high spectral resolution measurements with a simultaneously broad bandwidth due to the nature of the light source. The combination of these two properties means numerous different molecules can potentially be detected within one experiment. Furthermore, the 2D spatially dispersive detection method, in particular the VGC detection method in the spectrometer developed here, allows for comb-mode resolved detection of the frequency comb laser. Chapters 2 and 3 of this thesis gave a detailed account of the work undertaken to build, commission and characterise the frequency comb spectrometer. The major obstacles in building the spectrometer involved designing the optical set-up and alignment procedure of VGC detection, creating a *MATLAB* code to process the acquisition images to convert to spectra, and characterising the properties of the system such as baseline noise levels and minimum detectable concentrations. Furthermore, efforts were made to build a free-jet expansion apparatus in order to record cold temperature mid-IR spectra. However, the current cold spectra results showed promise but are currently not useable due to a poor SNR and an inability to observe low concentrations of the sample molecules. Hence, the future work will be to build an enhanced optical cavity which allows for an increased cavity length of over several kilometres in length, increasing the sensitivity of the measurement.

Secondly, the newly built direct frequency comb spectrometer was then utilised to record the room temperature mid-IR rovibrational spectra of CH_2I_2 and CH_2Br_2. For CH_2I_2, the experimental spectrum was recorded from 2960 to 3125 cm^{-1}, and for CH_2Br_2 the experimental spectrum was recorded from 2925 to 3125 cm^{-1}. Within both spectra many different vibrational transitions were observed: fundamental 6_0^1 and 1_0^1 transitions, alongside hypothesised hot-band transitions $6_0^1 4_n^n$ and $1_0^1 4_n^n$, where $n \leq 5$ for CH_2I_2 and $n \leq 3$ for CH_2Br_2. For each of these vibrational states, spectroscopic rotational constants were determined. The exception to this is the 1_0^1 band for CH_2Br_2 from 2935 to 3040 cm^{-1}, as the spectra were too congested to observe any rovibrational structure or hot-band transitions which are needed to determined rotational constants. For both CH_2I_2 and CH_2Br_2 computational results confirmed the hot-band transition hypothesis seen within the ν_6 and ν_1 bands. In addition, the effects of pressure broadening by N_2 and Ar on the observed rovibrational spectra of CH_2I_2 and CH_2Br_2 was studied. For CH_2I_2, the b_{N2} parameter = 0.143(6) cm^{-1} atm^{-1}, and the b_{Ar} parameter = 0.116(6) cm^{-1} atm^{-1}. For CH_2Br_2, the the b_{N2} parameter = 0.145(7) cm^{-1} atm^{-1}, and the b_{Ar} parameter = 0.105(5) cm^{-1} atm^{-1}.

Finally, comparisons are made between the room temperature mid-IR rovibrational spectra for all four dihalomethane molecules and the pressure broadening coefficients measured within this thesis are discussed in comparison to broadening coefficients for CH_2X_2, CH_3X, and CHX_3 molecules. For the room temperature spectra, CH_2F_2 and CH_2Cl_2 are not expected to exhibit the ν_4 hot-bands to such a degree as seen for CH_2I_2 and CH_2Br_2, owing to larger vibrational frequencies for the 4_0^1 fundamental transition. For CH_2F_2 we only expect to observe transitions from the ν_4 (v = 1) vibrational state and for CH_2Cl_2 we only expect to observe transitions from the ν_4 (v = 1) and ν_4 (v = 2) vibrational states. However, despite the lack of significant hot-band transitions, CH_2F_2 and CH_2Cl_2 demonstrate resonances and couplings between multiple vibrational states of which CH_2I_2 and CH_2Br_2 do not. With regards to the pressure broadening coefficients reported in this thesis, both values are higher than equivalent values reported in the literature. Across 12 different b_{N2} parameters for various CH_3X and CH_2F_2 molecules, the average is 0.103(18) cm^{-1} atm^{-1}, whereas for the b_{Ar} parameters the average across two values is 0.082(14) cm^{-1} atm^{-1}. The difference between the reported literature parameters and the parameters reported in this thesis is attributed to the potential shortcomings of the self-broadening parameters, over-predicting the contribution of the bath-gas, or using the wrong analysis method to analyse the pressure broadened spectra.

8. References

1. Allan, B.J. and J.M.C. Plane, *A study of the recombination of IO with NO_2 and the stability of INO_3: Implications for the atmospheric chemistry of iodine.* Journal of Physical Chemistry A, 2002. **106**(37): p. 8634-8641.
2. Cicerone, R.J., *Halogens in the Atmosphere.* Reviews of Geophysics, 1981. **19**(1): p. 123-139.
3. Schlesinger, W.H. and E.S. Bernhardt, *Chapter 3 - The Atmosphere*, in *Biogeochemistry (Fourth Edition)*, W.H. Schlesinger and E.S. Bernhardt, Editors. 2020, Academic Press. p. 51-97.
4. Molina, M.J. and F.S. Rowland, *Stratospheric Sink for Chlorofluoromethanes - Chlorine Atom Catalyzed Destruction of Ozone.* Bulletin of the American Meteorological Society, 1974. **55**(5): p. 491-491.
5. Secretariat, U.N.O., *Handbook for the International Treaties for the Protection of the Ozone Layer*, U.N.E. Programme, Editor. 2003, UNON: Kenya.
6. Pöhler, D., et al., *Observation of halogen species in the Amundsen Gulf, Arctic, by active long-path differential optical absorption spectroscopy.* Proceedings of the National Academy of Sciences of the United States of America, 2010. **107**(15): p. 6582-6587.
7. Buys, Z., et al., *High temporal resolution Br_2, BrCl and BrO observations in coastal Antarctica.* Atmospheric Chemistry and Physics, 2013. **13**(3): p. 1329-1343.
8. Commane, R., et al., *Iodine monoxide at a clean marine coastal site: observations of high frequency variations and inhomogeneous distributions.* Atmospheric chemistry and physics, 2011. **11**(13): p. 6721-6733.
9. Mehlmann, M., et al., *Natural and anthropogenic sources of bromoform and dibromomethane in the oceanographic and biogeochemical regime of the subtropical North East Atlantic.* Environmental Science: Processes & Impacts, 2020. **22**(3): p. 679-707.
10. Platt, U. and G. Honninger, *The role of halogen species in the troposphere.* Chemosphere, 2003. **52**(2): p. 325-338.
11. Finlayson-Pitts, B.J., *Halogens in the Troposphere.* Analytical Chemistry, 2010. **82**(3): p. 770-776.
12. Baker, A.R., *Marine aerosol iodine chemistry: The importance of soluble organic iodine.* Environmental Chemistry, 2005. **2**(4): p. 295-298.
13. Carpenter, L.J., *Iodine in the Marine Boundary Layer.* Chemical Reviews, 2003. **103**(12): p. 4953-4962.
14. García, M.G. and L. Borgnino, *Fluoride in the Context of the Environment*, in *Fluorine: Chemistry, Analysis, Function and Effects*. 2015, The Royal Society of Chemistry. p. 3-21.
15. Yi, X., et al., *Anthropogenic emissions of atomic chlorine precursors in the Yangtze River Delta region, China.* Science of The Total Environment, 2021. **771**: p. 144644.
16. Simpson, W.R., et al., *Halogens and their role in polar boundary-layer ozone depletion.* Atmospheric Chemistry and Physics, 2007. **7**(16): p. 4375-4418.
17. Bloss, W., et al., *Coupling of HOx, NOx and halogen chemistry in the antarctic boundary layer.* Atmospheric Chemistry and Physics, 2010. **10**(21): p. 10187-10209.
18. Li, Q., et al., *Potential Effect of Halogens on Atmospheric Oxidation and Air Quality in China.* J Geophys Res Atmos, 2020. **125**(9).
19. O'Doherty, S., et al., *Global emissions of HFC-143a (CH_3CF_3) and HFC-32 (CH_2F_2) from in situ and air archive atmospheric observations.* Atmos. Chem. Phys., 2014. **14**(17): p. 9249-9258.

20. Flerlage, H., G.J.M. Velders, and J. de Boer, *A review of bottom-up and top-down emission estimates of hydrofluorocarbons (HFCs) in different parts of the world.* Chemosphere, 2021. **283**: p. 131208.
21. Cox, M.L., et al., *Regional Sources of Methyl Chloride, Chloroform and Dichloromethane Identified from AGAGE Observations at Cape Grim, Tasmania, 1998–2000.* Journal of Atmospheric Chemistry, 2003. **45**(1): p. 79-99.
22. Elvidge, E., et al., *Increasing concentrations of dichloromethane, CH_2Cl_2, inferred from CARIBIC air samples collected 1998-2012.* Atmospheric Chemistry and Physics, 2015. **15**(4): p. 1939-1958.
23. Gautrois, M., et al., *Seasonal variability and trends of volatile organic compounds in the lower polar troposphere.* Journal of Geophysical Research: Atmospheres, 2003. **108**(D13).
24. Butler, R., et al., *Quantifying the vertical transport of $CHBr_3$ and CH_2Br_2 over the western Pacific.* Atmospheric Chemistry and Physics, 2018. **18**(17): p. 13135-13153.
25. Liu, S., Z. He, and G. Yang, *Bromoform, dibromochloromethane, and dibromomethane over the East China Sea and the western Pacific Ocean: Oceanic emission and spatial variation.* Chemosphere, 2020. **257**.
26. Kuyper, B., et al., *Volatile halocarbon measurements in the marine boundary layer at Cape Point, South Africa.* Atmospheric Environment, 2019. **214**.
27. Huang, R.J., et al., *In situ measurements of molecular iodine in the marine boundary layer: the link to macroalgae and the implications for O^{-3}, IO, OIO and NOx.* Atmospheric Chemistry and Physics, 2010. **10**(10): p. 4823-4833.
28. Jones, C.E., et al., *Quantifying the contribution of marine organic gases to atmospheric iodine.* Geophysical Research Letters, 2010. **37**(18).
29. Chen, W., D.S. Venables, and M.W. Sigrist, *Advances in Spectroscopic Monitoring of the Atmosphere*. 2021: Elsevier. iv.
30. Fang, M., et al., *Thermal Degradation of Small Molecules: A Global Metabolomic Investigation.* Analytical chemistry, 2015. **87**(21): p. 10935-10941.
31. Tuckett, R., et al., *The vacuum-ultraviolet photoelectron spectra of CH_2F_2 and CH_2Cl_2 revisited.* Journal of Molecular Spectroscopy, 2015. **315**: p. 172-183.
32. Wagner, P. and A.B.F. Duncan, *The Vacuum Ultraviolet Absorption Spectrum of Difluoromethane1.* Journal of the American Chemical Society, 1955. **77**(9): p. 2609-2610.
33. Pradeep, T. and D.A. Shirley, *High-Resolution Photoelectron-Spectroscopy of CH_2F_2, CH_2Cl_2, and CF_2Cl_2 using Supersonic Molecular Beams.* Journal of Electron Spectroscopy and Related Phenomena, 1993. **66**(1-2): p. 125-138.
34. Palmer, M.H., et al., *The valence and Rydberg states of difluoromethane: A combined experimental vacuum ultraviolet spectrum absorption and theoretical study by ab initio configuration interaction and density functional computations.* The Journal of Chemical Physics, 2018. **148**(21): p. 214304.
35. Petrenko, T. and G. Rauhut, *A General Approach for Calculating Strongly Anharmonic Vibronic Spectra with a High Density of States: The $\tilde{X}^2B_1 \leftarrow \tilde{X}^1A_1$ Photoelectron Spectrum of Difluoromethane.* Journal of Chemical Theory and Computation, 2017. **13**(11): p. 5515-5527.
36. Tasinato, N., et al., *Anharmonic force field and vibrational dynamics of CH_2F_2 up to 5000 cm^{-1} studied by Fourier transform infrared spectroscopy and state-of-the-art ab initio calculations.* Journal of Chemical Physics, 2012. **136**(21).
37. Amos, R.D., et al., *Anharmonic vibrational properties of CH_2F_2 : A comparison of theory and experiment.* The Journal of Chemical Physics, 1991. **95**(11): p. 8323-8336.
38. Porto, S.P.S., *Fine structure of some infrared bands of CH_2F_2 and CH_2ClF.* Journal of Molecular Spectroscopy, 1959. **3**(1): p. 248-258.

39. Stoppa, P., et al., *FTIR spectra of* CH_2F_2 *in the 1000-1300* cm^{-1} *region: Rovibrational analysis and modeling of the Coriolis and anharmonic resonances in the* ν_3, ν_5, ν_7, ν_9 *and* $2\nu_4$ *polyad.* Journal of Quantitative Spectroscopy & Radiative Transfer, 2016. **175**: p. 8-16.
40. Mizuno, M. and S. Saëki, *Infrared absorption intensities of methylene fluoride.* Spectrochimica Acta Part A: Molecular Spectroscopy, 1976. **32**(5): p. 1077-1082.
41. Petersen, J.C., D. Igner, and G. Duxbury, *Infrared-microwave double resonance as an aid in assignment of optically pumped submillimetre laser lines:* CH_2CF_2, CH_2F_2, *and* CH_3OH. Journal of Molecular Spectroscopy, 1983. **100**(2): p. 396-402.
42. Deo, M.N., R. Dcunha, and V.A. Job, *The* a_2 *"Forbidden" Band in* CH_2F_2*:* ν_5 - ν_7 *Coriolis Interaction.* Journal of Molecular Spectroscopy, 1993. **161**(2): p. 403-415.
43. Smith, K.M., et al., *A High-Resolution Analysis of the* ν_3 *and* ν_9 *Absorption Bands of Difluoromethane.* Journal of Molecular Spectroscopy, 1999. **193**(1): p. 166-173.
44. Deo, M.N., K. Kawaguchi, and R. D'Cunha, *High-resolution FTIR study of the* ν_2 *band of* CH_2F_2 *and Coriolis interaction between the* ν_2 *and* ν_8 *states.* Journal of Molecular Structure, 2000. **517-518**: p. 187-195.
45. Deo, M.N., et al., *High-resolution FTIR study of the* ν_4 *band of* CH_2F_2. Journal of Molecular Spectroscopy, 1992. **154**(1): p. 83-92.
46. Cronin, T.J., et al., *High-Resolution Infrared Spectra in the C–H Region of* CH_2F_2*: The* ν_6 *and* $2\nu_2$ *Bands.* Journal of Molecular Spectroscopy, 1999. **194**(2): p. 236 - 242.
47. Duarte, L.J., et al., *FTIR and dispersive gas phase fundamental infrared intensities of the fluorochloromethanes: Comparison with QCISD/cc-pVTZ results.* Spectrochimica Acta Part A: Molecular and Biomolecular Spectroscopy, 2018. **205**: p. 269-275.
48. Galabov, B., T. Dudev, and W.J. Orville-Thomas, *Interpretation and prediction of vibrational intensities in infrared spectra: fluorinated methanes.* Journal of Molecular Structure, 1986. **145**(1): p. 1-13.
49. Smith, K., et al., *Infrared band strengths and absorption cross-sections of HFC-32 vapour.* Journal of Quantitative Spectroscopy and Radiative Transfer, 1996. **56**(1): p. 73-82.
50. Fox, G.L. and H.B. Schlegel, *An ab initio study of the vibrational frequencies and infrared intensities of* CH_2F_2. The Journal of Chemical Physics, 1990. **92**(7): p. 4351-4356.
51. Furuya, K., A. Sakamoto, and M. Tasumi, *Anharmonic Vibrational Analysis of Dihalogenomethanes and Dihalogenoethanes by Density-Functional Theory Calculations.* Bulletin of the Chemical Society of Japan, 2019. **92**(12): p. 1993-2003.
52. Koutcher, J.A., et al., *Rotational absorption spectrum of methylene fluoride in the 20–100* cm^{-1} *region.* Journal of Molecular Spectroscopy, 1976. **60**(1): p. 373-380.
53. Lide, D.R., *The Microwave Spectrum and Structure of Methylene Fluoride1.* Journal of the American Chemical Society, 1952. **74**(14): p. 3548-3552.
54. Hirota, E., *Microwave spectrum of methylene fluoride in excited vibrational states.* Journal of Molecular Spectroscopy, 1978. **69**(3): p. 409-420.
55. Martinache, L., et al., *The ground state rotational spectrum of difluoromethane.* Journal of Molecular Spectroscopy, 1986. **119**(1): p. 225-228.
56. Gou, Q., et al., *Interactions between Freons: A Rotational Study of* CH_2F_2-CH_2Cl_2. Chemistry-an Asian Journal, 2014. **9**(4): p. 1032-1038.
57. Kukolich, S.G., J.H.S. Wang, and D.J. Ruben, *Measurement of hyperfine structure in* CH_2F_2 *by beam maser spectroscopy.* The Journal of Chemical Physics, 1973. **58**(12): p. 5474-5478.
58. Lange, E., et al., *The electronic excited states of dichloromethane in the 5.8-10.8 eV energy range investigated by experimental and theoretical methods.* Journal of Quantitative Spectroscopy and Radiative Transfer, 2020. **253**: p. 107172.
59. Simon, P.C., et al., *Ultraviolet absorption cross-sections of chloro and chlorofluoro-*

methanes at stratospheric temperatures. Journal of Atmospheric Chemistry, 1988. **7**(2): p. 107-135.

60. Mandal, A., et al., *Vacuum ultraviolet photoabsorption spectroscopy of* CH_2Cl_2 *and* CD_2Cl_2 *in the energy region 50,000–95,000* cm^{-1}*.* Journal of Quantitative Spectroscopy and Radiative Transfer, 2014. **149**: p. 291-302.
61. Hubrich, C. and F. Stuhl, *The ultraviolet absorption of some halogenated methanes and ethanes of atmospheric interest.* Journal of Photochemistry, 1980. **12**(2): p. 93-107.
62. Russell, B.R., L.O. Edwards, and J.W. Raymonda, *Vacuum ultraviolet absorption spectra of the chloromethanes.* Journal of the American Chemical Society, 1973. **95**(7): p. 2129-2133.
63. Nie, Z.-W., et al., *Electronic excitations of* CH_2Cl_2 *studied by fast electron scattering.* Journal of Quantitative Spectroscopy and Radiative Transfer, 2022. **287**: p. 108227.
64. Davis, R.W., A.G. Robiette, and M.C.L. Gerry, *The harmonic force fields of methylene chloride and dichlorosilane from combined microwave and infrared data.* Journal of Molecular Spectroscopy, 1981. **85**(2): p. 399-415.
65. Myers, R.J. and W.D. Gwinn, *The Microwave Spectra, Structure, Dipole Moment, and Chlorine Nuclear Quadrupole Coupling Constants of Methylene Chloride.* The Journal of Chemical Physics, 1952. **20**(9): p. 1420-1427.
66. Favero, L.B., et al., *Rotational Spectrum of Dichloromethane–Ne: Internal Dynamics and Cl Quadrupolar Hyperfine Effects.* The Journal of Physical Chemistry A, 2015. **119**(49): p. 11813-11819.
67. Wallington, T.J., et al., CH_3Cl*,* CH_2Cl_2*,* $CHCl_3$*, and* CCl_4*: Infrared spectra, radiative efficiencies, and global warming potentials.* Journal of Quantitative Spectroscopy & Radiative Transfer, 2016. **174**: p. 56-64.
68. Morcillo, J., L.J. Zamorano, and J.M.V. Heredia, *Infra-red intensities in* CH_2F_2*,* CH_2Cl_2 *and* CF_2Cl_2*.* Spectrochimica Acta, 1966. **22**(12): p. 1969-1980.
69. Shimanouchi, T. and I. Suzuki, *Infrared spectra and force constants of* CH_2Cl_2*,* $CHDCl_2$*, and* CD_2Cl_2*.* Journal of Molecular Spectroscopy, 1962. **8**(1): p. 222-235.
70. McKean, D.C., N.C. Craig, and M.M. Law, *Vibrational Anharmonicity and Harmonic Force Fields for Dichloromethane from Quantum-Chemical Calculations.* The Journal of Physical Chemistry A, 2008. **112**(40): p. 10006-10016.
71. Duncan, J.L., G.D. Nivellini, and F. Tullini, *Methylene chloride: The mid-infrared spectrum of an almost vibrationally unperturbed molecule.* Journal of Molecular Spectroscopy, 1986. **118**(1): p. 145-162.
72. Tullini, F., G.D. Nivellini, and M. Carlotti, *The Far-Infrared Spectrum of Methylene Chloride.* Journal of Molecular Spectroscopy, 1989. **138**(2): p. 355-374.
73. Liu, Q., et al., *Coupling among CH stretching, bending and rocking vibrational modes in* CH_2Cl_2*.* Chinese Journal of Chemical Physics, 2006. **19**(1): p. 15-19.
74. Tullini, F., et al., *High resolution vibration—rotation analyses for methylene chloride.* Spectrochimica Acta Part A: Molecular Spectroscopy, 1986. **42**(10): p. 1165-1169.
75. Kartha, V.B., *Infrared spectra of* CH_2Cl_2*,* CH_2Br_2*, and* CH_2I_2*: In the solid state.* Journal of Molecular Spectroscopy, 1967. **24**(1): p. 368-377.
76. Brown, C.W., et al., *Vibrational Spectra of Single Crystals and Polycrystalline Films of* CH_2Cl_2 *and* CH_2Br_2*.* The Journal of Chemical Physics, 1969. **51**(4): p. 1376-1384.
77. Devendorf, G.S., M.-H.A. Hu, and D. Ben-Amotz, *Pressure Dependent Vibrational Fermi Resonance in Liquid* CH_3OH *and* CH_2Cl_2*.* The Journal of Physical Chemistry A, 1998. **102**(52): p. 10614-10619.
78. Chen, M.-T., et al., *In-Situ FTIR Study of Adsorption and Photoreactions of* CH_2Cl_2 *on Powdered* TiO_2*.* The Journal of Physical Chemistry B, 2003. **107**(16): p. 3837-3843.
79. Fang, H.L. and R.L. Swofford, *Highly Excited Vibrational States of Molecules by Thermal Lensing Spectroscopy and the Local Mode Model:* $CHCl_3$*,* $CHBr_3$*,* CH_2Cl_2*,* CH_2Br_2*.* Journal

of Chemical Physics, 1980. **72**(12): p. 6382-6389.

80. Mossinger, J.C., D.E. Shallcross, and R.A. Cox, *UV-VIS absorption cross-sections and atmospheric lifetimes of CH_2Br_2, CH_2I_2 and CH_2BrI.* Journal of the Chemical Society-Faraday Transactions, 1998. **94**(10): p. 1391-1396.
81. Mandal, A., et al., *Rydberg and valence excited states of dibromomethane in 35,000-95,000 cm^{-1} region studied using synchrotron radiation.* Journal of Quantitative Spectroscopy & Radiative Transfer, 2014. **144**: p. 164-173.
82. Ito, M., P.-k.C. Huang, and E.M. Kosower, *Electronic absorption spectra of iodo- and bromomethanes.* Transactions of the Faraday Society, 1961. **57**(0): p. 1662-1673.
83. Molina, L.T., M.J. Molina, and F.S. Rowland, *Ultraviolet absorption cross sections of several brominated methanes and ethanes of atmospheric interest.* The Journal of Physical Chemistry, 1982. **86**(14): p. 2672-2676.
84. Gillotay, D. and P. Simon, *Ultraviolet absorption cross-sections of photoactive species of stratospheric interest. Part 1: The Halocarbons.* 1990.
85. Henry, B. and I.F. Hung, *Mass effects on the applicability of a local mode description - an analysis of the high energy overtone spectra of difluoro-, dichloro-, dibromo-, and diiodomethane.* Chemical Physics - CHEM PHYS, 1978. **29**: p. 465-475.
86. Chadwick, D. and D.J. Millen, *Microwave Spectrum of Dibromomethane Vol 1. Molecular Structure.* Transactions of the Faraday Society, 1971. **67**(582): p. 1539-&.
87. Chadwick, D. and D.J. Millen, *Microwave Spectrum of Dibromomethane Vol 2. Nuclear Quadrupole Coupling Tensor.* Transactions of the Faraday Society, 1971. **67**(582): p. 1551-&.
88. Davis, R.W. and M.C.L. Gerry, *The Microwave Spectrum, Centrifugal-Distortion Constants, Harmonic Force Field, and Structure of Dibromomethane.* Journal of Molecular Spectroscopy, 1985. **109**(2): p. 269-282.
89. Krishnaj, S.L. Srivastava, and A.S. Rajput, *Microwave Spectrum of Methylene Bromide.* Physics Letters A, 1970. **A 31**(7): p. 411-+.
90. Niide, Y., H. Tanaka, and I. Ohkoshi, *Microwave Spectrum of Dibromomethane in the Ground and Excited Bending Vibrational States - Hyperfine Structure by Coupling of ^{79}Br and ^{81}Br Nuclei.* Journal of Molecular Spectroscopy, 1990. **139**(1): p. 11-29.
91. Rice, T.E., et al., *Halogenated hydrocarbon gas sensing by rotational absorption spectroscopy in the 220-330 GHz frequency range.* Applied Physics B-Lasers and Optics, 2021. **127**(8).
92. Dennen, R.S., E.A. Piotrowski, and F.F. Cleveland, *Raman and Infrared Spectral Data for CH_2Br_2, $CHDBr_2$, and CD_2Br_2.* The Journal of Chemical Physics, 1968. **49**(10): p. 4385-4391.
93. Sadiek, I. and G. Friedrichs, *Doppler-limited high-resolution spectrum and VPT2 assisted assignment of the C-H stretch of CH_2Br_2.* Spectrochimica Acta Part a-Molecular and Biomolecular Spectroscopy, 2017. **181**: p. 180-191.
94. Brumfield, B.E., J.T. Stewart, and B.J. McCall, *High-resolution spectroscopy of the ν_8 band of methylene bromide using a quantum cascade laser.* Journal of Molecular Spectroscopy, 2011. **266**(1): p. 57-62.
95. Sharpe, S.W., et al., *Gas-Phase Databases for Quantitative Infrared Spectroscopy.* Applied Spectroscopy, 2004. **58**(12): p. 1452-1461.
96. Shimanouchi, T., *Tables of Molecular Vibrational Frequencies.* Journal of Physical and Chemical Reference Data, 1977. **6**(3): p. 993-1102.
97. Jamroz, M.H. and J.C. Dobrowolski, *IR Study on CH_2X_2 Double Hydrogen Bonding.* Journal of Molecular Structure, 1993. **293**: p. 143-146.
98. Marzocchi, M.P., et al., *Infrared Spectrum in Polarized Light of CH_2Br_2 and CD_2Br_2. Determination of the Crystal Structure.* The Journal of Chemical Physics, 1968. **49**(12): p. 5438-5444.

99. Paddison, S.J. and E. Tschuikow-Roux, *Structures, vibrational frequencies, thermodynamic properties, and bond dissociation energies of the bromomethanes and bromomethyl radicals: An ab initio study.* Journal of Physical Chemistry A, 1998. **102**(30): p. 6191-6199.
100. Venkatraman, R., et al., *Molecular structure and IR spectra of bromomethanes by DFT and post-Hartree-Fock MP2 and CCSD(T) calculations.* Molecular Physics, 2000. **98**(6): p. 371-386.
101. Liu, Y.S., et al., *Excited-state dynamics of CH_2I_2 and CH_2IBr studied with UV-pump VUV-probe momentum-resolved photoion spectroscopy.* Journal of Chemical Physics, 2020. **153**(18).
102. Mandal, A., et al., *Electronic state spectroscopy of diiodomethane (CH_2I_2): Experimental and computational studies in the 30 000-95 000 cm^{-1} region.* Journal of Chemical Physics, 2014. **140**(19).
103. Koffend, J.B. and S.R. Leone, *Tunable Laser Photo-dissociation - Quantum Yield of I* ($^2P_{1/2}$) from CH_2I_2.* Chemical Physics Letters, 1981. **81**(1): p. 136-141.
104. Schmitt, G. and F.J. Comes, *Spectroscopic Investigations of the Photolysis of Diiodomethane.* Journal of Molecular Structure, 1980. **61**(JAN): p. 51-54.
105. Kisiel, Z., et al., *First assignment of the rotational spectrum of a molecule containing two iodine nuclei: Spectroscopic constants and structure of CH_2I_2.* Journal of Chemical Physics, 1996. **105**(5): p. 1778-1785.
106. Kisiel, Z., E. Bialkowska-Jaworska, and L. Pszczolkowski, *The angle ICI bending satellites in the millimeter-wave rotational spectra of CH_2I_2 and CD_2I_2.* Journal of Molecular Spectroscopy, 2000. **199**(1): p. 5-12.
107. Johnson, T.J., T. Masiello, and S.W. Sharpe, *The quantitative infrared and NIR spectrum of CH_2I_2 vapor: vibrational assignments and potential for atmospheric monitoring.* Atmospheric Chemistry and Physics, 2006. **6**: p. 2581-2591.
108. Ford, T.A., *Infrared and Raman spectra and Vibrational Assignments of Diiodomethane and its Deuterated Analogs.* Journal of Molecular Spectroscopy, 1975. **58**(2): p. 185-193.
109. Kondo, J.N., et al., *IRAS study of adsorption and transformation of CH_2I_2 on Al(111) surface.* Surface Science, 1996. **349**(3): p. 294-300.
110. Marzocchi, M.P., V. Schettino, and S. Califano, *Infrared Spectrum of Crystalline CH_2I_2. Crystal Structure and Phase Transition.* The Journal of Chemical Physics, 1966. **45**(5): p. 1400-1404.
111. Voelz, F.L., et al., *Substituted methane .17. Vibrational Spectra, Potential Constants, and Calculated Thermodynamic Properties of Diiodomethane.* Journal of the Optical Society of America, 1953. **43**(11): p. 1061-1064.
112. Plyler, E.K. and W.S. Benedict, *Infrared Spectra of 18 Halogen-Substituted Methanes.* Journal of Research of the National Bureau of Standards, 1951. **47**(3): p. 202-220.
113. Walllace, R. and A.A. Wu, *Computation of Vibrational Stretching Spectra of CH_2X_2 and CD_2X_2 Molecules Using the Internal Coordinate Model.* Chemical Physics, 1979. **39**(2): p. 221-227.
114. Bernath, P.F., *Spectra of atoms and molecules*. Second edition. ed. 2005, Oxford: Oxford University Press.
115. Hollas, J.M., *Modern spectroscopy*. Third edition. ed. 1996, Chichester ;: J. Wiley.
116. Hilborn, R.C., *Einstein Coefficients, Cross Sections, F values, Dipole-Moments, and all that.* American Journal of Physics, 1982. **50**(11): p. 982-986.
117. Kakkar, R., *Atomic and Molecular Spectroscopy: Basic Concepts and Applications*. 2015, Cambridge: Cambridge University Press.
118. Giordano, N., *College Physics: Reasoning and Relationships*. 2009: Cengage Learning.
119. Foltynowicz, A., et al., *Sub-Doppler Double-Resonance Spectroscopy of Methane using

a Frequency Comb Probe. Phys. Rev. Lett., 2021. **126**: p. 063001.

120. Rutkowski, L., et al., *Optical frequency comb Fourier transform spectroscopy with sub-nominal resolution and precision beyond the Voigt profile.* Journal of Quantitative Spectroscopy and Radiative Transfer, 2018. **204**: p. 63-73.
121. Foltynowicz, A., et al., *Quantum-Noise-Limited Optical Frequency Comb Spectroscopy.* Physical Review Letters, 2011. **107**(23): p. 233002.
122. Masłowski, P., et al., *Surpassing the Path-Limited Resolution of Fourier-Transform Spectrometry with Frequency Combs.* Phys. Rev. A, 2016. **93**: p. 021802.
123. Griffith, D.W.T., et al., *Long open-path measurements of greenhouse gases in air using near-infrared Fourier transform spectroscopy.* Atmos. Meas. Tech., 2018. **11**(3): p. 1549-1563.
124. Heard, D.E., *Atmospheric field measurements of the hydroxyl radical using laser-induced fluorescence spectroscopy.* Annual Review of Physical Chemistry, 2006. **57**(1): p. 191-216.
125. Liu, F., et al., *Infrared-driven unimolecular reaction of* CH_3CHOO *Criegee intermediates to OH radical products.* Science, 2014. **345**(6204): p. 1596-1598.
126. Lin, H.-Y., et al., *Infrared identification of the Criegee intermediates syn- and anti-* CH_3CHOO*, and their distinct conformation-dependent reactivity.* Nature Communications, 2015. **6**(1): p. 7012.
127. Koshelev, M.A. and M.Y. Tretyakov, *Collisional broadening and shifting of OCS rotational spectrum lines.* Journal of Quantitative Spectroscopy and Radiative Transfer, 2009. **110**(1): p. 118-128.
128. Hollas, J.M., *High resolution spectroscopy*. 1982, London: Butterworth.
129. Stohner, J. and M. Quack, *Conventions, Symbols, Quantities, Units and Constants for High-Resolution Molecular Spectroscopy.* Handbook of High-resolution Spectroscopy, 2011.
130. Albert, S., et al., *Fundamentals of Rotation–Vibration Spectra.* Handbook of High-resolution Spectroscopy, 2011.
131. Herzberg, G. and J.W.T. Spinks, *Molecular spectra and molecular structure*. Prentice-Hall physics series. 1939, New York: Prentice-Hall.
132. Plastinin, I.V., et al., *The Role of Fermi and Darling–Dennison Resonances in the Formation of the Raman Spectra of Water and Water–Ethanol Solutions.* Bulletin of the Russian Academy of Sciences: Physics, 2019. **83**(3): p. 324-329.
133. Darling, B.T. and D.M. Dennison, *The Water Vapor Molecule.* Physical Review, 1940. **57**(2): p. 128-139.
134. *The Nobel Prize in Physics 2005*. Available from: https://www.nobelprize.org/prizes/physics/2005/summary/.
135. Demtröder, W., *Laser spectroscopy : basic concepts and instrumentation*. 3rd ed. ed. 2003, Berlin ; New York: Springer.
136. Waxman, E.M., et al., *Intercomparison of open-path trace gas measurements with two dual-frequency-comb spectrometers.* Atmospheric Measurement Techniques, 2017. **10**(9): p. 3295-3311.
137. Roberts, F.C., et al., *A Rapid, Spatially Dispersive Frequency Comb Spectrograph Aimed at Gas Phase Chemical Reaction Kinetics.* Mol. Phys., 2020. **118**: p. e1733116.
138. Pasquazi, A., et al., *Micro-combs: A novel generation of optical sources.* Physics Reports, 2018. **729**: p. 1-81.
139. Fortier, T. and E. Baumann, *20 Years of Developments in Optical Frequency Comb Technology and Applications.* Commun. Phys., 2019. **2**: p. 16.
140. Adler, F., et al., *Cavity-Enhanced Direct Frequency Comb Spectroscopy: Technology and Applications.* Annual Review of Analytical Chemistry, Vol 3, 2010. **3**: p. 175-205.
141. Holzwarth, R., et al., *Optical Frequency Synthesizer for Precision Spectroscopy.* Physical

Review Letters, 2000. **85**(11): p. 2264-2267.
142. Zhu, F., et al., *High-power mid-infrared frequency comb source based on a femtosecond Er:fiber oscillator.* Optics Letters, 2013. **38**(13): p. 2360-2362.
143. Kirchner, M., et al., *A low-threshold self-referenced Ti: Sapphire optical frequency comb.* Optics Express, 2006. **14**(20): p. 9531-9536.
144. Rausch, S., et al. *Ti:sapphire frequency comb with octave-spanning spectrum for spectroscopy and few-cycle pulse shaping*. in *CLEO/Europe - EQEC 2009 - European Conference on Lasers and Electro-Optics and the European Quantum Electronics Conference*. 2009.
145. Pollnau, M., et al., *Three-transition cascade erbium laser at 1.7, 2.7, and 1.6 µm.* Opt. Lett., 1997. **22**(9): p. 612-614.
146. Li, X., et al., *High-power ultrafast Yb:fiber laser frequency combs using commercially available components and basic fiber tools.* Review of Scientific Instruments, 2016. **87**(9): p. 093114.
147. Ye, J. and S.T. Cundiff, *Femtosecond optical frequency comb : principle, operation, and applications*. 2005, New York ; [Great Britain]: Springer.
148. Chen, Y., et al., *Tunable Visible Frequency Combs from a Yb-Fiber-Laser-Pumped Optical Parametric Oscillator.* Appl. Phys. B, 2019. **125**: p. 81.
149. Ricciardi, I., et al., *Frequency-comb-referenced singly-resonant OPO for sub-Doppler spectroscopy.* Optics Express, 2012. **20**(8): p. 9178-9186.
150. Abbas, M.A., et al., *Time-resolved mid-infrared dual-comb spectroscopy.* Scientific Reports, 2019. **9**.
151. Coddington, I., N. Newbury, and W. Swann, *Dual-comb spectroscopy.* Optica, 2016. **3**(4): p. 414-426.
152. Ideguchi, T., et al., *Adaptive real-time dual-comb spectroscopy.* Nature Communications, 2014. **5**.
153. de Cumis, M.S., et al., *Multiplexed direct-frequency-comb Vernier spectroscopy of carbon dioxide* $2\nu_1 + \nu_3$ *ro-vibrational combination band.* Journal of Chemical Physics, 2018. **148**(11).
154. Gohle, C., et al., *Frequency Comb Vernier Spectroscopy for Broadband, High-Resolution, High-Sensitivity Absorption and Dispersion Spectra.* Phys. Rev. Lett., 2007. **99**: p. 263902.
155. Khodabakhsh, A., et al., *Fourier Transform and Vernier Spectroscopy using an Optical Frequency Comb at 3-5.4 mm.* Opt. Lett., 2016. **41**: p. 2541.
156. Zhu, F., et al., *Near infrared frequency comb vernier spectrometer for broadband trace gas detection.* Optics Express, 2014. **22**(19): p. 23026-23033.
157. Friedlein, J.T., et al., *Dual-Comb Photoacoustic Spectroscopy.* Nat. Commun., 2020. **11**: p. 10.
158. Sadiek, I., et al., *Optical Frequency Comb Photoacoustic Spectroscopy.* Phys. Chem. Chem. Phys., 2018. **20**: p. 27849.
159. Kim, J., et al., *Dual-Frequency Comb Transient Absorption: Broad Dynamic Range Measurement of Femtosecond to Nanosecond Relaxation Processes.* Journal of Physical Chemistry Letters, 2018. **9**(8): p. 1866-1871.
160. Berera, R., R. van Grondelle, and J.T.M. Kennis, *Ultrafast Transient Absorption Spectroscopy: Principles and Application to Photosynthetic Systems.* Photosynth. Res., 2009. **101**: p. 105.
161. Kowligy, A.S., et al., *Infrared Electric Field Sampled Frequency Comb Spectroscopy.* Sci. Adv., 2019. **5**: p. eaaw8794.
162. Finneran, I.A., et al., *Decade-Spanning High-Precision Terahertz Frequency Comb.* Phys. Rev. Lett., 2015. **114**: p. 163902.
163. Nugent-Glandorf, L., et al., *Mid-Infrared Virtually Imaged Phased Array Spectrometer*

for Rapid and Broadband Trace Gas Detection. Opt. Lett., 2012. **37**: p. 3285.

164. Bailey, D.M., G. Zhao, and A.J. Fleisher, *Precision Spectroscopy of Nitrous Oxide Isotopocules with a Cross-Dispersed Spectrometer and a Mid-Infrared Frequency Comb.* Analytical Chemistry, 2020. **92**(20): p. 13759-13766.
165. Iwakuni, K., et al., *Comb-resolved spectroscopy with immersion grating in long-wave infrared.* Optics Express, 2019. **27**(3): p. 1911-1921.
166. Davis, S.P., M.C. Abrams, and J.W. Brault, *Fourier transform spectrometry*. 2001, San Diego ; London: Academic Press.
167. Foltynowicz, A., et al., *Quantum-Noise-Limited Optical Frequency Comb Spectroscopy.* Phys. Rev. Lett., 2011. **107**: p. 233002.
168. Coddington, I., W.C. Swann, and N.R. Newbury, *Time-domain spectroscopy of molecular free-induction decay in the infrared.* Optics Letters, 2010. **35**(9): p. 1395-1397.
169. Hecht, J., *The Laser Guidebook*. 1999: McGraw-Hill Education.
170. Partin, D.L., *Lead salt quantum well diode lasers.* Superlattices and Microstructures, 1985. **1**(2): p. 131-135.
171. Tacke, M., *Lead-Salt Lasers.* Philosophical Transactions: Mathematical, Physical and Engineering Sciences, 2001. **359**(1780): p. 547-566.
172. Mirov, S., et al., *Progress in* Cr^{2+} *and* Fe^{2+} *doped mid-IR laser materials.* Laser & Photonics Reviews, 2010. **4**(1): p. 21-41.
173. Stowe, M.C., et al., *Direct frequency comb spectroscopy*, in *Advances In Atomic, Molecular, and Optical Physics*, E. Arimondo, P.R. Berman, and C.C. Lin, Editors. 2008, Academic Press. p. 1-60.
174. Thorpe, M.J., et al., *Cavity-enhanced optical frequency comb spectroscopy: application to human breath analysis.* Optics Express, 2008. **16**(4): p. 2387-2397.
175. Weichman, M.L., et al., *Broadband molecular spectroscopy with optical frequency combs.* Journal of Molecular Spectroscopy, 2019. **355**: p. 66-78.
176. Ye, J., H. Schnatz, and L. Hollberg, *Optical frequency combs: From frequency metrology to optical phase control.* Ieee Journal of Selected Topics in Quantum Electronics, 2003. **9**(4): p. 1041-1058.
177. Picque, N. and T.W. Hänsch, *Frequency comb spectroscopy.* Nature Photonics, 2019. **13**(3): p. 146-157.
178. Lehman, J.H. and M.L. Weichman, *Optical Frequency Combs for Molecular Spectroscopy, Kinetics, and Sensing*, in *Emerging Trends in Chemical Applications of Lasers*. 2021, American Chemical Society. p. 61-88.
179. Luo, P.L., Y. Endo, and Y.P. Lee, *Identification and Self-Reaction Kinetics of Criegee Intermediates syn-CH3CHOO and CH2OO via High-Resolution Infrared Spectra with a Quantum-Cascade Laser.* J. Phys. Chem. Lett., 2018. **9**: p. 4391.
180. Luo, P.-L., *Long-wave mid-infrared time-resolved dual-comb spectroscopy of short-lived intermediates.* Opt. Lett., 2020. **45**(24): p. 6791--6794.
181. Luo, P.-L. and E.-C. Horng, *Simultaneous determination of transient free radicals and reaction kinetics by high-resolution time-resolved dual-comb spectroscopy.* Communications Chemistry, 2020. **3**(1): p. 95.
182. Bjork, B.J., et al., *Direct Frequency Comb Measurement of OD + CO → DOCO Kinetics.* Science, 2016. **354**: p. 444.
183. Bui, T.Q., et al., *Direct Measurements of DOCO Isomers in the Kinetics of OD + CO.* Sci. Adv., 2018. **4**: p. eaao4777.
184. Bui, T., et al., *Spectral analyses of trans- and cis-DOCO transients via comb spectroscopy.* Molecular Physics, 2018. **116**(23-24): p. 3710-3717.
185. Fleisher, A.J., et al., *Mid-Infrared Time-Resolved Frequency Comb Spectroscopy of Transient Free Radicals.* The Journal of Physical Chemistry Letters, 2014. **5**(13): p. 2241-2246.

186. Luo, P.-L., Y. Endo, and Y.-P. Lee, *Identification and Self-Reaction Kinetics of Criegee Intermediates syn-CH_3CHOO and CH_2OO via High-Resolution Infrared Spectra with a Quantum-Cascade Laser.* The Journal of Physical Chemistry Letters, 2018. **9**(15): p. 4391-4395.
187. Liang, Q., et al., *Ultrasensitive multispecies spectroscopic breath analysis for real-time health monitoring and diagnostics.* Proceedings of the National Academy of Sciences, 2021. **118**(40): p. e2105063118.
188. Alden, C.B., et al., *Bootstrap inversion technique for atmospheric trace gas source detection and quantification using long open-path laser measurements.* Atmospheric Measurement Techniques, 2018. **11**(3): p. 1565-1582.
189. Cossel, K.C., et al., *Open-path dual-comb spectroscopy to an airborne retroreflector.* Optica, 2017. **4**(7): p. 724-728.
190. Nugent-Glandorf, L., F.R. Giorgetta, and S.A. Diddams, *Open-air, broad-bandwidth trace gas sensing with a mid-infrared optical frequency comb.* Applied Physics B-Lasers and Optics, 2015. **119**(2): p. 327-338.
191. Schliesser, A., et al., *Frequency-Comb Infrared Spectrometer for Rapid, Remote Chemical Sensing.* Opt. Express, 2005. **13**: p. 9029.
192. Ycas, G., et al., *Mid-Infrared Dual-Comb Spectroscopy of Volatile Organic Compounds Across Long Open-Air Paths.* Optica, 2019. **6**: p. 165.
193. Ycas, G., et al., *Compact Mid-Infrared Dual-Comb Spectrometer for Outdoor Spectroscopy.* Opt. Express, 2020. **28**: p. 14740.
194. Waxman, E.M., et al., *Estimating Vehicle Carbon Dioxide Emissions from Boulder, Colorado, Using Horizontal Path-Integrated Column Measurements.* Atmos. Chem. Phys., 2019. **19**: p. 4177.
195. Coburn, S., et al., *Regional trace-gas source attribution using a field-deployed dual frequency comb spectrometer.* Optica, 2018. **5**(4): p. 320-327.
196. Henderson, B., et al., *Laser spectroscopy for breath analysis: towards clinical implementation.* Applied Physics B, 2018. **124**(8): p. 161.
197. Prabhu, P. and C. Shelton, *Detection and Quantification of Formaldehyde by Derivatization with Pentafluorobenzylhydroxyl Amine in Pharmaceutical Excipients by Static Headspace GC/MS.* MS, Perkin Elmer Application Note, 2011.
198. Jackie, C. Lee, and A. Toyama, *Shimadzu's Fundamental Guide to Gas Chromatography Mass Spectrometry (GCMS)*. 2020, Shimadzu.
199. Baumann, E., et al., *Spectroscopy of the methane v_3 band with an accurate midinfrared coherent dual-comb spectrometer.* Physical Review A, 2011. **84**(6): p. 9.
200. Gambetta, A., et al., *Versatile mid-infrared frequency-comb referenced sub-Doppler spectrometer.* APL Photonics, 2018. **3**(4): p. 046103.
201. Long, D.A., et al., *Multiplexed Sub-Doppler Spectroscopy with an Optical Frequency Comb.* Phys. Rev. A, 2016. **94**: p. 061801.
202. Changala, P.B., et al., *Sensitivity and Resolution in Frequency Comb Spectroscopy of Buffer Gas Cooled Polyatomic Molecules.* Appl. Phys. B, 2016. **122**: p. 292.
203. Changala, P.B., et al., *Rovibrational Quantum State Resolution of the C60 Fullerene.* Science, 2019. **363**: p. 49.
204. Liu, L.R., et al., *Collision-induced C_{60} rovibrational relaxation probed by state-resolved nonlinear spectroscopy.* arXiv, 2022.
205. Rey, M., et al., *TheoReTS – An information system for theoretical spectra based on variational predictions from molecular potential energy and dipole moment surfaces.* Journal of Molecular Spectroscopy, 2016. **327**: p. 138-158.
206. Steinmetz, A., et al., *Nonlinear compression of Q-Switched laser pulses to the realm of ultrashort durations.* Optics Express, 2011. **19**(4): p. 3758-3764.
207. Hawkes, J. and I. Latimer, *Lasers: Theory and Practice*. 1994, Hertfordshire, UK: Prentice

Hall International Limited.

208. Paschotta, R. *Time-Bandwidth Product*. *Encyclopedia of Laser Physics and Technology* 2008 [cited 2022 20/03/2022]; Available from: https://www.rp-photonics.com/time_bandwidth_product.html.

209. Hänsel, W., et al., *Laser with non-linear optical loop mirror*, E.P. Office, Editor. 2013, Menlo Systems GmbH: Germany.

210. Myers, L.E., et al., *Quasi-phase-matched optical parametric oscillators in bulk periodically poled LiNbO3.* J. Opt. Soc. Am. B, 1995. **12**(11): p. 2102--2116.

211. *FC1500-250-WG User Manual*. 2016, Munich, Germany: Menlo Systems GmbH.

212. Herriott, D.R. and H.J. Schulte, *Folded Optical Delay Lines.* Applied Optics, 1965. **4**(8): p. 883-889.

213. Herriott, D., H. Kogelnik, and R. Kompfner, *Off-Axis Paths in Spherical Mirror Interferometers.* Applied Optics, 1964. **3**(4): p. 523-526.

214. Dong, M., et al., *Herriott Cell Design With Minimum Volume and Multiple Reflection Rings for Infrared Gas Sensing.* IEEE Photonics Technology Letters, 2019. **31**(7): p. 541-544.

215. Gordon, I.E., et al., *The HITRAN2016 molecular spectroscopic database.* Journal of Quantitative Spectroscopy & Radiative Transfer, 2017. **203**: p. 3-69.

216. Gordon, I.E., et al., *The HITRAN2020 molecular spectroscopic database.* Journal of Quantitative Spectroscopy and Radiative Transfer, 2022. **277**: p. 107949.

217. Bronkhorst, *Mass Flow / Pressure meters and controllers for gases and liquids*. 2016.

218. Havenith, M., *The Molecular Beam*, in *Infrared Spectroscopy of Molecular Clusters: An Introduction to Intermolecular Forces*. 2002, Springer Berlin Heidelberg: Berlin, Heidelberg. p. 35-46.

219. Bucher, J.P., et al., *A pulsed supersonic expansion with a source temperature below 100 K.* Review of Scientific Instruments, 1990. **61**(9): p. 2374-2377.

220. Scoles, G., *Atomic and molecular beam methods*. 1988, New York, N.Y.: OUP.

221. Precision-Fluidics-Division, *Pulse - High Speed High Vacuum Valve Datasheet*. 2016, Parker Hannifin.

222. Hecht, E. and A. Zajac, *Optics*. Addison-Wesley World Student Series. 1974, Reading, Mass.: Addison-Wesley Pub. Co. viii, 565p.

223. Yeh, C., *Handbook of fiber optics : theory and applications*. 1990, San Diego: London : Academic. xv, 382 p.

224. Kao, C.K., *Optical fibre*. IEE materials devices series. 1988, London: Peregrinus. ix, 158 p.

225. Shirasaki, M., *Virtually imaged phased array.* Fujitsu Scientific & Technical Journal, 1999. **35**(1): p. 113-125.

226. Grzegorz, K., et al., *Self-referenced, accurate and sensitive optical frequency comb spectroscopy with a virtually imaged phased array spectrometer.* Opt. Lett., 2016. **41**(5): p. 974-977.

227. Xiao, S.J., A.M. Weiner, and C. Lin, *A dispersion law for virtually imaged phased-array spectral dispersers based on paraxial wave theory.* Ieee Journal of Quantum Electronics, 2004. **40**(4): p. 420-426.

228. Hansel, A., et al., *Temperature measurement using frequency comb absorption spectroscopy of CO_2.* Review of Scientific Instruments, 2017. **88**(5).

229. Thorlabs. *Diffraction Gratings Tutorial*. 2019 [cited 2019 25/07/2019]; Available from: https://www.thorlabs.com/newgrouppage9.cfm?objectgroup_id=9026.

230. Western, C.M., *PGOPHER: A program for simulating rotational, vibrational and electronic spectra.* Journal of Quantitative Spectroscopy & Radiative Transfer, 2017. **186**: p. 221-242.

231. ThorLabs. *Camera Noise and Temperature Tutorial*. 2018 [cited 2022 14/06/2022];

Available from: https://www.thorlabs.com/newgrouppage9.cfm?objectgroup_id=10773.

232. Fellers, T.J. and M.W. Davidson. *CCD Noise Sources and Signal-to-Noise Ratio*. 2015 [cited 2022 14/06/2022]; Available from: https://hamamatsu.magnet.fsu.edu/articles/ccdsnr.html#:~:text=The%20three%20primary%20broad%20components,they%20are%20temporal%20or%20spatial.

233. Kochanov, R.V., et al., *HITRAN Application Programming Interface (HAPI): A comprehensive approach to working with spectroscopic data.* Journal of Quantitative Spectroscopy & Radiative Transfer, 2016. **177**: p. 15-30.

234. Frisch, M.J., et al., *Gaussian 09*. 2009, Gaussian, Inc.: Wallingford.

235. Albrecht, T., et al., *Deep learning for single-molecule science.* Nanotechnology, 2017. **28**(42).

236. Cossel, K.C., et al., *Gas-phase broadband spectroscopy using active sources: progress, status, and applications.* Journal of the Optical Society of America B-Optical Physics, 2017. **34**(1): p. 104-129.

237. Foltynowicz, A., et al., *Cavity-enhanced optical frequency comb spectroscopy in the mid-infrared application to trace detection of hydrogen peroxide.* Applied Physics B-Lasers and Optics, 2013. **110**(2): p. 163-175.

238. Jones, C.E. and L.J. Carpenter, *Solar photolysis of* CH_2I_2*,* CH_2ICl*, and* CH_2IBr *in water, saltwater, and seawater.* Environmental Science & Technology, 2005. **39**(16): p. 6130-6137.

239. Saiz-Lopez, A., et al., *Atmospheric Chemistry of Iodine.* Chemical Reviews, 2012. **112**(3): p. 1773-1804.

240. Saiz-Lopez, A., et al., *Iodine chemistry in the troposphere and its effect on ozone.* Atmospheric Chemistry and Physics, 2014. **14**(23): p. 13119-13143.

241. Calvert, J.G. and S.E. Lindberg, *Potential influence of iodine-containing compounds on the chemistry of the troposphere in the polar spring. I. Ozone depletion.* Atmospheric Environment, 2004. **38**(30): p. 5087-5104.

242. Jimenez, J.L., et al., *New particle formation from photooxidation of diiodomethane (*CH_2I_2*).* Journal of Geophysical Research-Atmospheres, 2003. **108**(D10).

243. Dillon, T.J., et al., *LIF studies of iodine oxide chemistry Part 3. Reactions* $IO + NO_3 \rightarrow OIO + NO_2$*,* $I + NO_3 \rightarrow IO + NO_2$*, and* $CH_2I + O_2 \rightarrow$ *(products): implications for the chemistry of the marine atmosphere at night.* Physical Chemistry Chemical Physics, 2008. **10**(11): p. 1540-1554.

244. Welz, O., et al., *Direct Kinetic Measurements of Criegee Intermediate (*CH_2OO*) Formed by Reaction of* CH_2I *with* O_2*.* Science, 2012. **335**(6065): p. 204-207.

245. Orphal, J., N. Ibrahim, and C.E. Fellow, *The* v_1 *and* v_6 *bands of diiodomethane* CH_2I_2 *around 3.3 um studied by high resolution FTS*, in *19th Colloquium on High Resolution Molecular Spectroscopy*. 2005: Salamanca, Spain.

246. Satta, M., et al., *A joint theoretical and experimental study on diiodomethane: Ions and neutrals in the gas phase.* Journal of Chemical Physics, 2015. **143**(24).

247. Elles, C.G., et al., *Vibrational relaxation of* CH_2I_2 *in solution: Excitation level dependence.* Journal of Chemical Physics, 2003. **118**(12): p. 5587-5595.

248. Bingemann, D., A.M. King, and F.F. Crim, *Transient electronic absorption of vibrationally excited* CH_2I_2*: Watching energy flow in solution.* Journal of Chemical Physics, 2000. **113**(12): p. 5018-5025.

249. Kwok, W.M. and D.L. Phillips, *Solvation and solvent effects on the short-time photodissociation dynamics of* CH_2I_2 *from resonance Raman spectroscopy.* Journal of Chemical Physics, 1996. **104**(7): p. 2529-2540.

250. Heckscher, M.M., et al., *Relaxation of the C-H stretching fundamental vibrations of* CHI_3*,* CH_2I_2*, and* CH_3I *in solution.* Journal of Chemical Physics, 2002. **117**(19): p. 8917-8925.

251. Cheatum, C.M., et al., *CH_2I_2 fundamental vibrational relaxation in solution studied by transient electronic absorption spectroscopy.* Journal of Chemical Physics, 2001. **115**(15): p. 7086-7093.

252. Carl L. Yaws, P.D., *Chemical Properties Handbook*. 1999, New York: McGraw-Hill Education.

253. Johnson, T., S. Sharpe, and M. Covert, *Disseminator for rapid, selectable, and quantitative delivery of low and semivolatile liquid species to the vapor phase.* Review of Scientific Instruments, 2006. **77**(9).

254. Ofcom, *UK Frequency Allocation Table (UKFAT)*. 2020, Ofcom.

255. Weigend, F. and R. Ahlrichs, *Balanced basis sets of split valence, triple zeta valence and quadruple zeta valence quality for H to Rn: Design and assessment of accuracy.* Physical Chemistry Chemical Physics, 2005. **7**(18): p. 3297-3305.

256. Easton, R.E., et al., *The MIDI! basis set for quantum mechanical calculations of molecular geometries and partial charges.* Theoretica chimica acta, 1996. **93**(5): p. 281-301.

257. Curtiss, L.A., et al., *Extension of Gaussian-2 theory to molecules containing third-row atoms Ga–Kr.* The Journal of Chemical Physics, 1995. **103**(14): p. 6104-6113.

258. Roberts, F.C. and J.H. Lehman, *Infrared frequency comb spectroscopy of CH_2I_2: Influence of hot bands and pressure broadening on the v_1 and v_6 fundamental transitions.* The Journal of Chemical Physics, 2022. **156**(11): p. 114301.

259. Carpenter, J.H., *Choice of Reduction for the Asymmetric Top Hamiltonian in HNO_3.* Journal of Molecular Spectroscopy, 1985. **111**: p. 198-200.

260. Jabłoński, A., *General Theory of Pressure Broadening of Spectral Lines.* Physical Review, 1945. **68**(3-4): p. 78-93.

261. Rabitz, H., *Rotation and Rotation-Vibration Pressure-Broadened Spectral Lineshapes.* Annual Review of Physical Chemistry, 1974. **25**(1): p. 155-177.

262. Tsao, C.J. and B. Curnutte, *Line-Widths of Pressure Broadened Spectral Lines.* Journal of Quantitative Spectroscopy & Radiative Transfer, 1962. **2**(1): p. 41-91.

263. Tasinato, N., et al., *Self-, N_2-, O_2-broadening coefficients and line parameters of HFC-32 for v_7 band and ground state transitions from infrared and microwave spectroscopy.* Molecular Physics, 2014. **112**(18): p. 2384-2396.

264. Attafi, Y., et al., *Self and N_2 collisional broadening of rovibrational lines in the v_6 band of methyl iodide ($^{12}CH_3I$) at room temperature: The J and K dependence.* Journal of Quantitative Spectroscopy and Radiative Transfer, 2019. **231**: p. 1-8.

265. Lepère, M., et al., *K-dependence of broadening coefficients for CH_3F–N_2 and for other systems involving a symmetric top molecule.* Journal of Molecular Structure, 2000. **517-518**: p. 493-502.

266. Dhib, D., et al., *Measurements and calculations of Ar-broadening and shifting parameters of CH_3F transitions in the v_6 band.* Journal of Quantitative Spectroscopy and Radiative Transfer, 2019. **231**: p. 115-125.

267. MELLOUKI, A., et al., *Atmospheric Lifetimes and Ozone Depletion Potentials of Methyl-Bromide (CH_3Br) and Dibromomethane (CH_2Br_2).* Geophysical Research Letters, 1992. **19**(20): p. 2059-2062.

268. Nakajima, M. and Y. Endo, *Communication: Determination of the molecular structure of the simplest Criegee intermediate CH_2OO.* Journal of Chemical Physics, 2013. **139**(10).

269. Bertrán, J.F., et al., *Assignment of the forbidden level of the Fermi doublet in the Raman spectrum of CH_2Br_2.* Journal of Raman Spectroscopy, 1988. **19**(1): p. 33-35.

270. Boussetta, Z., F. Kwabia Tchana, and H. Aroui, *Self- and N_2-broadening of CH_3Br ro-vibrational lines in the v_2 band: The J and K dependence.* Journal of Molecular Spectroscopy, 2015. **308-309**: p. 33-40.

271. Pandey, P.C. and S.L. Srivastava, *Self Broadening of Microwave Spectral Lines of Slightly Asymmetric Top Molecule CH_2F_2.* Journal of Physics Part B Atomic and Molecular Physics, 1972. **5**(7): p. 1427-+.
272. Lance, B., et al., *Self-Broadening and Linestrength in the ν_2 and ν_5 Bands of CH_3F.* Journal of Molecular Spectroscopy, 1996. **180**(1): p. 100-109.
273. Ramchani, A.B., et al., *Measurements and modeling of N_2-broadening coefficients for the ν_6 band of CH_3F, comparison with CH_3Cl and CH_3Br molecules.* Journal of Quantitative Spectroscopy & Radiative Transfer, 2017. **203**: p. 480-489.
274. Lepere, M., et al., *Collisional-broadening coefficients in the ν_6 band of CH_3F perturbed by Ar.* Journal of Molecular Spectroscopy, 1998. **192**(1): p. 231-234.
275. Blanquet, G., J. Walrand, and J.P. Bouanich, *Diode Laser Measurements of N_2 Broadening Coefficients in the ν_3 band of CH_3Cl.* Journal of Molecular Spectroscopy, 1993. **160**(1): p. 253-257.
276. Dudaryonok, A.S., N.N. Lavrentieva, and J.V. Buldyreva, *CH_3Cl self-broadening coefficients and their temperature dependence.* Journal of Quantitative Spectroscopy and Radiative Transfer, 2013. **130**: p. 321-326.
277. Bray, C., D. Jacquemart, and N. Lacome, *Temperature dependence for self- and N_2-broadening coefficients of CH_3Cl.* Journal of Quantitative Spectroscopy and Radiative Transfer, 2013. **129**(Complete): p. 186-192.
278. Ramchani, A.B., et al., *N_2-broadening coefficients of methyl chloride: Measurements at room temperature and calculations at atmospheric temperatures.* Journal of Quantitative Spectroscopy & Radiative Transfer, 2014. **148**: p. 186-196.
279. Hoffman, K.J. and P.B. Davies, *Pressure broadening coefficients of transitions in the ν_5 band of methyl bromide from fitting to Voigt and Galatry line profiles.* Journal of Molecular Spectroscopy, 2009. **254**(2): p. 69-77.
280. Jacquemart, D. and H. Tran, *Temperature dependence of self- and N_2-broadening coefficients of CH_3Br ν_6 band.* Journal of Quantitative Spectroscopy & Radiative Transfer, 2008. **109**(4): p. 569-579.
281. Ben Fathallah, O., et al., *Line intensities and self-broadening coefficients of CH_3I in the region of ν_5 and ν_3+ν_6 bands.* Journal of Quantitative Spectroscopy & Radiative Transfer, 2021. **275**.
282. Dudaryonok, A., et al., *Temperature-dependence exponents for CH_3I-N_2 line-broadening coefficients.* Journal of Quantitative Spectroscopy & Radiative Transfer, 2022. **277**.
283. Hoffman, K.J. and P.B. Davies, *Pressure broadening coefficients of ν_5 fundamental band lines of CH_3I at 7μm measured by diode laser absorption spectroscopy.* Journal of Molecular Spectroscopy, 2008. **252**(2): p. 101-107.
284. Masłowski, P., et al., *Cavity-Enhanced Direct Frequency Comb Spectroscopy*, in *Cavity-Enhanced Spectroscopy and Sensing*, G. Gagliardi and H.-P. Loock, Editors. 2014, Springer Berlin Heidelberg: Berlin, Heidelberg. p. 271-321.
285. Kowzan, G., et al. *Direct Comparison of PDH and Swept Locking Scheme for Cavity-Enhanced Absorption Spectroscopy*. in *2015 European Conference on Lasers and Electro-Optics - European Quantum Electronics Conference*. 2015. Munich: Optical Society of America.